CZECH TECHNICAL UNIVERSITY IN PRAGUE
Faculty of Nuclear Sciences and Physical Engineering
Department of Physics

DISSERTATION

Low-x QCD studies using the Balitsky–Kovchegov equation

Prague 2022 Ing. Dagmar Bendová

Bibliographic Entry

Author	Ing. Dagmar Bendová Czech Technical University in Prague Faculty of Nuclear Sciences and Physical Engineering Department of Physics
Title of Dissertation	Low-x QCD studies using the Balitsky–Kovchegov equation
Degree Programme	Applications of Natural Sciences
Field of Study	Nuclear Engineering
Supervisor	doc. Ing. Jan Čepila, Ph.D. Czech Technical University in Prague Faculty of Nuclear Sciences and Physical Engineering Department of Physics
Specialist supervisor	prof. Jesús Guillermo Contreras, Ph.D. Czech Technical University in Prague Faculty of Nuclear Sciences and Physical Engineering Department of Physics
Academic Year	2022/2023
Number of Pages	140
Keywords	quantum chromodynamics, deeply inelastic scattering, structure functions parton saturation, colour dipole model, vector mesons, hot-spot model, Balitsky–Kovchegov evolution equation

Bibliografický záznam

Autorka	Ing. Dagmar Bendová České vysoké učení technické v Praze Fakulta jaderná a fyzikálně inženýrská Katedra fyziky
Název práce	Studium kvantové chromodynamiky při nízkých hodnotách Bjorkenova x pomocí Balitsky–Kovchegovovy rovnice
Studijní program	Aplikace přírodních věd
Studijní obor	Jaderné inženýrství
Školitel	doc. Ing. Jan Čepila, Ph.D. České vysoké učení technické v Praze Fakulta jaderná a fyzikálně inženýrská Katedra fyziky
Školitel specialista	prof. Jesús Guillermo Contreras, Ph.D. České vysoké učení technické v Praze Fakulta jaderná a fyzikálně inženýrská Katedra fyziky
Akademický rok	2022/2023
Počet stran	140
Klíčová slova	kvantová chromodynamika, hluboce nepružný rozptyl, strukturní funkce, partonová saturace, model barevného dipolu, vektorové mezony, hot-spot model, Balitsky–Kovchegovova evoluční rovnice

Abstract

Although quantum chromodynamics (QCD) in general allows us to calculate processes governed by the strong interaction, the behaviour of objects as complex as hadrons is still beyond the reach of exact perturbative calculations. Therefore, we have to invent QCD-based models in order to describe some aspects of strong interaction at high energies. One of them is the dipole model which can be used to calculate predictions for various QCD observables. A necessary ingredient of this model is the dipole-target scattering amplitude, which can be obtained from several theory-inspired models or from numerical solutions to the BK equation. Within this work, I studied both approaches and I start this collection of my results by a project based on the first approach, in which I study fluctuations of the proton structure (using the hot-spot model) and their influence on the saturation phenomena. Then I present an overview of the current development of the solutions to the BK equation. Using the latest approach to solve the Balitsky–Kovchegov (BK) equation for proton and nuclear targets including an explicit dependence on the impact parameter, I present predictions for several QCD processes at low-x in the colour dipole picture which are of interest for current hadron-hadron and future electron-hadron colliders. In these results, the influence from the different energy evolutions of the available approaches to the nuclear BK evolution are studied in the following photo-nuclear processes: inclusive and diffractive deeply inelastic scattering, coherent production of a J/psi meson in ultra-peripheral collisions, and deeply virtual Compton scattering. By comparison to the available data from HERA and the LHC and to the other models inspired by the colour glass condensate framework, it is demonstrated that the future measurements will be useful to discriminate amongst different approaches to saturation physics. These studies are therefore of interest for future measurements at the currently planned electron-ion colliders, which can allow us to constrain the description of QCD dynamics in high parton densities. Finally, following the recent development on the QCD phenomenology towards the next-to-leading order precision, I developed an algorithm to obtain the solutions to the BK equation at next-to-leading order including an explicit dependence on the impact parameter and studied its properties.

Key words: quantum chromodynamics, deeply inelastic scattering, structure functions, parton saturation, colour dipole model, vector mesons, hot-spot model, Balitsky–Kovchegov evolution equation

Abstrakt

Přestože nám kvantová chromodynamika (QCD) umožňuje provádět analytické výpočty pro fundamentální procesy zprostředkované silnou interakcí, chování hadronů jako celku představuje příliš komplexní problém, jenž zatím nelze přesně spočítat. K popisu chování hadronů při vysokých energiích tak používáme modely inspirované QCD a v oblastech, kde nelze aplikovat poruchovou teorii, využíváme vhodné aproximace. Jedním z takovýchto přístupů je tzv. model barevného dipólu. Nezbytnou ingrediencí pro výpočty v rámci dipólového modelu je amplituda rozptylu barevného dipólu na hadronovém terči. Tuto amplitudu lze získat z evolučních rovnic pro změnu struktury hadronů s rostoucí energií, příkladem takové rovnice je Balitsky-Kovchegovova (BK) rovnice. Další možností je využití různých modelů popisujících interakci dipólu s hadronem na základě vhodných aproximací z teorie. V této práci jsou aplikovány a srovnány oba zmíněné přístupy. První část je věnována studiu fluktuací ve struktuře protonu pomocí tzv. hot-spot modelu a jejich vlivu na jev partonové saturace. Následuje přehled vývoje a současného stavu poznání týkající se numerických řešení Balitsky-Kovchegovovy rovnice. Dále jsou prezentovány předpovědi pro několik různých procesů v rámci QCD při nízkých hodnotách Bjorkenova x, které jsem vypočítala v rámci modelu barevného dipólu s použitím nejnovějšího přístupu k řešení BK rovnice pro protony a jádra zahrnujícího explicitní závislost dipólové amplitudy na srážkovém parametru. V těchto výsledcích dále zkoumám vliv dvou různých přístupů k popisu rozptylu dipólu na jaderném terči – výpočet založený na tzv. Glauber-Gribovově modelu vs evoluce počáteční podmínky popisující dané jádro – pomocí předpovědí pro následující procesy: inkluzivní a difraktivní hluboce nepružný rozptyl, koherentní produkce mezonu J/ψ v ultraperiferních srážkách a hluboce virtuální Comptonův rozptyl. Srovnáním s dostupnými daty z experimentů na urychlovačích HERA a LHC a také porovnáním vůči jiným modelům vycházejících z teorie tzv. color glass condensate ukazuji, že budoucí měření mohou pomoci rozlišit různé přístupy k zahrnutí jevů partonové saturace. Studie předložená v této práci je tak zajímavá z hlediska měření plánovaných na budoucích elektron-jaderných urychlovačích, u kterých se očekává, že výrazně zlepší naše porozumění kvantové chromodynamice při vysokých energiích, kdy struktuře hadronů dominují gluony. V závěru práce navazuji na nejnovější vývoj fenomenologie kvantové chromodynamiky do vyšších řádů poruchové teorie a popisuji mnou vyvinutý algoritmus pro numerické řešení Balitsky-Kovchegovovy rovnice ve formě vycházející z jejího vyjádření v 1. řádu poruchové teorie a zahrnující explicitní závislost na srážkovém parametru, a studuji vlastnosti řešení této verze BK rovnice.

Klíčová slova: kvantová chromodynamika, hluboce nepružný rozptyl, strukturní funkce, partonová saturace, model barevného dipolu, vektorové mezony, hot-spot model, Balitsky–Kovchegovova evoluční rovnice

Acknowledgement

I would like to express my gratitude to all people in my life, without whom this long pursued dream could never have come true.

First, I would like to thank to my supervisors, doc. Jan Čepila and prof. Jesús Guillermo Contreras, for their kind support, patience and time they devoted to addressing all my questions and research problems, and an endless effort with which they guided me through my whole doctorate.

I would also like to thank prof. Victor Goncalves for his inspiring ideas and fruitful cooperation which led to many interesting results and successful publications. Big thanks also goes to my former colleague Marek Matas, with whom we worked on several projects during his and mine doctorate and who set up an example of a successful PhD candidate for me.

I would also like to appreciate my PhD colleagues, who inspired me with their work and many discussions about physics. Together with all colleagues, my classmates, and other students from our study branch, they have managed to create an amazing work environment and a friendly community within our department.

I am also grateful to the Czech Technical University in Prague, Faculty of Nuclear Sciences and Physical Engineering, for being my Alma Mater, for the great education it gave me, and for the material support provided during my doctorate. It has been a great institution to study and work at, and I hope it will thrive further to bring up many great scientists.

The biggest "thank you" goes to my family and loved ones for their intense support, especially to Robert for standing by my side during all those hard times. Finally, I would like to thank all my friends for their encouragement and for exploring the world with me.

Declaration

I hereby declare that this thesis is the result of my own work and all the sources I used (literature, projects, software, etc.) are in the list of references. I have no objection against the use of this work in compliance with the act §60 Law No. 121/2000 Coll. (Copyright Act), and with the rights connected with the copyright act including the changes in the act.

In Prague, December 2022 Ing. Dagmar Bendová

Contents

Introduction

Studying the nature of matter around us has been one of the main knowledge pursuits since the natural philosophy of the ancient times, through the establishment of classical physics in the 17^{th} - 19^{th} centuries, the birth of quantum mechanics at the beginning of the 20^{th} century, and towards the present era of the standard model of particle physics, which encompasses all current knowledge about elementary particles and the fundamental forces governing their interaction (excluding gravity). One of these three forces is the strong interaction between quarks and gluons, described by quantum chromodynamics (QCD). Due to the non-Abelian nature of QCD, the strength of the interaction increases at large distances and therefore, quarks and gluons are confined within the colour neutral hadrons such as protons or neutrons. Furthermore, the strong interaction between the constituent quarks and gluons causes an attractive force which binds nucleons within the nuclei.

Even though it is possible to perform exact calculations for a single interaction between the free quarks or gluons, their confinement within hadrons and the related non-perturbative effects make the task almost impossible. Not only the hadrons such as protons are composed of valence quarks, as predicted by the additive quark model by Gell-Mann and Zweig [1, 2], but also of an abundance of mediating gluons and sea quarks emerging from the vacuum. All these constituents interact among themselves, creating an object with rich inner dynamics. Although the outer quantum numbers of hadrons such as its spin or mass can be measured precisely, the inner dynamics of its constituents and their individual contribution to these overall quantities remain an untangled problem of QCD from both the theoretical and experimental perspectives.

The structure of the proton has been extensively studied in deeply inelastic scattering (DIS) experiments at HERA in interactions of electrons with protons via the exchange of a virtual photon. One of the important results coming from these measurements is that the inner structure of the proton changes with energy and it also depends on the scale at which it is measured. With an increasing scale of the process, given by the virtuality Q^2 of the photon, one observes not only valence quarks, but also an increasing number of sea quarks (and indirectly also gluons) coming from the quantum fluctuations of the proton structure. This can be interpreted such that with increasing resolution, the original constituents split into smaller ones, allowing to observe the finer structure of the proton. This evolution of the proton structure with increasing Q^2 is described by the Dokshitser–Gribov–Lipatov–Altarelli–Parisi (DGLAP) equations [3–5]. Moreover, quarks and gluons (collectively denoted as partons) are considered to carry a fraction x of the proton's longitudinal momentum within the so called infinite momentum frame, where the associated momenta are considered to be large enough to neglect their transverse component. Therefore, the structure of the proton may not only depend on the resolution of the photon probe, but also on the change of the redistribution of the proton's longitudinal momentum. At large values of x, valence quarks are considered to dominate the structure of the proton, carrying most of its momentum. However, when going towards very small values of Bjorken-x, gluons start to dominate as they emerge wildly with increasing energy due to gluon splitting. The evolution of gluon densities with decreasing x for a fixed Q^2 is described by the Balitsky–Fadin–Kuraev–Lipatov (BFKL) evolution equation [6, 7]. This

equation gives the linear evolution of gluon densities with increasing rapidity $Y \sim \ln\left(\frac{1}{x}\right)$. Moreover, it predicts an infinite growth of gluon densities with decreasing x, which contradicts the unitarity of the cross section and therefore violates the Martin–Froissart bound [8, 9]. The growth of the gluon densities is expected to be tamed by gluon recombination, which causes the evolution of gluon densities to become nonlinear with decreasing x. This phenomenon is called *parton saturation* and it is connected to the *saturation scale* $Q_s(x)$, at which the nonlinear effects start to manifest themselves. Moreover, these effects are expected to be enhanced in nuclei, which is one of the motivations for the planned electron-ion facilities [10, 11].

The non-linear evolution of parton densities including saturation is naturally incorporated within the Balitsky–Kovchegov (BK) equation [12–14], which gives the evolution with rapidity Y of the colour dipole scattering amplitude N. The colour dipole model [15–18] represents an approach to describe the strong interaction within deeply inelastic scattering at low-x, where the virtual photon emitted by the incoming lepton can be seen as fluctuating into a $q\bar{q}$ pair. This colour dipole then interacts strongly with the target hadron via gluon exchange and therefore serves as a probe of the hadronic structure. Within a proper reference frame, the evolved dipole structure can be related to the wave function of the target hadron. Dipole amplitudes can be therefore used to calculate structure functions and the cross section of DIS at low-x. The colour dipole approach can also be extended to diffractive processes, characterised by the exchange of quantum numbers of vacuum (which can also be viewed through the interaction of the dipole with the hadron). Their advantage is a modified sensitivity to the gluon part of the target structure, thus they can provide additional information on the QCD dynamics of the hadron structure, including the saturation phenomenon. Moreover, the cross sections for the exclusive processes such as vector meson production and deeply virtual Compton scattering are directly related to the generalised parton distributions and therefore are sensitive to the transverse shape of hadrons and the spatial distribution of gluons in the impact-parameter plane.

The BK equation is in general a four-dimensional integro-differential equation which does not have an analytical solution. The dipole amplitudes are therefore obtained from numerical solutions to the BK equation. Due to the dimensionality of the problem and the related high demand on computing power, some approximations are usually made to obtain the numerical results within a reasonable timescale. The numerical solution to the BK equation at leading-order accuracy has been successfully obtained by several groups, see e.g. Refs. [19–21]. Moreover, the BK equation has been recently extended into the next-to-leading order (NLO) accuracy of the perturbative theory [22], and there have been several attempts to include some of the NLO contributions into the LO calculation [23–25] and to obtain its full numerical solutions [26, 27]. On the other hand, there has also been a development in the solutions of the BK equation including the explicit impact-parameter dependence for proton [28, 29] and nuclear [30] targets and their subsequent applications to QCD phenomenology [29, 31–33].

There has also emerged an interest to study the fluctuations of the hadronic structure using the description of QCD processes within the dipole approach, see e.g. Refs. [34–38]. Proton structure fluctuations have been shown to be useful to correctly describe the production of vector mesons in the incoherent process, where the target hadron is dissociated as a result of the interaction. Such studies are interesting due to the quantum nature of hadrons. We already know that their structure cannot be taken as a simple static set of quarks and gluons, but more appropriately, they should be viewed as dynamical objects whose number and distributions of partons change with energy. Models including partonic fluctuations can be therefore used to describe the initial state of the proton or nuclei in the early stages of the hadronic interactions and to study the effects of the initial geometry on the final state observables such as flow effects in small systems – for a recent review see e.g. [39].

This thesis is organised as follows: In Chapter 1, I introduce deeply inelastic scattering as a tool to

study the proton structure. Following the historical context, I describe the early interpretations of the experimental observations and the subsequent theoretical development of our understanding of the proton structure. Subsequently, the evolution of parton densities with increasing energy and its saturation in the low-x region are described. The regime of DIS at low-x and the necessity for the description of the strong interaction within the photon-proton scattering brings us to the dipole model approach to DIS and its extension to other QCD processes such as diffractive DIS and the production of exclusive final states. Chapter 2 starts with introducing the approximations used in QCD phenomenology to calculate the dipole-target cross section and describes how the fluctuations of the proton structure in the transverse plane can be included into the calculation of QCD observables within the so called *hot-spot model*. This chapter also presents my results from Ref. [37] on the exclusive and dissociative production of vector mesons in photon-proton collisions and the implications of the dissociative cross section behaviour for gluon saturation. Chapter 3 presents the Balitsky–Kovchegov equation as a general tool to obtain the dipole scattering amplitude, starting from its simplest leading-order (LO) approximations, introducing the incorporation of the next-to-leading order corrections and finalising the review with the full next-to-leading order (NLO) version of the equation. The approach to solve the BK equation with an explicit impact-parameter dependence is also introduced, including the recent development to solve this equation for both protons and nuclei. Chapter 4 presents a summary of the results I published together with my colleagues in papers [29,31–33]. These publications provide predictions for several QCD observables within the colour dipole approach using numerical solutions to the impact-parameter dependent Balitsky–Kovchegov equation at leading-order accuracy. These predictions are also compared to other dipole models used in QCD phenomenology and together, the results provide predictions to study these processes in future measurements at the LHC and at the proposed electron-ion colliders. Finally, Chapter 5 presents my work on the numerical solutions to the BK equation at the next-to-leading order accuracy with an explicit dependence on the impact-parameter and summarises the obtained results and their implications to further development in this direction. The thesis concludes with a summary, followed by the list of conference proceedings and papers I have published with my collaborators in peer-reviewed journals during my doctorate, and by the reproduction of the said papers.

Chapter 1

The QCD structure of the proton

1.1 Deeply inelastic scattering

Before we immerse ourselves into the low-x phenomenology, let us first introduce the process through which the journey of studying the proton structure began. Deeply inelastic scattering allows us to study the hadronic structure using the interaction of a nucleon (or nucleus) with a high-energy lepton. It played a key role in the development of QCD through the identification of the point-like constituents of the proton from data measured in fixed-target experiments at SLAC [40, 41] in the late sixties and seventies. At the same period of time, the quark model [1, 2] and the parton model [42, 43] were developed providing, together with these experimental results, a new insight into the structure of hadrons. Later on, the process was intensively studied in the H1 and ZEUS experiments at HERA where the proton structure has been measured with great precision (see e.g. [44–49]) and its results initiated a large interest in QCD phenomenology at low-x.

1.1.1 Kinematics and DIS cross section

Deeply inelastic scattering can be, in short, denoted by the following equation

$$l(k) + N(P) \rightarrow l'(k') + X \tag{1.1}$$

and its graphical representation can be seen in Fig. 1.1. It shows that the incoming high-energy lepton with four-momentum k emits a virtual photon with momentum q. The lepton's four-momentum has changed to k' and the momentum carried by the photon can be estimated from the measurement of the electron scattering angle. The photon interacts with the hadron (here we will consider a proton to be more specific), which has a four-momentum P. As a result of this interaction, the proton is broken apart and a final state hadronic system X is created with a mass M_X, given by the centre-of-mass energy of the photon-proton system as

$$W^2 \equiv (P + q)^2 = M_X^2, \tag{1.2}$$

where the natural system of units with $c = 1$ is used. The scale at which the target proton is probed is called virtuality and it is defined as the negative square of the four-momentum q

$$Q^2 \equiv -q^2 = -(k - k')^2. \tag{1.3}$$

The inelasticity of the collision is defined as

$$y \equiv \frac{P \cdot Q}{P \cdot k}, \tag{1.4}$$

and represents the fraction of the electron energy transferred by the photon to the hadron in its rest frame. These two variables are related to the centre-of-mass energy $s \equiv (P + k)^2$ of the DIS process as

$$xys = Q^2, \tag{1.5}$$

where the Bjorken-x variable is defined as

$$x \equiv \frac{Q^2}{2P \cdot q}. \tag{1.6}$$

For the case of elastic scattering ($Q^2 = 0$ and $y = 0$), the wavelength of the probing photon is large and the proton is seen as a point-like particle of charge $+e$. If the momentum-transfer is increased, so is the photon wavelength decreased and the proton interacts as an object of finite size $\sim$ 1 fm. For a very large momentum transfer, the photon wavelength is much smaller than the size of the probed object and it is possible to "see" the inner structure of the target. Therefore, the virtuality sets the distance scale probed in the process. Also, let us note that the DIS process could, in theory, be also mediated by the electroweak bosons. However, these channels are suppressed due to the large mass of these bosons and therefore, we will consider only the virtual photon as a mediator of the interaction in the rest of the text.

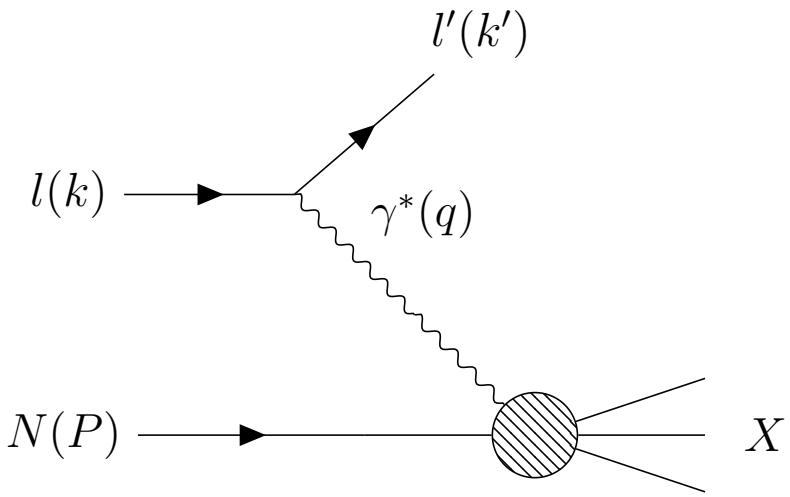

Figure 1.1: A schematic diagram of electron-proton scattering. The incoming, resp. outgoing lepton four-momentum is denoted by k, resp. k', q denotes the virtual photon γ^* four-momentum, P denotes the incoming hadron four-momentum and X denotes the final state system. Figure adapted from the previous work [50].

As we described above, the DIS process can be divided into two parts. The emission of the photon from a lepton is a well understood process which can be computed from quantum electrodynamics (QED). However, the proton structure is completely unknown at this stage and we cannot calculate the photon-proton interaction part from perturbative QCD directly. Yet, it is possible to parametrise it by introducing a general hadronic tensor. By accounting for the symmetry requirements, omitting the parity violating terms and the terms which would result in zero when contracted with the leptonic part (for a detailed derivation see e.g. [51, 52]), we can express the differential cross section for the high-energy deeply inelastic electron-proton scattering process as

$$\frac{\mathrm{d}^2\sigma}{\mathrm{d}x\mathrm{d}Q^2} = \frac{4\pi\alpha^2}{Q^4}\left[y^2F_1(x,Q^2) + \left(1 - y - \frac{m_p^2x^2y^2}{Q^2}\right)\frac{F_2(x,Q^2)}{x}\right] \xrightarrow{s\to\infty} \frac{4\pi\alpha^2}{Q^4}\frac{F_2(x,Q^2)}{x}, \tag{1.7}$$

where $\alpha = \frac{e^2}{4\pi\epsilon_0} \approx \frac{1}{137}$ is the electromagnetic coupling constant. The functions F_1 and F_2 include the photon-proton interaction and therefore carry the information about the proton structure.

Experimental measurements of the structure functions are often expressed by the reduced cross section

$$\sigma_r(y,x,Q^2) = F_2(x,Q^2) - \frac{y^2}{1+(1-y^2)}F_L(x,Q^2), \tag{1.8}$$

in order to eliminate the QED part of the interaction. Here the function F_L is the longitudinal structure function given by

$$F_L = F_2 - 2xF_1. \tag{1.9}$$

1.1.2 The parton model and the structure of the proton

Based on the above derivation, one can now ask: "What is the behaviour of structure functions $F_i(x,Q^2)$ depending on x and Q^2?". Based on observations from data, J. D. Bjorken suggested that the structure functions depend only on the x variable and therefore, do not change with increasing Q^2 – a phenomenon called *Bjorken scaling*. In order to interpret the experimental results, R. Feynman proposed a model in which the photon scatters off elastically on one of a quasi-free point-like constituents of the proton, as depicted in Fig. 1.2. The existence of such point-like constituents would be in accordance with Bjorken scaling, as was indeed confirmed by the first measurements of F_2 [52, 53]. However as will be discussed later, it holds only in a limited region of (x,Q^2) due to the complex dynamics of the proton structure. Since the idea of the quark model [1, 2] was not yet generally accepted at that time, the constituents were called partons (standing for "part of the proton") and within the infinite momentum frame, they were supposed to be massless and each carries a fraction of the total proton longitudinal momentum while their transverse momenta are supposed to be negligible. This momentum fraction then corresponds to the variable x defined in Eq. (1.6) and one expects that the sum over all fractional momenta xP should add up to the original proton momentum P.

Comparing the high-energy limit for the single electron-parton scattering [52]

$$\frac{\mathrm{d}\sigma}{\mathrm{d}Q^2} = \frac{4\pi\alpha^2e^2}{Q^4} \tag{1.10}$$

with the high-energy limit of DIS cross section (1.7) and with the assumption that partons are spin-$\frac{1}{2}$ particles, one can obtain the following expression for the F_2 structure function

$$F_2(x) = x\sum_i e_i^2 f_i(x). \tag{1.11}$$

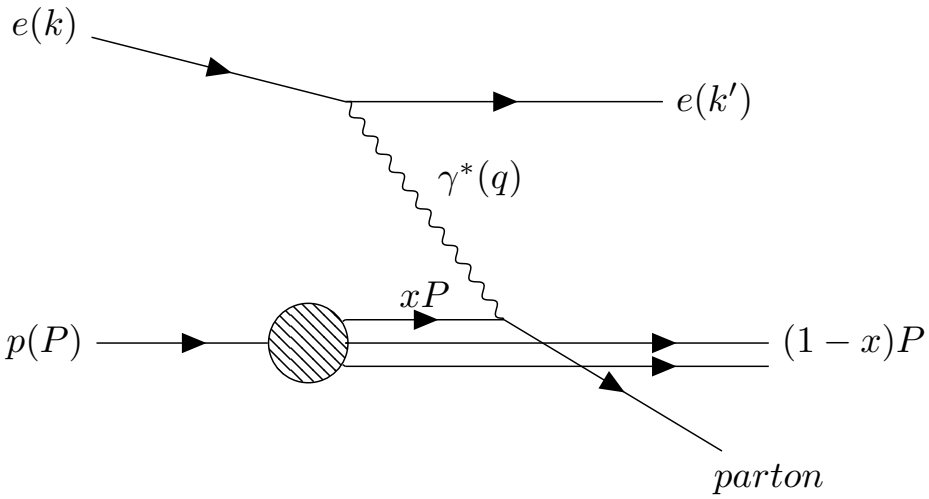

Figure 1.2: Sketch of the parton model interpretation of deeply inelastic scattering. Figure adapted from the previous work [50].

At finite collisions energies, F_1 may be rewritten equivalently as

$$F_1(x) = \frac{1}{2} \sum_i e_i^2 f_i(x), \tag{1.12}$$

where the sum runs over all parton flavours and e_i is the effective charge of the parton of flavour i. The functions $f_i(x)$ are the parton distribution functions (PDFs) which give us the probability to find the parton of type i with a momentum fraction x within the proton. These two formulas lead us to the so-called Callan-Gross relation [54]

$$F_2(x) = 2xF_1(x). \tag{1.13}$$

The experimental measurements at the time showed the validity of the Callan-Gross relation [55], which confirmed the link between partons and the spin-$\frac{1}{2}$ quarks of the additive quark model [1, 2].

The total momentum P of the proton should be reconstructed from the sum over the momenta of all partons. Any deviance from the total sum being P (or 1 if we sum up the momentum fractions x) would advocate for the presence of additional constituents within the proton. Due to the experimental results of that time, these particles would have to occupy the yet unprobed low-x region of momentum fractions and at the same time, they could not be fermions. Moreover, they would be electrically neutral as they were not directly probed by the virtual photons.

Indeed if we perform this sum for the proton and neutron structure functions F_2, we arrive to the conclusion that up and down quarks carry approximately 36 % and 18 % of the total proton momentum, respectively. Since the strange (sea) quarks carry even tinier portion of the momentum P, it is obvious that $\sim$ 50 % of the proton momentum was unaccounted for by the charged quarks and has to be carried by those neutral partons, called gluons. This observation was also supported from the theoretical analysis of the cross section measurements [43]. As we can see now, the longitudinal structure function F_L

(1.9) represents the measure of the violation of the Callan-Gross relation (1.13), as $F_L = 0$ if the proton consists of only spin-$\frac{1}{2}$ fermions (i.e. quarks). The longitudinal structure function therefore gives a direct measure of the gluonic contribution to the inner structure of the proton. The structure function F_L was indeed measured by later experiments at HERA [56, 57], however the precision of such measurement is limited as can be seen from the plots in the said papers and even more strikingly from the recent proton F_2 results [48, 49].

1.1.3 The QCD-improved parton model

Although Bjorken scaling can be observed in the region of $x \sim 10^{-1}$, it is clearly violated when one observes the low-x region as can be seen from Fig. 1.3. It is therefore necessary to include corrections to the quark distribution functions which involve the gluon contribution to the proton structure and would explain the divergence from the naive quark parton model assumptions. We will start from the leading order QCD correction $\sim O(\alpha_S)$ in which the parton radiates a gluon before the interaction with the probing photon. The correction to the structure function F_2^p is then [51, 52]

$$\frac{F_2^{\gamma^* q \to qg}}{x} = \sum_i e_i^2 \int_x^1 \frac{\mathrm{d}y}{y} f_i(y) \left[\frac{\alpha_S}{2\pi} P_{qq}(z) \ln\left(\frac{Q^2}{\mu^2}\right) \right], \tag{1.14}$$

where μ is the infrared cut-off to regularise soft gluon emission and P_{qq} is the quark splitting function giving the probability that a quark with momentum fraction y emits a gluon, which results in the momentum fraction x of the "new" quark. The logarithmic term in (1.14) is responsible for the Bjorken scaling violation as F_2 is no longer function of the x alone, but of both variables (x, Q^2) simultaneously. This requires a redefinition of parton distribution functions for the case of interacting quarks as a sum of the "bare" quark distribution $q(x)$ and the QCD-correction term – resulting in so called "dressed" PDFs. The change of the quark distribution function at the higher resolution caused by gluon radiation can be expressed by the evolution equation

$$\frac{\mathrm{d}q(x, Q^2)}{\mathrm{d}\ln Q^2} = \frac{\alpha_S(Q^2)}{2\pi} \int_x^1 \frac{\mathrm{d}y}{y} P_{qq}\left(\frac{x}{y}\right) q(y, Q^2), \tag{1.15}$$

which is the so called Altarelli-Parisi evolution equation [4] for the dressed non-singlet[1] quark distribution function $q(x, Q^2)$.

Gluon radiation from the quark is not the only possible scenario of QCD corrections. At the leading order of the strong coupling α_S, there are four possible splitting scenarios:

- Gluon emission from the quark, resulting in a quark with a new momentum fraction (the above described case). Corresponds to the splitting function $P_{qq}(z)$.
- Quark-antiquark recombination, resulting in a gluon with changed momentum fraction with respect to the original quark. Corresponds to the splitting function $P_{gq}(z)$.
- Emergence of a quark-antiquark pair from a gluon. Corresponds to the splitting function $P_{qg}(z)$.
- A gluon emission from its parent gluon (represented by the triple-gluon vertex). Corresponds to the splitting function $P_{gg}(z)$.

[1] The non-singlet quark distribution function coincide with the valence quark distribution at the leading order.

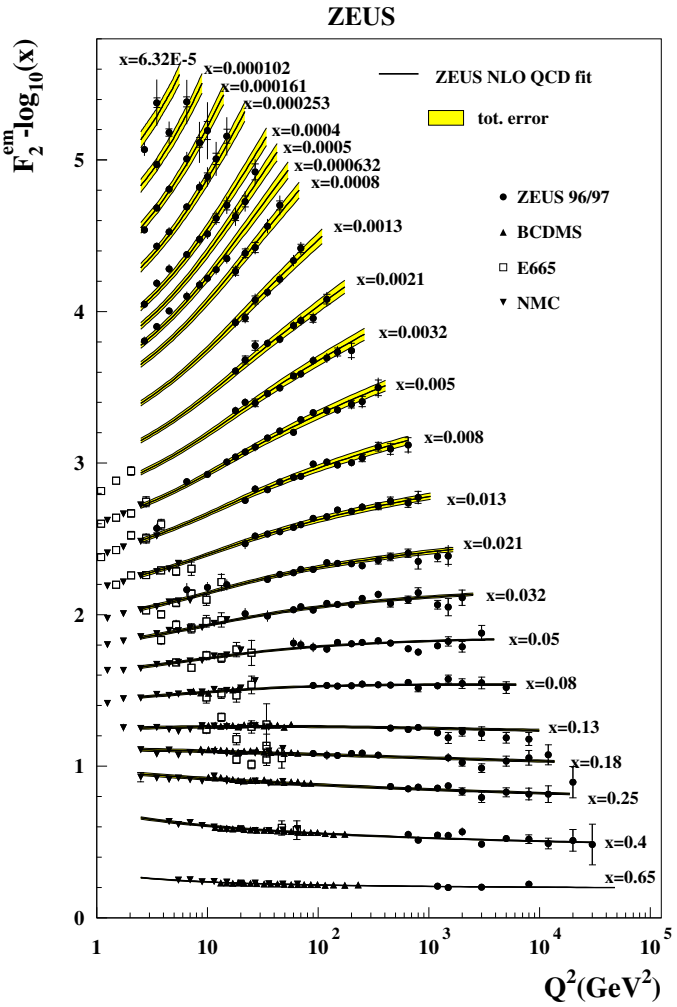

Figure 1.3: The compilation of the proton structure function F_2 measurements from several DIS experiments. Figure from Ref. [46].

The splitting functions are coupled to the quark and gluon distribution functions, forming the set of DGLAP equations [3–5] for the evolution of (anti)quark and gluon distributions

$$\frac{\mathrm{d}}{\mathrm{d}\ln \mathrm{Q}^2}\begin{pmatrix} q(x,Q^2) \\ g(x,Q^2) \end{pmatrix} = \frac{\alpha_S}{2\pi}\int_x^1 \frac{\mathrm{d}z}{z}\begin{pmatrix} P_{qq}(z) & P_{qg}(z) \\ P_{gq}(z) & P_{gg}(z) \end{pmatrix} \otimes \begin{pmatrix} q(\frac{x}{z},Q^2) \\ g(\frac{x}{z},Q^2) \end{pmatrix}, \tag{1.16}$$

where $z = x/y$ represent the change of the momentum fraction due to the one of the above described processes. These equations describe the change in the PDFs to leading-logarithmic accuracy. They also allow for a new interpretation of Q^2 as an upper bound for the transverse momentum k_T of the emitted partons – increasing Q^2 provides more transverse phase space for new emissions. These transverse momenta in turn restrict the phase space over which the partons are located in the transverse plane $r_T \sim 1/Q^2$. Therefore, Q^2 can also be interpreted as the resolution at which the proton structure is

probed. With these additional emissions, the distribution functions are changed accordingly and the resulting F_2 grows with increasing resolution Q^2.

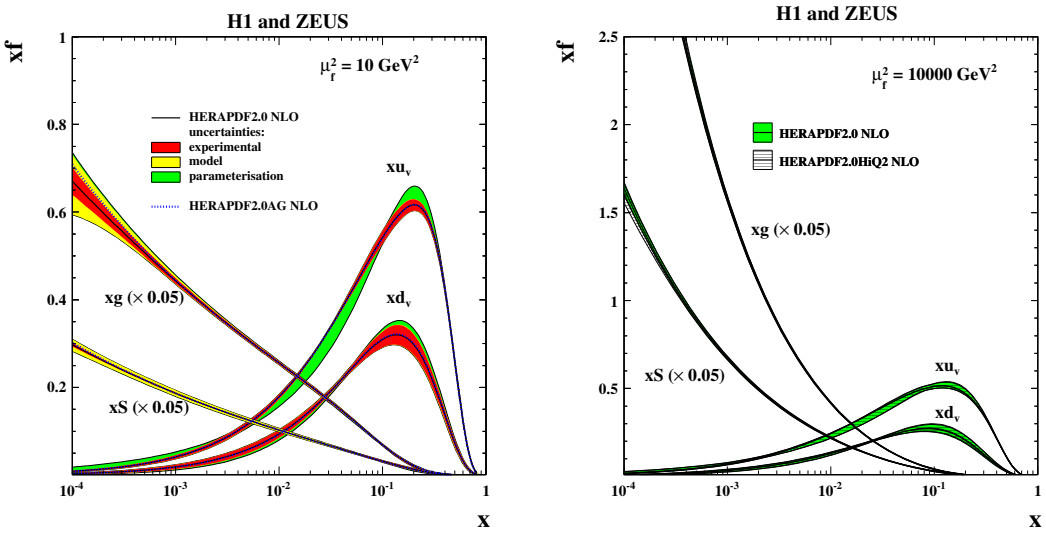

Figure 1.4: The evolution in Bjorken-x of the gluon, sea-quarks and valence-quarks distributions for scale 10 GeV^2 (left) and $Q^2 = 10^4$ GeV^2 (right) measured at HERA [48].

1.2 Parton saturation

With increasing resolution Q^2 of the probing photon, the direction of the evolution of PDFs goes towards increasing the transverse phase space for new emissions and hence towards the so called dilute regime of the proton structure. Although the gluon distribution also obeys this evolution, we can observe from Fig. 1.4 that it grows faster when x is substantially decreased. This is due to the fact that the gluon splitting function entering Eq. (1.16) has a singularity at very small z and therefore, the gluon distribution evolves much faster towards low-x compared to the quark PDF. It can be shown that gluons are emitted even more often due to the large logarithms present in their emission probability coming from the Bremsstrahlung law (see e.g. [58])

$$P_{gluon\ emission} \sim \alpha_S \ln \frac{Q^2}{Q_0^2} \ln \frac{1}{x}. \tag{1.17}$$

If one or both of these two logarithms are large enough to compensate for the value of the strong coupling constant at the given scale (which is small in the perturbative region), then the probability of gluon emission grows (and can even diverge). The same conclusion can also be made based on the approximate solution of the gluon DGLAP equation which involves powers of Eq. (1.17) as a resummation parameter – the resummation of such terms containing two large logarithms is then called a double logarithmic approximation (DLA)[2]. From that, it can be shown [59] that the growth of the gluon distribution is faster

[2]Since Q^2 determines the resolution in the transverse size, the associated $\ln Q^2$ is often called the transverse logarithm and vice versa, the $\ln(1/x)$ is called the longitudinal logarithm, since Bjorken-x determines the longitudinal lifetime of the parton [59].

than a power of $\ln(1/x)$, but it should be slower than a power of $1/x$. The dominance of gluons in the small-x region is therefore a direct implication coming from the DGLAP equations, although they fail to describe its behaviour correctly in this regime.

1.2.1 Small-x evolution

The logarithm involving Q^2 was taken care of by the resummations in the DGLAP equation. We will now have a closer look at the behaviour with $x \to 0$ at a fixed scale [3] Q^2 (corresponding to partons having roughly the same transverse size), where a more appropriate equation is necessary to describe such evolution where

$$\alpha_S(Q^2) \ln \frac{1}{x} >> \alpha_S(Q^2) \ln \frac{Q^2}{Q_0^2}.$$

It is important to point out that the small-x regime corresponds to the high energy limit of QCD, as can be seen from Eq. (1.5) – at a fixed scale Q^2, a large CMS energy s results in a small Bjorken-x.

The equation which resums the large logarithms of order $\alpha_S \ln \frac{1}{x}$ is called the BFKL equation [6, 7] and it describes the regime where with increasing energy, gluons are emitted in abundance. The BFKL equation strongly orders the successive gluon emissions with respect to their decreasing momenta fractions as

$$x_0 >> x_1 >> ... >> x_i >> ...x_{n-1} >> x_n$$

and "builds" so called gluon ladders from the proton towards the parton scattering. In the momentum representation, its leading logarithmic approximation reads as [59, 60]

$$\frac{\partial f(x,k_T^2)}{\partial \ln \frac{1}{x}} = \frac{2\alpha_S}{\pi} k_T^2 \int_0^\infty \frac{\mathrm{dk}_\mathrm{T}'^2}{k_T'^2} \left[\frac{f(x,k_T'^2) - f(x,k_T^2)}{|k_T'^2 - k_T^2|} + \frac{f(x,k_T^2)}{\sqrt{4k_T'^4 + k_T^4}} \right], \tag{1.18}$$

where $f(x,k_T^2)$ represents the unintegrated gluon distribution which gives the number of partons at a certain value of (x,k_T^2), where k_T is their transverse momentum. It is related to the gluon PDF (which counts all partons with $k_T^2 \leq Q^2$) through the k_T^2-integral as

$$xg(x,Q^2) \equiv \int_0^{Q^2} \frac{\mathrm{d}k_T^2}{k_T^2} f(x,k_T^2). \tag{1.19}$$

For an analytical solution of the BFKL equation at fixed α_S, it can be shown [58, 59] that the gluon distribution grows with decreasing x as

$$f(x,k_T^2) \sim x^{-\lambda}; \qquad \lambda = \frac{\alpha_S N_c}{\pi} 4 \ln 2. \tag{1.20}$$

It is straightforward to see from the above expression that the gluon density does not grow logarithmically with $1/x$, but even more dramatically as a power of $1/x$; meaning that the growth of the gluon distribution at small-x given by the BFKL equation is much faster than the growth given by the DGLAP equation. This results in regions of high partonic density in the hadron wave function and leads to the very interesting problem of unitarity violation. The unitarity constraint known as the Froissart-Martin bound [8, 9] gives a restriction on the total cross section growth with CMS energy s as

$$\sigma(s) \leq C \ln^2(s), \tag{1.21}$$

[3] We assume that the fixed scale is large enough to work in the perturbative regime where $\alpha_S < 1$.

where C is a constant fitted from data. However, the growth of the gluon distribution from Eq. (1.20) given by the BFKL equation implies

$$\sigma(s) \sim s^{\lambda}, \tag{1.22}$$

resulting in a power-like growth of the cross section and subsequent violation of the Froissart bound in Eq (1.21).

1.2.2 Saturation at low-x

The divergence of the cross section represents a serious problem for our theory. It is therefore desirable to introduce a mechanism which would restore the unitarity by taming the violent grow of gluon densities at small-x. Let us imagine such situation with the help of Fig. 1.5, which schematically shows the two directions of evolution using the transverse plane representation of the proton structure. When the proton is subject to a probe with increasing virtuality, smaller transverse distances are probed and new partons with smaller transverse size are seen by the probe, as a consequence of the DGLAP evolution. On the other hand, for a fixed scale Q^2, partons retain the same transverse size while new emissions with decreasing x are generated. This behaviour is driven by the BFKL evolution equation. To a certain point, the evolution of parton densities with $\ln(1/x)$ is linear, however when evolving further and reaching a certain low value of x, the proton enters a state where it is filled with gluons, the so called dense regime. When the resolution Q^2 is again increased, so is the transverse size of partons decreased and the phase space for new emissions is again available and the proton returns to the dilute regime. However if Q^2 is kept fixed, a critical density of gluons is reached, their wave functions start to overlap and an opposite process to gluon branching, namely gluon recombination, starts to play a significant role. The growth of the gluon density is tamed by their recombination and therefore, the parton density becomes saturated and its subsequent evolution is non-linear. The recombination of gluons also vacates some phase space for new emissions, generating a dynamical balance between the emergence of new fluctuations and their recombination. Such balance is reached at some critical scale $Q_s(x)$ called the *saturation scale*, which therefore determines the region where saturation becomes significant and separates the dilute and dense regimes. Moreover it is expected that this scale is modified in nuclei as [61, 62]

$$Q^2_{s,A} \sim A^{\frac{1}{3}} Q^2_{s,p} \sim A^{\frac{1}{3}} x^{-\lambda}, \tag{1.23}$$

which means that the saturation regime is reached sooner in heavy nuclei as a result of the abundance of gluons in the nuclear matter accelerated to high energies.

As suggested above, the gluon recombination process is not included in the BFKL evolution equation. To describe such states where high densities of gluons are reached, the effective field theory known as Colour Glass Condensate (CGC) has been established. In its formalism, the incoming probe obtains an internal structure which is perturbatively calculable within the light-cone QCD formalism, e.g. the virtual photon can be seen as a $q\bar{q}$ fluctuation with the quantum numbers of vacuum. It interacts with the target hadron, which is seen as a set of strong colour fields emerging from the high density of gluons. The evolution of the hadronic system with decreasing x is described by an infinite hierarchy of coupled JIMWLK equations [63–69]. It works with two "types" of partons, where those with large x serve as sources of strong colour fields which generate the small-x partons. With the decreasing-x, the originally low-x partons become the further sources of colour fields and generate new emissions at even smaller x. At the same time, the possibility for recombinations of low-x gluons is incorporated. The derivation and further description of the JIMWLK equation and the CGC formalism is outside the scope of this work, more details can be found e.g. in [59, 70–73].

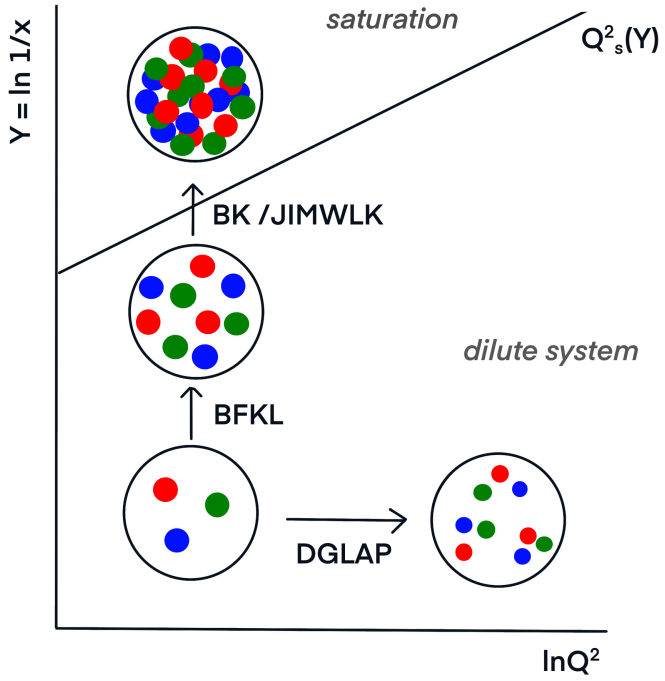

Figure 1.5: Diagram showing the QCD evolution of the partonic structure of the proton and the validity range for the different evolution equations.

Due to the complexity of the JIMWLK evolution, there is no analytical solution to this equation and it has to be calculated numerically. This is also true for a special case of the JIMWLK equation called the Balitsky-Kovchegov equation [12–14], which represents the main topic of this thesis. The equation can be obtained from the hierarchy of JIMWLK equations in the mean-field approximation and in the limit of large N_c as a non-linear evolution equation for the scattering of a colour dipole off the hadronic target [13, 14], or it can be equivalently obtained as a generalisation of the BFKL equation (which is also a special case of the JIMWLK hierarchy) [12].

Although the concept of parton saturation seems compelling and straightforward, the main problem is that there has never been its direct and unequivocal experimental observation. The precision of suitable measurements does not allow for conclusive statements about experimental signs of saturation and even the measurements at HERA did not reach low-enough x where the saturation could manifest fully. However, there are hints from different experimental observables where the signs of saturation could manifest themselves and it is expected that saturation effects will emerge even sooner in nuclear DIS experiments to be performed at currently planned electron-ion colliders [10, 11]. Moreover, the CGC framework can be used to describe the QCD evolution of the initial state and its study is therefore useful for the description of the ultra-relativistic heavy-ion collisions.

This thesis is devoted to the description of such processes where saturation phenomena are expected to emerge, using the phenomenological calculations based on the CGC theory. In order to present these results, I shall first introduce an approach to describe deeply inelastic scattering at low-x — the colour

dipole model — and how to extend this approach to the description of other QCD observables. In the following chapter, I will use this approach and introduce the so called hot-spot model for the description of the proton structure at high gluon densities. The BK equation will also be properly introduced within the colour dipole formalism and I will describe my work on its solutions and applications to QCD phenomenology in the later chapters.

1.3 Colour dipole model of DIS

The strong interaction within DIS can be described using the colour dipole approach [15–18]. In the high-energy limit, which corresponds to small-x, it is useful to move from the infinite momentum frame to a frame where the hadron as a target particle is at rest. In such a reference frame, the interaction between the virtual photon and the proton can be factorised out into two steps, as depicted in Fig. 1.6:

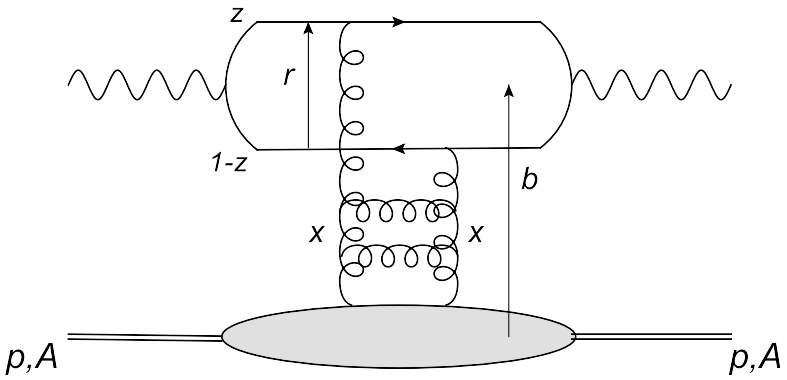

Figure 1.6: A schematic diagram for deeply inelastic scattering within the colour dipole approach.

1. Formation of the colour dipole

In the target-hadron rest frame, the photon can be seen as fluctuating into one of its Fock's states. Any such fluctuation has the quantum numbers of the original photon and at leading-order, it is represented by a $q\bar{q}$ pair. This results into the presence of colour-charge carriers in the interaction, however from the external point of view, this state is colourless. The colour dipole model is thought to be valid for $x \sim 10^{-2}$ or less; under this conditions, the lifetime of the $\gamma^* \to q\bar{q}$ fluctuation is much longer than the timescale of the interaction with the target.

The probability of the $\gamma^* \to q\bar{q}$ splitting can be calculated from light-cone perturbative theory. The photon wave functions, squared and summed over the polarisations of the virtual photon and over the $q\bar{q}$ helicities, can be written [59] as

$$|\Psi^*\Psi|_T^f = \frac{N_c\alpha}{2\pi^2} e_f^2 \left[\left(z^2 + (1-z)^2 \right) \epsilon^2 K_1^2(\epsilon r) + m_f^2 K_0^2(\epsilon r) \right], \tag{1.24}$$

$$|\Psi^*\Psi|_L^f = \frac{N_c\alpha}{2\pi^2} e_f^2 \left[4Q^2 z^2 (1-z)^2 K_0^2(\epsilon r) \right], \tag{1.25}$$

where T and L refer to transverse and longitudinal polarisation of the virtual photon, $\alpha \approx \frac{1}{137}$ is the fine structure constant, e_f is the electric charge of the quark of flavour f in the units of elementary charge, K_0 and K_1 are modified Bessel functions of the second kind, z is the momentum fraction of the original

photon carried by the quark (the other carries a momentum fraction 1-z), $r \equiv |\vec{r}|$ is the transverse size of the colour dipole and

$$\epsilon^2 = z(1-z)Q^2 + m_f^2, \tag{1.26}$$

where m_f is an effective mass of the quark with flavour f.

2. Interaction of the colour dipole with the target hadron

The interaction between the dipole and the hadron is mediated by a colourless state with the quantum numbers of vacuum, called Pomeron. Although in theory, there are many possible structures of such colourless object, the simplest approximation is that it can be seen as a pair of gluons. Here we again see that although the interaction proceeds via colourless objects from an outer perspective, the possibility of colour exchange and hence the strong interaction is internally present. The interaction of the colour dipole with the target's structure is incorporated within the dipole-proton cross section, which is related via the optical theorem to the dipole scattering amplitude $N(x, \vec{r}, \vec{b})$ as

$$\frac{\mathrm{d}\sigma_{q\bar{q}}}{\mathrm{d}\vec{b}} = 2N(x, \vec{r}, \vec{b}), \tag{1.27}$$

where $\vec{b}$ is the impact parameter between the dipole and the target. The dipole amplitude therefore contains all the information about the strong interaction with the target proton structure (for both perturbative and non-perturbative contributions) and therefore, it is directly linked to the gluonic structure of the target at low-x. The perturbative contribution to N can be obtained from various CGC based models (described in the following section) or directly from the CGC framework as a solution to the Balitsky-Kovchegov equation (described in Chapter 3).

Using this two-step factorisation of the photon-proton interaction, the total $\gamma^* p$ cross section of deeply inelastic scattering can be written as

$$\sigma_{T,L}^{\gamma^* p}(x, Q^2) = \sum_f \int \mathrm{d}\vec{r} \int_0^1 \mathrm{d}z |\Psi^* \Psi|_{T,L}^f \sigma_{q\bar{q}}(\tilde{x}, \vec{r}), \tag{1.28}$$

where the dipole cross section $\sigma_{q\bar{q}}$ is integrated over the impact parameter $\vec{b}$ and it is evaluated at the shifted value of x in order to safely approach the photoproduction limit [74] as

$$\tilde{x} = x\left(1 + \frac{4m_f^2}{Q^2}\right), \tag{1.29}$$

The structure function F_2 can be then calculated within the dipole model framework using Eq. (1.28) as

$$F_2(x, Q^2) = \frac{Q^2}{4\pi^2\alpha}\left(\sigma_T^{\gamma^* p} + \sigma_L^{\gamma^* p}\right), \tag{1.30}$$

and the longitudinal structure function is given by

$$F_L(x, Q^2) = \frac{Q^2}{4\pi^2\alpha}\sigma_L^{\gamma^* p}. \tag{1.31}$$

1.3.1 Dipole models in QCD phenomenology

The first phenomenological dipole model to successfully describe the DIS data by incorporating saturation effects was the model by Golec-Biernat and Wusthoff (denoted as GBW model) [74, 75]. It parametrises the dipole-proton scattering cross section as

$$\sigma_{q\bar{q}}^{\mathrm{GBW}}(x,r) = \sigma_0 \left[1 - \exp\left(-\frac{r^2 Q_s^2(x)}{4}\right)\right]; \qquad Q_s^2(x) = Q_0^2 \left(\frac{x_0}{x}\right)^{\lambda_{\mathrm{GBW}}} \ [\mathrm{GeV}^2], \tag{1.32}$$

where σ_0 is a parameter obtained from a fit to DIS data and it is related to the proton size. $Q_s(x)$ denotes the x-dependent saturation scale, which is closely related to the gluon density in the transverse plane. The exponent λ_{GBW} determines the growth of the dipole cross section with decreasing x, and Q_0, x_0 are free parameters. For large dipoles, the cross section given by Eq. (1.32) saturates and its value approaches the constant σ_0. An interesting result connected to the GBW model is the presence of so called geometrical scaling in DIS data. It was shown by Stasto et al. [76] that the total photon-proton cross section measured at HERA at $x < 0.01$ approximately scales as a function of one dimensionless variable $\tau = Q^2 R_0^2(x)$, where $R_0(x)$ is the saturation radius related to the saturation scale $Q_s^2(x)$ as $R_0 \sim 1/Q_s$. This result is particularly interesting because the emergence of the scaling phenomenon can indicate the presence of saturation effects and it has been observed in both ep and eA inclusive DIS data [76, 77].

Although the GBW model successfully described the early HERA data such as [44, 45], and can still find its use in some phenomenological studies due to its simplicity, it has been since superseded by more sophisticated models, which incorporate a broader range of both perturbative and non-perturbative behaviour of the proton structure, e.g. the DGLAP evolution with Q^2 [78] or the b-dependence [79]. The recent years have also seen an emergence of the dipole amplitudes obtained directly from the CGC framework as a solution to the BK or JIMWLK equations (see Chapter 3).

Because of their use in some of the results presented in this thesis, two of the those models deserve to be briefly mentioned. The first model to incorporate the b-dependence was the the Impact Parameter Saturation model (IP-Sat) [78, 79] which aimed to describe exclusive processes where (unlike in DIS) the b-dependence is explicitly present. The model parametrises the proton in the impact-parameter plane with a gaussian profile and couples it to the parametrised gluon distribution evolved by the DGLAP equation. The model has been further improved [80, 81] by the fits to newer HERA data. The model was also extended to a nuclear case and served as a basis for the IP-Glasma model [82, 83] of initial conditions in heavy ion collisions. The IIM model by Iancu, Itakura, and Munier is based on the GBW model, however it includes some of the features of the BK evolution to the dipole amplitude [84]. Its updated version denoted as b-CGC [85, 86] also includes an impact-parameter dependence.

1.3.2 Vector meson production within the colour dipole model

The dipole model provides not only a description of DIS at small-x, but also a much broader approach to naturally incorporate saturation phenomena into other QCD processes. These may provide additional channels to study the proton structure and can be sensitive to some aspects of QCD dynamics which may not be accessible in DIS. Measurements of exclusive processes where the interacting hadron remains intact after the scattering and only one resulting particle is created, e.g. a vector meson, represent a useful tool to access the hadronic structure and shape in the impact-parameter space due to the connection of the exclusive scattering amplitude to the generalised parton distributions (GPDs), and especially to the gluon PDF which is the special case of the gluon GPD at the forward limit. [87, 88].

Similarly to the DIS process, the diffractive production of a vector meson as a result of the interaction of a virtual photon with the target hadron can be calculated within the colour dipole approach, the

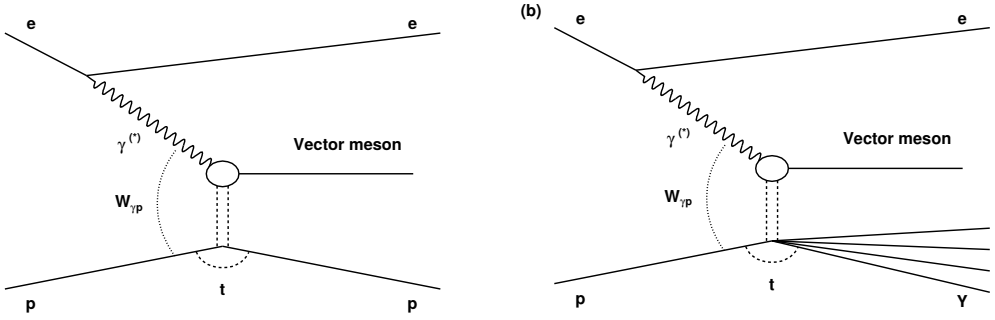

Figure 1.7: A schematic diagram for the exclusive (left) and dissociative (right) vector meson production within the colour dipole approach. Figures from Ref. [37].

situation is depicted in Fig. 1.7 (left). In this formalism, the exclusive cross section to produce a vector meson V in the interaction of transversely, resp. longitudinally, polarised virtual photons with the proton target is given by [85]

$$\left.\frac{\mathrm{d}\sigma^{\gamma^* p\to \mathrm{V}p}}{\mathrm{d}|t|}\right|_{T,L} = \frac{\left(1+\beta_{T,L}^2\right)\left(R_g^{T,L}\right)^2}{16\pi}|\mathcal{A}_{T,L}|^2, \tag{1.33}$$

where $\mathcal{A}_{T,L}$ is the scattering amplitude. The term $(1+\beta_{T,L}^2)$ accounts for the real part of the amplitude, where β is the ratio of real to imaginary parts of the scattering amplitude. The other correction, denoted as $R_g^{T,L}$, takes into account that there are two values of x involved in the interaction of the dipole with the hadron. For the calculation of the vector meson production, one should therefore use the off-diagonal gluon distribution. This effect can be accounted for by multiplying the scattering amplitude by the so called skewedness correction [87]. The total exclusive cross section to produce a vector meson V is then given by the sum of the transverse and the longitudinal contributions defined by Eq. (1.33), integrated over $|t|$, which is the square of the four-momentum transfer at the proton vertex.

The scattering amplitude of the process is given by (for more details see e.g., [85, 89])

$$\mathcal{A}_{T,L}\left(x,Q^2,\vec{\Delta}\right) = i\int \mathrm{d}\vec{r}\int_0^1 \frac{\mathrm{d}z}{4\pi}\int \mathrm{d}\vec{b}|\Psi_{\mathrm{V}}^*\Psi_{\gamma^*}|_{T,L}\exp\left[-i\left(\vec{b}-(1-z)\vec{r}\right)\vec{\Delta}\right]\frac{\mathrm{d}\sigma_{q\bar{q}}}{\mathrm{d}\vec{b}}, \tag{1.34}$$

where Ψ_{γ^*} is the wave function of a virtual photon which fluctuates into a dipole, Ψ_{V} represents the wave function of the produced vector meson, and x is the Bjorken-x of the exchanged Pomeron, which under the assumption of large energies W is given by

$$x = \frac{Q^2+M_V^2}{Q^2+W^2}, \tag{1.35}$$

where M_V is the mass of the produced vector meson. There has been a recent discussion regarding the argument of the exponential term in Eq. (1.34). This factor arises as a result of the Fourier transform of the amplitude from the momentum-space to the position space, modified to the non-forward case, and was first introduced in [90] and implemented in phenomenology in [85]. The recent work [88] proposes to use $(1-2z)/2$ instead of $(1-z)$, based on symmetry arguments. However, this change produces only a marginal difference in the resulting cross sections presented in this thesis, as discussed in [32], and therefore for the vector meson results, we stick to the formalism of [85] in order to stay consistent with the past results published by the group.

The overlap of the photon-meson wave functions is given as [85]

$$|\Psi_{\mathrm{V}}^{*}\Psi_{\gamma^{*}}|_{T} = \hat{e}_{f}e\frac{N_{\mathrm{c}}}{\pi z(1-z)}\left[m_{f}^{2}K_{0}(\epsilon r)\phi_{T}(r,z) - \left(z^{2}+(1-z)^{2}\right)\epsilon K_{1}(\epsilon r)\partial_{r}\phi_{T}(r,z)\right], \tag{1.36}$$

and

$$|\Psi_{\mathrm{V}}^{*}\Psi_{\gamma^{*}}|_{L} = \hat{e}_{f}e\frac{N_{\mathrm{c}}}{\pi}2Qz(1-z)K_{0}(\epsilon r)\left[M_{V}\phi_{L}(r,z) + \delta\frac{m_{f}^{2}-\nabla_{r}^{2}}{z(1-z)M_{V}}\phi_{L}(r,z)\right], \tag{1.37}$$

where $\hat{e}_f$ is the effective charge of the given vector meson, ϵ is defined in Eq. (1.26), and the parameter δ is a switch to include ($\delta = 1$) or exclude ($\delta = 0$) the non-local term in the longitudinal contribution. The scalar part $\phi_{T,L}$ of the wave function is, in general, model dependent and it is one of the two main sources of the model-related uncertainties in the description of the vector meson production within the dipole model; for a recent study on wave function uncertainties in different models see e.g. [91, 92]. For our studies, we use the boosted Gaussian model [93–95], in which the δ parameter is fixed to one and the functions $\phi_{T,L}$ for $1S$ states are expressed as

$$\phi_{T,L}(r,z) = N_{T,L}z(1-z)\exp\left(-\frac{m_{f}^{2}R^{2}}{8z(1-z)} - \frac{2z(1-z)r^{2}}{R^{2}} + \frac{m_{f}^{2}R^{2}}{2}\right). \tag{1.38}$$

The parameters $N_{T,L}$ and R^2, are fixed using a normalisation condition and the measured electronic decay width (see, e.g. [85]). The updated values of the parameters for the wave functions of all vector mesons according to PDG2016 [96] were calculated in [37] and are used in the results presented in this thesis.

Dissociative production of vector mesons

Since the cross section for the exclusive process from Eq. (1.33) is given as the squared mean of the related amplitude, we can use it to study the hadron structure in terms of its distribution functions, however we cannot access the event-by-event fluctuations using this process. For such studies, the production of a vector meson accompanied by the dissociation of the target particle (see right plot of Fig. 1.7) represents a suitable tool, as it can be related to the fluctuations in the proton structure within the Good-Walker approach [97, 98]. The fluctuations of the geometrical configurations in the impact-parameter plane determine the different configurations of the partonic structure and the cross section for the production of a vector meson where the proton dissociates into a system Y can be calculated as the variance over different configurations

$$\left.\frac{\mathrm{d}\sigma^{\gamma^{*}p\to \mathrm{V}Y}}{\mathrm{d}|t|}\right|_{T,L} = \frac{\left(1+\beta_{T,L}^{2}\right)\left(R_{g}^{T,L}\right)^{2}}{16\pi}\left(\langle|\mathcal{A}_{T,L}|^{2}\rangle - |\langle\mathcal{A}_{T,L}\rangle|^{2}\right). \tag{1.39}$$

There has been an emergence of various models studying the fluctuations of the proton structure [34, 38, 99–101], their influence on the description of the vector meson production data from HERA, and the use of such models for the heavy-ion initial state description [102]; for a recent review see e.g. [39]. In this work, the original model by Cepila et al. [34] will be used to further extend these studies. Each of these so called hot-spot models represents a different approach to the description of the fluctuating structure of the proton. However, what is common to all of them is the conclusion, that the dissociative $|t|$−distribution data cannot be described without taking these fluctuations into consideration.

Chapter 2

The hot-spot model

2.1 The fluctuating structure of the proton

The full dipole scattering amplitude is a difficult object to calculate and, therefore, several simplifications are taken within QCD phenomenology. For example, it is a common approach to approximate the proton as a homogeneous object. The dipole amplitude then depends only on the magnitudes of the related vectors and can be then obtained either from models which include the b-dependence [78,79,85,86] or from the solutions to the b-dependent BK equation [28, 29, 103, 104]. In order to study changes of the proton structure in the impact-parameter plane, it can be useful to factorise out the impact-parameter dependence into a separate function as

$$N\left(x, \vec{r}, \vec{b}\right) \to \sigma_0 N(x, \vec{r}) T_p(\vec{b}), \tag{2.1}$$

where σ_0 is a normalisation parameter. One more simplification can be made for the dipole amplitude to depend only on the size of the dipole $r \equiv |\vec{r}|$. Obtaining the impact-parameter independent amplitude is then a much simpler task which can be done either from phenomenological models such as GBW (see Section 1.3.1) or from the one-dimensional BK equation (see Chapter 3). Since the DIS cross section given by Eq. (1.28) does not explicitly depend on the impact parameter, the calculation of the dipole cross section in this case simplifies to

$$\sigma_{q\bar{q}}(x, r) = \sigma_0 \int \mathrm{d}\vec{b} N(x, r) T_p(\vec{b}) = \sigma_0 N(x, r) \tag{2.2}$$

where σ_0 is obtained either as a free parameter of the fit to DIS data, or using the radius of the proton in the transverse plane [21].

Although the formula (2.1) represents a substantial simplification of the full kinematic richness of the dipole amplitude, it allows us to independently study the proton structure in the transverse plane and its evolution in a convenient way using the proton profile function $T_p(\vec{b})$. This function parametrises the transverse distribution of the proton and there are several choices one can make, depending on the level of details to be included:

1. **Step function**: the simplest, yet unrealistic description of the proton shape.

2. **Gaussian distribution** (and its modifications like double Gaussian): provides a more realistic description of the proton transverse profile. It has been used in several phenomenological studies (see e.g. [85]).

3. **Set of random fluctuations**: a set of partonic clusters (hot spots) whose number and positions fluctuate event-by-event. Most common are two main branches of such models — three hot spots [99, 100] which may be surrounded by a cloud of newly emerging gluons, or a set of N_{hs} regions of high gluonic density [34]. However, these approaches can also be combined, see e.g. [101].

In this work based on the model by Cepila et al. [34], the proton is seen as a set of N_{hs} regions of high gluonic density, with the profile function defined as

$$T_p(\vec{b}) = \frac{1}{N_{hs}} \sum_{j=1}^{N_{hs}} T_g\left(\vec{b} - \vec{b}_j\right), \tag{2.3}$$

where each hot spot has a Gaussian distribution

$$T_g(b) = \frac{1}{2\pi B_{hs}} \exp\left(-\frac{b^2}{2B_{hs}}\right). \tag{2.4}$$

The positions of the hot spots $\vec{b}_j$ are obtained from a two-dimensional gaussian distribution with width B_p, which is fixed by the average of the squared transverse radius of the proton (and which can be related to the slope of the vector meson cross section t-distribution [105]). The parameter B_{hs} can be interpreted as an average of the squared transverse radius of an individual hot spot.

The proton profile is made energy-dependent at a given scale Q^2 by making the number of hot spots grow with decreasing x, using a prescription inspired by parameterisations of the gluon PDF. The formula for $N_{hs}(x)$ in this case reads

$$N_{hs}(x) = p_0 x^{p_1}\left(1 + p_2\sqrt{x}\right), \tag{2.5}$$

where p_0, p_1 and p_2 are parameters to be fixed by data. Moreover, to generate configurations which truly change from interaction to interaction, we take N_{hs} as a random number from a zero-truncated Poisson distribution with the mean value given by Eq. (2.5). This ensures that each configuration differs in both number of fluctuations and their relative positions. An example of two such configurations for two different energies is given in Fig. 2.1.

In order to make the model as simple as possible, the GBW model from Eq. (1.32) is used to obtain the dipole scattering amplitude $N(x, r)$ and the σ_0 parameter is calculated as $\sigma_0 = 4\pi B_p$. The parameters entering the GBW model and the $T_p(\vec{b})$ prescription from Eq. (2.3) were fixed in earlier studies [34–36]. For completeness, they are listed, together with the updated parameters for the vector meson wave functions from Eqs. (1.24) and (1.25), in the reported paper [37]. Also note that the above described approach can be extended to the nuclear case, as was done in [35].

2.2 QCD observables with the hot-spot model

As the first part of my work on this model, I calculated structure functions $F_2(x, Q^2)$ and the cross section for the photoproduction[1] of the J/ψ vector meson (for both exclusive and dissociative process) and next, I extended the calculation to other types of vector mesons, namely J/ψ, ρ^0, and $\Upsilon(1S)$; the results are in accordance with [34, 36]. Based on this progress, I extended the calculation to the case of

[1]The term photoproduction denotes situation where the intermediating photon has a very low virtuality $Q^2 \to 0$. On the other hand, electroproduction denotes processes where $Q^2 >> 0$.

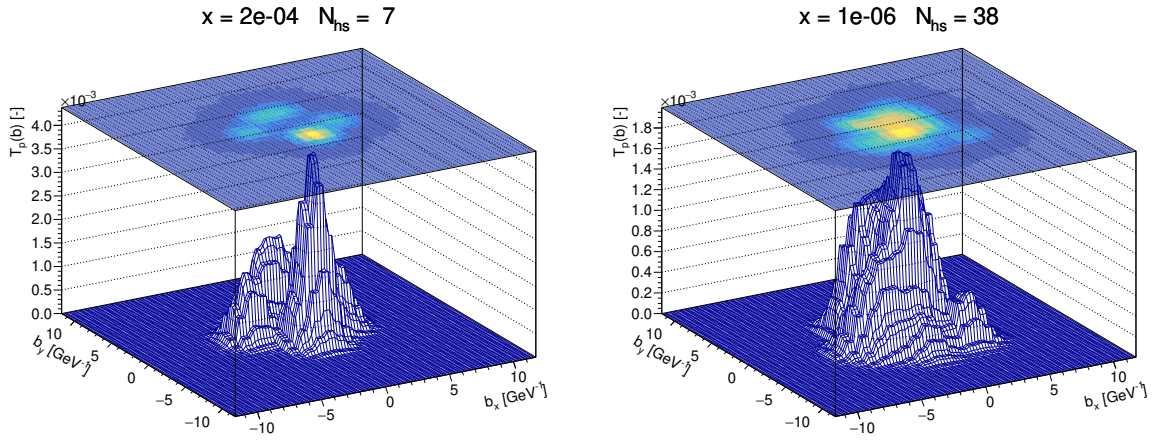

Figure 2.1: An example of the shape of the transverse profile of the proton generated from the hot-spot model for $x = 2 \cdot 10^{-4}$ (left) and for $x = 10^{-6}$ (right).

electroproduction of the said mesons and also to incorporate other vector mesons such as ϕ and $2S$ states of the heavy quarkonia.

These result were (for the first time) reported in the paper [37] and represent an extensive set of predictions for the energy dependence of the exclusive and dissociative production of ρ_0, ϕ, J/ψ, $\psi(2S)$, Υ and $\Upsilon(2S)$ vector mesons off proton targets at different photon virtualities. The predictions are compared with the experimental data from HERA and the LHC, where available. Two examples from all the results of Ref. [37] are depicted in Figs. 2.2 and 2.3, which show the sets of predictions for ρ^0 and J/ψ mesons, respectively. These two cases were chosen because they illustrate particularly well the main implications of the hot-spot model and because there is enough data to benchmark our calculations and demonstrate that they are able to describe the corresponding measurements.

The cross section energy W-dependence of the ρ^0 vector meson is compared with the H1 [106–108] and ZEUS data [109, 110] and also with the data from CMS [111] for photoproduction in p–Pb collisions at the centre-of-mass energy $\sqrt{s} = 5.02$ TeV. The data for both exclusive and dissociative cross section are well described by the model for a broad range of Q^2 values of the exchanged photon. The predictions for the exclusive and dissociative cross sections of the J/ψ vector meson also show a good agreement with the photoproduction data from H1 [112] and ALICE p–Pb data [113, 114], and with the electroproduction data from H1 [115]. In overall, the conclusion is that the model is in a good agreement with the currently existing experimental data for the exclusive and the dissociative photo- and electroproduction of ρ_0, ϕ, J/ψ, and Υ mesons. Moreover, Ref. [37] also includes predictions of the same quantities for $\psi(2S)$ and $\Upsilon(2S)$ mesons. Such measurements are expected to be performed, together with the measurements of the dissociative process, at the planned future facilities.

A striking feature of this model is the behaviour of the dissociative cross section with increasing energy W of the photon-target system, which was first noticed in [34] for the case of J/ψ photoproduction and further confirmed in [36] for the ρ^0 and Υ photoproduction. From low energies, the cross section rises with the increasing W, as can be seen in Fig. 2.3. However, unlike in the exclusive case, the dissociative cross section rises only up to a certain point where it reaches its maximal value and from that point further, it starts to decrease with increasing energy. The same behaviour is observed for the dissociative electroproduction and in all types of vector mesons. Comparing the J/ψ and ρ case in Figs. 2.3 and 2.2,

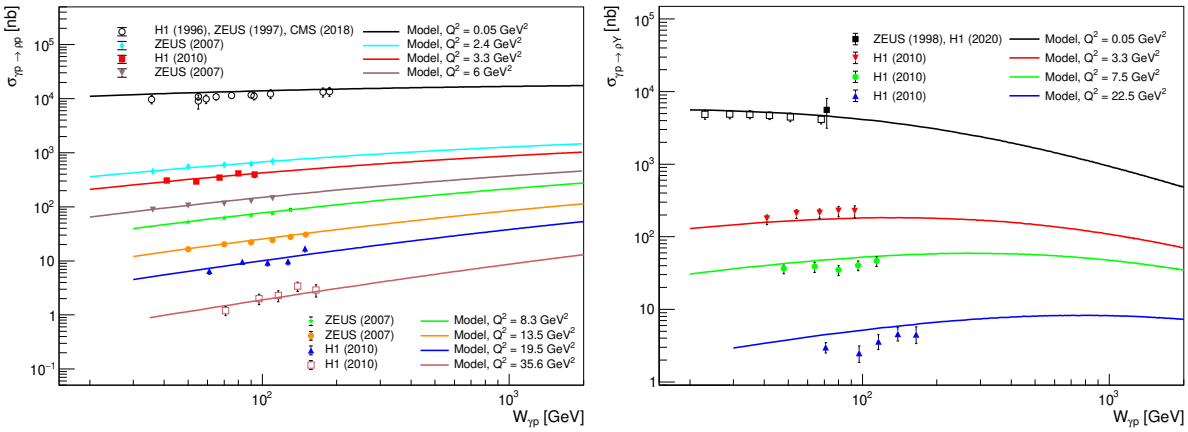

Figure 2.2: Comparison of the model predictions (solid lines) with HERA [106–110] and CMS data [111] for the $W_{\gamma p}$ dependence of the exclusive (left) and dissociative (right) photo- and electroproduction cross section of a ρ^0 meson. Figures from Ref. [37]. The new data [116] on the dissociative photoproduction of ρ^0 (empty black boxes) were added to the right plot.

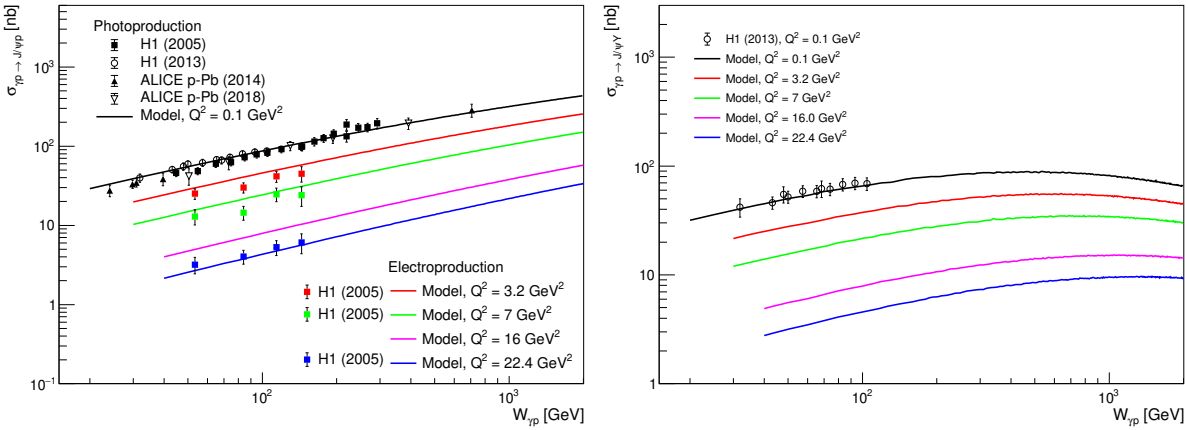

Figure 2.3: Comparison of the model predictions (solid lines) with H1 [112, 115] and ALICE data [113, 114] for the $W_{\gamma p}$ dependence of the exclusive (left) and dissociative (right) photo- and electroproduction cross section of a J/ψ meson. Figures from Ref. [37].

respectively, it can be seen that the position of this cross section maximum strongly depends not only on the Q^2 of the exchanged photon, but also on the type of the vector meson, which differ in their masses.

The explanation of this behaviour can be made from the analysis of the form of the cross section in Eq. (1.39). Since the dissociative cross section is given as a variance over the different configurations of the proton structure, the result will be sensitive to such configurations which look alike. In our model, the different configurations of the proton structure are given from the fluctuating number of hot spots and their geometrical placement in the impact-parameter plane, with individual hot spots occupying the same magnitude of the transverse area. With increasing energy, which corresponds to decreasing Bjorken-x, the number of hot spots grows as can be seen from Fig. 2.1, and the proton area is gradually filled. At some point, these hot spots start to overlap in a way similar to percolation [117], and fill all the

available transverse space within the proton. As a result, different configurations start to look alike and the variance, which measures the difference among all configurations, starts to decrease. Sadly, there are currently no data available which could directly describe this behaviour of the cross section in its entirety; data from H1 [112] on the J/ψ production only confirm the initial rise of the cross section at low energies. However, the behaviour of the ρ^0 dissociative photoproduction cross section in Fig. 2.2 (right) suggests that the maximum is reached at low energies, near the boundary of the applicability of the model, or it has already been reached at even lower energies (higher x). As shown in Fig. 2.2 (right), the observation is also supported by the recent (after the publication of [37]) H1 data [116], which is very promising.

2.3 Geometrical saturation scale

Apart from the correct description of the available data and predictions for future measurements, another interesting observation can be made based on Figs. 2.3 and 2.2 (and the rest of predictions from [37]). It can be seen that the maximum of the dissociative cross section does not occur at the same energy for every case, but at an energy which can be pinpointed using the virtuality of the exchanged photon Q^2 and the vector meson mass M; together they represent a measure of the scale of the process. Since this behaviour results from the variance over different geometric configurations of the proton structure, we have named this point the *geometric saturation scale* (GSS) and in the following, some of its properties I studied in [37] are summarised.

First of all, the energy W_{GSS} at which the maximum occurs for each vector meson and Q^2 was determined. Due to the randomness of the process, the actual position of the maximum may fluctuate. This is incorporated in the associated uncertainty which is taken as the region containing the 1% largest values of the cross section around W_{GSS}.

The left plot of Fig. 2.4 shows the position and the associated uncertainty of the extracted maxima as a function of the scale of the process given by $Q^2 + M^2$. In order to confirm the observation on the linear behaviour of the quantity, I performed a simple linear fit resulting in the χ^2 per degree-of-freedom being 0.41; this small value reflects the rather large uncertainties. Subsequently, W_{GSS} values are transformed into x_{GSS} via Eq. (1.35) and the result can be seen in the right plot of Fig. 2.4. The observed linear behaviour (in the logarithmic plane) strongly reminds of the saturation scale as described in Sec. 1.2.2 and depicted in Fig. 1.5.

The same plot shows the kinematic limit of several proposed electron-ion colliders obtained from Eq. (1.5), with the inelasticity set to $y = 1$ and the beam energies for the calculation of s are taken from Tab. I of [118]. From Fig. 2.4 (right), some conclusive observations can be made.

- The maxima for the light vector mesons ρ^0 and ϕ could have been observed even at the now decommissioned HERA accelerator. This is partially confirmed by the description of the data presented in Fig. 2.2 (right) and the recently published H1 data [116]. Yet, it is not expected that the remaining unpublished HERA data (which are still being analysed) will bring any revolutionary conclusions in the future.

- Even for the colliders with the planned energy lower than that of HERA, the linear behaviour of GSS could be measured using the ρ^0 and ϕ electroproduction at moderately small Q^2 (with $Q^2 > 1$ GeV^2 in order to stay in the perturbative region). Of this two competitive projects for the US-based electron-ion collider [10], the JLEIC project has been suspended and eRHIC has been selected as a vital plan to be built at the Brookhaven National Laboratory [119], with its detectors and their envisaged capabilities still being under development.

- For the investigation of the positions of the maxima for the ρ^0 and ϕ electroproduction at large Q^2 and moreover for the J/ψ meson, the energies of the LHC and the LHeC [11, 120, 121] are needed.
- The positions of the maxima for the Υ meson and its higher mass states seem to be out of reach of any past or currently planned facilities, even the LHeC.

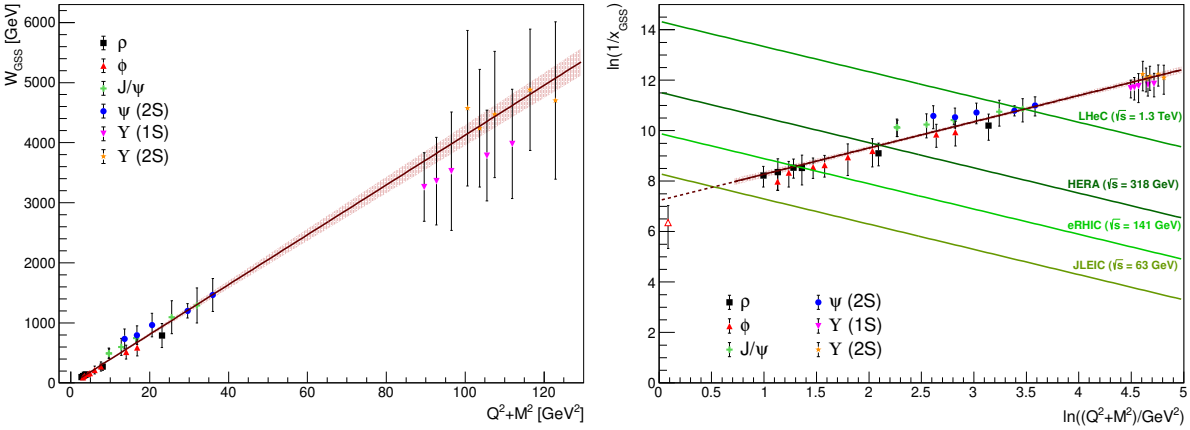

Figure 2.4: (Left): Maxima of the dissociative cross sections (markers) with the estimation of their related uncertainty (bars) as a function of scale $Q^2 + M^2$. The full line is a linear fit to the maxima values and the band represents the one sigma contour.
(Right): The same quantity as in the left plot, but expressed in x_{GSS} corresponding to W_{GSS} and shown in logarithmic scale. The full red line is a linear fit (in the logarithmic plane). Kinematic reaches of some of the (at that time) proposed electron-ion colliders are in full green lines. Figures from Ref. [37].

Chapter 3

Balitsky–Kovchegov evolution equation

In Section 1.2.2, the concept of gluon saturation and its description using the Colour Glass Condensate effective theory has been introduced. This Chapter will describe the Balitsky–Kovchegov equation and its properties in detail. The Balitsky–Kovchegov equation was independently derived by Balitsky [12] as a special case of the JIMWLK evolution equations, see Sec. 1.2.2 and references therein. In the mean-field approximation and the large-number-of-colours limit, the first of JIMWLK equations decouples into a single integro-differential equation which describes the evolution with rapidity $Y \sim \ln\left(\frac{1}{x}\right)$ of the scattering amplitude $N(\vec{x}, \vec{y})$ of a $q\bar{q}$ dipole off a hadronic target (the dense CGC matter). It was also independently derived by Kovchegov [13, 14] from the colour dipole model introduced in Sec. 1.3.

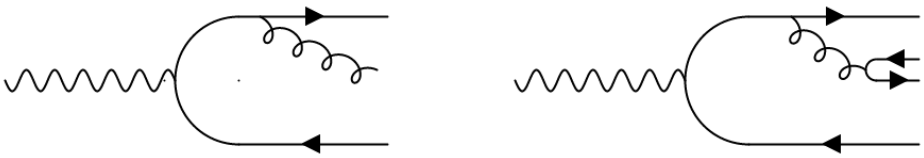

Figure 3.1: A diagram for the gluon emission during the colour dipole evolution (left) and its large-N_c limit (right). Figure adapted from previous work [50].

The evolution starts with a $q\bar{q}$ dipole with its end-points located at transverse positions $\vec{x}$ and $\vec{y}$. As a result of the evolution to higher energies (corresponding to a boost in rapidity Y), the (anti)quark wave function develops an extra gluon component which corresponds to a gluon emission at a transverse position $\vec{z}$. The new gluon can be, in the limit of large N_c, seen as a new quark-antiquark pair. Therefore, the dipole can be seen as two new independent daughter dipoles instead of the original parent one, as depicted in Fig. 3.1. In this way, adding energy into the system results in a dressing of the original bare dipole with a cloud of gluons, viewed as additional daughter dipoles. This new partonic composition can be then related to that of the target hadron, which makes the BK equation an effective tool to study the structure of hadrons at high energies. The general form of the BK equation at leading-order reads [28]

$$\begin{aligned}\frac{\partial N(\vec{r}_{xy}, \vec{b}_{xy}, Y)}{\partial Y} &= \int \mathrm{d}\vec{r}_{xz}\, K(\vec{r}_{xy}, \vec{r}_{xz}, \vec{r}_{zy}) \Big[N(\vec{r}_{xz}, \vec{b}_{xz}, Y) + N(\vec{r}_{zy}, \vec{b}_{zy}, Y) - N(\vec{r}_{xy}, \vec{b}_{xy}, Y) \\ &\quad - N(\vec{r}_{xz}, \vec{b}_{xz}, Y)\, N(\vec{r}_{zy}, \vec{b}_{zy}, Y) \Big], \end{aligned} \tag{3.1}$$

where the function $K(\vec{r}_{xy}, \vec{r}_{xz}, \vec{r}_{zy})$ is the kernel of the integro-differential equation which represents the probability of a new gluon emission. At leading order, we consider only one emission, resulting in two daughter dipoles. Eq. (3.1) therefore contains the terms corresponding to the parent and daughter dipole scattering amplitudes and a non-linear term, which accounts for the recombination of these emissions and prevents double-counting. It is this last term which is responsible for the unitarity restoration of the divergent BFKL evolution. This work uses the equation formulated in the position-space representation as shown above. In such case, the size of the parent dipole can be defined as a vector connecting its end-points $\vec{r}_{xy} = \vec{x} - \vec{y}$ and for the daughter dipoles as $\vec{r}_{xz} = \vec{x} - \vec{z}$ and $\vec{r}_{zy} = \vec{z} - \vec{y}$. The impact parameters for the parent and daughter dipoles, which represent its distance from the centre of the target hadron, can be expressed correspondingly as $\vec{b}_{xy} = \frac{\vec{x}+\vec{y}}{2}$, $\vec{b}_{xz} = \frac{\vec{x}+\vec{z}}{2}$, and $\vec{b}_{zy} = \frac{\vec{z}+\vec{y}}{2}$. The graphical representation of such configuration of the parent and daughter dipoles and the corresponding vectors can be seen in Fig. 3.2. The BK equation can also be written in the momentum-space representation, see e.g. [122].

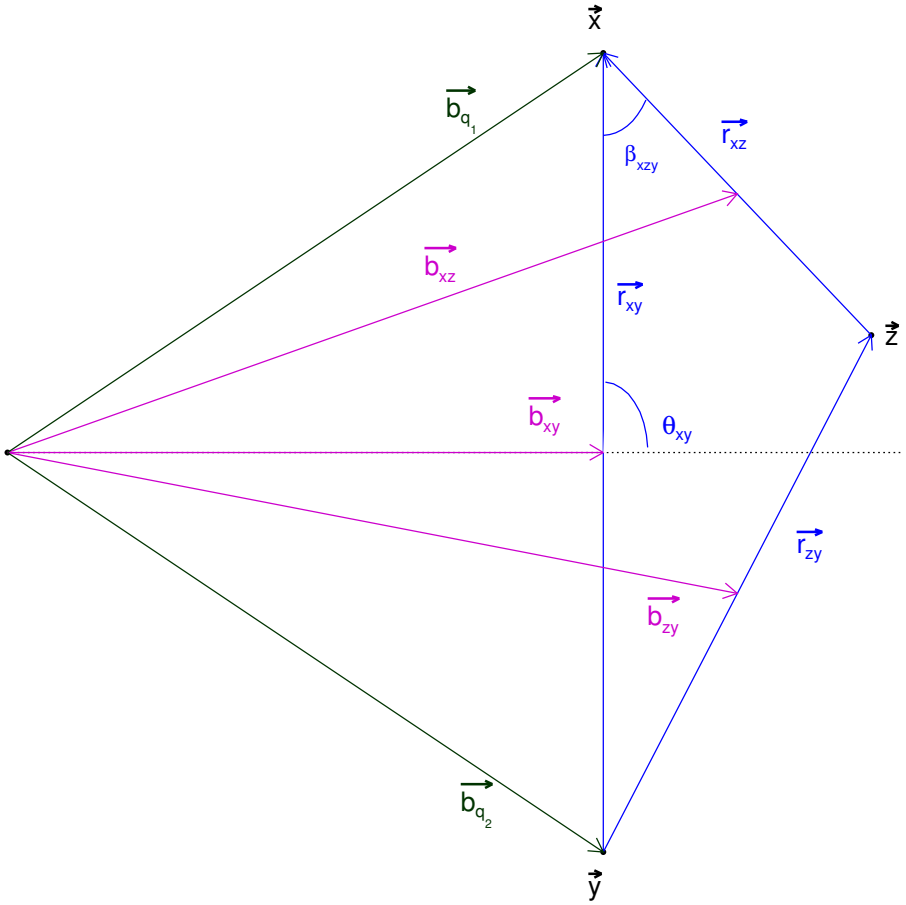

Figure 3.2: Schematic picture of the vectors $\vec{r}$ and $\vec{b}$ corresponding to the parent and daughter dipoles in the Balitsky–Kovchegov equation.

The general behaviour of the dipole scattering amplitude is that it is small for the dilute target and approaches unitarity ("black disk" limit) in the regime where the target is dense. This corresponds to the growth of the gluon densities with decreasing x, which is subsequently tamed by saturation effects. The solution of the BK equation, at a given rapidity Y, depends on two 2-dimensional vectors $\vec{r}$ and

$\vec{b}$, making it a four-dimensional problem; the amplitude depends on the sizes of the dipole size and its impact parameter vectors, their respective angle, and the angle of the impact parameter with respect to the origin of the coordinates. In order to simplify the problem, the dimensionality of the equation can be reduced by considering some symmetry approximations. This can be desirable for some applications, since the BK equation does not have any known analytical solution and one has to use computing-power demanding numerical methods in order to obtain its solution. On the other hand, this approach reduces the amount of information which is possible to obtain from the BK equation solutions and also limits the rigorousness of the problem.

In our work, the evolution in rapidity from the given initial condition is performed using the Runge-Kutta (RK) methods [123]. The numerical methods are summarised in my Master's thesis [50], where several numerical studies of the LO BK equation were performed, e.g. comparison of the different kernel prescriptions, choice of the initial condition, and the influence of the order of Runge-Kutta method. Some of these results are reproduced in the following section in order to illustrate the development of the BK equation from its simplest approximation towards including higher-order corrections and restoring its full dimensionality.

First, I will introduce the approach to the BK equation without the dependence on the impact-parameter, starting from its simplest leading-order approximation, through introducing higher-order corrections to the evolution kernel, and finalising with the next-to-leading order BK equation, which represents the most recent development in the field. The BK equation with an explicit dependence on the impact-parameter between the dipole and the target hadron shall be discussed separately and my work on the applications of these solutions into QCD phenomenology will be described in Chapter 4. As the last part of this thesis, the project to generalise the b-dependent calculation to the next-to-leading order accuracy will be described in Chapter 5.

3.1 Balitsky–Kovchegov equation at leading-order

In the approximation of an infinite homogeneous target, the dependence on the impact parameter $\vec{b}_{xy}$ and the dipole orientation in the transverse space can be neglected, which allows us to work with the scattering amplitudes N depending only on the dipole sizes. The information about the b-dependence is factorised out into a separate parameter or a function as in Eqs. (2.1) and (2.2). The impact-parameter independent Balitsky–Kovchegov equation at leading order then reads [19]

$$\frac{\partial N(r_{xy}, Y)}{\partial Y} = \int \mathrm{d}\vec{r}_{xz}\, K(r_{xy}, r_{xz}, r_{zy}) \Big[N(r_{xz}, Y) + N(r_{zy}, Y) - N(r_{xy}, Y) - N(r_{xz}, Y)\, N(r_{zy}, Y) \Big], \quad (3.2)$$

where r_{ij} are the magnitudes of dipole sizes $\vec{r}_{ij}$.

3.1.1 Initial conditions

In order to solve the integro-differential equation, one of the basic ingredients is an appropriate initial condition, which in this case describes the behaviour of the dipole scattering amplitude at the initial rapidity $Y = \ln\left(\frac{x_0}{x}\right) = 0$, where x_0 is an initial Bjorken-x obtained from a fit to data. One of the prescriptions used in numerical studies is the GBW initial condition

$$N(r_{xy}, Y = 0) = 1 - \exp\left[-\frac{(r_{xy}^2 Q_{s_0}^2)^\gamma}{4} \right], \quad (3.3)$$

which is inspired by the phenomenological model by Golec-Biernat and Wusthoff [74] introduced in Sec. 1.3.1. Another widely used form of the initial dipole amplitude, denoted as the MV initial condition, comes from the semiclassical calculation of multiple rescatterings of the dipole off a nuclear target by McLerran and Venugopalan [61, 62, 124] and has the following form

$$N(r_{xy}, Y = 0) = 1 - \exp\left[-\frac{(r_{xy}^2 Q_{s_0}^2)^\gamma}{4} \ln\left(\frac{1}{r_{xy}\Lambda} + e\right)\right]. \tag{3.4}$$

There are several parameters in the prescriptions given by Eqs. (3.3) and (3.4) which are usually obtained from fits to data. The parameter $Q_{s_0}^2$ is the initial saturation scale at $x = x_0$, i.e. at the largest value of x considered in the calculation, and γ is the anomalous dimension, a parameter which controls the steepness of the fall of the dipole amplitude towards the small-r region. Λ corresponds to the infrared cut-off of the dipole-nucleon cross section and e is the Euler number.

It is also common in numerical studies like [20, 21] to use an arbitrary prescription with behaviour similar to the ones introduced above and devoid of most of the parameters in order to study the large-Y behaviour of the dipole amplitude and its generic properties. It has been shown in several works [19, 21, 125–127] that the asymptotic solutions of the impact-parameter independent BK equation are independent of the initial conditions. Moreover, their behaviour no longer depends on the two variables (r, Y) separately, but on their combination into a single dimensionless variable $\tau = rQ_s(Y)$, which is related to the already discussed phenomenon of geometric scaling.

3.1.2 Approach to the strong coupling constant

One of the ingredients for solving BK equation is the choice of the prescription for the running of the strong coupling constant α_S. The simplest approach is to take a fixed value of $\alpha_S \sim 1$. The inclusion of the running of the coupling represents a first step towards higher order of accuracy in perturbative QCD beyond leading-order. A proper treatment of α_S is therefore one of the important issues addressed by numerical studies of the BK equation. A standard choice for the running coupling evaluation is the one loop expression of the perturbative series for α_S in the form [21]

$$\alpha_S(r) = \frac{4\pi}{\beta_{n_f} \ln\left(\frac{4C^2}{r^2\Lambda_{n_f}^2}\right)}, \tag{3.5}$$

where $\beta_{n_f} = 11 - \frac{2}{3}n_f$, with n_f being the number of quark flavours included in the calculation, and C is a parameter which is fixed by comparing to data. The parameter Λ_{n_f} is the QCD scaling parameter and can be obtained either from a fit to data, or it can be calculated from the experimentally measured value of α_S at a given scale, e.g. the mass of the Z^0 boson.

The most straightforward way to include running coupling into the LO BK equation is to evaluate the expression in Eq. (3.5) at the parent dipole size r_{xy}, as studied in e.g. [19]. A very popular prescription in phenomenological applications is the prescription by Balitsky included in the kernel K_{rc} given by Eq. (3.12) which evaluates the running coupling not only at the parent dipole size, but also using daughter dipole sizes r_{xz} and r_{zy} as relevant scales. In Ref. [23], the authors argue that the Balitsky's prescription may not be the best choice towards next-to-leading order accuracy since it leads to an unphysically small coupling in a large region of phase space. Therefore, the authors propose as a proper way to treat α_S the so called *smallest dipole prescription*, which cancels large logarithms caused by terms proportional to β_{n_f} in all kinematic regions and reads

$$\bar{\alpha}_S = \bar{\alpha}_S(r_{min}); \qquad r_{min} = \min\left\{r_{xy}, r_{xz}, r_{zy}\right\}, \tag{3.6}$$

where $\bar{\alpha}_S = \frac{\alpha_S N_c}{\pi}$.

In order to determine the value of Λ_{n_f} from the experimantally measured data of α_S, the so called *variable number of flavours scheme* [21] is used. It is a recurrent relation to determine Λ_{n_f}, which allows to include contributions from heavy quarks into the α_S calculation. The relation reads

$$\Lambda_{n_f-1} = m_f^{1-\frac{\beta_{n_f}}{\beta_{n_f-1}}} \Lambda_{n_f}^{\frac{\beta_{n_f}}{\beta_{n_f-1}}}, \tag{3.7}$$

where m_f is the mass of the quark of the given flavour f. Values of Λ_{n_f} are calculated starting from Λ_5 (dipoles associated with the top quark are not considered), which is determined from the experimentally measured value of α_S at the Z^0 mass as

$$\Lambda_5 = M_Z \exp\left(-\frac{2\pi}{\beta_5\, \alpha_{S,M_Z}}\right). \tag{3.8}$$

The number of active flavours is set depending on the transverse size of the mother dipole as a relevant scale according to the condition

$$r^2 < \frac{4C^2}{m_f^2}, \tag{3.9}$$

and the matching is done according to

$$\alpha_{S,n_{f-1}}(r_*^2) = \alpha_{S,n_f}(r_*^2), \tag{3.10}$$

with r_*^2 equal to the expression in Eq. (3.9).

In order to regularise the infrared behaviour, α_S is usually frozen to a fixed value $\alpha_S \approx 1$ at the values of dipole sizes larger than the scale at which the running coupling constant reaches this given fixed value. A comparison of $\alpha_S(r)$ for the fixed vs the variable flavour scheme, and also its dependence on the number of active flavours, can be seen in Fig. 3.3. It shows that for small dipoles, the value of the strong coupling constant is small, allowing for perturbative calculations. The main difference amongst the given approaches arises above $r \sim 10^{-1}$ GeV^{-1}, meaning that the choice of the prescription is important for the correct descriptions of scenarios where large dipoles give a significant contribution.

3.1.3 Overview of the kernel prescriptions

There are several prescriptions for the kernel $K(r_{xy}, r_{xz}, r_{zy})$, which in general differ in the range of effects they take into account such as their approach to the strong coupling constant α_S, or including higher-order corrections to the kernel prescription itself.

At leading-order, the most basic kernel prescription is the so called BFKL kernel which reads

$$K_{\mathrm{BFKL}}(r_{xy}, r_{xz}, r_{zy}) = \bar{\alpha}_S \frac{r_{\mathrm{xy}}^2}{r_{\mathrm{xz}}^2 r_{\mathrm{zy}}^2}, \tag{3.11}$$

where the coupling constant is fixed to a constant value, with the usual choice $\alpha_S \approx 1$. The behaviour of the solution to the BK equation with the BFKL kernel has been studied in Ref. [19]. Inspired by similar studies with BFKL equation, the authors of Ref. [19] also introduced the running of the coupling into this kernel, using different prescriptions for the scales at which the coupling is evaluated, in order to study the sensitivity of the result to the coupling $\bar{\alpha}_S$. The comparison between the fixed vs running coupling cases can be seen in Fig. 3.4. It confirms the observation of Ref. [128] that the evolution is extremely

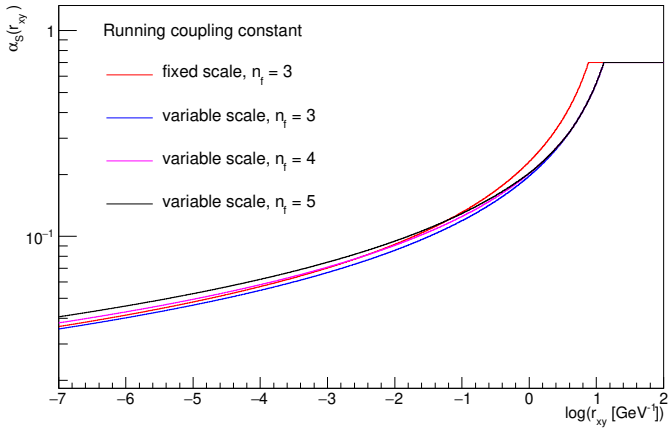

Figure 3.3: Running coupling constant α_S from Eq. (3.5) depending on the number of active flavours. α_S is fixed to 0.7 in the large-r region. Figure adapted from previous work [50].

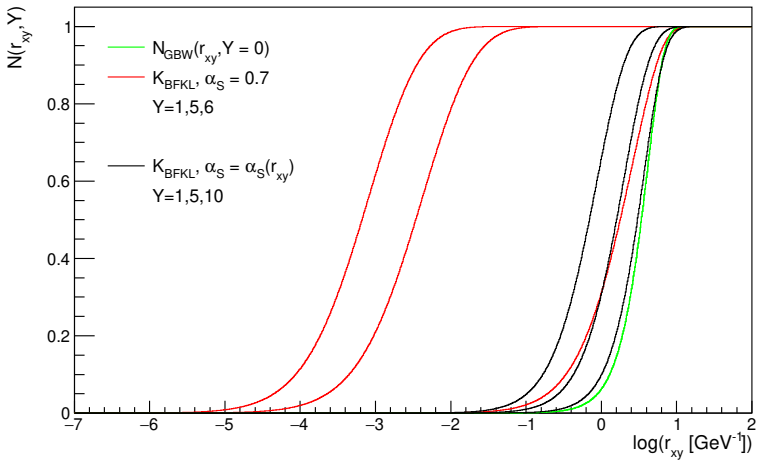

Figure 3.4: The scattering amplitude in dependence on r_{xy} as a solution to the b-independent LO BK equation (3.2) using the BFKL kernel given by Eq. (3.11) and the GBW initial condition given by (3.3) for the fixed vs. running coupling scenario. Figure adapted from previous work [50].

sensitive to the running vs fixed coupling approach, with the latter case showing much faster evolution. Moreover, the solution is rather insensitive to the precise prescription with which the running coupling effects are implemented into the BFKL kernel.

Since the running of the coupling constant $\bar{\alpha}_S$ introduces a sizeable modification to the evolution behaviour, it is important to treat its inclusion into the BK equation properly. The inclusion of the running coupling into the LO BK equation (3.2) has been done by Balitsky [129] and the relevant kernel reads

$$K_{\mathrm{rc}}(r_{xy}, r_{xz}, r_{zy}) = \frac{\bar{\alpha}_S(r_{xy})}{2\pi}\left[\frac{r_{\mathrm{xy}}^2}{r_{\mathrm{xz}}^2 r_{\mathrm{zy}}^2} + \frac{1}{r_{\mathrm{xz}}^2}\left(\frac{\alpha_S(r_{xz})}{\alpha_S(r_{zy})} - 1\right) + \frac{1}{r_{\mathrm{zy}}^2}\left(\frac{\alpha_S(r_{zy})}{\alpha_S(r_{xz})} - 1\right)\right]. \tag{3.12}$$

The resulting equation is commonly called the "running coupling BK equation" (rcBK) in the literature. It is an improved version of the LO BK equation which resums corrections associated with the running coupling. Since these corrections are numerically large, their resummation within the BK equation significantly slows down the growth of the dipole amplitude with increasing rapidity, as can be seen from the left plot of Fig. 3.5. This feature of the rcBK equation is a key ingredient to the success of the BK fits to HERA data such those from Refs. [20, 21], providing a very good description of the recent HERA data from the combined analysis by H1 and ZEUS collaborations in Ref. [47], an example can be seen in Fig. 3.6.

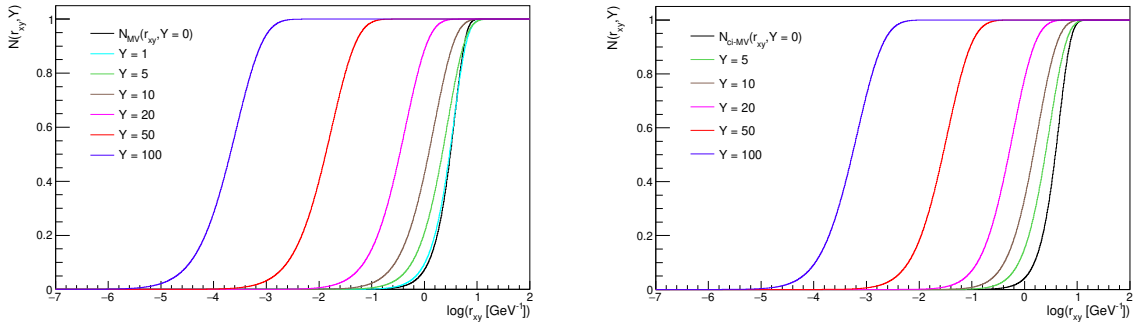

Figure 3.5: (Left): The scattering amplitude in dependence on r_{xy} as a solution to the b-independent LO BK equation (3.2) with the Balitsky's kernel given by Eq. (3.12). Figure adapted from previous work [50].
(Right): Same calculation, but with the collinerly-improved kernel from Eq. (3.13) using the smallest dipole prescription given by Eq. (3.6).

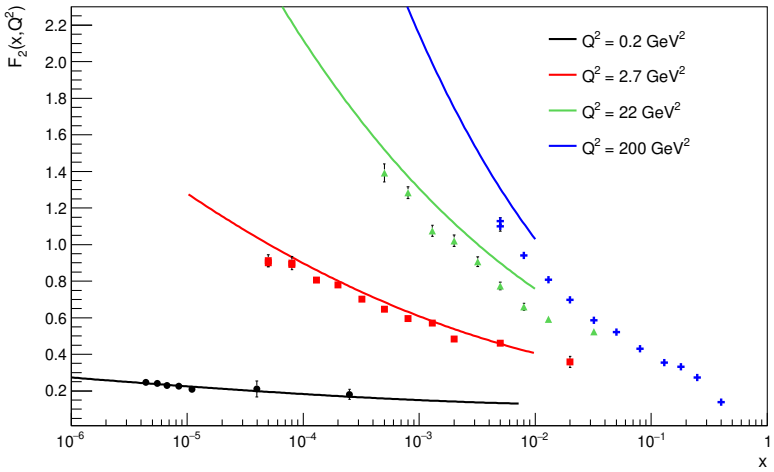

Figure 3.6: Predictions (lines) for the structure function $F_2(x, Q^2)$ calculated using the LO BK equation (3.2) with the running coupling kernel given by Eq. (3.12), compared to HERA data [47].

The BK equation including some corrections from its full next-to-leading order prescription (which will be described in detail in the following section) was introduced as the so called collinearly-improved leading-order Balitsky–Kovchegov equation (ciBK) in [23,130]. In this approach, both the kernel and the

initial condition at leading-order obtain corrections coming from the double and single collinear logarithmic contributions at NLO. The main implication is that the ciBK prescription imposes a time-ordering of the dipole lifetimes. This suppresses emissions of very large daughter dipoles which would live longer than the parent one, and it has further implications in the impact-parameter dependent calculation, which will be discussed in Sec. 3.3. The collinearly-improved kernel reads

$$K_{\text{ci}} = \frac{\bar{\alpha}_S}{2\pi}\frac{r_{xy}^2}{r_{xz}^2 r_{zy}^2}\left[\frac{r_{xy}^2}{\min\left\{r_{xz}^2, r_{zy}^2\right\}}\right]^{\pm\bar{\alpha}_S A_1} K_{\text{DLA}}(\rho), \tag{3.13}$$

where the single-transverse logarithms are treated by including the term $A_1 = \frac{11}{12}$ as an anomalous dimension, i.e. as an extra power-law suppression of the kernel. The positive sign in the exponent $\pm\bar{\alpha}_S A_1$ is taken when $r_{xy} < \min\left\{r_{xz}, r_{zy}\right\}$ and the negative sign otherwise.

The "DLA kernel" [131] resums the double collinear logarithms to all orders

$$K_{\text{DLA}}(\rho) = \frac{J_1\left(2\sqrt{\bar{\alpha}_S\rho^2}\right)}{\sqrt{\bar{\alpha}_S\rho^2}} = 1 - \frac{\bar{\alpha}_S\rho^2}{2} + \frac{(\bar{\alpha}_S\rho^2)^2}{12} + \ldots, \tag{3.14}$$

where J_1 is the Bessel function. In case the argument of the square root of K_{DLA} is negative, the absolute value is taken and the Bessel function J_1 is exchanged by the modified Bessel function I_1. The kernel is evaluated at

$$\rho = \sqrt{L_{r_{xz}r_{xy}} L_{r_{zy}r_{xy}}}; \qquad L_{r_i r_{xy}} = \ln\left(\frac{r_i^2}{r_{xy}^2}\right). \tag{3.15}$$

This collinearly-improved kernel has also been used in [23] to perform a fit to HERA data and to successfully describe the proton structure functions measured in HERA experiments. From the dipole amplitudes shown in Fig. 3.5 (right), it is observed that this type of the BK equation provides again a slower evolution speed when compared to the previous results. This is mainly due to the resummation of higher order corrections in the kernel K_{ci}. It is important to point out, that although this version of the equation was successfully used in fitting the description of DIS data [23], so far, there has been no successful description of data on other QCD processes, e.g. production of vector mesons, using this set of solutions to the b-independent LO BK equation.

Several general observations regarding the properties of the above presented solutions to the b-independent LO BK equation can be summarised as follows:

- **The dependence of N on the dipole size r_{xy}:** The amplitude is ~ 0 for very small dipole sizes; this region is called the dilute regime and corresponds to colour transparency. At a certain dipole size, the amplitude starts to grow exponentially and with increasing dipole size, the saturation effects start to manifest by changing the exponential behaviour. The system enters a so called dense regime and the amplitude reaches its maximal value $N = 1$ for very large dipoles. When evolved in rapidity, the amplitude starts to grow and saturates to 1 for smaller dipole sizes, corresponding to a higher scattering probability of such dipoles at higher energies. This causes saturation to become more apparent even for small dipoles.

- **Geometric scaling:** Another important observation is that the choice of the specific initial condition does not have an influence on the evolution to very high rapidities, as observed in [50]. In the asymptotic limit of high rapidities, the solution to the BK evolution is no longer a function of the two variables r_{xy} and Y separately, but instead the solution depends on a single scaling variable, denoted as $\tau \equiv rQ_s(Y)$. The saturation scale $Q_s(Y)$ determines a transverse momentum below

which the unintegrated gluon distribution saturates and is obtained from the amplitude $N(r_{xy}, Y)$ as $N(r_{xy} = 1/Q_s(Y), Y) = k$, where the constant $k \lesssim 1$ is usually taken to be 0.5. The scaling causes the solution $N(r_{xy}, Y)$ to propagate independently on its original prescription at $Y = 0$. The geometric scaling in the BK equation solutions has been studied in detail in [19, 132–136] and it is related to the geometric scaling of the inclusive DIS data introduced in Sec 1.3.1.

3.2 Balitsky–Kovchegov equation at next-to-leading order

The full Balitsky–Kovchegov equation at next-to-leading order accuracy (NLO BK) was introduced in [137] within the framework of light-cone QCD. It is an equation for the trace of the product of two Wilson lines, $\mathrm{Tr}\{\hat{U}_x\hat{U}_y^\dagger\}$. The Wilson lines at transverse coordinates $\vec{x}$ and $\vec{y}$ represent the quark and the anti-quark, respectively, forming a colour dipole as introduced above. The theoretical background behind the light-cone QCD calculations using Wilson lines is beyond the scope of this work, more insight can be found in books [59, 138]. The coordinates for the eikonal Wilson lines and their separations, which can be related to transverse dipole sizes, can be seen in Fig. 3.7 and I follow this notation with slight changes with respect to my own notation introduced in the preceding section. At the next-to-leading order, the BK equation obtains several extra contributions from quark and gluon loops and from the three gluon diagrams. Simply said, the equation describes the transition from the parent dipole to three daughters (and their recombination) and includes corrections of higher orders in α_S.

The original equation, with changes respecting our notation, is written as

$$
\begin{aligned}
&\frac{\mathrm{d}}{\mathrm{d}Y}\,\mathrm{Tr}\{\hat{U}_x\hat{U}_y^\dagger\} = \qquad (3.16)\\
&= \frac{\alpha_S}{2\pi^2}\int \mathrm{d}^2z\;\frac{\vec{r}_{xy}^{\,2}}{\vec{r}_{xz}^{\,2}\vec{r}_{zy}^{\,2}}\left\{1+\frac{\alpha_S}{4\pi}\left[\beta_{n_f}\ln\left(\vec{r}_{xy}^{\,2}\mu^2\right)-\beta_{n_f}\frac{\vec{r}_{xz}^{\,2}-\vec{r}_{zy}^{\,2}}{\vec{r}_{xy}^{\,2}}\ln\frac{\vec{r}_{xz}^{\,2}}{\vec{r}_{zy}^{\,2}}+\left(\frac{67}{9}-\frac{\pi^2}{3}\right)N_\mathrm{c}-\frac{10}{9}n_f\right.\right.\\
&\qquad\left.\left.-2N_\mathrm{c}\ln\frac{\vec{r}_{xz}^{\,2}}{\vec{r}_{xy}^{\,2}}\ln\frac{\vec{r}_{zy}^{\,2}}{\vec{r}_{xy}^{\,2}}\right]\right\}\times\left[\mathrm{Tr}\{\hat{U}_x\hat{U}_z^\dagger\}\mathrm{Tr}\{\hat{U}_z\hat{U}_y^\dagger\}-N_\mathrm{c}\mathrm{Tr}\{\hat{U}_x\hat{U}_y^\dagger\}\right]\\
&+\frac{\alpha_S^2}{16\pi^4}\int \mathrm{d}^2z\,\mathrm{d}^2w\left[\left(-\frac{4}{\vec{r}_{zw}^{\,4}}+\left\{2\,\frac{\vec{r}_{xz}^{\,2}\,\vec{r}_{wy}^{\,2}+\vec{r}_{xw}^{\,2}\,\vec{r}_{zy}^{\,2}-4\,\vec{r}_{xy}^{\,2}\,\vec{r}_{zw}^{\,2}}{\vec{r}_{zw}^{\,4}\left[\vec{r}_{xz}^{\,2}\,\vec{r}_{wy}^{\,2}-\vec{r}_{xw}^{\,2}\,\vec{r}_{zy}^{\,2}\right]}+\frac{\vec{r}_{xy}^{\,4}}{\vec{r}_{xz}^{\,2}\,\vec{r}_{wy}^{\,2}-\vec{r}_{xw}^{\,2}\,\vec{r}_{zy}^{\,2}}\left[\frac{1}{\vec{r}_{xz}^{\,2}\,\vec{r}_{wy}^{\,2}}+\frac{1}{\vec{r}_{zy}^{\,2}\,\vec{r}_{xw}^{\,2}}\right]+\right.\right.\\
&\qquad\left.\left.+\frac{\vec{r}_{xy}^{\,2}}{\vec{r}_{zw}^{\,2}}\left[\frac{1}{\vec{r}_{xz}^{\,2}\,\vec{r}_{wy}^{\,2}}-\frac{1}{\vec{r}_{xw}^{\,2}\,\vec{r}_{zy}^{\,2}}\right]\right\}\ln\frac{\vec{r}_{xz}^{\,2}\,\vec{r}_{wy}^{\,2}}{\vec{r}_{xw}^{\,2}\,\vec{r}_{zy}^{\,2}}\right)\times\\
&\qquad\times\left[\mathrm{Tr}\{\hat{U}_x\hat{U}_z^\dagger\}\mathrm{Tr}\{\hat{U}_z\hat{U}_w^\dagger\}\mathrm{Tr}\{\hat{U}_w\hat{U}_y^\dagger\}-\mathrm{Tr}\{\hat{U}_x\hat{U}_z^\dagger\hat{U}_wU_y^\dagger\hat{U}_z\hat{U}_w^\dagger\}-(w\to z)\right]+\\
&\qquad+\left\{\frac{\vec{r}_{xy}^{\,2}}{\vec{r}_{zw}^{\,2}}\left[\frac{1}{\vec{r}_{xz}^{\,2}\,\vec{r}_{wy}^{\,2}}+\frac{1}{\vec{r}_{zy}^{\,2}\,\vec{r}_{xw}^{\,2}}\right]-\frac{\vec{r}_{xy}^{\,4}}{\vec{r}_{xz}^{\,2}\,\vec{r}_{wy}^{\,2}\,\vec{r}_{xw}^{\,2}\,\vec{r}_{zy}^{\,2}}\right\}\ln\frac{\vec{r}_{xz}^{\,2}\,\vec{r}_{wy}^{\,2}}{\vec{r}_{xw}^{\,2}\vec{r}_{zy}^{\,2}}\times\\
&\qquad\times\left[\mathrm{Tr}\{\hat{U}_x\hat{U}_z^\dagger\}\mathrm{Tr}\{\hat{U}_z\hat{U}_w^\dagger\}\mathrm{Tr}\{\hat{U}_w\hat{U}_y^\dagger\}\right]+\\
&\qquad+4n_f\left\{\frac{4}{\vec{r}_{zw}^{\,4}}-2\,\frac{\vec{r}_{xw}^{\,2}\,\vec{r}_{zy}^{\,2}+\vec{r}_{wy}^{\,2}\,\vec{r}_{xz}^{\,2}-\vec{r}_{xy}^{\,2}\,\vec{r}_{zw}^{\,2}}{\vec{r}_{zw}^{\,4}\left[\vec{r}_{xz}^{\,2}\,\vec{r}_{wy}^{\,2}-\vec{r}_{xw}^{\,2}\,\vec{r}_{zy}^{\,2}\right]}\ln\frac{\vec{r}_{xz}^{\,2}\,\vec{r}_{wy}^{\,2}}{\vec{r}_{xw}^{\,2}\,\vec{r}_{zy}^{\,2}}\right\}\times\\
&\qquad\times\left[\mathrm{Tr}\{t^a\hat{U}_xt^b\hat{U}_y^\dagger\}\left(\mathrm{Tr}\{t^a\hat{U}_zt^b\hat{U}_w^\dagger\}-(w\to z)\right)\right]\Bigg],
\end{aligned}
$$

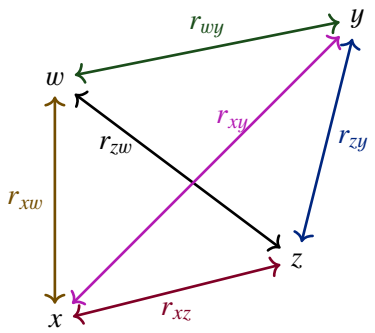

Figure 3.7: Coordinates for the eikonal Wilson lines and their separations, drawn according to Ref. [141].

where μ is the renormalisation scale. The quark part of the NLO BK equation, which is proportional to n_f, was derived in [129, 139], the terms with the cubic non-linearities were introduced in [140]. The gluon part of the equation was introduced in [137], which also concluded the whole BK equation at next-to-leading order and proposed the argument of α_S to be determined by the size of the smallest dipole.

Compared to the LO equation (3.2), we can observe several changes in the structure of the equation. In the first part with single integration over transverse coordinate $\vec{z}$, a correction of order $\sim \alpha_S^2$ to the kernel is present. Second, there are two new terms of order $\sim \alpha_S^2$ with double integration over transverse coordinates $\vec{z}$ and $\vec{w}$ which correspond to partonic fluctuations involving two additional partons at the time of the scattering, besides the parent dipole. The term independent of n_f represents the gluon part, where both daughter partons are gluons. The sequence of emissions goes as follows: the parent dipole $\vec{r}_{xy}$ emits a gluon at $\vec{z}$, effectively creating daughter dipoles $\vec{r}_{xz}$ and $\vec{r}_{zy}$; then the dipole $\vec{r}_{zy}$ emits a gluon at $\vec{w}$ which again is approximated by a $q\bar{q}$ pair. The resulting daughter dipoles are then $\vec{r}_{xz}$, $\vec{r}_{zw}$, and $\vec{r}_{wy}$. The cubic term gives the "real" contribution and describes the situation where all daughter dipoles interact with the target, while the quadratic term represents the "virtual" contribution where the gluon at $\vec{w}$ has been emitted and reabsorbed either before or after the interaction, and which also subtracts the contribution from the situation where gluons are emitted at $\vec{z} = \vec{w}$. A similar situation applies for the part proportional to n_f, however instead of the gluons, the daughter partons at the time of the scattering are a quark or an antiquark.

From Eq. (3.17), its mean-field approximation can be derived [26] and the NLO BK equation can be rewritten in terms of scattering amplitudes N as

$$\begin{aligned}
\partial_Y N(r_{xy}) \;=\; & \int \mathrm{d}^2 z K_\mathrm{a}\Big[N(r_{xz}) + N(r_{zy}) - N(r_{xy}) - N(r_{xz})N(r_{zy})\Big] \\
+ \; & \int \mathrm{d}^2 z\, \mathrm{d}^2 w\, K_\mathrm{b}\Big[N(r_{wy}) + N(r_{zw}) - N(r_{zy}) - N(r_{xz})N(r_{zw}) - N(r_{xz})N(r_{wy}) - \\
& \qquad -N(r_{zw})N(r_{wy}) + N(r_{xz})N(r_{zy}) + N(r_{xz})N(r_{zw})N(r_{wy})\Big] \\
+ \; & \int \mathrm{d}^2 z\, \mathrm{d}^2 w\, K_\mathrm{f}\Big[N(r_{xw}) - N(r_{xz}) - N(r_{zy})N(r_{xw}) + N(r_{xz})N(r_{zy})\Big].
\end{aligned} \tag{3.17}$$

The expression for the first kernel K_a according to Ref. [26] is

$$K_\mathrm{a} = K_\mathrm{rc} + \frac{\alpha_S^2(r_{xy})N_\mathrm{c}^2}{8\pi^3}\frac{r_{xy}^2}{r_{xz}^2 r_{zy}^2}\left[\frac{67}{9} - \frac{\pi^2}{3} - \frac{10}{9}\frac{n_f}{N_\mathrm{c}} - 2\ln\frac{r_{xz}^2}{r_{xy}^2}\ln\frac{r_{zy}^2}{r_{xy}^2}\right]. \tag{3.18}$$

From Eq. (3.17), it can be seen that the first part of the kernel in the first integral consists of the leading-order BK kernel, which is given by Eq. (3.11), and an NLO correction $\sim \alpha_S^2$, where the part of the NLO corrections including the term involving the renormalisation scale μ can be absorbed into the running coupling; the exact approach depends on the scheme choice.

The explicit expressions for the purely NLO kernels K_{b} and K_{f} in Eq. (3.17) are

$$K_{\mathrm{b}} = \frac{\alpha_S^2 N_{\mathrm{c}}^2}{8\pi^4}\left(-\frac{2}{r_{zw}^4} + \left[\frac{r_{xz}^2 r_{wy}^2 + r_{xw}^2 r_{zy}^2 - 4r^2 r_{zw}^2}{r_{zw}^4(r_{xz}^2 r_{wy}^2 - r_{xw}^2 r_{zy}^2)} + \frac{r_{xy}^4}{r_{xz}^2 r_{wy}^2(r_{xz}^2 r_{wy}^2 - r_{xw}^2 r_{zy}^2)} + \frac{r_{xy}^2}{r_{xz}^2 r_{wy}^2 r_{zw}^2}\right]\ln\frac{r_{xz}^2 r_{wy}^2}{r_{xw}^2 r_{zy}^2}\right), \quad (3.19)$$

$$K_{\mathrm{f}} = \frac{\alpha_S^2 n_f N_C^2}{8\pi^4}\left(\frac{2}{r_{zw}^4} - \frac{r_{xw}^2 r_{zy}^2 + r_{wy}^2 r_{xz}^2 - r_{xy}^2 r_{zw}^2}{r_{zw}^4(r_{xz}^2 r_{wy}^2 - r_{xw}^2 r_{zy}^2)}\ln\frac{r_{xz}^2 r_{wy}^2}{r_{xw}^2 r_{zy}^2}\right). \quad (3.20)$$

The first numerical study with the full NLO BK equation was performed in Ref. [26], where the authors directly solved equation (3.17) in one-dimensional coordinate space (i.e. the resulting dipole amplitudes depend only on the magnitude of the dipole size r) using the initial condition given by Eq. (3.4) and studied the influence of NLO corrections and the choice of initial condition parameters on the behaviour of the numerical solution. The authors showed that the evolution is unstable because NLO corrections decrease the evolution speed and the scattering amplitude can even turn negative for small dipoles, which is an unphysical behaviour. A reasonably stable solution was obtained only with unphysical values for the initial condition parameters. The conclusion is that the problematic behaviour of the equation is (partially) due to the large double-logarithmic correction in kernel K_{a} which is not taken into account properly.

In order to prepare for the two-dimensional NLO calculation, I derived the Runge-Kutta methods of the second and fourth order for the NLO BK equation and calculated the one-dimensional dipole amplitudes, the result I obtained is in accordance with those of Ref. [26]. As can be seen from Fig. 3.8, the calculation is stable for rather unphysical parameters; $Q_{s,0}/\Lambda_{QCD} = 19$ results in the initial saturation scale $Q_{s,0}^2 \approx 21$ GeV^2 which is a much larger value than the usual choice $Q_{s,0}^2 \lesssim 1$ GeV^2. Moreover, the γ parameter is also much larger than the value $\gamma \approx 1$ which is the usual value extracted from the fits to DIS data. For lower values of the $Q_{s,0}^2$ parameter, I observed the same instabilities as reported in Ref. [26] which caused the amplitude to turn negative in the region of small r_{xy}.

3.2.1 Resummations to the full NLO BK equation

As the first attempt to tame the problem of the unstable NLO BK numerical solution, the authors of Ref. [130] proposed the collinearly-improved BK equation described in Sec. 3.1.3. The applied resummation scheme deals with the corrections where each power of α_S is accompanied by a double-transverse logarithm. In the subsequent publication [23], the authors also performed a partial resummation of collinear single-logarithmic terms coming from the purely NLO contributions from Eq. (3.17), which play an important role in the weak scattering regime where all the dipoles are small. They showed that in a strongly ordered regime where the daughter dipoles are larger than the parent one, apart from a dominant double transverse logarithm in the single integration term, a single transverse logarithm emerges from kernel K_{b}; hence both of them causing the NLO contributions to become comparable to, or even larger than, the LO contribution, which in turn causes the instability of the NLO BK equation solution.

Following the work of Refs. [23, 130], the full NLO BK equation with resummations was studied in Ref. [27]. The authors introduced a modification of the original kernel K_{a} to take into account single

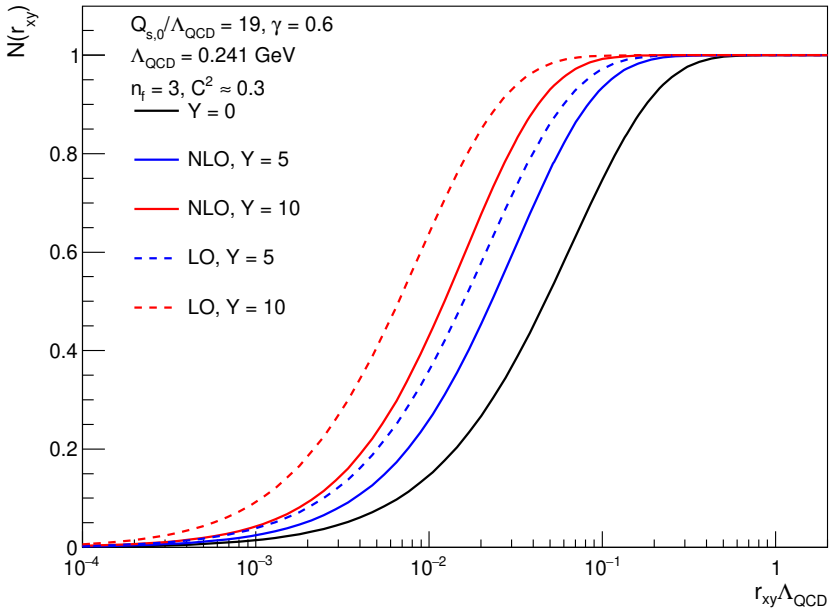

Figure 3.8: The scattering amplitude in dependence on r_{xy} as a solution to the b-independent NLO BK equation (3.17) (full lines) compared to the solution of the LO rcBK equation (dashed lines) using the same setup for both calculations.

and double logarithmic resummations, while the other two kernels — K_{b} and K_{f} — were left unchanged. The modified kernel K_{a} is denoted as K_1 and reads

$$K_1(r_{xy}, r_{xz}, r_{zy}) = K_{\mathrm{rc}} K_{\mathrm{STL}} K_{\mathrm{DLA}} - K_{\mathrm{sub}} + K_{\mathrm{fin}}, \tag{3.21}$$

where K_{rc} is defined by Eq. (3.12) and K_{DLA} is defined by Eq. (3.14). The term K_{STL} is given by

$$K_{\mathrm{STL}} = \exp\left[-\bar{\alpha}_S A_1 \left| \ln\left(\frac{C_{\mathrm{sub}} r_{xy}}{\min\left\{r_{xz}, r_{zy}\right\}}\right)\right|\right], \tag{3.22}$$

where the factor C_{sub} is a constant which was not fixed in Ref. [23], however the authors of Ref. [27] set it to 0.65 in order to accurately capture the full small-r_{xy} limit of the single-transverse logarithm term. In order to avoid double counting, the term K_{sub} takes into account the subtraction of the α_S^2 part of the single transverse logarithm K_{STL} that is already included in K_{b}. This subtraction term is given as

$$K_{\mathrm{sub}} = \frac{\bar{\alpha}_S}{2\pi}\left[-\bar{\alpha}_S A_1 \left| \ln\left(\frac{C_{\mathrm{sub}} r_{xy}}{\min\left\{r_{xz}^2, r_{zy}^2\right\}}\right)\right|\right] \frac{r_{xy}^2}{r_{xz}^2 r_{zy}^2}. \tag{3.23}$$

The remaining NLO term from K_{a}, which is not included in resummation, is denoted by K_{fin} and reads

$$K_{\mathrm{fin}} = \frac{\bar{\alpha}_S^2}{8\pi} \frac{r_{xy}^2}{r_{xz}^2 r_{zy}^2}\left[\frac{67}{9} - \frac{\pi^2}{3} - \frac{10}{9}\frac{n_{\mathrm{f}}}{N_{\mathrm{c}}}\right]. \tag{3.24}$$

In Ref. [27], the authors numerically prove that the most important NLO corrections can be included into the BK equation at large saturation scales and at small dipoles by the resummation of large transverse

logarithms. They also show that the evolution of the resummed equation is stable and gives physically reasonable results for the dipole scattering amplitude, as can be seen from my own calculation using the one-dimensional resummed NLO BK equation depicted in Fig. 3.9. It can be seen that the stable solution is now reached with the initial parameters $\gamma = 1$ and $Q_{s,0}/\Lambda_{QCD} = 2$.

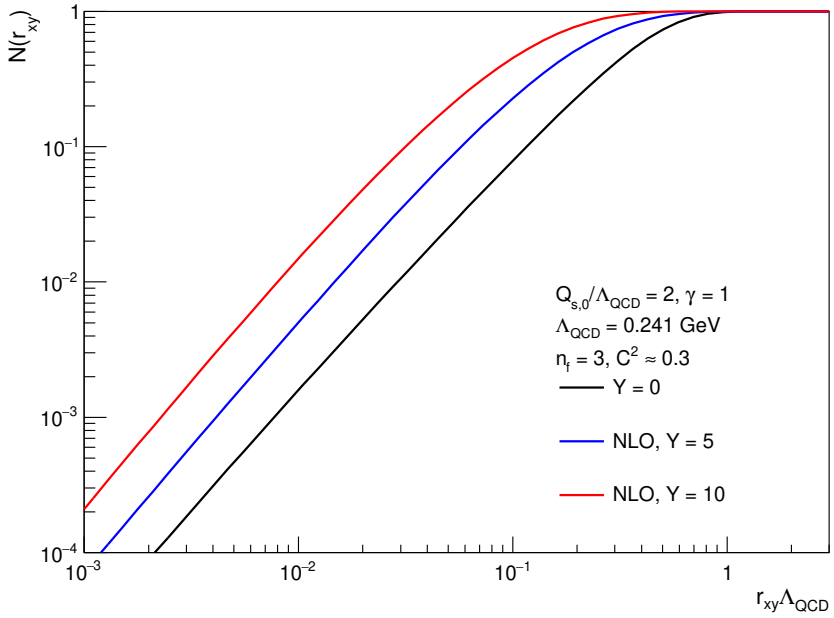

Figure 3.9: The scattering amplitude in dependence on r_{xy} as a solution to the b-independent NLO BK equation (3.17) with the resummed kernel given by Eq. (3.21) and using the variable n_f prescription for the α_S calculation.

The NLO corrections are numerically important for the phenomenological applications and therefore its proper treatment is a key for future successful studies using the BK equation. Therefore, the first fit to HERA structure function data using the NLO BK equation was performed in Ref. [25]. Moreover, the authors of the ciBK equation calculated the resummation of the radiative corrections to NLO BK enhanced by (anti)-collinear logarithms and proposed the NLO BK equation non-local in rapidity in Ref. [24]. This new version of the collinearly-improved BK is solved in the target rapidity $\eta = \ln(1/x)$, instead of the projectile dipole rapidity, which should be correctly defined as $Y = (\ln 1/x) + \ln(Q^2/Q_s^2)$. However, the authors of Ref. [25] conclude that at the NLO accuracy, the choice of the rapidity for the evolution does not significantly influence the results and quality of the fits.

3.3 Balitsky–Kovchegov equation with an impact-parameter dependence

In the previous section, the dependence of the dipole scattering amplitude on the impact parameter $\vec{b}$ has been neglected under the presumption of an infinite homogeneous target. However, this in theory justifiable approximation can appear to be unphysical when confronted to the experimental findings on the finite size of hadrons. Moreover, the solution of the BK equation including the impact-parameter dependence brings a more elegant input for phenomenological applications, in which the b-dependence of the dipole-hadron cross section has to be modelled in other means, e.g. as described in Chapter 2. Let us therefore move to the case of the finite target. This implies that the scattering amplitude depends on the magnitude of b, but not on its orientation. Also, the angle between the vectors $\vec{r}$ and $\vec{b}$ is kept

fixed under the assumption that the dipole amplitude does not depend strongly on the mutual orientation of the vectors, but predominantly on their magnitude. Under these assumptions, the impact-parameter dependent leading-order BK equation (denoted as b-BK in the following text) reads

$$\frac{\partial N(r_{xy}, b_{xy}, Y)}{\partial Y} = \int \mathrm{d}\vec{r}_{xz}\, K(r_{xy}, r_{xz}, r_{zy}) \Big[N(r_{xz}, b_{xz}, Y) + N(r_{zy}, b_{zy}, Y) - N(r_{xy}, b_{xy}, Y) - N(r_{xz}, b_{xz}, Y)\, N(r_{zy}, b_{zy}, Y) \Big]. \tag{3.25}$$

This equation has been solved for the first time in Refs. [103, 142] using the running coupling kernel in Eq. (3.12). It was found that the solution presents so-called Coulomb tails — a power-like tail at large impact parameters causing the amplitude to grow too fast in this region when evolved to a higher rapidity Y. This effect destroys the predictive power of the BK equation for phenomenological applications because the resulting cross section violates the Froissart bound. In order to obtain a reasonable description of the data, a cut-off to the running coupling kernel in Eq. (3.12) was introduced in Ref. [104] in order to suppress emissions of large daughter dipoles which cause the growth of the amplitude at large b. This approach was able to describe HERA data on both structure functions [104] and vector meson production in DIS [143], however an extra "soft" contribution had to be included in order to correctly describe F_2.

A new way to solve the problem of Coulomb tails has been proposed in Ref. [28], where the collinearly-improved kernel given by Eq. (3.13) was used in Eq. (3.25). The authors also provide a new form of the b-dependent initial condition. It is inspired by the GBW model, Eq. (1.32), in order to describe the behaviour in r and it is combined with a Gaussian distribution which reflects the profile of the proton in the impact-parameter space, inspired by phenomenological models and their applications, see e.g. Refs. [86, 144].

The prescription for the initial condition reads

$$N(r_{xy}, b_{xy}, Y = 0) = 1 - \exp\left[-\frac{1}{2} \frac{Q_{s0}^2}{4} r_{xy}^2 T(b_{q_1}, b_{q_2}) \right], \tag{3.26}$$

where

$$T(b_{q_1}, b_{q_2}) = \left[\exp\left(-\frac{b_{q_1}^2}{2B_G} \right) + \exp\left(-\frac{b_{q_2}^2}{2B_G} \right) \right], \tag{3.27}$$

and b_{q_i} are the impact parameters of the quark and anti-quark forming the dipole given as

$$b_{q_i}^2 = \left(\frac{r_{xy}}{2} \right)^2 + b_{xy}^2, \tag{3.28}$$

The parameter B_G has an interpretation as the variance of the Gaussian distribution of the target. The new ingredient in this prescription with respect to previous works is the explicit separation of the contributions from the individual quark and antiquark forming the parent dipole; the situation is depicted in Fig. 3.2. Including the explicit angle dependence between the vectors and the angle of orientation of $\vec{b}$ would allow for a more complex calculation and moreover, to include fluctuations of the proton structure and calculate their evolution.

The authors of Ref. [28] showed that unlike the case with $K_{\mathrm{rc}}^{\mathrm{bdep}}$, the Coulomb tails are strongly suppressed when K_{ci} is used, giving this success partially to the form of the initial condition in Eq. (3.26) and to the suppression of large daughter dipoles within the collinearly-improved kernel given by Eq. (3.13). The power-like tails are still present, however their contribution is small, which allows for phenomenological applications without the need for any additional modifications of the evolution kernel or the dipole amplitude, as can be seen in Fig. 3.10 for the inclusive DIS observables.

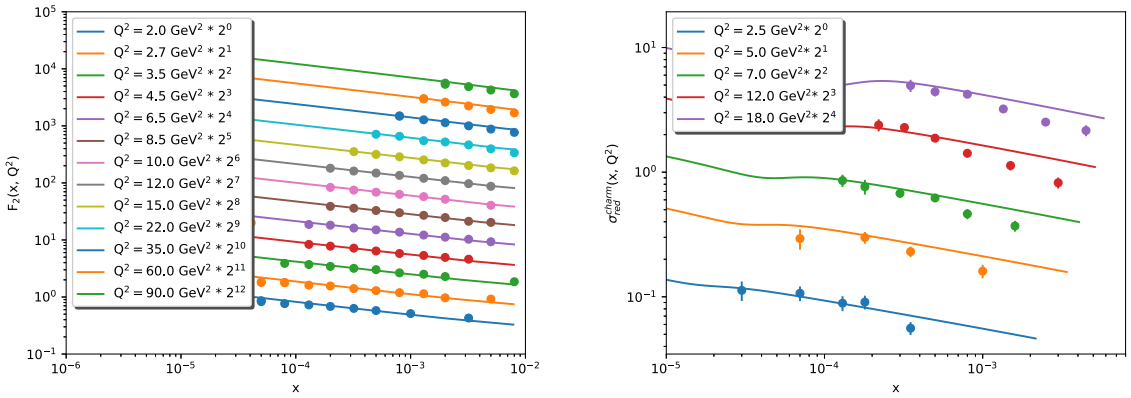

Figure 3.10: (Left): Predictions (lines) for the structure function $F_2(x, Q^2)$ calculated using the impact-parameter dependent BK equation (3.25) with the collinearly-improved kernel, given by Eq. (3.13), compared to HERA data [47]. (Right): The comparison of the predictions for the reduced cross section for charm to data from HERA [47]. Figures from Ref. [29].

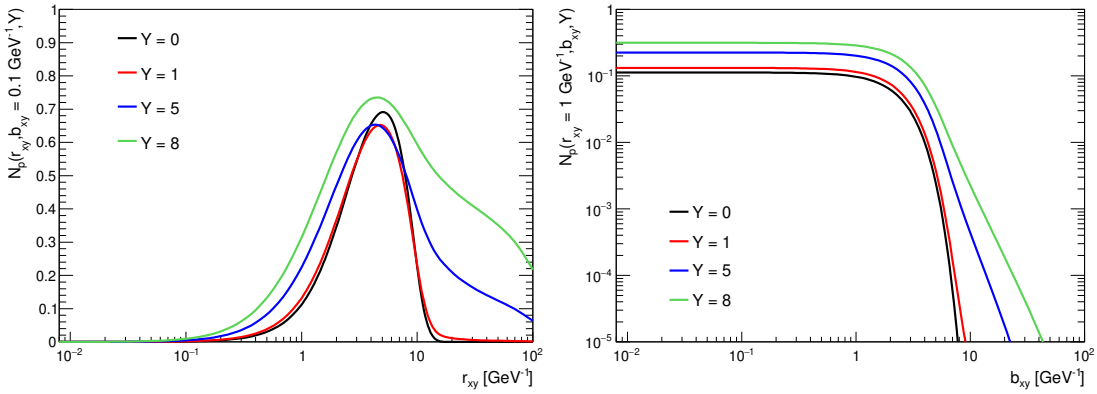

Figure 3.11: The solution to the b-dependent BK equation (3.25) using the collinearly-improved kernel, given by Eq. (3.13), and initial condition from Eq. (3.26):
(Left): dependence on r_{xy} for $b_{xy} = 0.1\,\mathrm{GeV}^{-1}$; (Right): dependence on b_{xy} for $r_{xy} = 1\,\mathrm{GeV}^{-1}$.

Since one of the aims of this work was to implement the approach to solve the b-dependent BK equation into its next-to-leading order form and develop an impact-parameter dependent NLO BK calculation, I obtained the b-dependent dipole amplitudes for the proton target. In Fig. 3.11, the dipole-proton scattering amplitude $N_p(r, b, Y)$ is shown for two cases: the r-dependence at a fixed impact parameter $b_{xy} = 0.1\ \mathrm{GeV}^{-1}$ in the left plot, and the b-dependence for a fixed dipole size $r_{xy} = 1\ \mathrm{GeV}^{-1}$ in the right plot. As in the case of BK solutions without an impact-parameter dependence, the amplitude decreases fast for small dipoles. On the other hand, large dipoles are suppressed in the initial condition given by Eq. (3.26) and with increasing rapidity, this suppression is being lifted. The b-behaviour at a fixed r_{xy} shows a constant amplitude for small impact parameters and at some point, the solution starts to decrease with increasing values of b_{xy}. However at large b_{xy}, the amplitude presents a change in its behaviour and again starts to grow. This is due to the development of so called *Coulomb tails*, which are however suppressed by the properties of the collinearly-improved kernel. I conclude that my results

are both quantitatively and qualitatively in agreement with Ref. [28]. The detailed discussion on the influence of the collinearly-improved kernel and its individual contributions to the development of the Coulomb tails can be found in Refs. [28, 29].

3.3.1 Dipole-nucleus scattering amplitudes

The solution of the BK equation for nuclear targets including the impact-parameter dependence of the dipole-nucleus scattering amplitude in the framework introduced above was developed in Ref. [30], where two approaches are proposed. The first one, so called Glauber–Gribov (b-BK-GG) approach, relies on the use of the solution of the BK equation (3.25) for the proton target from the initial condition given by Eq. (3.26), which is then inserted into the Glauber–Gribov approach (used in several other studies, e.g. [145–147]) to the dipole-nucleus amplitude

$$N^A_{\mathrm{GG}}(r_{xy}, b_{xy}, Y) = \left[1 - \exp\left(-\frac{1}{2} T_A(b_{xy}) \sigma_{q\bar{q}}(Y, r_{xy})\right)\right], \tag{3.29}$$

where the dipole cross section is obtained from the dipole-proton amplitude as

$$\sigma_{q\bar{q}}(Y, r_{xy}) = \int \mathrm{d}^2 b \, 2N^p(r_{xy}, b_{xy}, Y). \tag{3.30}$$

The $T_A(b_{xy})$ is a nuclear thickness function which is obtained from the integral over the longitudinal coordinate z,

$$T_A(b_{xy}) = \int_{-\infty}^{+\infty} \mathrm{d}z \, \rho_A(x, y, z), \tag{3.31}$$

of a Woods–Saxon distribution for the density of nuclear matter

$$\rho_A(x, y, z) = \frac{\rho_0}{1 + \exp\left[\frac{r-R}{a}\right]}, \tag{3.32}$$

where $r \equiv \sqrt{x^2 + y^2 + z^2}$,$x$ and y are coordinates in the impact-parameter plane, and the values of the parameters a and R are given by Table I in Ref. [30]. The thickness function is normalised according to

$$\int \mathrm{d}\vec{b}_{xy} \, T_A(b_{xy}) = A,$$

where A is the mass number of the given nucleus.

The second approach, denoted as b-BK-A, proposes to directly solve the impact-parameter dependent BK equation (3.25) with an initial condition representing a specific nucleus. The initial condition from Eq. (3.26) is modified for a specific nucleus using the Woods–Saxon distribution instead of the Gaussian (used in the proton case)

$$N^A(r_{xy}, b_{xy}, Y = 0) = 1 - \exp\left[-\frac{1}{2} \frac{Q^2_{s_0}(A)}{4} r^2_{xy} T_A\left(b_{q_1}, b_{q_2}\right)\right], \tag{3.33}$$

with

$$T_A\left(b_{q_1}, b_{q_2}\right) = k\left[T_A(b_{q_1}) + T_A(b_{q_2})\right], \tag{3.34}$$

where k ensures that $kT_A(0) = 1$. In order to obtain the initial nuclear saturation scale $Q^2_{s_0}(A)$, the nuclear structure function is calculated at the initial condition and compared to the predictions of the

EPPS16 [148] nuclear parton distributions. The dipole-nucleus amplitudes for these two approaches have been used in Ref. [30] to calculate nuclear structure functions and the nuclear suppression factors, which provide a measure of nuclear shadowing (for references on these observables see e.g. Ref. [10]).

The dipole-nucleus amplitudes $N_A(r, b, Y)$ are shown in Fig. 3.12 for the dependence on r_{xy} at a fixed b_{xy} (left panels) and for the dependence on b_{xy} at a fixed r_{xy} (right panels). The plots compare two approaches to obtain the dipole-nucleus amplitudes, denoted as b-BK-A (full lines) and b-BK-GG (dashed lines), while depicting the amplitudes for calcium nucleus in the upper panels and for the lead nucleus in lower panels. There is a clear difference between the two models, especially for the r-behaviour where the evolved amplitude for the b-BK-A case is suppressed to 0 for large dipole sizes, while the b-BK-GG amplitude remains flat at value $N = 1$ in this region. It can also be observed from the plots showing the b-behaviour, that the magnitude of the amplitude is much smaller in the b-BK-A approach. When comparing the results for the two nuclei, it is apparent that both the initial and evolved amplitudes are larger for the lead nucleus, i.e. the scattering probability is enhanced with higher A. The details on the behaviour of dipole-nucleus amplitudes and the related conclusions are discussed in Ref. [30]. I used the results of Refs. [28–30] to study the structure of hadrons by calculating the predictions for several QCD observables within the colour dipole approach. These studies will be described in the following chapter.

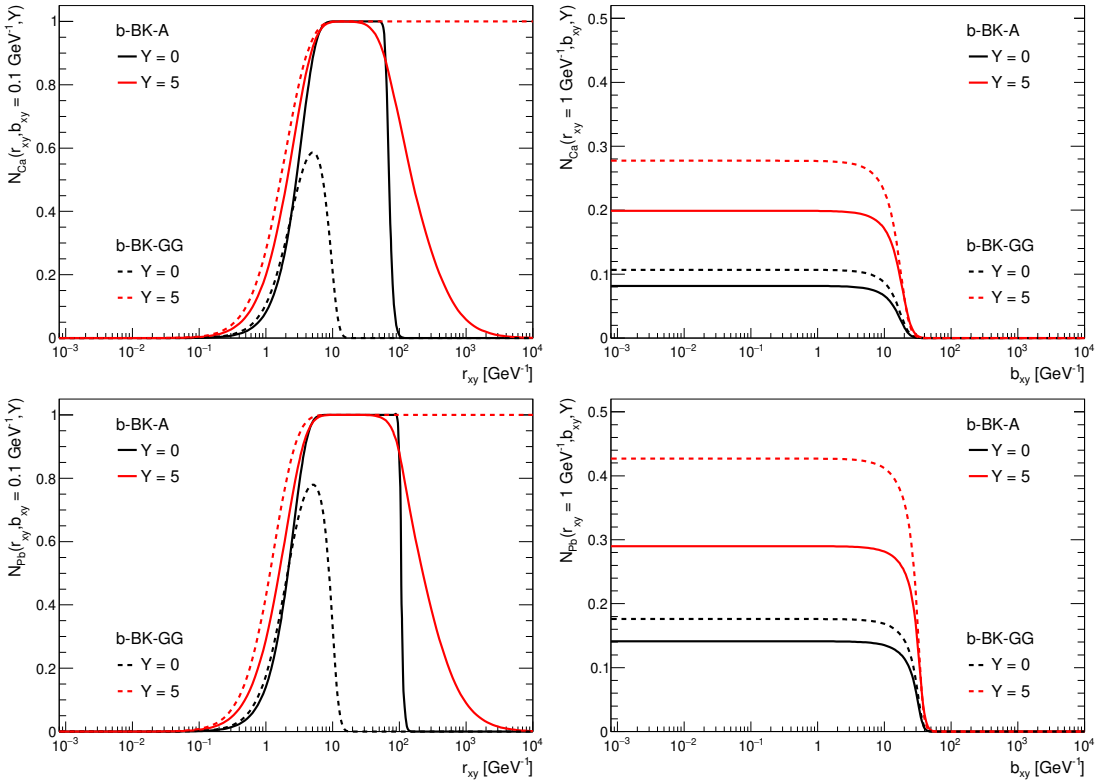

Figure 3.12: Dipole-nucleus scattering amplitudes as a solution to the b-dependent BK equation (3.25) using the collinearly-improved kernel given by Eq. (3.13) and initial conditions from Eqs. (3.29) and (3.33) for the b-BK-GG and b-BK-A approach, respectively. Upper plots depict the amplitudes for calcium nucleus (A = 40), lower plots are for lead (A = 208). Figures drawn using the amplitudes from Ref. [30].
(Left): Dependence on r_{xy} for $b_{xy} = 0.1\,\mathrm{GeV}^{-1}$; (Right:) Dependence on b_{xy} for $r_{xy} = 1\,\mathrm{GeV}^{-1}$.

Chapter 4

Applications of the solutions of b-BK equation to QCD phenomenology

In this chapter, I summarise the results of papers [29,31–33] I published together with my colleagues. In these papers, we were interested in the study of the hadronic structure using different QCD observables. Each of these processes has a different sensitivity to the underlying QCD dynamics and therefore, one can access different information about the hadronic structure through them. For example, one can obtain the structure functions and consequently, the unpolarised parton distribution functions from DIS and also the corresponding diffractive case, while it is possible to obtain the generalised parton distributions from the exclusive processes. Proposing realistic models which can correctly describe the current data and provide predictions for future measurements across various processes is therefore a highly desirable goal. Moreover, the correct description of some minimal set of data serves as a determination for the parameters of the given model. Namely for the Balitsky–Kovchegov equation, the aim is to obtain the simultaneous description of the inclusive DIS data and a correct description of one exclusive observable, e.g. $|t|$-dependence of the J/ψ photoproduction cross section, in order to fix the parameters of the initial condition. The obtained dipole scattering amplitudes evolved in rapidity can be then used for the calculation of various QCD processes presented in the following sections. For these predictions, I used the numerical solutions to the b-dependent BK equation described in Sec. 3.3, and I compare these predictions with the available data and also with other CGC-inspired models.

4.1 Diffractive deeply inelastic scattering with protons and nuclei

4.1.1 Diffractive DIS formalism within the dipole model

Diffractive deeply inelastic scattering represents a process where a diffractive system X is created while the target hadron remains intact in the final state and carries most of the beam momentum. Moreover, the hadronic system X and the final state hadron are separated by a large rapidity gap, which is a region in rapidity where no particles are produced as a result of the $\gamma^* h$ interaction being mediated by the Pomeron exchange, and therefore we observe no activity in the detector in this (pseudo)rapidity region. The size of the gap is $\Delta\eta \sim 1/x_{\mathbb{P}}$. The variable $x_{\mathbb{P}}$ is a momentum fraction carried by the Pomeron. It represents the fraction of the longitudinal momentum lost by the hadron in the interaction and is defined as

$$x_{\mathbb{P}} = \frac{Q^2 + M_X^2}{Q^2 + W^2}. \tag{4.1}$$

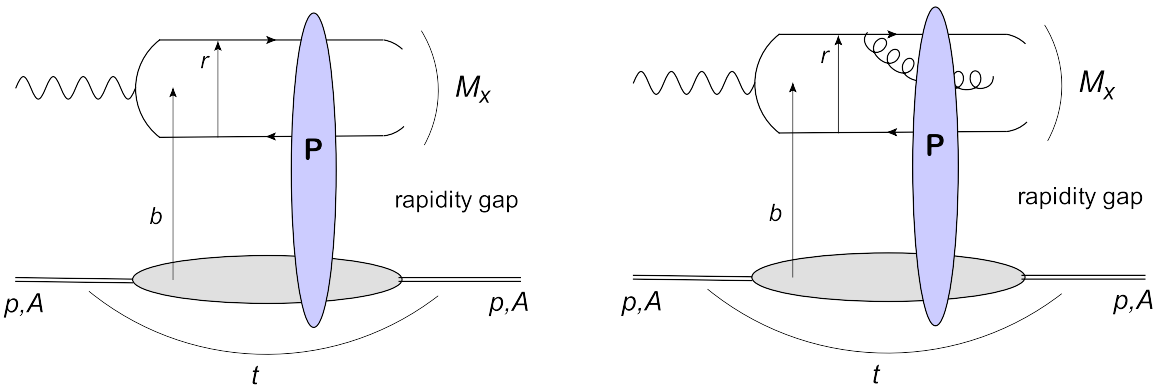

Figure 4.1: A sketch of the diffractive deeply inelastic scattering process within the colour dipole approach, showing the contributions from $q\bar{q}$ (left) and $q\bar{q}g$ (right) Fock states. Figures from Ref. [31].

We also define the variable β as

$$\beta = \frac{Q^2}{Q^2 + M_X^2}, \tag{4.2}$$

which is related to $x_{\mathbb{P}}$ and to the Bjorken-x variable, defined by Eq. (1.6), as $x = \beta x_{\mathbb{P}}$. It has been observed in ep collisions at HERA that diffraction represents a substantial contribution (approx. 15 %) to the total inelastic cross section and the process has also been observed in hadronic collisions at Tevatron and at the LHC [149]. It is expected that in nuclear DIS, i.e. in eA collisions, the diffractive events have even a larger contribution, predicted to be almost half of the total cross section in the asymptotic limit of very high energies. Therefore, due to the enhancement of the saturation scale Q_s^2 in nuclei, which determines the onset of nonlinear effects, the diffractive nuclear DIS can serve as a good probe of saturation effects in hadrons and the underlying QCD dynamics. For a review see e.g. [10, 149–152].

The advantage of the colour dipole approach of DIS, introduced in Section 1.3, is that it can incorporate both the inclusive and the diffractive case into one theoretical framework. Fig. 4.1 shows the two main contributions to diffractive DIS within the colour dipole approach. One of the very successful frameworks to describe the diffractive contribution is the saturation approach [74,75,144]. In this picture, the diffractive part of the total cross section from Eq. (1.7) is given as

$$\sigma_{\text{diff}}(x, Q^2) = \frac{1}{4} \sum_{i=L,T} \sum_f \int \mathrm{d}\vec{r} \int \mathrm{d}z |\Psi^* \Psi|^f_{T,L} \int \mathrm{d}\vec{b} \left(\frac{\mathrm{d}\sigma}{\mathrm{d}\vec{b}} \right)^2, \tag{4.3}$$

where the wave functions $|\Psi^* \Psi|^f_{T,L}$ are given by Eqs. (1.24) and (1.25), and the dipole-hadron cross section is given by Eq. (1.27).

The diffractive DIS cross section is usually measured as a function of three variables — $x_{\mathbb{P}}$, β, and the photon virtuality Q^2 — and is given by

$$\frac{\mathrm{d}\sigma^{eh \to eXh}}{\mathrm{d}\beta \mathrm{d}Q^2 \mathrm{d}x_{\mathbb{P}}} = \frac{4\pi\alpha_{em}^2}{\beta Q^4} \left[1 - y + \frac{y^2}{2} \right] \sigma_r^{D(3)}(x_{\mathbb{P}}, \beta, Q^2), \tag{4.4}$$

where $\sigma_r^{D(3)}$ is the diffractive reduced cross section, given by the diffractive structure functions as

$$\sigma_r^{D(3)}(x_{\mathbb{P}}, \beta, Q^2) = F_2^{D(3)}(x_{\mathbb{P}}, \beta, Q^2) - \frac{y^2}{1 + (1-y)^2} F_L^{D(3)}(x_{\mathbb{P}}, \beta, Q^2). \tag{4.5}$$

The diffractive structure function is a sum of the individual components contributing to the process

$$F_2^{D(3)}(Q^2,\beta,x_{\mathbb{P}}) = F^D_{q\bar{q},L} + F^D_{q\bar{q},T} + F^D_{q\bar{q}g,T}, \tag{4.6}$$

where $F^D_{q\bar{q},L}$, $F^D_{q\bar{q},T}$ represent contribution from the longitudinal, resp. transverse polarisation of the virtual photon which fluctuates into a $q\bar{q}$ dipole (left panel of Fig. 4.1). The function $F^D_{q\bar{q}g,T}$ represents the contribution from the situation where the photon fluctuates into the $q\bar{q}g$ Fock state (right panel of Fig. 4.1). The contribution from this fluctuation has only the transverse part, since the longitudinal part has no leading logarithm in Q^2. Detailed formulas for the individual contributions to the diffractive structure function F_2^D used in this work are listed in the Ref. [31], which follows the computation by [74, 75, 144, 153] and adapts the notation of [153]. Recently, the full NLO $q\bar{q}g$ contribution to the diffractive DIS has been calculated [154][1].

An important property of the diffractive DIS is its enhanced sensitivity to the dipole-target amplitude (and especially to its gluon contribution) since the $q\bar{q}g$-hadron cross section entering the $F^D_{q\bar{q}g,T}$ formula in Eq. (4.6) is given by

$$\frac{\mathrm{d}\sigma_g}{\mathrm{d}\vec{b}} = 2\left[1 - \left(1 - \frac{1}{2}\frac{\mathrm{d}\sigma_{q\bar{q}}}{\mathrm{d}\vec{b}}\right)^2\right]. \tag{4.7}$$

In addition to the predictions that the diffractive events may contribute with up to half of the total cross section in the asymptotic high-energy limit [153, 155, 156], this enhanced gluon contribution makes the diffractive events strongly sensitive to the QCD dynamics of the hadron structure and a useful tool to study the emergence of saturation effects both in protons and nuclei.

4.1.2 Results

The diffractive events represent a substantial contribution to the total inelastic cross section and it is expected that the contribution in nuclear interactions is even higher than in the proton case. Moreover, as introduced in the theoretical overview in Sec. 4.1.1, the process has an enhanced sensitivity to the gluon component of the hadronic structure. Therefore, the diffractive observables can serve as a complementary probe to the inclusive DIS. The presented results for diffractive DIS observables in protons and nuclei form the selection of my results published in Ref. [31]. These predictions were obtained using the dipole-hadron amplitudes $N(x,r,b)$ as a solution to the impact-parameter dependent BK equation (3.25) from Ref. [29] for the proton case and the nuclear amplitudes obtained in Ref. [30]. In these two publications, the inclusive DIS observables were also studied, concluding that the b-BK numerical solutions can provide a good description of the proton structure functions and reduced cross section data from HERA. In Ref. [30], the extension of the b-BK calculation to the nuclear case was proposed and the nuclear structure functions and suppression factors were studied, concluding that both approaches to the nuclear b-BK provide a reasonable description of the available data and that in future measurements, the approaches could be distinguished as the difference of their predictions increases with decreasing x and simultaneously with increasing Q^2 and in heavier nuclei. Therefore, we have decided to study the corresponding observables for the diffractive case in order to provide more information on this matter, and to complement the previous studies [74, 75, 144, 146, 153, 155] by the BK-based results, and also to provide predictions for future measurements such as those expected at the EIC [10, 119].

First, the predictions for the $x_{\mathbb{P}}$-dependence of the diffractive reduced cross section given by Eq. (4.5) for the proton case are compared to data from H1 [157] in Fig. 4.2 for several combinations of the β

[1] This contribution is not incorporated into the results presented in this thesis, because the related paper [154] was made available after our work [31] has been published.

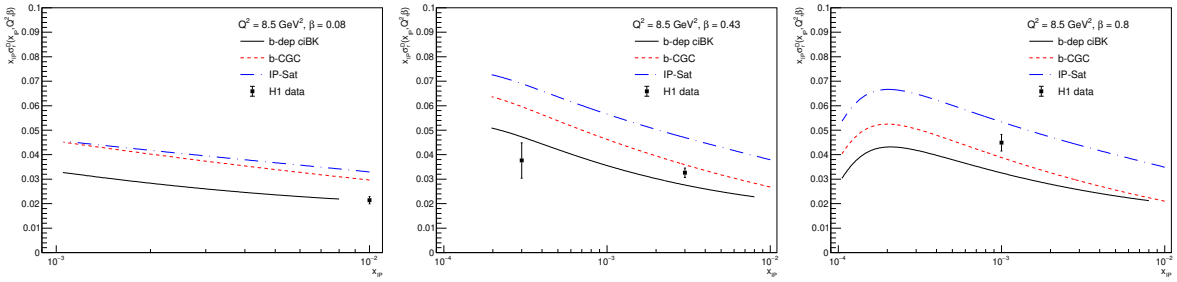

Figure 4.2: Predictions of the $x_{\mathbb{P}}$-dependence of the diffractive reduced cross section $\sigma_r^{D(3)}(x_{\mathbb{P}}, \beta, Q^2)$ at several combinations of Q^2 and β compared with H1 data [157]. Figures from Ref. [31].

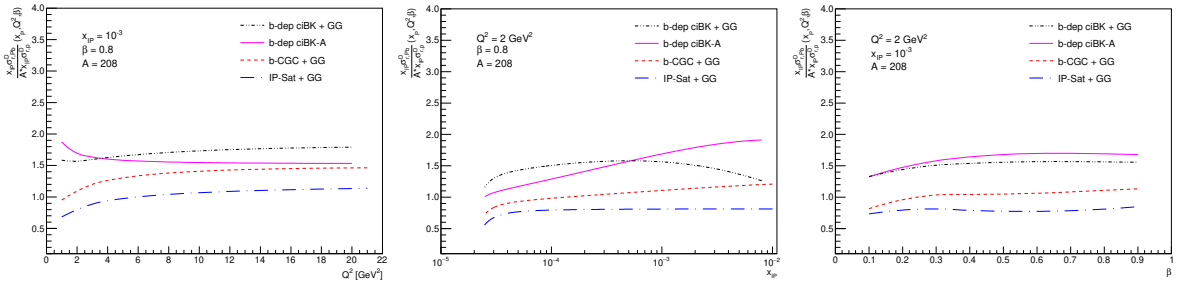

Figure 4.3: Predictions for the ratio $\sigma_{r,A}^{D(3)}(x_{\mathbb{P}}, \beta, Q^2)/A \cdot \sigma_{r,p}^{D(3)}(x_{\mathbb{P}}, \beta, Q^2)$ of the reduced diffractive cross sections for $A = 208$ using the b-BK model and several CGC-inspired models. Figures from Ref. [31]. (Left): Q^2-dependence for $\beta = 0.8$ and $x_{\mathbb{P}} = 10^{-3}$; (Middle): $x_{\mathbb{P}}$-dependence for $\beta = 0.8$ and $Q^2 = 2$ GeV^2; (Right): β-dependence for $x_{\mathbb{P}} = 10^{-3}$ and $Q^2 = 2$ GeV^2.

variable (more comparisons can be seen in Ref. [31]). The predictions using the b-BK equation are in a good agreement with the data at small and medium values of β, however the predictions underestimate the data in the large-β region. I also compare these predictions with the b-CGC [86] and IP-Sat [79] models and conclude that these models give larger values than the b-BK approach. Since the non-linear effects are expected to be enhanced in nuclei, the predictions for the nuclear case are also studied. In Fig. 4.3, the ratio of the diffractive reduced cross section to the proton case, rescaled by the atomic number A, is presented for the lead ($A = 208$) nucleus. The predictions are obtained using two different approaches to the nuclear b-BK evolution: the proton based coupled to a Glauber-Gribov prescription [145], denoted as b-BK-GG, and evolution from an initial condition describing the specific nucleus, denoted as b-BK-A (for details see Sec. 3.3.1). These predictions are compared to each other and to the other models for the Q^2-dependence, $x_{\mathbb{P}}$-dependence, and for the β-dependence of the diffractive to inclusive cross section ratio. For the very low Q^2 and large $x_{\mathbb{P}}$, the ratio is enhanced for the b-BK-A case when compared to the b-BK-GG predictions. However with decreasing $x_{\mathbb{P}}$ and increasing Q^2, the behaviour changes with b-BK-GG approach giving a larger contribution at low $x_{\mathbb{P}}$. The β-dependence for the reduced diffractive cross section ratio is mostly flat, with b-BK-A giving larger values in the prediction for the calcium nucleus. In overall, both b-BK predictions give larger ratios than the b-CGC and IP-Sat models.

I also investigated the ratio of diffractive and total cross sections $R_\sigma = \sigma_{\text{diff}}/\sigma_{\text{tot}}$ as this observable is sensitive to the differences in the energy-dependence between the diffractive and the inclusive cross sections and also to the way different models include saturation effects. This ratio is plotted in Fig. 4.4 for the proton (left panel) and lead nucleui (middle and right panels). From the comparison between the proton and lead scenario at the same Q^2, it can be seen that the diffractive processes are enhanced in

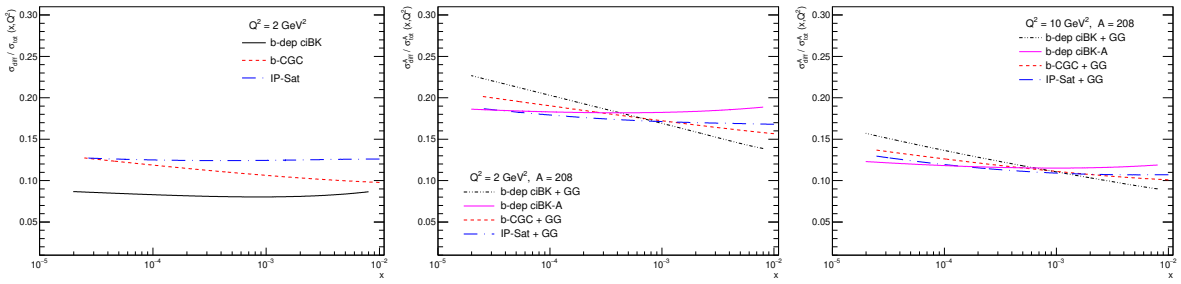

Figure 4.4: Predictions for the x-dependence of the ratio of diffractive and total cross sections for protons at $Q^2 = 2$ GeV^2 (left), and for lead nuclei at $Q^2 = 2$ GeV^2 (middle) and $Q^2 = 10$ GeV^2 (right), considering different models for the dipole amplitude. Figures from Ref. [31].

heavy nuclei. Moreover, the ratio decreases with increasing Q^2 in case of the lead nucleus,. The presented models show a different x-behaviour which can be associated with the treatment of the transition from the linear to nonlinear regime and also to the description of the impact-parameter dependence in these models. In general, the proton and also nuclear BK evolution (the b-BK-A approach) predict a flat behaviour of R_σ and smaller values in the low-x region compared to other models. Moreover, while IP-Sat model shows a flat behaviour for protons and only very slow increase towards low-x for lead, the b-CGC model predicts an increase of the ratio in both cases. This is due to the different treatment of the b-behaviour in these models; for the b-BK evolution and the IP-Sat, the impact parameter dependence is given by the hadronic profile, in the case of b-CGC, it is incorporated in the saturation scale. One can also observe that the two approaches to the nuclear BK predict different x-behaviour, with the proton solution coupled to the Glauber–Gribov prescription giving a grow of the ratio with decreasing x. This is associated to the faster evolution for the intermediate dipole sizes r, as can be seen from Fig. 3.12.

Let us now investigate the proton and nuclear diffractive structure functions, given by Eq. (4.6). In Fig. 4.5, the proton diffractive F_2 and its individual components are compared for three different models. It can be seen that the models give a similar behaviour of F_2^D and its components. This observation is expected as their β-dependence is given mainly by the photon wave functions. However, the overall normalisation is sensitive to the dipole amplitude coming from different models and it can be seen that the b-BK approach (right panel) gives smaller values of F_2^D and its components, which is in agreement with the observations from previous plots. Moreover, I show the $x_{\mathbb{P}}$-dependence at low and high β for F_2^D and its components calculated using the b-BK approach in Fig. 4.6. It can be observed that in low-β region, the dominant contribution comes from the $q\bar{q}g$ component while in the large-β region, the longitudinal $q\bar{q}$ component gives the largest contribution. The transverse $q\bar{q}$ component has its maximal contribution in the region of medium-β, where the longitudinal and the gluon components are of similar magnitude. It can also be observed that at fixed β, the contributions do not change dramatically with decreasing $x_{\mathbb{P}}$.

Equivalently to the previous case, the ratios to the scaled proton case for the nuclear diffractive structure functions and its components are presented in Fig. 4.7 using the b-BK-A predictions for calcium (upper panels) and lead (lower panels). In general, a nuclear enhancement of the individual components is observed in most cases and their total sum is enhanced when compared to the proton F_2^D. It is also observed that the ratio of the sum of the components is similar for both studied nuclei. This can be associated to the suppression of the $q\bar{q}g$ component with increasing atomic number A, observed when comparing predictions for calcium and lead nuclei, prominently visible in the left panels of Fig. 4.7. Also, one specific observation can be made. The longitudinal contribution is suppressed for medium β values in the case of b-BK-A approach, the suppression being larger for the calcium nucleus. This

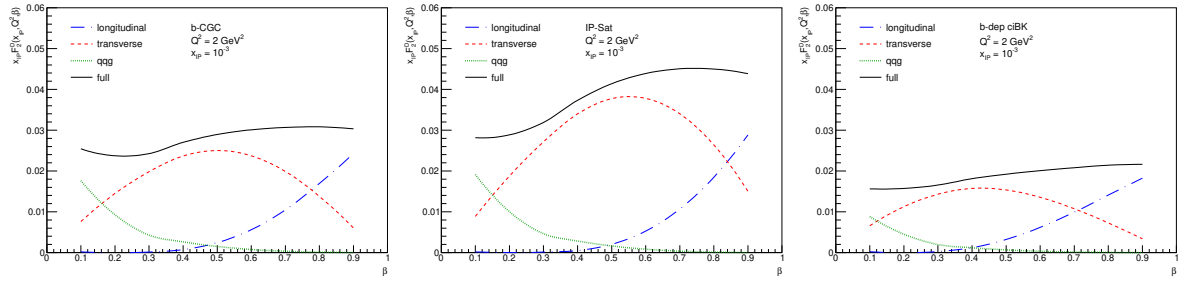

Figure 4.5: Predictions for the β-dependence of the individual components of the proton diffractive structure function $F_2^{D(3)}(Q^2, \beta, x_{\mathbb{P}})$ and their sum for $Q^2 = 2$ GeV^2 and $x_{\mathbb{P}} = 10^{-3}$. Figures from Ref. [31]. (Left): the b-CGC model; (Middle): the IP-Sat model; (Right): b-BK model.

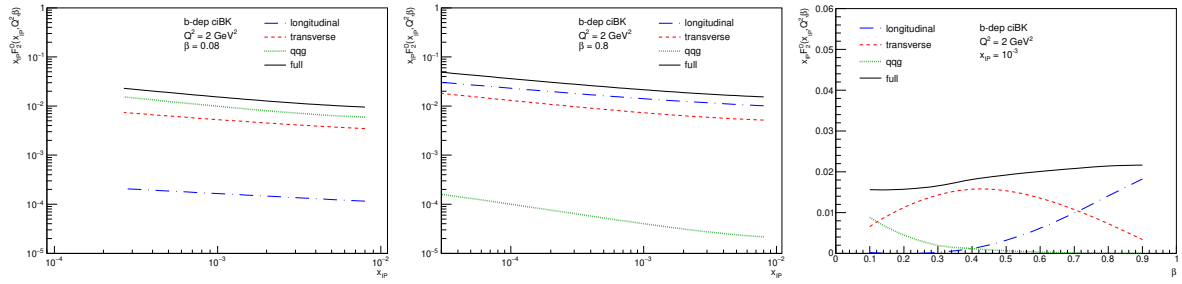

Figure 4.6: Predictions for the individual components of the proton diffractive structure function $F_2^{D(3)}(Q^2, \beta, x_{\mathbb{P}})$ and their sum for $Q^2 = 2$ GeV^2 using the b-dependent BK equation (3.25). Figures from Ref. [31].
(Left): $x_{\mathbb{P}}$-dependence for $\beta = 0.08$; (Middle): $x_{\mathbb{P}}$-dependence for $\beta = 0.8$; (Right): β-dependence for $x_{\mathbb{P}} = 10^{-3}$.

behaviour is in contradiction with the predictions using the Glauber-Gribov approach. Not only it is opposite when compared to the b-BK-GG approach presented in Ref. [31], but also when compared to previous results using the IP-Sat + GG model [153]; this specific work shows a large enhancement of the longitudinal component in the medium-β region, especially in heavy nuclei. A more detailed comparison of the predictions using both nuclear b-BK approaches and the predictions obtained from other phenomenological models, namely IP-Sat and b-CGC models coupled to the Glauber-Gribov approach, is presented in Ref. [31].

To conclude, the predictions for the ratio of the diffractive to total cross section are in agreement with previous results (see e.g. [153]), being of order 20% for electron-lead collisions. Moreover, these predictions depend only negligibly on the specific model for the dipole amplitude. I have shown that the b-BK predictions for the reduced cross section can satisfactorily describe available data from ep collisions at HERA and are therefore suitable to provide predictions for future measurements. As the distinct models predict different behaviour for the individual contributions to the nuclear diffractive structure functions and also for the diffractive to inclusive cross section ratio R_σ, it is expected that future experimental measurements will provide a better understanding of the underlying QCD dynamics.

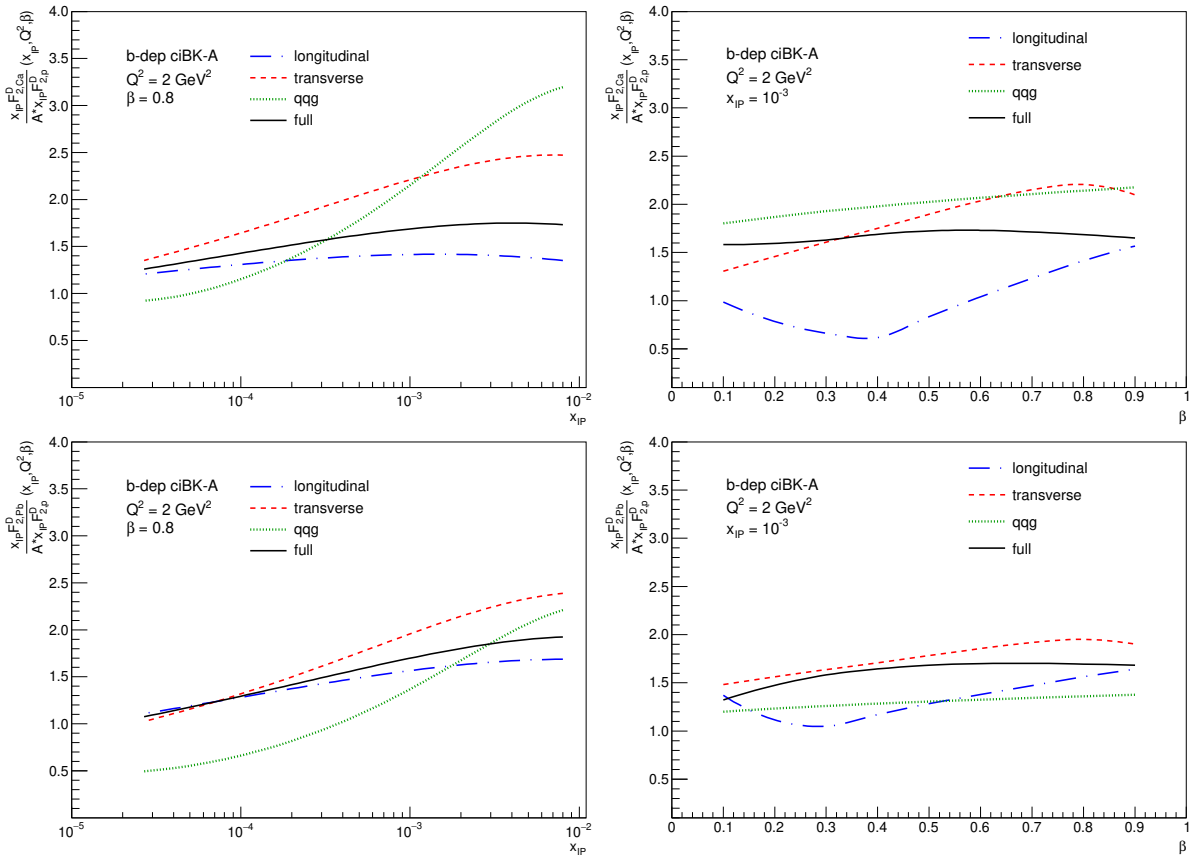

Figure 4.7: Predictions for the ratio $F_{2,A}^{D(3)}(Q^2,\beta,x_{\mathbb{P}})/A \cdot F_{2,p}^{D(3)}(Q^2,\beta,x_{\mathbb{P}})$ of the diffractive structure function F_2^D and its individual components at $Q^2 = 2$ GeV^2 for $A = 40$ (upper panels) and $A = 208$ (lower panels), using the dipole-nucleus amplitudes from the b-BK-A model. Figures from Ref. [31].
(Left panels): $x_{\mathbb{P}}$-dependence for $\beta = 0.8$. (Right panels): β-dependence for $x_{\mathbb{P}} = 10^{-3}$.

4.2 Deeply virtual Compton scattering

4.2.1 Colour dipole approach to DVCS

Similarly to the exclusive production of vector mesons, deeply virtual Compton scattering (DVCS) represents a useful tool to investigate the tomography picture of hadrons, as the Fourier transform of the cross section $|t|$-distribution can be used to obtain the distribution of gluons in the transverse space. The DVCS process is depicted in Fig. 4.8 and can be described in the same manner as the vector meson production (see Section 1.3.2), with the main difference in the exclusive final state particle which is a real photon in the case of DVCS.

The scattering amplitude takes the same form as in the vector meson case, see Eq. (1.34). However, in order to be consistent with previous DVCS studies, the exponential term containing $(1-z)$ is replaced by $(1-2z)/2$, as discussed in Ref. [88]. The wave function for the production of a real photon has only the transverse component and is given by

$$|\Psi_{\gamma^*}^{*}\Psi_{\gamma}|^f = \frac{N_c\alpha}{2\pi^2}e_f^2\left[\left(z^2+(1-z)^2\right)\epsilon_1^2K_1(\epsilon_1 r)\epsilon_2K_2(\epsilon_2 r)+m_f^2K_0(\epsilon_1 r)K_0(\epsilon_2 r)\right]. \tag{4.8}$$

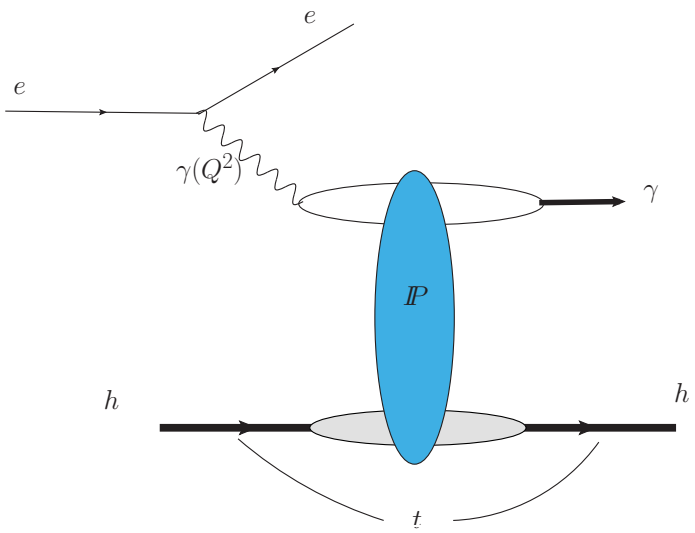

Figure 4.8: A schematic diagram for the real photon production within the colour dipole approach to DVCS. Figure from Ref. [33].

The advantage of DVCS process for phenomenological studies can be seen directly from the wave function prescription. Compared to the photon-meson wave functions given by Eqs. (1.24) and (1.25), respectively, the photon-photon wave function is much simpler and contains less model-dependent parameters. It is therefore less susceptible to the specific approach chosen to model the wave functions and the related theoretical uncertainties, and can serve as a direct probe of the QCD dynamics for the dipole-hadron interaction.

A disadvantage to the DVCS process comes mainly from the experimental point of view due to the small values of the cross section (compared to the DIS and vector meson production cases), together with the presence of the competing Bethe–Heitler process. The Bethe–Heitler process represents the elastic scattering of the electron off the hadron, followed by the photon emission from the rescattered electron. Therefore, it produces the same final state at the DVCS process, which has to be distinguished and separated by appropriate kinematical constraints.

4.2.2 Results

To complement the studies of inclusive and diffractive deeply inelastic scattering using the impact-parameter dependent BK equation, I also published, together with my colleagues, predictions for exclusive processes, which can serve as a clean probe of the gluon component of the hadronic structure. First, I will summarise the predictions for the deeply virtual Compton scattering published in Ref. [33] and in the following section, the production of vector mesons in several types of colliding systems will be discussed. DVCS is expected to be measured at future electron-ion colliders and from the theoretical and phenomenology point of view, it presents some advantages, mainly coming from the form of the wave function which can be calculated directly from QED and does not depend on additional modelling (unlike the vector meson wave function).

The first set of results are the predictions obtained using the b-BK evolution and CGC-inspired models for the $|t|$-distribution and the energy dependence of the DVCS cross section, compared to the available data from HERA [158] in Figs. 4.9 and 4.10, respectively. The CGC-inspired models are the following: IP-Sat and IP-nonSat, where the later disregards saturation effects, both are based on Ref. [81],

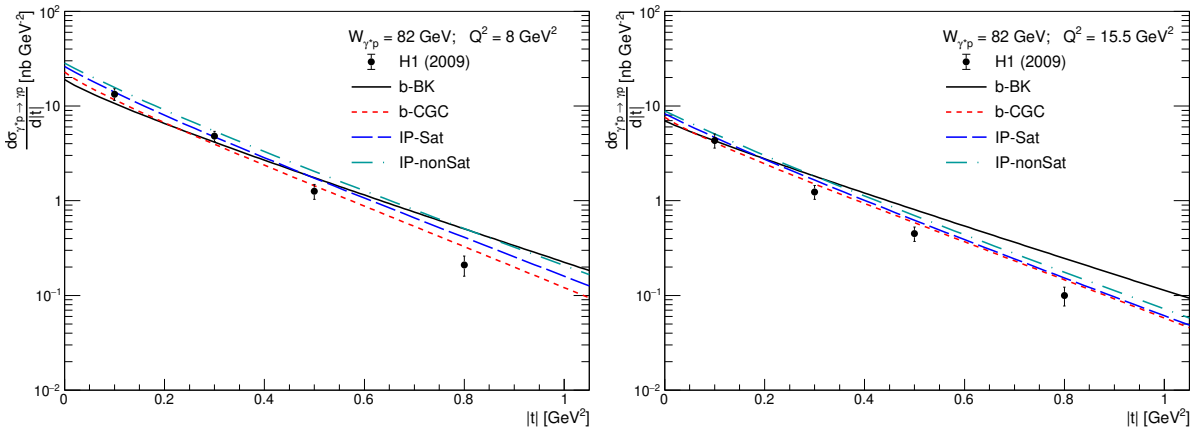

Figure 4.9: Predictions for the $|t|$-distribution of the DVCS cross section in ep scattering for two values of Q^2 considering b-BK and CGC-inspired models. Predictions are compared to HERA data [158]. Figures from Ref. [33].

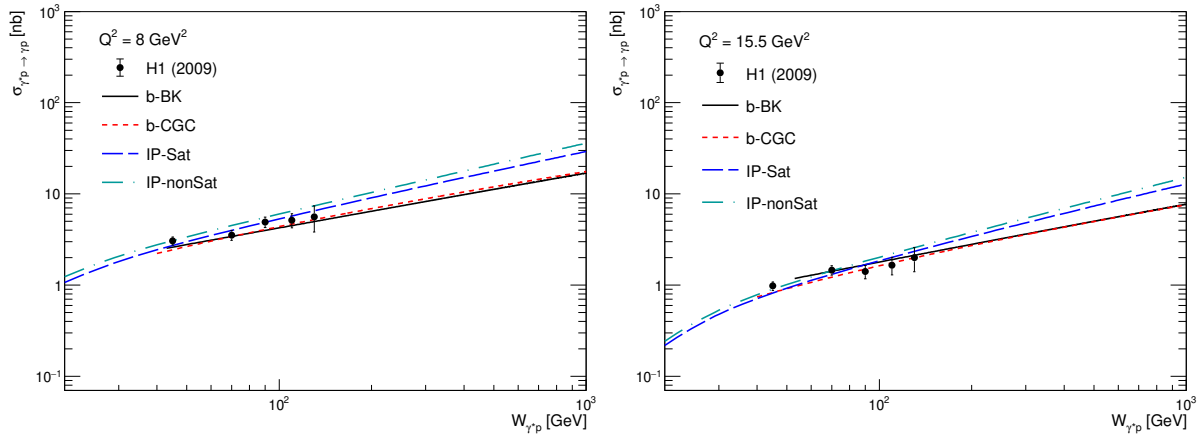

Figure 4.10: Predictions for the energy $W_{\gamma p}$ dependence of the DVCS cross section in ep scattering for two values of Q^2 considering b-BK and CGC-inspired models. Predictions are compared to HERA data [158]. Figures from Ref. [33].

and the b-CGC model, where I used the latest parameters from Ref. [159]. The conclusion from these plots is that the b-BK model again provides lower overall predictions compared to the other models and moreover, it predicts a milder $|t|$-behaviour. This observation may disfavour the b-BK calculation, especially towards large $|t|$ and with increasing Q^2 where the discrepancy with respect to the data and to the other CGC-inspired models is quite large. This may be due to Q^2 evolution effects towards large virtualities, which are not explicitly included in the BK evolution, yet the presented CGC-inspired models contain some form of the Q^2 dependence. However, since the description of the total cross section is reasonable and the b-BK model provides good description of other processes, it would be unwise to swiftly disregard it based on this one observable. Moreover, future experiments may bring new results to provide a more decisive picture. From Fig. 4.10, it can also be seen that both IP-Sat models predict a steeper increase of the total cross section with energy compared to the b-BK and b-CGC models. Such behaviour is expected as the impact of saturation effects is expected to be larger at low x, a behaviour

which can be useful to distinguish among different models.

Since it is expected that ep collisions at future colliders will measure the cross section $|t|$-distributions towards larger momenta transfers compared to HERA, it is envisioned that the measurement of the diffractive minima will be possible. A sample of my predictions for such measurements is presented in Fig. 4.11 for the expected energies at the EIC (left panel) and at the LHeC (right panel). A strong dependence of the result on the given model can be observed. The IP-nonSat model does not predict the presence of the dips, while the other models which include saturation effects do. The position of the dip strongly depends on the model considered and with increasing energy, the dips occur at lower values of $|t|$.

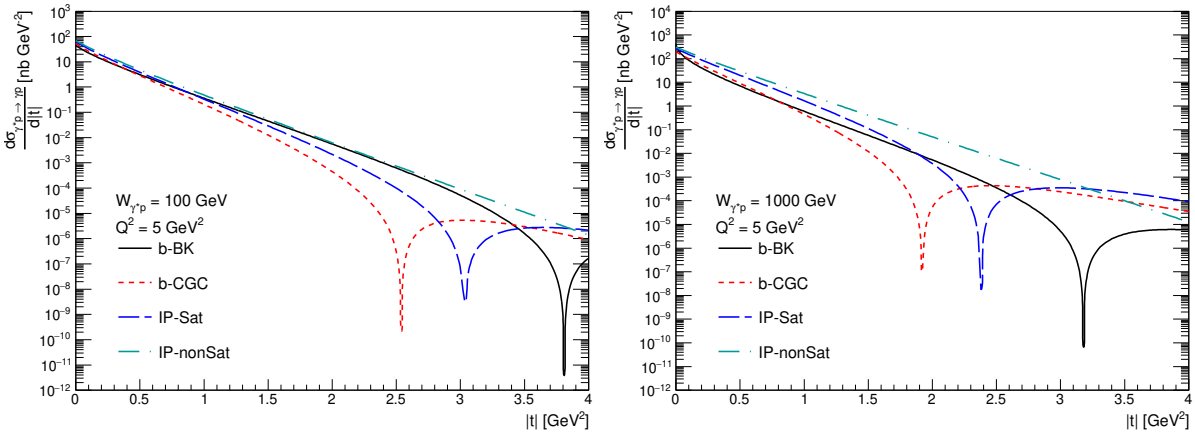

Figure 4.11: Predictions for the $|t|$-distribution of the DVCS cross section in ep scattering at $Q^2 = 5$ GeV^2 considering b-BK and CGC-inspired models. Predictions are presented for the expected energies at the EIC (left) and at the LHeC (right). Figures from Ref. [33].

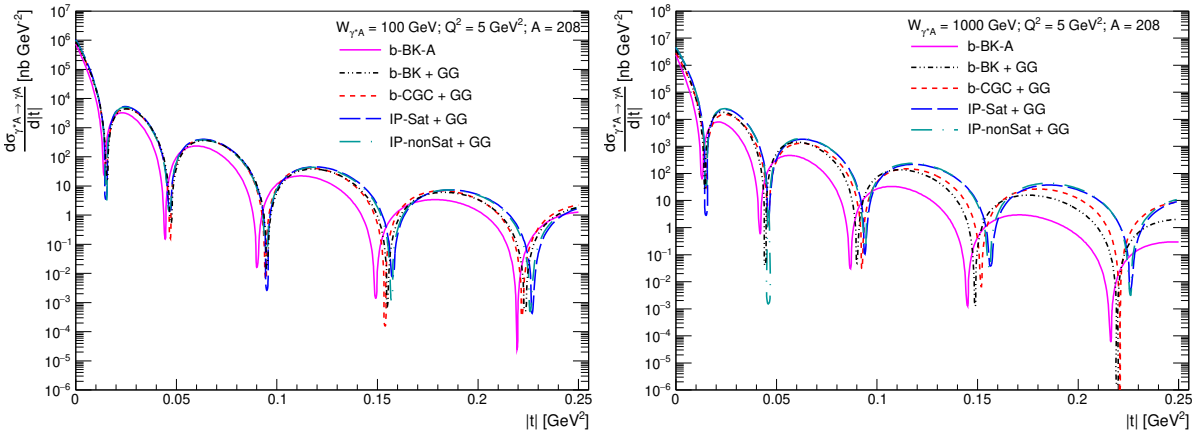

Figure 4.12: Predictions for the $|t|$-distribution of the DVCS cross section in ePb scattering at $Q^2 = 5$ GeV^2 considering b-BK and CGC-inspired models. Predictions are presented for the expected energies at the EIC (left) and at the LHeC (right). Figures from Ref. [33].

I also studied the energy and $|t|$-dependence for eA collisions where the nonlinear effects are expected to be stronger. As an example, I show the predictions for the $|t|$-distribution of the ePb DVCS cross section for two values of photon-target CMS energies expected at future colliders in Fig. 4.12. It can be

again seen that the nuclear evolution of the dipole scattering amplitude (b-BK-A) predicts smaller values of the cross section compared to other models, and also the dips are present at lower $|t|$, being distinctly different from other models for the LHeC energies. This can be traced down to the different behaviour in the large-b region[2] for the models considered, where the b-BK-A amplitudes present larger tails (for further discussion, see Fig. 3 in Ref. [33]).

The presented results therefore suggest, that a future measurements of the DVCS process will allow to distinguish among different approaches to the inclusion of saturation phenomena and impact parameter distribution of hadrons in dipole-model based calculations and to improve our understanding of the underlying QCD dynamics and non-perturbative effects (which are related to large b) in the hadron structure.

4.3 Exclusive production of vector mesons off protons and nuclei

In the last part of this chapter, I summarise the results for the exclusive production of vector mesons in interactions of photons with protons and lead nuclei using the b-dependent BK equation. Such processes bring both advantages and disadvantages compared to other exclusive channels such as DVCS. The main advantage from the experimental point of view is a larger cross section compared to DVCS. Moreover, the exclusive photoproduction of J/ψ meson provides a very good probe for saturation effects, as it gives a clean signal in the detector where only the decay products of J/ψ should be present. The main challenge is then to tag the outgoing hadron and distinguish the exclusive process from the situation when the target hadron dissociates. Moreover, the high mass of its constituting charm quark provides a large enough fixed scale for perturbative calculations, which at leading-order predict the charmonium cross section to depend on the square of the target gluon density [160]. On the other hand, modelling the vector meson production presents some challenges with respect to the uncertainties associated to the photon-meson wave function. However, when the model is fixed using other observables and with the same set-up applied further, its predictions are still trustworthy.

4.3.1 Results for vector meson production in ep and p–Pb collisions

In this section, a selection of my results from Ref. [29] for the exclusive production of vector mesons in γp interactions is presented. The results are compared with data from HERA experiments, where an electron is a source of (virtual) photons, and with data from several LHC experiments measured in ultraperipheral p–Pb collisions, where a Pb nucleus serves as a source of photons. The results were obtained using dipole amplitudes $N(x, r, b)$ as a solution to the impact-parameter dependent BK equation (3.25). Moreover, these results, specifically the $|t|$-distribution of the exclusive J/ψ photoproduction, served as one of the two processes to constrain the initial condition for the b-BK evolution developed in Ref. [28], and therefore these studies helped to improve the model in the subsequent publication [29].

In Fig. 4.13 (left), the predictions for the $|t|$-distribution of the cross section for the exclusive electroproduction of the ϕ meson at several values of centre-of-mass energy $W_{\gamma p}$ are presented. The right panel presents the results for the total cross section as a function of $W_{\gamma p}$ for several values of Q^2. All predictions give a reasonable agreement with H1 [108] and ZEUS [161] data. The $|t|$-distribution of the J/ψ meson photoproduction cross section is presented in Fig. 4.14 (left) and compared with data from H1 [112, 115]. The predictions give a very good agreement with the data for photoproduction at $W_{\gamma p} = 55$ GeV and $W_{\gamma p} = 100$ GeV, the result for $W_{\gamma p} = 78$ GeV slightly underestimates the data. However, it is important to point our that the value of $W_{\gamma p}$ is estimated as a mean value from the measured

[2]This is due to the fact that the squared four-momentum transfer $|t|$ is a Fourier conjugate variable to the impact parameter.

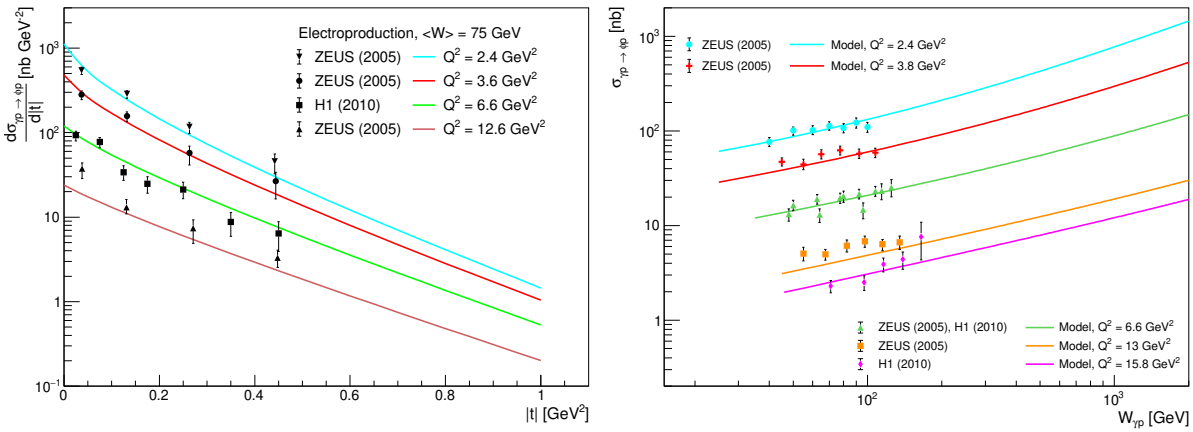

Figure 4.13: Comparison of the predictions of the model (solid lines) with HERA data from H1 [108] and ZEUS [161] for the $|t|$ dependence (left) and the $W_{\gamma p}$ dependence (right) of the exclusive electroproduction cross section of the ϕ meson. Figures from Ref. [29].

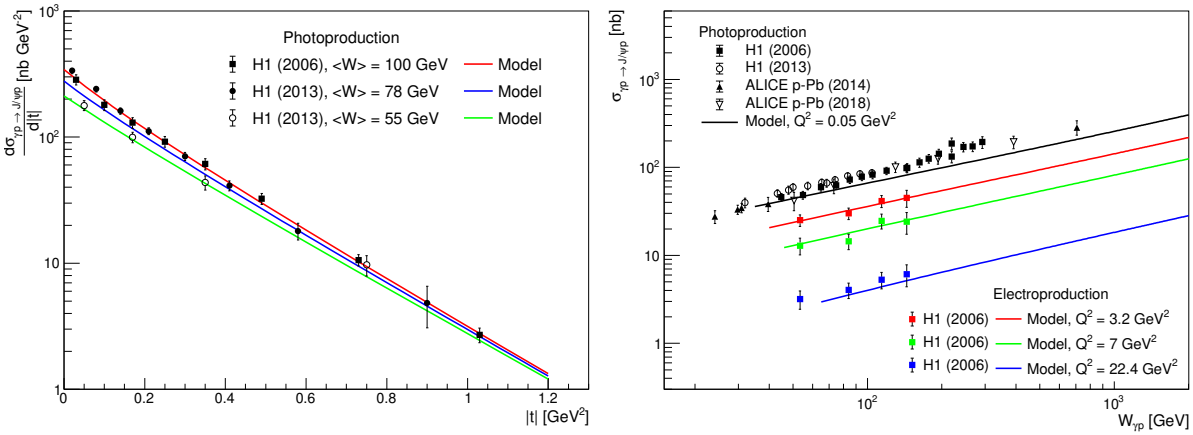

Figure 4.14: Comparison of the predictions of the model using the b-BK equation (3.25) with data for the $W_{\gamma p}$ dependence of:
(Left): The exclusive photo- and electroproduction cross section of the J/ψ meson, compared with data from H1 [112, 115] and ALICE [113, 114]. (Right): The exclusive photoproduction cross section of the Υ(1S) meson compared with HERA data from H1 [162] and ZEUS [163], and LHC data from LHCb [164] and CMS [165]. Figures from Ref. [29].

energy range in experimental data. Therefore the results of the model can be considered satisfactory. In the right plot of Fig. 4.14, the predictions for the energy $W_{\gamma p}$ dependence of the total cross section are compared with HERA data from H1 [112, 115] and LHC data from ALICE [113, 114] for photo- and electroproduction at several values of Q^2. The results for electroproduction give a very good agreement with the data. The prediction for photoproduction gives a good description of the data at low $W_{\gamma p}$; at high energies the result slightly underestimates the data. The production of other vector mesons such as Υ(1S) and $\psi(2S)$ (where its ratio to the J/ψ production is studied) is also reasonably described by the model, see additional plots in Ref. [29]. However, the large uncertainties in data prevent from any strong conclusion regarding the agreement of these predictions with the data.

4.3.2 Coherent production of J/ψ vector meson in γ–Pb interactions

The emergence of new measurements of exclusive charmonium photoproduction in nuclear collisions at the LHC sparked an interest in the question how the model stands against that data and if it can provide some interesting predictions for future measurements. The results for the coherent production of a J/ψ meson in γ–Pb interactions from the Ref. [32] are summarised in this section. The results were obtained using the two versions of the dipole-nucleus scattering amplitudes described in Sec. 3.3.1.

Fig. 4.15 presents the results for the $|t|$-distribution (left plot) at $W_{\gamma Pb} \approx 120$ GeV and for the energy $W_{\gamma Pb}$ dependence (right plot) of the J/ψ cross section. It can be observed that the two predictions calculated using the distinct dipole-nucleus amplitudes give different results for both energy and $|t|$ dependence. Moreover, not only the values of the cross section at given $|t|$ differ, but also the positions of the diffractive minima are shifted with respect to each other. The difference between the two predictions for the total cross section increases with increasing $W_{\gamma Pb}$, starting from approx. 30 % at $W_{\gamma Pb} = 35$ GeV and reaching a roughly factor of two at $W_{\gamma Pb} \approx 1$ TeV. Currently, there are no data available for comparison of the presented results. However, such observables as the two presented here are planned to be measured in future electron-ion colliders [10, 11]. These future measurements cannot only enable to distinguish between the models, but hopefully will provide an answer to several open questions in QCD, such as the existence and nature of gluon saturation in hadrons. Especially the measurement of the location of diffractive dips, shown in Fig. 4.15 (left), has been proposed as a signature of saturation in γp [166] and γA [167] interactions.

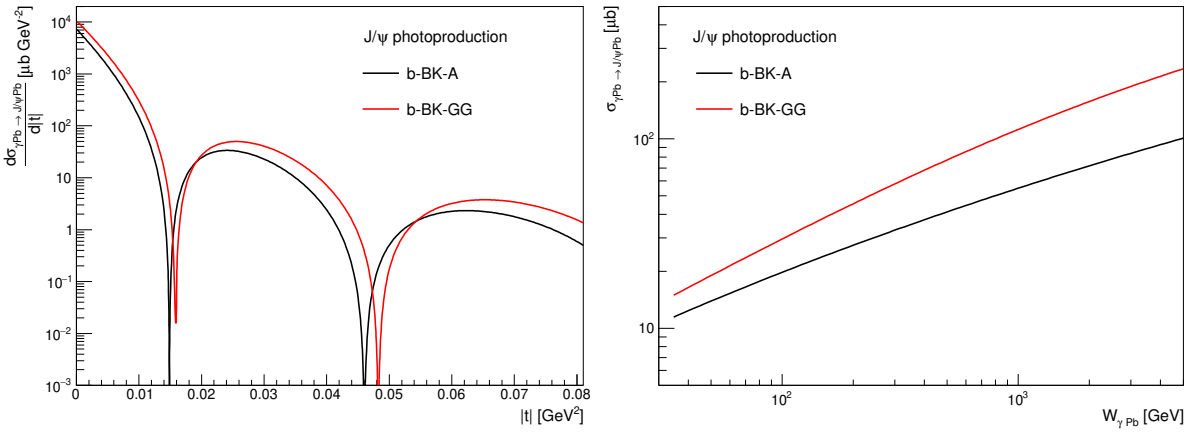

Figure 4.15: (Left): Predictions using nuclear b-BK amplitudes [30] for the differential cross section for the coherent photoproduction of a J/ψ vector meson off a Pb target as a function of $|t|$ at rapidity $Y = 2.5$, which corresponds to a centre-of-mass energy $W_{\gamma \mathrm{Pb}} \approx 120$ GeV. (Right): Energy $W_{\gamma \mathrm{Pb}}$ dependence for the total cross section. Figures from Ref. [32].

I also compare the predictions for the rapidity dependence of the coherent J/ψ cross section in the ultraperipheral Pb–Pb collisions using the two approaches to the nuclear dipole amplitude. In these collisions, one of the lead nuclei serves as a source of the flux of photons which interact with the other (target) nucleus. The cross section is then calculated combining the photon-target cross section with the photon flux at given rapidity y [168]. The results are compared to experimental data from the LHC measured in Run 1 at ALICE [169, 170] and CMS [171] experiments, and in Run 2 at ALICE [172] and at LHCb [173]. The two approaches yield a similar result in the large $|y|$ regions, where the contribution from low $W_{\gamma Pb}$ energies is dominant. In the central region, the two approaches differ significantly. Data from Run 1 show a preference for the b-BK-A approach, while the data from Run 2 do not provide a

clean message as their uncertainties are quite large. However, a more recent study of the coherent J/ψ $|t|$-distribution from ALICE [174] depicted in Fig. 4.17, shows a good description of the measurement by the nuclear b-BK-A calculation; although a small discrepancy in the lowest $|t|$ region can be observed for both models incorporating effects beyond the simple electromagnetic interaction of the photon and the target nucleus.

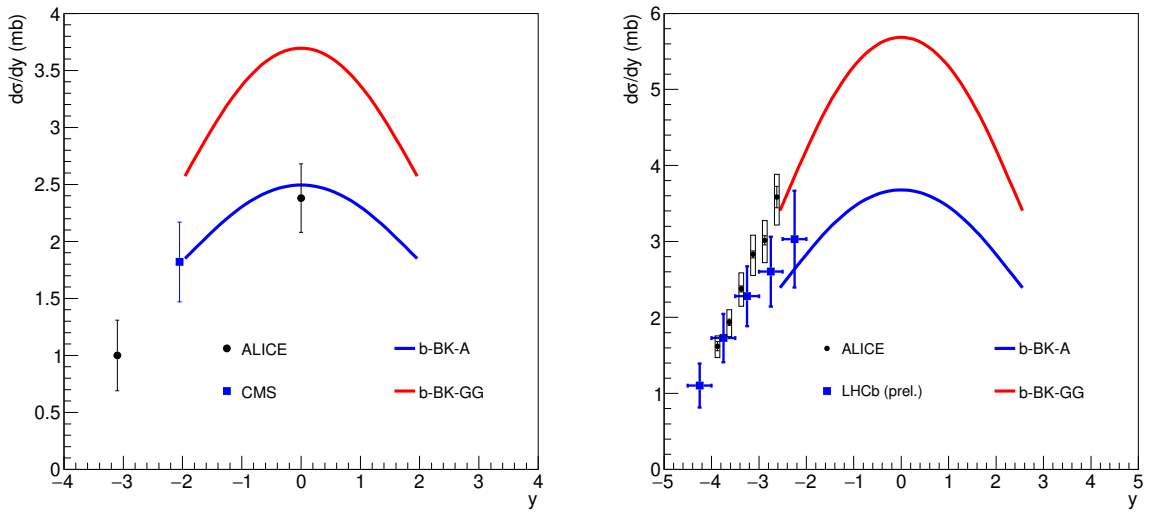

Figure 4.16: Predictions using nuclear b-BK amplitudes [30] for the cross section for the coherent photoproduction of a J/ψ vector meson off a Pb target as a function of rapidity y compared to Run 1 (left)) and Run 2 (right) data measured at the LHC [169–173]. Figures from Ref. [32].

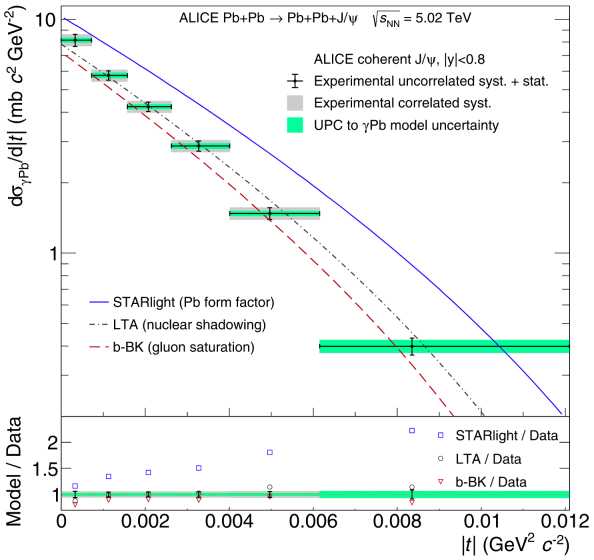

Figure 4.17: The $|t|$-dependence of the coherent photonuclear J/ψ production off *Pb* measured at ALICE in Run 2 and compared to several model predictions (for further references see the original publication), including the b-BK model from Ref. [32] discussed above. Figure taken from Ref. [174].

Chapter 5

Next-to-leading order impact-parameter dependent Balitsky–Kovchegov equation

As the next step of this work, I tried to take the impact-parameter dependent calculation towards the next-to-leading order accuracy of the BK equation. Such calculations are desirable not only to follow the success of the NLO BK fits performed in Ref. [25] for the impact-parameter independent BK, but also to keep up with the newest development of the theoretical calculations within the dipole model such as photon impact factors [175–179] leading to the DIS calculations at NLO [180–182], the $q\bar{q}g$ component of the diffractive DIS cross section [154], and vector meson production [183]. Performing these calculations at next-to-leading order accuracy and comparing the predictions for QCD observables to data could bring new insights into our understanding of saturation effects.

In this last chapter, I will present a more technical overview of my work on the connection of the NLO calculation from Sec. 3.2 and the b-dependent approach to LO BK from Sec. 3.3. This calculation relies on the approximation of a finite target (as in the LO b-BK calculation) in order to keep the computational time reasonable. The NLO BK equation with b-dependence now reads as

$$\begin{aligned}
\partial_Y N(r_{xy}, b_{xy}) &= \int \mathrm{d}^2 z\, K_\mathrm{a} \Big[N(r_{xz}, b_{xz}) + N(r_{zy}, b_{zy}) - N(r_{xy}, b_{xy}) - N(r_{xz}, b_{xz})\, N(r_{zy}, b_{zy}) \Big] \\
&+ \int \mathrm{d}^2 z\, \mathrm{d}^2 w\, K_\mathrm{b} \Big[N(r_{wy}, b_{wy}) + N(r_{zw}, b_{zw}) - N(r_{zy}, b_{zy}) - N(r_{xz}, b_{xz})\, N(r_{zw}, b_{zw}) - \\
&\quad - N(r_{xz}, b_{xz})\, N(r_{wy}, b_{wy}) - N(r_{zw}, b_{zw})\, N(r_{wy}, b_{wy}) + N(r_{xz}, b_{xz})\, N(r_{zy}, b_{zy}) + \\
&\quad + N(r_{xz}, b_{xz})\, N(r_{zw}, b_{zw})\, N(r_{wy}, b_{wy}) \Big] \\
&+ \int \mathrm{d}^2 z\, \mathrm{d}^2 w\, K_\mathrm{f} \Big[N(r_{xw}, b_{xw}) - N(r_{xz}, b_{xz}) - N(r_{zy}, b_{zy})\, N(r_{xw}, b_{xw}) + \\
&\quad + N(r_{xz}, b_{xz})\, N(r_{zy}, b_{zy}) \Big]. \qquad (5.1)
\end{aligned}$$

First line of Eq. (5.1) is referred to as "LO-type integral" in the following text, since the term is integrated only over the first emission, and the second and third integrals can be together denoted as purely NLO contributions. The equation above brings several new vectors into the calculation, therefore I will start by introducing the approach to calculate all the dipole sizes and impact parameters. Next, the calculation itself will be described. This chapter will conclude with the discussion on the obtained numerical results.

5.1 Input variables and set-up for the calculation

5.1.1 Geometry of the problem

Let us start with reminding the coordinates used to define the vectors $\vec{r}$ and $\vec{b}$. Vectors $\vec{x}$ and $\vec{y}$ connect the origin of the impact parameter vector $\vec{b}_{xy}$ with the parent dipole endpoints. These vectors correspond to the distances b_{q_i} of the quark and antiquark from the centre of the target hadron, given by Eq. (3.28). The vector $\vec{z}$ connects the origin of $\vec{b}_{xy}$ with the daughter emission endpoint and the vector $\vec{w}$ connects the origin of $\vec{b}_{xy}$ with the second emission endpoint. Note that some works use the following notation for the leading-order BK calculation: $\vec{r}_{xy} \equiv \vec{r}$, $\vec{r}_{xz} \equiv \vec{r}_1$ and $\vec{r}_{zy} \equiv \vec{r}_2$. However, due to the complexity of the b-dependent calculation at NLO, it is reasonable to use a notation where all the variables are easily distinguishable.

The parent dipole is defined by the vectors $\vec{r}_{xy} = \vec{x} - \vec{y}$ and $\vec{b}_{xy} = \frac{1}{2}(\vec{x} + \vec{y})$. The daughter dipole sizes which enter the integral measure are defined as $\vec{r}_{xz} = \vec{x} - \vec{z}$ and $\vec{r}_{xw} = \vec{x} - \vec{w}$. In this way, the integral measures are changed as $\mathrm{d}^2 z \to \mathrm{d}\vec{r}_{xz}$ and $\mathrm{d}^2 w \to \mathrm{d}\vec{r}_{xw}$. Using these coordinates, all other dipole sizes and impact parameters can be computed. The remaining dipole sizes are:

$$\begin{aligned} \vec{r}_{zy} &= \vec{z} - \vec{y} = \vec{r}_{xy} - \vec{r}_{xz}, \\ \vec{r}_{wy} &= \vec{w} - \vec{y} = \vec{r}_{xy} - \vec{r}_{xw}, \\ \vec{r}_{zw} &= \vec{z} - \vec{w} = \vec{r}_{xw} - \vec{r}_{xz}, \end{aligned} \tag{5.2}$$

while the other impact parameters are given by

$$\begin{aligned} \vec{b}_{xz} &= \frac{1}{2}(\vec{x} + \vec{z}) = \vec{b}_{xy} + \frac{1}{2}\vec{r}_{zy} = \vec{b}_{xy} + \frac{1}{2}(\vec{r}_{xy} - \vec{r}_{xz}), \\ \vec{b}_{zy} &= \frac{1}{2}(\vec{z} + \vec{y}) = \frac{1}{2}(\vec{x} + \vec{y}) - \frac{1}{2}(\vec{x} - \vec{z}) = \vec{b}_{xy} - \frac{1}{2}\vec{r}_{xz}, \\ \vec{b}_{xw} &= \frac{1}{2}(\vec{x} + \vec{w}) = \vec{b}_{xy} + \frac{1}{2}\vec{r}_{wy} = \vec{b}_{xy} + \frac{1}{2}(\vec{r}_{xy} - \vec{r}_{xw}), \\ \vec{b}_{wy} &= \frac{1}{2}(\vec{w} + \vec{y}) = \vec{b}_{xy} - \frac{1}{2}\vec{r}_{xw}, \\ \vec{b}_{zw} &= \frac{1}{2}(\vec{z} + \vec{w}) = \vec{b}_{xy} + \frac{1}{2}(\vec{r}_{xy} - \vec{r}_{xz} - \vec{r}_{xw}). \end{aligned} \tag{5.3}$$

One possible configuration of the vectors is shown in Fig. 5.1.
The next step is to chose a coordinate system to express the dipole sizes and their impact parameters.

- For $\vec{b}_{xy}$, its magnitude b_{xy} and its polar angle φ are used. Since a cylindrical symmetry is considered in this calculation, the results do not depend on the polar angle. Therefore, φ is chosen to be zero, as in previous works.
- For $\vec{r}_{xy}$, its magnitude r_{xy} and the angle with respect to its own impact parameter θ_{xy} are used.
- The integral over $\vec{r}_{xz}$ transforms to $\mathrm{d}\vec{r}_{xz} \to r_{xz}\mathrm{d}r_{xz}\mathrm{d}\beta_{xzy}$, where β_{xzy} is the angle between the parent dipole $\vec{r}_{xy}$ and the daughter dipole $\vec{r}_{xz}$.
- The integral over $\vec{r}_{xw}$ transforms to $\mathrm{d}\vec{r}_{xw} \to r_{xw}\mathrm{d}r_{xw}\mathrm{d}\beta_{xwy}$, where β_{xwy} is the angle between the parent dipole $\vec{r}_{xy}$ and the daughter dipole $\vec{r}_{xw}$.
- The evaluation of $N(\vec{r}_{xz}, \vec{b}_{xz})$ is done in the magnitudes of its vectors r_{xz} and b_{xz} as follows

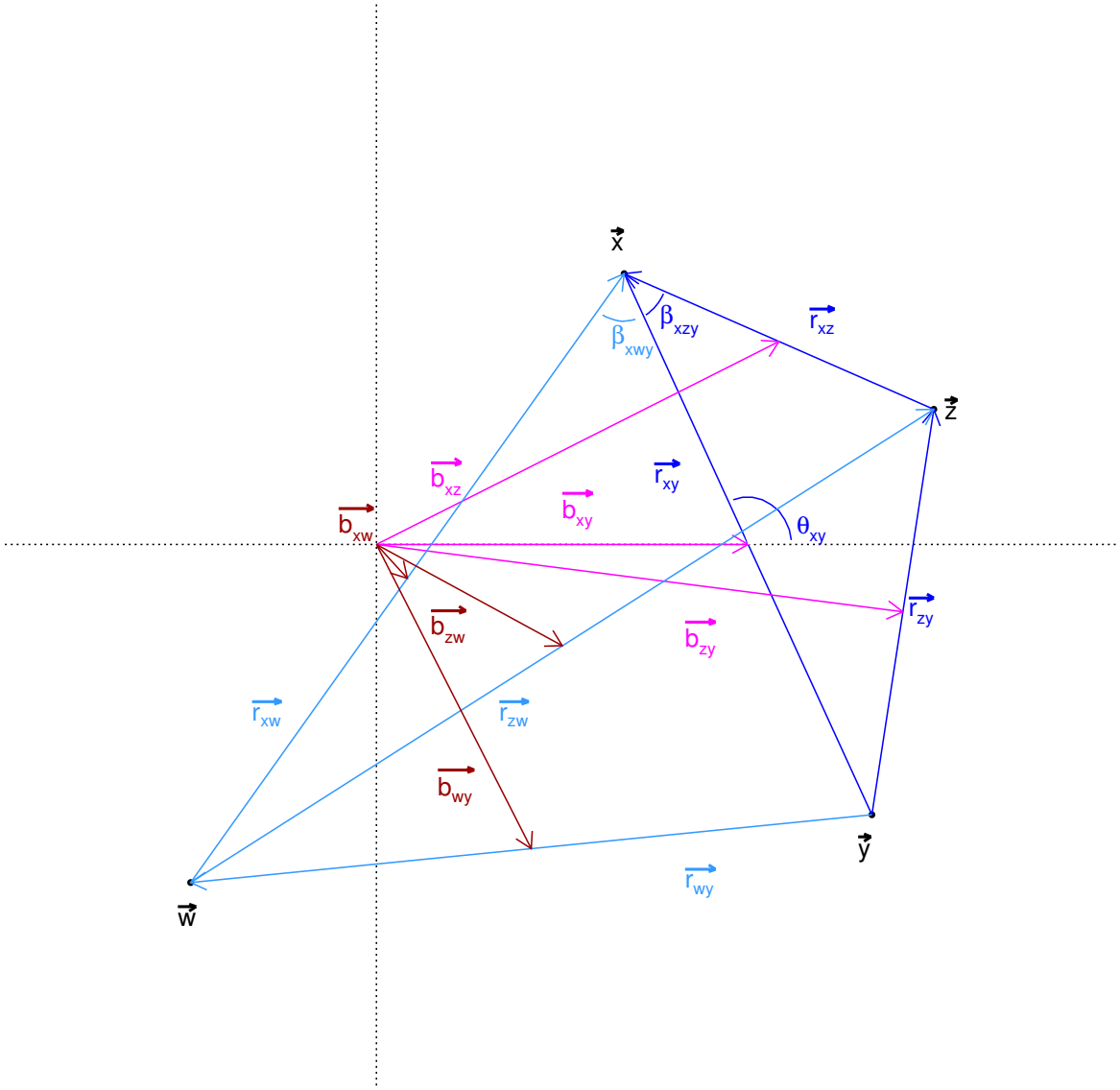

Figure 5.1: A possible configuration of the dipoles. The vectors for the dipoles that appear at LO are shown in blue and magenta. The two new dipoles appearing at NLO are shown in light blue and dark red. The coordinate system has been chosen such that the vector $\vec{b}_{xy}$ has polar angle zero.

- The value of r_{xz} is given by the integral measure.
- The value of b_{xz} can be computed using the first line in Eq. (5.3) as

$$\begin{aligned}(\vec{b}_{xz})^2 &= \left(\vec{b}_{xy}+\frac{1}{2}(\vec{r}_{xy}-\vec{r}_{xz})\right)^2 \\ &= b_{xy}^2+\frac{1}{4}\left(r_{xy}^2+r_{xz}^2-2r_{xy}r_{xz}\cos(\beta_{xzy})\right)+b_{xy}r_{xy}\cos(\theta_{xy})-b_{xy}r_{xz}\cos(\theta_{xy}+\beta_{xzy}).\end{aligned} \tag{5.4}$$

- The evaluation of $N(\vec{r}_{zy},\vec{b}_{zy})$ is done in the magnitudes of its vectors r_{zy} and b_{zy} as follows

– The value of r_{zy} is given from the first line of Eq. (5.2) by

$$(\vec{r}_{zy})^2 = \left(\vec{r}_{xy} - \vec{r}_{xz}\right)^2 = r_{xy}^2 + r_{xz}^2 - 2r_{xy}r_{xz}\cos(\beta_{xzy}). \tag{5.5}$$

– The value of b_{zy} is given from the second line of Eq. (5.3) by

$$(\vec{b}_{zy})^2 = \left(\vec{b}_{xy} - \frac{1}{2}\vec{r}_{xz}\right)^2 = b_{xy}^2 + \frac{1}{4}r_{xz}^2 - b_{xy}r_{xz}\cos(\theta_{xy} + \beta_{xzy}). \tag{5.6}$$

- The evaluation of $N(\vec{r}_{xw}, \vec{b}_{xw})$ is done in the magnitudes of its vectors r_{xw} and b_{xw} as follows

  – The value of r_{xw} is given by the integral measure.

  – The value of b_{xw} can be computed using the third line in Eq. (5.3) as

$$\begin{aligned}(\vec{b}_{xw})^2 &= \left(\vec{b}_{xy} + \frac{1}{2}(\vec{r}_{xy} - \vec{r}_{xw})\right)^2 \\ &= b_{xy}^2 + \frac{1}{4}\Big(r_{xy}^2 + r_{xw}^2 - 2r_{xy}r_{xw}\cos(\beta_{xwy})\Big) + b_{xy}r_{xy}\cos(\theta_{xy}) - b_{xy}r_{xw}\cos(\theta_{xy} - \beta_{xwy}).\end{aligned} \tag{5.7}$$

- The evaluation of $N(\vec{r}_{wy}, \vec{b}_{wy})$ is done in the magnitudes of its vectors r_{wy} and b_{wy} as

  – The value of r_{wy} is given from the second line of Eq. (5.2) by

$$(\vec{r}_{wy})^2 = \left(\vec{r}_{xy} - \vec{r}_{xw}\right)^2 = r_{xy}^2 + r_{xw}^2 - 2r_{xy}r_{xw}\cos(\beta_{xwy}). \tag{5.8}$$

  – The value of b_{wy} is given from the fourth line of Eq. (5.3) by

$$(\vec{b}_{wy})^2 = \left(\vec{b}_{xy} - \frac{1}{2}\vec{r}_{xw}\right)^2 = b_{xy}^2 + \frac{1}{4}r_{xw}^2 - b_{xy}r_{xw}\cos(\theta_{xy} - \beta_{xwy}). \tag{5.9}$$

- The evaluation of $N(\vec{r}_{zw}, \vec{b}_{zw})$ is done in the magnitude of its vectors r_{zw} and b_{zw} as follows

  – The value of r_{zw} is given from the third line of Eq. (5.2) by

$$(\vec{r}_{zw})^2 = \left(\vec{r}_{xw} - \vec{r}_{xz}\right)^2 = r_{xw}^2 + r_{xz}^2 - 2r_{xw}r_{xz}\cos(\beta_{xzy} + \beta_{xwy}). \tag{5.10}$$

  – The value of b_{zw} is given from the last line of Eq. (5.3) as

$$\begin{aligned}(\vec{b}_{zw})^2 &= \left(\vec{b}_{xy} + \frac{1}{2}(\vec{r}_{xy} - \vec{r}_{xz} - \vec{r}_{xw})\right)^2 \\ &= b_{xy}^2 + \frac{1}{4}\left(r_{xy}^2 + r_{xz}^2 + r_{xw}^2\right) \\ &\quad -\frac{1}{2}r_{xy}r_{xz}\cos(\beta_{xzy}) - \frac{1}{2}r_{xy}r_{xw}\cos(\beta_{xwy}) + \frac{1}{2}r_{xz}r_{xw}\cos(\beta_{xzy} + \beta_{xwy}) \\ &\quad +b_{xy}r_{xy}\cos(\theta_{xy}) - b_{xy}r_{xz}\cos(\theta_{xy} + \beta_{xzy}) - b_{xy}r_{xw}\cos(\theta_{xy} - \beta_{xwy}).\end{aligned} \tag{5.11}$$

5.1.2 Numerical setup

I developed the numerical solutions for the b-dependent BK equation at next-to-leading order using Eq. (5.1) and considering two cases:

1. Taking the non-resummed kernel K_{a}, given by Eq. (3.18), and following the first attempt to solve the NLO BK equation independent on impact parameter [26].

2. Taking the resummed kernel K_1, given by Eq. (3.21), into the LO-type integral. The rest of the equation remains the same.

As an initial condition, I use the prescription with the exponential fall-off for the dipole ends from Eq. (3.26) with the parameters given by the previous works on the LO BK calculation including the impact-parameter dependence in Refs. [28, 29].

The strong coupling constant α_S is calculated from the variable flavour scheme described in Sec. 3.1.2 taking all five possible active flavours and with the rest of the parameters according to Ref. [29]. For the two purely NLO kernels K_{b} and Kf, α_S is taken at the parent dipole r_{xy} size according to Refs. [26, 27, 137].

All calculations were performed using the Runge-Kutta methods [123] to solve an integro-differential equation and using the Simpson's rule to calculate the integrals. I derived a second order Runge-Kutta method for the NLO b-BK equation, however after emergence of some serious problems which required fast testing of the evolution behaviour, I decided to use the first order method in order to simplify the numerical routine. The lower order method brings just a small difference in the evolved amplitudes, where the difference is significant only at asymptotically large rapidities Y. The choice of an order of the Runge-Kutta method does not influence the behaviour described in the following sections.

The calculation is local in rapidity, which is given as $Y = \ln(x_0/x)$, where $x_0 = 0.008$, and the step of the numerical method is $Y = 0.05$. Arrays in the impact parameter b and the dipole size r are uniformly logarithmically spaced from 10^{-6} to 10^{2} GeV^{-1}, angles between the parent and daughter dipoles are evenly spaced from 0 to 2π, and the angle θ_{xy} is set to zero according to Ref. [29], although I also tested some other choices.

5.2 Numerical results with the non-resummed NLO BK

Results for the numerical calculation of the b-dependent NLO BK equation (5.1) with the kernel (3.18), given by Eq. K_{a}, evolved from the initial condition (3.26) up to rapidity $Y = 10$ are presented in Figures 5.2 and 5.3 for the r_{xy}-dependence at two values of b_{xy} and for the b_{xy}-dependence at two values of r_{xy}, respectively. The evolution is observed to be unstable, especially in the large b_{xy} and r_{xy} region, where for the later case it is clearly visible from Fig. 5.2 that the amplitude turns negative after several steps in rapidity and this behaviour gets even more pronounced with the evolution. It can be seen from the left panel of Fig. 5.3 that in some regions, evolution causes the amplitude to decrease with respect to the initial condition over the whole range of plotted values. Moreover, from the right panel of the same figure, a growth of the amplitude at large impact parameters reminding of the Coulomb tails (see Sec. 3.3) is observed, although the evolution starts from the initial condition where large r_{xy} and b_{xy} are suppressed.

The instability of the calculation manifests immediately after the first step in rapidity at $Y = 0.05$ for the whole range of b_{xy}. These negative values cover a wide range of values of order 10^{-30} to 10^{-3}. Therefore, they cannot be considered to be just a small numerical error of the calculation. They first appear simultaneously for very small and large r_{xy} near the borders of the array. Due to the evolution,

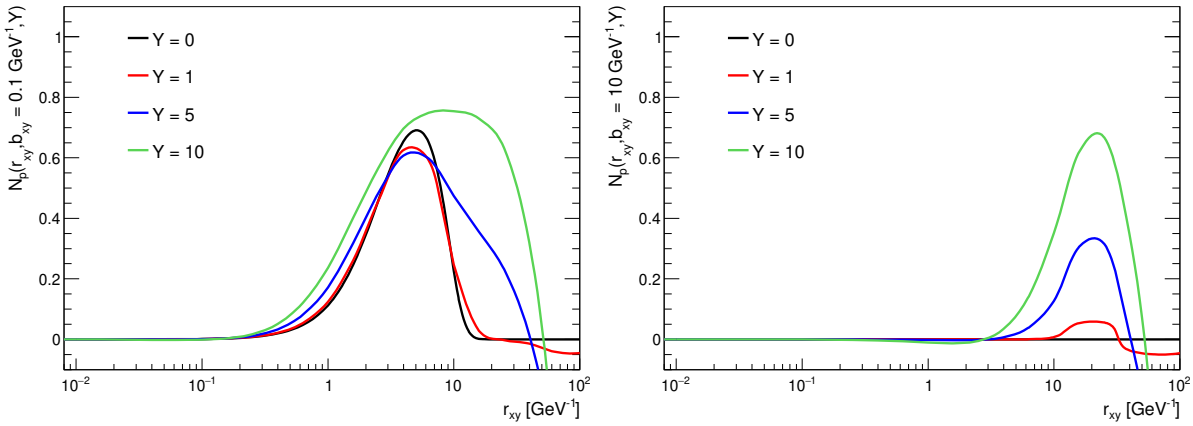

Figure 5.2: Evolution of the full NLO b-BK with the non-resummed kernel K_{a} in Eq. (3.18) from the exponential initial condition in Eq. (3.26) for fixed values of b_{xy} and depending on r_{xy}.

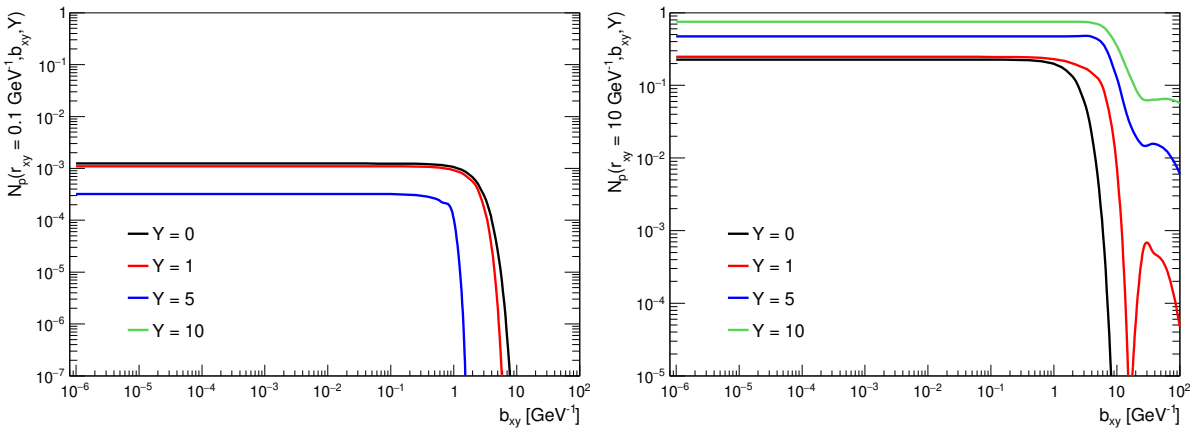

Figure 5.3: Evolution of the full NLO b-BK with the non-resummed kernel K_{a} in EEq. (3.18) from the exponential initial condition in Eq. (3.26) for fixed values of r_{xy} and depending on b_{xy}.

they gradually spread over the whole range of r_{xy} for large values of impact parameters b_{xy} and grow in magnitude, with the largest observed negative values being $N = -1.26$ for $b_{xy} = r_{xy} = 100$ GeV^{-1} at $Y = 10$.

In order to find the origin of this behaviour, I investigated the effect of the NLO integrals containing kernels K_{b} and K_{f} — equations (3.19) and (3.20), respectively — and the effect of the b-dependence in the initial condition. First, evolution of the NLO b-BK with only the LO-type integral, which corresponds to the first line of Eq. (5.1), is presented in Figs. 5.4 and 5.5 for the r_{xy} and b_{xy} dependence, respectively.

As can be seen from Fig. 5.4, at the given b_{xy}, the evolution increases the values in the originally suppressed large-r region towards the $N = 1$ boundary and the wavefront slowly shifts towards lower r_{xy}. Fig. 5.5 shows that at a given r_{xy}, evolution proceeds towards higher values of N for the whole range of b_{xy}. Large values of b_{xy} remain suppressed and no Coulomb tails are present at large impact parameters. However at $r_{xy} = 0.1$ GeV^{-1}, an unusual fluctuation is observed at rapidity $Y = 10$; first N dramatically drops to negative numbers at $b_{xy} \approx 3$ GeV^{-1} and then again increases for larger b_{xy}.

In overall, the evolution seems to be stable at the first sight, however some very small negative values

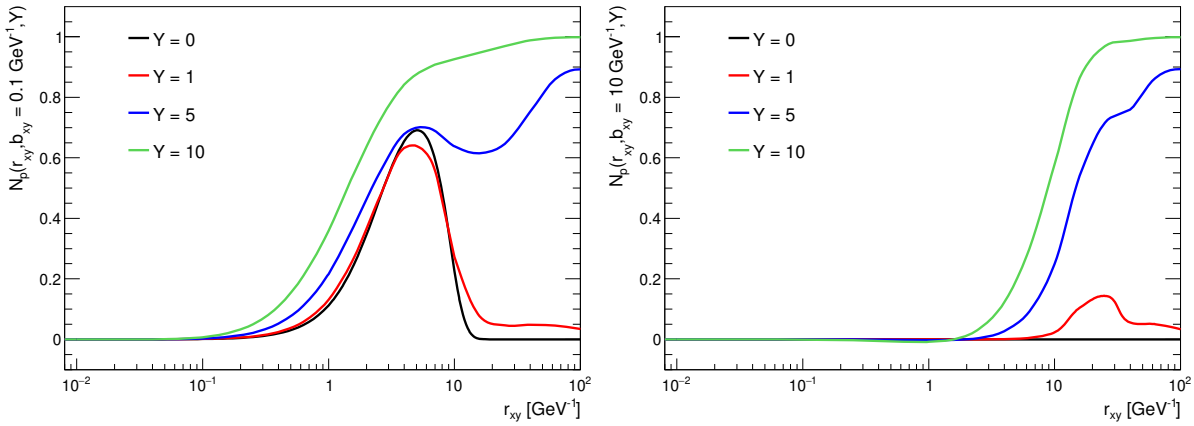

Figure 5.4: Evolution of the NLO b-BK from the exponential initial condition from Eq. (3.26) with only LO-type integral with kernel K_{a}, given by Eq. (3.18), for fixed values of b_{xy} and depending on r_{xy}.

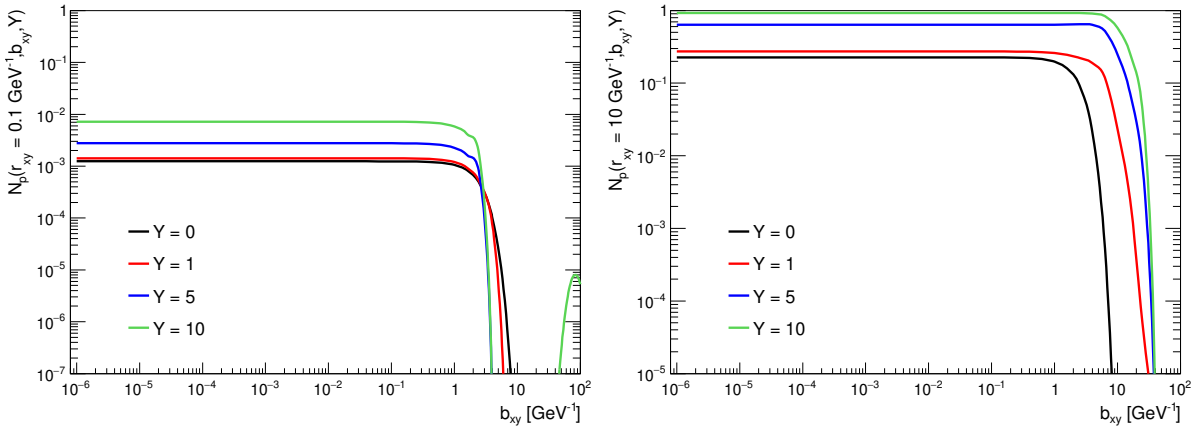

Figure 5.5: Evolution of the NLO b-BK from the exponential initial condition from Eq. (3.26) with only LO-type integral with kernel K_{a}, given by Eq. (3.18), for fixed values of r_{xy} and depending on b_{xy}.

still appear after few steps in rapidity. First, the negative values of the amplitude appear at large values of b_{xy} and for very small r_{xy} at the border of the array and are of order $10^{-17} - 10^{-8}$. Gradually, negative values propagate towards larger dipole sizes up to those of order $r_{xy} \sim 1$ GeV^{-1}, to all values of b_{xy}, and are amplified, reaching values of order $10^{-14} - 10^{-2}$ at rapidity $Y = 10$. The higher the value of r_{xy} is, the larger negative numbers appear. These negative numbers seem to originate from the configurations where both daughter dipole amplitudes are zero and the parent dipole amplitude is a small positive number. Then for $K_{\mathrm{a}} > 0$, the product of the kernel and the given configuration of the dipoles in the first line of (5.1) is negative. As I tested using the collinearly-improved kernel, this behaviour also appeared in previous versions of the b-BK calculation, however it was compensated by the rest of the configurations which yielded positive values entering the sum of the integral. It is also important to point out that the value of the kernel itself can be negative, however this contribution to the integral is compensated by the majority of positive values; the same also applied to the previous versions of LO BK described in Sec. 3.1. When comparing b_{xy}-dependent amplitudes in Fig. 5.5 (K_{a}-only) and Fig. 5.3 (full NLO), it is evident that with the full equation, one gets consistently lower values of N. It can be therefore concluded,

that the purely NLO integrals — second and third line in Eq. (5.1) — bring additional suppression of the resulting amplitude.

Next, I studied the influence of the impact-parameter profile to the evolution. Figure 5.6 shows results for the dipole amplitudes evolved using the LO-type integral from Eq. (5.1) and introducing a uniform profile for the impact-parameter dependence in the initial condition from Eq. (3.26), thus effectively reducing it to the GBW-type initial condition. Its evolution therefore behaves exactly as the other b-independent calculations; the amplitude shifts towards lower values of r_{xy} with increasing rapidity, as can be seen from the left panel of Fig. 5.6. The right panel shows the b_{xy}-dependence of the resulting amplitude which remains flat, exactly as expected. The only change is the magnitude of N which grows towards $N = 1$ limit for a given r_{xy}. At first sight, the evolution may seem stable, however some small negative numbers of order 10^{-14} appear after few steps in rapidity at low values of r_{xy}. These negative numbers are again amplified through the evolution and shifted towards larger values of r_{xy} and appear for more of them than at the beginning of the evolution. At rapidity $Y = 10$, these negative numbers reach values of order 10^{-4}. The unstable behaviour is therefore less severe than with the initial condition with exponential profile in b. The origin of the negative numbers was traced to the same point as in the previous case.

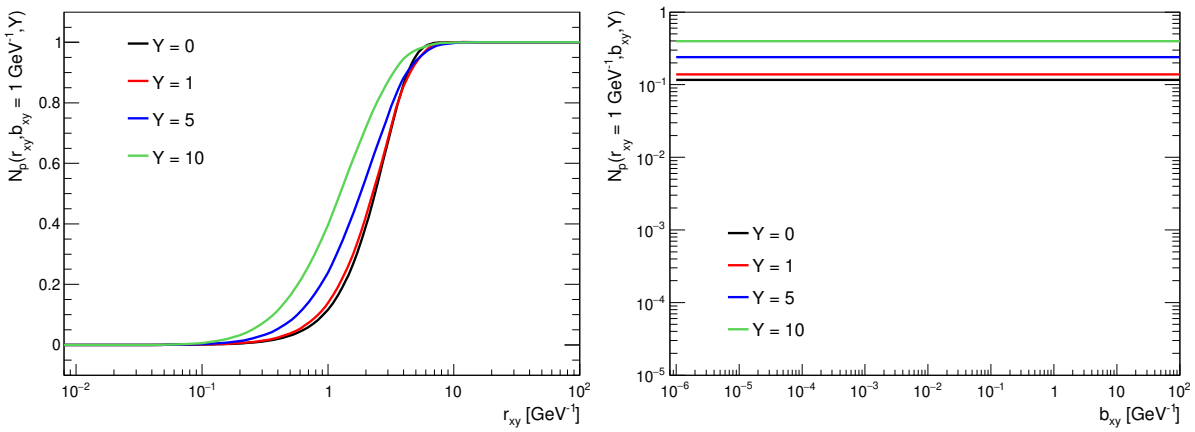

Figure 5.6: Dipole scattering amplitudes as a result of the evolution with the first line of Eq. (5.1) with the non-resummed kernel K_a, given by Eq. (3.18), from an initial condition flat in b, showed for a fixed value of b_{xy} (left panel) and for a fixed value of r_{xy} (right panel).

When performing the same test with the flat profile in b, but this time using the full NLO BK equation, it can be seen from the plots in Fig. 5.7 that the evolution is significantly suppressed by the inclusion of the two purely NLO integrals in Eq. (5.1), e.g. the right plot shows a suppression by approximately 30 % for $r_{xy} = 1$ GeV^{-1} at rapidity $Y = 10$. A similar behaviour as in calculation with the flat profile in b_{xy} combined with the LO-type integral is observed, however the appearance of negative values and their influence within the evolution is much more severe. Negative numbers of order $10^{-12} - 10^{-10}$ appear immediately after the first step in rapidity for all values of b_{xy} and for small values of r_{xy}. With increasing Y, negative numbers spread to larger dipole sizes up to $r_{xy} = 0.1$ GeV^{-1} and reach the order 10^{-3} at this value of dipole size.

To summarise, the evolution with the flat profile in b_{xy} exhibits the same behaviour as the other b-independent calculations. With increasing rapidity, the wave front shifts towards lower r_{xy}, giving small dipoles more probability to interact, and $N \to 1$ for large dipoles, see Figure 5.6. With the initial condition which has an exponential profile in b and gives a suppression of dipoles with large r_{xy} and b_{xy}, it

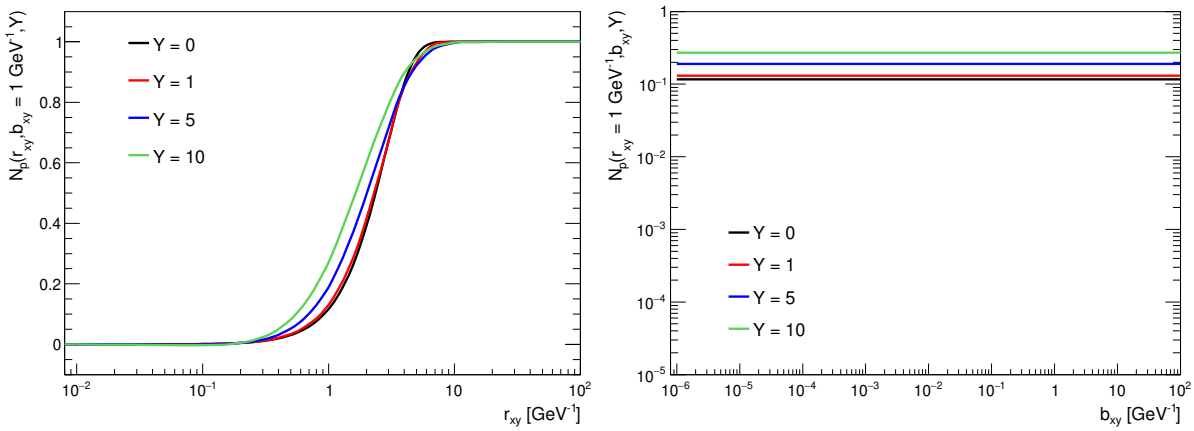

Figure 5.7: Dipole scattering amplitudes as a result of the full NLO b-BK evolution with the non-resummed kernel K_{a}, given by Eq. (3.18), from an initial condition flat in b, showed for a fixed value of b_{xy} (left panel) and for a fixed value of r_{xy} (right panel).

can be seen that the probability of interaction for large dipoles increases with rapidity when the evolution is done using only the LO-type integral, and the wavefront at intermediate r_{xy} moves towards lower r_{xy}, see Figure 5.4. However, the purely NLO integrals subtract a considerable part of the amplitude from the LO-type part, which slows the shift of the wavefront at intermediate r_{xy}, see Figure 5.2. Moreover, they cause a sudden drop of N to negative values at large r_{xy} and b_{xy} due to the amplified propagation of instabilities appearing at the beginning of the evolution.

5.3 Numerical results with the resummed NLO BK

Numerical solutions to the NLO BK equation (5.1) show instabilities due to the appearance of negative values at small r_{xy} at the beginning of the evolution. For the solutions independent on the impact parameter, it was proposed in Ref. [27] that resummations to the kernel K_{a} resulting in the form of kernel given by Eq. (3.21) and denoted as K_1 can cure the instability problem. Therefore, I decided to investigate the effect of the resummed kernel K_1 on the numerical solution to the b-dependent NLO BK equation (5.1) evolved from the initial condition in the form given by Eq. (3.26).

However, even initial steps of the evolution of the full NLO b-BK equation with the resummed kernel K_1 cast a warning that the problem of instability may not be solved in the b-dependent case. Although the calculation gives suppression at large r_{xy} and b_{xy} inherited from the initial condition (as can be seen from the left part of Tab. 5.1 for rapidity $Y = 0.05$) the amplitude is flipped to small negative values in some configurations. After approximately 10 steps in rapidity, the amplitude attains values $N > 1$ and after few additional steps, the whole calculation diverges, giving large positive and negative values of N, see right part of Tab. 5.1 for several configurations at $Y = 1$. The calculation is therefore wildly unstable and gives nonphysical values of N.

Using a flat profile in the impact parameter dependence of the initial condition (3.26) yields a result similar to the corresponding case with the NLO b-BK equation without resummations to the kernel K_{a}, as can be seen from Fig. 5.8. Evolution again seems to give reasonable results, however some small negative values of the amplitude of order 10^{-13} – 10^{-10} appear for few points at small-r_{xy} and for all b_{xy} at the same time. The propagation of negative values is less dramatic than in previous cases; the negative values remain restricted to the low r_{xy} region and reach the order 10^{-8} at $Y = 10$. No amplitudes with

	Y = 0.05			Y = 1		
	$r_{xy} = 10^{-6}$	$r_{xy} = 1$	$r_{xy} = 100$	$r_{xy} = 10^{-6}$	$r_{xy} = 1$	$r_{xy} = 100$
$b = 10^{-6}$	3.2809e-09	0.11319	−1.9367e-07	−109.69	−3801.03	−4.5858e+11
$b = 1$	2.8940e-09	0.09777	−1.0667e-07	−109.69	−3865.78	−4.6134e+11
$b = 100$	3.0988e-31	−4.20098e-27	−1.7152e-08	−6188.17	−1.025e+07	−2.3952e+11

Table 5.1: Evolution to $Y = 0.05$ (left part) and to $Y = 1$ (right part) of the full NLO b-BK equation (5.1) with the the kernel K_1, given by Eq. (3.21), and using the b-dependent initial condition from Eq. (3.26). The values of r_{xy} and b_{xy} are in [GeV^{-1}].

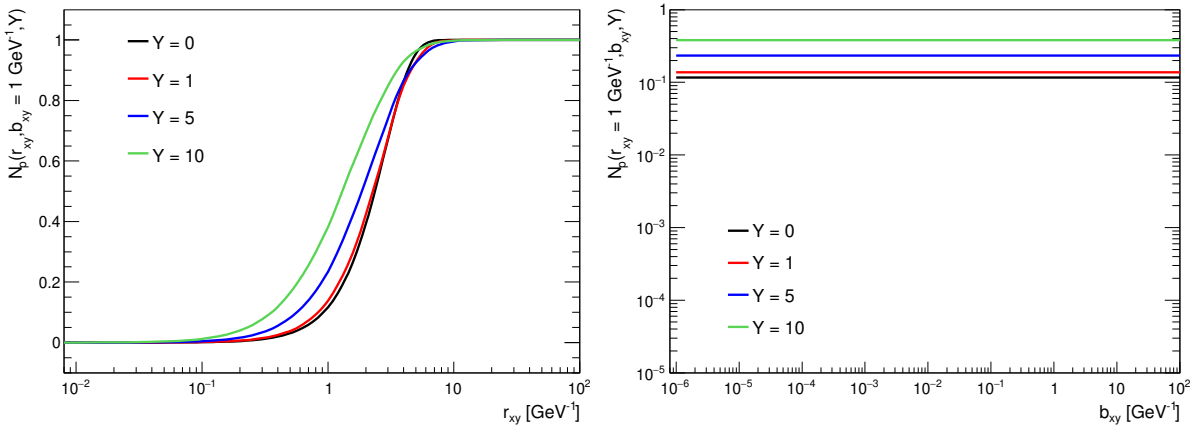

Figure 5.8: Dipole scattering amplitudes as a result of the full NLO b-BK evolution with the resummed kernel K_1, given by Eq. (3.21), from an initial condition flat in b, showed for a fixed value of b_{xy} (left panel) and for a fixed value of r_{xy} (right panel).

values $N > 1$ were observed with this setup. Even more appealing is the observation that when only the LO-type integral with kernel K_1 and a flat profile in b_{xy} is used, not only the amplitude does not evolve any $N > 1$, but also no negative values are present up to rapidity $Y = 10$ at all and the calculation seems to be stable, in accordance with the conclusions of Ref. [27].

Moreover, it can be seen from the comparison of Figs. 5.7 and 5.8 that with the same set-up, the full NLO equation with the resummed kernel K_1 gives amplitudes by approx. 30 % larger than for the case where kernel K_a without resummations is used. Which is an interesting observation when confronted with the comparison between the running coupling and collinearly-improved BK equations, where a slower evolution for the kernel containing resummations was observed, see Fig. 3.5 in this thesis for the b-independent solutions and Fig. 1 in Ref. [28] for the b-dependent solutions.

Influence of the kernel K_1 to the instability of the b-dependent calculation

By evolving only the first line of Eq. (5.1) with the kernel K_1, the contribution from the purely NLO integrals can be estimated. It can also be used to study the influence of individual parts of the kernel K_1 on the calculation with the exponential impact-parameter profile in the initial condition given by Eq. (3.26). The left part of Tab. 5.2 again shows dipole amplitudes after the first step in rapidity at $Y = 0.05$ for

	Y = 0.05			Y = 1		
	$r_{xy} = 10^{-6}$	$r_{xy} = 1$	$r_{xy} = 100$	$r_{xy} = 10^{-6}$	$r_{xy} = 1$	$r_{xy} = 100$
$b = 10^{-6}$	1.29438e-13	0.113503	0	2.68012e-13	0.134499	1.9412e+09
$b = 1$	1.10916e-13	0.098074	0	2.30354e-13	0.117322	17.8086
$b = 100$	0	0	0	−1.62449e-13	−0.533595	32314.3

Table 5.2: Evolution to $Y = 0.05$ (left part) and to $Y = 1$ (right part) of the first LO-type term from Eq. (5.1) with the kernel K_1, given by Eq. (3.21), and using the b-dependent initial condition from Eq. (3.26). The values of r_{xy} and b_{xy} are in [GeV^{-1}].

several combinations of r_{xy} and b_{xy}, this time for the evolution using the LO-type integral with kernel K_1. These results seem reasonable, no negative values are observed and the amplitude is suppressed for large dipoles at large impact parameters. This again shows that the NLO integrals indeed subtract a substantial part of the amplitude (compare to Tab. 5.1), which may send it to negative values. Moreover, it suggests that for the NLO BK with the impact-parameter dependence, these resummations may not be a solution for its instability. Substantial negative values suddenly appear after approximately 10 steps in rapidity in the region of low b_{xy} for large r_{xy}, specifically for $r_{xy} = 100$ GeV^{-1} which is at the border of the array. These negative values emerge from a previously reasonable value of $N \sim 10^{-1}$ and in the following step, they cause N to be substantially larger than 1. Subsequently, negative values develop towards the whole large-b_{xy} region, where they start to occupy the whole range of r_{xy} and cause the calculation to diverge for rapidities $Y > 1$ in regions where the amplitudes were initially suppressed, see the right part of Tab. 5.2. These negative values seem to originate in the combined region of small-b_{xy} and large-r_{xy}, where the previously mentioned situation of the kernel reaching large positive values and a combination with the dipole amplitudes being a small negative value occurs. A problem with the resummed kernel now is, that its value in these cases is a very large number, which turns even a very small negative number into a substantial negative contribution which propagates through the calculation. A typical configuration, for which the above situation appears, is when either both daughter dipole amplitudes are zero, or N_{zy} is much smaller than both N_{xz} and N_{xy} and at the same time, $N_{xy} > N_{xz}$.

Since the resummed kernel consists of several parts with different dependencies on the given dipole sizes, I decided to investigate the influence of the parts of kernel K_1 on the instability behaviour reported above. An interesting point here is that when using the collinearly-improved kernel within the LO BK equation with the b-dependence, given by Eq. (3.25), these instability problems were not observed. Since the kernel K_1 has partially similar structure to the collinearly-improved kernel, it is important to identify the part which causes the unstable evolution. Here, an inspection of the values of $K_{\rm ci}$ in Eq. (3.13) showed that $K_{\rm ci} = 0$ at several places where problematic configurations appear and moreover, $K_{\rm ci}$ gives smaller values than K_1 in other potentially problematic regions, see Fig. 5.9 for a situation where the product of kernel with the combination of dipole amplitudes is less than zero.

Also, there is a significant difference in the extent of instabilities between the non-resummed kernel $K_{\rm a}$ (3.18) and the resummed one. In the first case, the negative values were small, with the most problematic values around $\sim -10^{-2}$ at $Y = 10$. However with the resummed kernel, the calculation starts to diverge at very small rapidities $Y < 1$. This can be again traced to the problematic configurations where K_1 reaches substantially larger values than $K_{\rm a}$ and causes a large (negative) weight being given to this configuration. In Table 5.3, dipole amplitudes resulting from using different kernels in the first line of equation (5.1) are compared for one of the problematic points: $b_{xy} = 10^{-6}$ GeV^{-1} and $r_{xy} = 100$ GeV^{-1}.

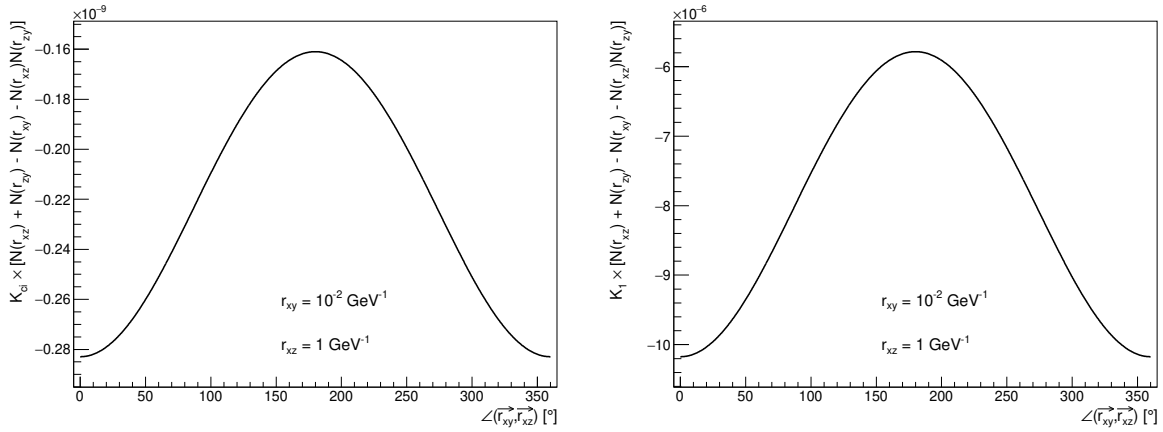

Figure 5.9: Comparison between the collinearly-improved kernel (left plot) and the kernel K_1 (right plot) for a situation where the integrand of the first line of E. (5.1) is less than zero.

	$N(K_{\rm ci})$	$N(K_{\rm a})$	$N(K_1)$
Y = 0.55	8.89368e-04	7.06418e-03	−0.838303

Table 5.3: Values of the dipole amplitude $N(Y, r_{xy}, b_{xy})$ resulting from using three different kernels in the first line of Eq. (5.1) for configuration $b_{xy} = 10^{-6}$ GeV^{-1} and $r_{xy} = 100$ GeV^{-1}.

A substantial contribution to kernel K_1 comes from the $K_{\rm sub}$ and $K_{\rm fin}$ parts, given by Eqs. (3.23) and (3.24), respectively. Indeed if these two terms are excluded from the kernel K_1 and the LO-type integral from Eq. (5.1) is evolved using the exponential initial condition in b, given by Eq. (3.26), a reasonably looking result is obtained. As can be seen from the values in Tab. 5.4, large b_{xy} and r_{xy} configurations are suppressed both at the beginning and through the evolution. Although some small negative values still appear for large b_{xy}, in general, no divergent behaviour with $N > 1$ was observed up to rapidity $Y = 10$.

	Y = 0.05			Y = 1		
	$r_{xy} = 10^{-6}$	$r_{xy} = 1$	$r_{xy} = 100$	$r_{xy} = 10^{-6}$	$r_{xy} = 1$	$r_{xy} = 100$
$b = 10^{-6}$	1.25131e-13	0.113195	0	1.48481e-13	0.12778	2.4749e-04
$b = 1$	1.07206e-13	0.097787	0	1.27199e-13	0.11098	2.4228e-04
$b = 100$	0	0	0	1.36710e-24	−1.04512e-11	6.6048e-05

Table 5.4: Evolution to $Y = 0.05$ (left part) and to $Y = 1$ (right part) of the first (LO-type) term of Eq. (5.1) with the first term of kernel K_1 in Eq. (3.21), i.e. $K_{\rm rc} K_{\rm STL} K_{\rm DLA}$, and using the b-dependent initial condition from Eq. (3.26). The values of r_{xy} and b_{xy} are in [GeV^{-1}].

Since the terms of the $K_{\rm fin}$ part are also present in the non-resummed kernel $K_{\rm a}$ (3.18), the problematic case can be potentially narrowed to the term $K_{\rm sub}$. Indeed when using the kernel K_1 with the combined first and third term, i.e. $K_{\rm rc} K_{\rm STL} K_{\rm DLA} + K_{\rm fin}$, no values of $N > 1$ appear up to rapidity $Y = 10$ and moreover, no negative numbers emerge within the evolution up to this rapidity. A comparison of the values of the dipole amplitude at two different rapidities is summarised in Tab. 5.5. It can be seen that

large b_{xy} and r_{xy} configurations are suppressed, as expected. Moreover, the K_{fin} part gives a substantial positive contribution to the kernel and consequently, the amplitudes are by two orders of magnitude larger than in the previous case where only the term $K_{\text{rc}}K_{\text{STL}}K_{\text{DLA}}$ was used.

	Y = 0.05			Y = 1		
	$r_{xy} = 10^{-6}$	$r_{xy} = 1$	$r_{xy} = 100$	$r_{xy} = 10^{-6}$	$r_{xy} = 1$	$r_{xy} = 100$
$b = 10^{-6}$	1.25306e-13	0.113301	0	1.52763e-13	0.130001	0.015672
$b = 1$	1.07357e-13	0.097883	0	1.30878e-13	0.113021	0.015479
$b = 100$	0	0	0	3.43794e-22	3.20996e-09	0.00330033

Table 5.5: Evolution to $Y = 0.05$ (left part) and to $Y = 1$ (right part) of the first (LO-type) term of Eq. (5.1) with the first term of kernel K_1 in Eq. (3.21), i.e. $K_{\text{rc}}K_{\text{STL}}K_{\text{DLA}} + K_{\text{fin}}$, and using the b-dependent initial condition from Eq. (3.26). The values of r_{xy} and b_{xy} are in [GeV^{-1}].

It is apparent from the comparison of Tabs. 5.2 and 5.5 that adding the K_{sub} term into the picture gives additional contribution which causes the calculation to diverge. Even though this term has a negative sign in the formula (3.21), as it should subtract some part of the kernel after the resummations to the whole NLO BK equation (for details see Ref. [27]), the value of Eq. (3.23) is negative by itself. This means that the contribution from K_{sub} to K_1 is in overall a large positive number. Since this term was not present in the collinearly-improved kernel given by Eq. (3.13), which was successfully combined with the initial condition given by Eq. (3.26) in Ref. [28, 29], it can be concluded that its contribution to the whole NLO BK equation (5.1) is incompatible with the initial condition exponential in impact parameter in the form of Eq. (3.26).

5.4 Summary

To conclude, the evolution using the non-resummed version of the NLO BK with impact-parameter dependence shows an instability of the calculation. Tests with a uniform profile in b confirm the observation of Ref. [26] that small negative values of the dipole amplitude appear in the small-r_{xy} region. These negative values then propagate towards larger dipole sizes and moreover, the purely NLO integrals provide further suppression of the evolution to the extent that they significantly amplify the evolution of the instabilities. The origin of the negative values was traced to configurations where the kernel is a significantly positive number and the combination of amplitudes on the r.h.s. gives small negative values. Regions where the values of kernels are negative seem not to be the main source of the problem, however they can further amplify the unstable behaviour.

Following the restoration of the evolution stability for the b-independent scenario reported in Ref. [27], the evolution using the resummed version of the NLO BK equation with impact-parameter dependence was studied. It was observed that both full and LO-type equations evolved from the initial condition exponential in impact-parameter dependence develop substantial negative values of N. They then propagate through the evolution and cause the calculation to diverge after few steps in rapidity. Tests with the LO-type integral show that the term K_{sub} gives the decisive contribution to this behaviour. Without this term in kernel K_1, no divergence with $N > 1$ is present and moreover, using the combined terms $K_{\text{rc}}K_{\text{STL}}K_{\text{DLA}} + K_{\text{fin}}$ gives no negative values of amplitude at all. The calculation using a flat profile in the impact parameter brings a stable evolution of the dipole amplitude, as no negative values are ob-

served when using the LO-type integral and only negligible negative numbers appear when the purely NLO contributions are added. This leads to the conclusion that an initial condition in the form given by Eq. (3.26) is incompatible with the NLO BK equation in its current form Refs. [26,27], especially with its resummed version. Including the angle between (b_{xy}, r_{xy}) explicitly into the definition of b_{q_i} (3.28) and changing its value from 0 to $\pi/2$ did not make any significant difference, it just delayed the occurrence of the problem by several steps in rapidity. Eventually, the same problems with the divergent behaviour appeared. Using a different form of the initial condition which also contained an exponential fall-off at large-b_{xy}, but with a different magnitude, gave the same outcome.

In agreement with the results of Refs. [26,27], a suppression of the speed of the evolution is observed when the full NLO BK is used, compared to the evolution with only the LO-type integral. This was observed among all studied cases. When using a flat profile in the impact parameter, the resummed NLO BK equation gave dipole amplitudes larger by approx. 30 % compared to the equation without resummations. Moreover, a shift of the wavefront towards small r_{xy} is observed for the case of a uniform profile in the impact parameter, just as in previous b-independent calculations.

Conclusions

This work was devoted to studying the hadronic structure at low-x within the colour dipole formalism, with emphasis on the Balitsky–Kovchegov equation as a tool to obtain the dipole-hadron scattering amplitude. The structure of hadrons, of which the proton is the most prominent representative, has been extensively studied in deeply inelastic scattering at HERA in the past, as described in Chapter 1. I presented an overview on the conclusions coming from the DIS measurements, the evolution of the proton structure in the high-energy regime, and the dipole model as a tool to describe DIS and other QCD processes at low-x. Thanks to the vast amount of DIS data spanning over several orders of magnitudes of the photon virtuality Q^2 and Bjorken-x [47–49], we have a good understanding of the evolution of parton densities with increasing Q^2 via the DGLAP evolution equations. However, the nature of the evolution of parton densities at very low Bjorken-x, specifically that of the gluon distribution, still remains an open question. It is expected that the gluon density grows with decreasing x as more gluons are being radiated. However, at a fixed scale of the process, individual gluons span over the same transverse area in the proton and therefore at some point, it is expected that they start to overlap and recombine together as a result. This marks the onset of saturation effects which result in a dynamical balance between the gluon emission and recombination when the proton reaches the dense state. The Balitsky–Kovchegov equation describes dressing of an initially bare $q\bar{q}$ dipole with gluons and therefore, it gives the non-linear evolution of parton densities in the low-x regime. As a result of the interaction between the dressed dipole and the hadron, the evolved structure of the dipole can be included into the wave function of the hadron, and therefore, we can obtain information about the evolution of its gluonic structure in the transverse plane.

Since obtaining the full dipole scattering amplitude from the BK equation is an enormous task as it has to be solved numerically, several approximations have been used in QCD phenomenology. First successful numerical studies of inclusive observables [19, 20] have approximated the proton as an infinite homogeneous target, thus factorising out any impact-parameter dependence of the dipole-target amplitude into a separate numerical parameter obtained from a fit to data. Another possible approach, described in Chapter 2, is to include the dependence of the amplitude on the impact parameter into a function which describes the proton profile in the transverse plane. The dipole amplitude can be then obtained as a solution to the one-dimensional BK equation (as described in Sec. 3.1) or from a phenomenological model (see Sec. 1.3.1). This allows us to study the shape and distribution of partons in the transverse plane. I studied the gluonic fluctuations of the transverse proton structure within the hot-spot model and I presented my results for predictions of exclusive and dissociative production of vector mesons. It has been shown in previous works that, within this formalism, one needs to include fluctuations in order to correctly describe HERA data on the later case [99]. Since the dissociative cross section is given as the variance over the different proton configurations within the Good-Walker approach [97,98], it was shown in Ref. [34] that the resulting cross section as a function of energy presents a maximum after which it decreases as the hot spots overlap and the different configurations starts to look alike. This allows to study the effect we call geometrical saturation and I have presented predictions for its onset in the production of various vector mesons and the possibility to measure this phenomenon at future electron-ion collid-

ers [10, 11]. This extensive set of predictions was published in Ref. [37] and I presented an overview of its main results and their interpretation in Chapter 2.

Chapter 3 was fully devoted to the BK equation and the choices one can make in order to calculate the dipole scattering amplitude from its simplest approximation described above, towards including more dimensions into the problem, and also extending the calculation to higher order accuracy. I presented a review of the numerical solutions to the BK equation from its LO version under the approximation of an infinite homogeneous target, through including higher-order corrections, and towards the one-dimensional BK equation at next-to-leading accuracy. Moreover, I included a review of the recent solutions of the leading-order BK equation with an explicit dependence on the impact parameter, which generalises the dipole amplitude to the case of a finite target. In Ref. [28], it has been shown that the collinearly-improved kernel (which imposes a life-time ordering of daughter dipole emissions) together with a new form of the initial condition suppress the so-called Coulomb tails — an unphysical growth of the scattering amplitude at large impact parameters. This new approach to solve the impact-parameter dependent BK equation at leading order accuracy including some of the higher order contributions within the collinearly-improved kernel allowed for a correct description of both inclusive and exclusive observables [29] without any additional parameters or modifications. This approach has also been extended to the nuclear case [30], providing two approaches to obtain the dipole-nucleus scattering amplitude: (i) coupling of the BK solution for the proton case to a Glauber-Gribov approach to model the nuclear interactions, or (ii) to obtain the dipole-nucleus amplitude directly from the BK evolution from the initial conditions which represents the specific nucleus.

Using these impact-parameter dependent dipole amplitudes, I was able to obtain a good description of data for several QCD processes and also to provide predictions for future measurements expected at LHC, EIC, and LHeC. These results were published in papers [29, 31–33] and I provided their summary in Chapter 4. As the case of the inclusive DIS with protons and nuclei was studied in previous works [29, 30], I presented the results which are devoted to study the relevant diffractive processes. It is shown that the b-BK model can correctly describe various sets of data coming from HERA and LHC experiments for the three studied processes: diffractive DIS, deeply virtual Compton scattering, and exclusive production of vector mesons. Also, it was confirmed that the predictions for the ratio of diffractive events within the total cross section are in agreement with previous phenomenological calculations. I also summarised predictions for the proton and nuclear diffractive structure functions which are expected to be measured at future electron-ion colliders. The comparison of the predictions using the b-BK evolution to those obtained using other CGC-inspired models shows a different behaviour of predictions for the individual contributions to the nuclear F_2^D. Moreover, the predictions show that its gluon component is substantially suppressed with increasing atomic number A. For the DVCS process, I summarised predictions for its cross section at energies expected to be measured at the EIC and at the LHeC. It is expected that in the future experiments, the $|t|$-distribution of the DVCS cross section will be measured to an yet unexplored area of large momenta transfers in the ep collisions and that it will be measured in eA collisions for the first time. As various models predict different magnitudes of the cross section and positions of diffractive minima, it is expected that such measurements could distinguish among different approaches to modelling the proton and nuclear dipole amplitudes. Moreover, the exclusive processes such as DVCS and production of vector mesons are expected to be directly sensitive to the distribution of gluons. Constraining the description of exclusive processes by phenomenological models could therefore allow us to directly access and study gluon distributions in the transverse plane. I conclude the summary of my results with the predictions for the production of vector mesons off protons and nuclei. The proton case shows a good description of available data on cross sections for production of various mesons such as J/ψ, ϕ or Υ. For the nuclear case, a comparison to the LHC data on the coherent

J/ψ photoproduction in ultraperipheral Pb–Pb collisions is presented. It can be observed that although the comparison between the Run 1 and Run 2 data for the rapidity distribution of the J/ψ cross section does not provide a clear preference for any of the two nuclear BK approaches, the latest data on the first measurement of the coherent J/ψ $|t|$-distribution presents a nice agreement with the evolution from a nuclear initial condition (b-BK-A approach). I also showed predictions for the energy and $|t|$-dependence of the cross section which are expected to be measured in future experiments and it is concluded that the two nuclear approaches yield significantly distinct results, which notably differ with increasing energy of the process. It is therefore expected that future measurements of the discussed QCD observables will provide better understanding of the underlying QCD dynamics of the proton and nuclear structure and its description by various dipole models and as a result, it will allow us to study the nature of saturation phenomena.

In the last chapter of this thesis, I presented my work on the numerical solution to the impact-parameter Balitsky–Kovchegov equation at next-to-leading order accuracy. This project aimed to connect the two directions of the numerical solutions to the BK equation: higher order accuracy and the two-dimensional solutions. For this purpose, I derived the formulas for the impact-parameter dependent geometry of the problem for the NLO dipole emissions. I calculated the impact-parameter independent numerical solution of the NLO BK equation and conclude that the results presented in Sec. 3.2 are in accordance with those in Refs. [26, 27]. Subsequently, I implemented the impact-parameter dependent geometry into the calculation. I obtained the numerical solutions for the b-dependent mean-field approximation of the NLO BK equation (5.1). First, I used the equation from Ref. [26], confirming that the b-dependent calculation suffers from the numerical instabilities in a similar manner as the b-independent calculation and that the NLO integrals provide a substantial subtraction from the dipole amplitude. Subsequently, I implemented the resummed version of the NLO BK equation from Ref. [27]. The observation from the b-dependent solutions of the resummed NLO BK is that the calculation diverges after several steps in rapidity as a result of development of large negative values of the amplitude. Tests with the individual contributions to the equation showed that the problematic contribution comes from the K_{sub} part of the K_1 kernel given by Eq. (3.21). From additional tests using the flat profile in impact parameter and other modifications to the initial condition from Eq. (3.26), I conclude that the form of the initial condition with the exponential profile in b seems to be incapable in providing physically reasonable results from the numerical solutions to the full NLO BK equation in its current form.

Bibliography

[1] M. Gell-Mann, "A Schematic Model of Baryons and Mesons," *Phys. Lett.*, vol. 8, pp. 214–215, 1964.

[2] G. Zweig, *An SU(3) model for strong interaction symmetry and its breaking. Version 2*, pp. 22–101. 2 1964.

[3] V. Gribov and L. Lipatov, "Deep inelastic e p scattering in perturbation theory," *Sov. J. Nucl. Phys.*, vol. 15, pp. 438–450, 1972.

[4] G. Altarelli and G. Parisi, "Asymptotic Freedom in Parton Language," *Nucl. Phys. B*, vol. 126, pp. 298–318, 1977.

[5] Y. L. Dokshitzer, "Calculation of the Structure Functions for Deep Inelastic Scattering and e+ e- Annihilation by Perturbation Theory in Quantum Chromodynamics.," *Sov. Phys. JETP*, vol. 46, pp. 641–653, 1977.

[6] E. A. Kuraev, L. N. Lipatov, and V. S. Fadin, "The Pomeranchuk Singularity in Nonabelian Gauge Theories," *Sov. Phys. JETP*, vol. 45, pp. 199–204, 1977. [Zh. Eksp. Teor. Fiz.72,377(1977)].

[7] I. I. Balitsky and L. N. Lipatov, "The Pomeranchuk Singularity in Quantum Chromodynamics," *Sov. J. Nucl. Phys.*, vol. 28, pp. 822–829, 1978. [Yad. Fiz.28,1597(1978)].

[8] M. Froissart, "Asymptotic behavior and subtractions in the Mandelstam representation," *Phys. Rev.*, vol. 123, pp. 1053–1057, 1961.

[9] A. Martin, "Unitarity and high-energy behavior of scattering amplitudes," *Phys. Rev.*, vol. 129, pp. 1432–1436, 1963.

[10] A. Accardi *et al.*, "Electron Ion Collider: The Next QCD Frontier," *Eur. Phys. J.*, vol. A52, no. 9, p. 268, 2016.

[11] J. Abelleira Fernandez *et al.*, "A Large Hadron Electron Collider at CERN: Report on the Physics and Design Concepts for Machine and Detector," *J.Phys.*, vol. G39, p. 075001, 2012.

[12] I. Balitsky, "Operator expansion for high-energy scattering," *Nucl. Phys.*, vol. B463, pp. 99–160, 1996.

[13] Y. V. Kovchegov, "Small x F(2) structure function of a nucleus including multiple pomeron exchanges," *Phys. Rev.*, vol. D60, p. 034008, 1999.

[14] Y. V. Kovchegov, "Unitarization of the BFKL pomeron on a nucleus," *Phys. Rev.*, vol. D61, p. 074018, 2000.

[15] A. H. Mueller, "Small x Behavior and Parton Saturation: A QCD Model," *Nucl.Phys.*, vol. B335, p. 115, 1990.

[16] A. H. Mueller, "Soft gluons in the infinite momentum wave function and the BFKL pomeron," *Nucl. Phys.*, vol. B415, pp. 373–385, 1994.

[17] A. H. Mueller and B. Patel, "Single and double BFKL pomeron exchange and a dipole picture of high-energy hard processes," *Nucl. Phys.*, vol. B425, pp. 471–488, 1994.

[18] N. N. Nikolaev and B. Zakharov, "Color transparency and scaling properties of nuclear shadowing in deep inelastic scattering," *Z.Phys.*, vol. C49, pp. 607–618, 1991.

[19] J. L. Albacete, N. Armesto, J. G. Milhano, C. A. Salgado, and U. A. Wiedemann, "Numerical analysis of the Balitsky-Kovchegov equation with running coupling: Dependence of the saturation scale on nuclear size and rapidity," *Phys. Rev.*, vol. D71, p. 014003, 2005.

[20] J. L. Albacete, N. Armesto, J. G. Milhano, and C. A. Salgado, "Non-linear QCD meets data: A Global analysis of lepton-proton scattering with running coupling BK evolution," *Phys. Rev.*, vol. D80, p. 034031, 2009.

[21] J. L. Albacete, N. Armesto, J. G. Milhano, P. Quiroga-Arias, and C. A. Salgado, "AAMQS: A non-linear QCD analysis of new HERA data at small-x including heavy quarks," *Eur. Phys. J.*, vol. C71, p. 1705, 2011.

[22] I. Balitsky and G. A. Chirilli, "NLO evolution of color dipoles in N=4 SYM," *Nucl.Phys.*, vol. B822, pp. 45–87, 2009.

[23] E. Iancu, J. D. Madrigal, A. H. Mueller, G. Soyez, and D. N. Triantafyllopoulos, "Collinearly-improved BK evolution meets the HERA data," *Phys. Lett.*, vol. B750, pp. 643–652, 2015.

[24] B. Ducloue, E. Iancu, A. H. Mueller, G. Soyez, and D. N. Triantafyllopoulos, "Non-linear evolution in QCD at high-energy beyond leading order," *JHEP*, vol. 04, p. 081, 2019.

[25] G. Beuf, H. Hänninen, T. Lappi, and H. Mäntysaari, "Color Glass Condensate at next-to-leading order meets HERA data," *Phys. Rev. D*, vol. 102, p. 074028, 2020.

[26] T. Lappi and H. Mäntysaari, "Direct numerical solution of the coordinate space Balitsky-Kovchegov equation at next to leading order," *Phys. Rev.*, vol. D91, no. 7, p. 074016, 2015.

[27] T. Lappi and H. Mantysaari, "Next-to-leading order Balitsky-Kovchegov equation with resummation," *Phys. Rev.*, vol. D93, no. 9, p. 094004, 2016.

[28] J. Cepila, J. G. Contreras, and M. Matas, "Collinearly improved kernel suppresses Coulomb tails in the impact-parameter dependent Balitsky-Kovchegov evolution," *Phys. Rev.*, vol. D99, no. 5, p. 051502, 2019.

[29] D. Bendova, J. Cepila, J. Contreras, and M. Matas, "Solution to the Balitsky-Kovchegov equation with the collinearly improved kernel including impact-parameter dependence," *Phys. Rev. D*, vol. 100, no. 5, p. 054015, 2019.

[30] J. Cepila, J. Contreras, and M. Matas, "Predictions for nuclear structure functions from the impact-parameter dependent Balitsky-Kovchegov equation," *Phys. Rev. C*, vol. 102, no. 4, p. 044318, 2020.

[31] D. Bendova, J. Cepila, J. G. Contreras, t. V. P. Gonçalves, and M. Matas, "Diffractive deeply inelastic scattering in future electron-ion colliders," *Eur. Phys. J. C*, vol. 81, no. 3, p. 211, 2021.

[32] D. Bendova, J. Cepila, J. G. Contreras, and M. Matas, "Photonuclear J/ψ production at the LHC: Proton-based versus nuclear dipole scattering amplitudes," *Phys. Lett. B*, vol. 817, p. 136306, 2021.

[33] D. Bendova, J. Cepila, V. P. Gonçalves, and C. R. Sena, "Deeply virtual Compton scattering at the EIC and LHeC: a comparison among saturation approaches," *Eur. Phys. J. C*, vol. 82, no. 2, p. 99, 2022.

[34] J. Cepila, J. G. Contreras, and J. D. Tapia Takaki, "Energy dependence of dissociative J/ψ photoproduction as a signature of gluon saturation at the LHC," *Phys. Lett.*, vol. B766, pp. 186–191, 2017.

[35] J. Cepila, J. G. Contreras, and M. Krelina, "Coherent and incoherent J/ψ photonuclear production in an energy-dependent hot-spot model," *Phys. Rev.*, vol. C97, no. 2, p. 024901, 2018.

[36] J. Cepila, J. Contreras, M. Krelina, and J. Tapia Takaki, "Mass dependence of vector meson photoproduction off protons and nuclei within the energy-dependent hot-spot model," *Nucl. Phys. B*, vol. 934, pp. 330–340, 2018.

[37] D. Bendova, J. Cepila, and J. G. Contreras, "Dissociative production of vector mesons at electron-ion colliders," *Phys. Rev.*, vol. D99, no. 3, p. 034025, 2019.

[38] H. Mäntysaari and B. Schenke, "Revealing proton shape fluctuations with incoherent diffraction at high energy," *Phys. Rev. D*, vol. 94, no. 3, p. 034042, 2016.

[39] H. Mäntysaari, "Review of proton and nuclear shape fluctuations at high energy," *Rept. Prog. Phys.*, vol. 83, no. 8, p. 082201, 2020.

[40] E. D. Bloom *et al.*, "High-Energy Inelastic e p Scattering at 6-Degrees and 10-Degrees," *Phys. Rev. Lett.*, vol. 23, pp. 930–934, 1969.

[41] M. Breidenbach, J. I. Friedman, H. W. Kendall, E. D. Bloom, D. H. Coward, H. C. DeStaebler, J. Drees, L. W. Mo, and R. E. Taylor, "Observed behavior of highly inelastic electron-proton scattering," *Phys. Rev. Lett.*, vol. 23, pp. 935–939, 1969.

[42] R. P. Feynman, "Very high-energy collisions of hadrons," *Phys. Rev. Lett.*, vol. 23, pp. 1415–1417, Dec 1969.

[43] J. D. Bjorken and E. A. Paschos, "Inelastic electron-proton and γ-proton scattering and the structure of the nucleon," *Phys. Rev.*, vol. 185, pp. 1975–1982, Sep 1969.

[44] M. Derrick *et al.*, "Measurement of the proton structure function F2 at low x and low q**2 at HERA," *Z. Phys. C*, vol. 69, pp. 607–620, 1996.

[45] S. Aid *et al.*, "A Measurement and QCD analysis of the proton structure function f2 (x, q**2) at HERA," *Nucl. Phys. B*, vol. 470, pp. 3–40, 1996.

[46] S. Chekanov *et al.*, "A ZEUS next-to-leading-order QCD analysis of data on deep inelastic scattering," *Phys. Rev. D*, vol. 67, p. 012007, 2003.

[47] F. D. Aaron *et al.*, "Combined Measurement and QCD Analysis of the Inclusive e+- p Scattering Cross Sections at HERA," *JHEP*, vol. 01, p. 109, 2010.

[48] H. Abramowicz *et al.*, "Combination of measurements of inclusive deep inelastic $e^{\pm}p$ scattering cross sections and QCD analysis of HERA data," *Eur. Phys. J. C*, vol. 75, no. 12, p. 580, 2015.

[49] H. Abramowicz *et al.*, "Combination and QCD analysis of charm and beauty production cross-section measurements in deep inelastic ep scattering at HERA," *Eur. Phys. J. C*, vol. 78, no. 6, p. 473, 2018.

[50] D. Bendova, "Study of hadron structure within quantum chromodynamics," Master's thesis, Czech Technical University in Prague, 2018.

[51] F. Halzen and A. D. Martin, *QUARKS AND LEPTONS: AN INTRODUCTORY COURSE IN MODERN PARTICLE PHYSICS*. 1984.

[52] J. Chýla, *Quarks, partons and Quantum Chromodynamics*. textbook for lectures in Quantum Chromodynamics, 2009.

[53] J. I. Friedman and H. W. Kendall, "Deep inelastic electron scattering," *Annual Review of Nuclear Science*, vol. 22, no. 1, pp. 203–254, 1972.

[54] C. G. Callan and D. J. Gross, "High-energy electroproduction and the constitution of the electric current," *Phys. Rev. Lett.*, vol. 22, pp. 156–159, Jan 1969.

[55] A. Bodek, M. Breidenbach, D. L. Dubin, J. E. Elias, J. I. Friedman, H. W. Kendall, J. S. Poucher, E. M. Riordan, M. R. Sogard, D. H. Coward, and D. J. Sherden, "Experimental studies of the neutron and proton electromagnetic structure functions," *Phys. Rev. D*, vol. 20, pp. 1471–1552, Oct 1979.

[56] F. D. Aaron *et al.*, "Measurement of the Proton Structure Function F(L)(x, Q**2) at Low x," *Phys. Lett. B*, vol. 665, pp. 139–146, 2008.

[57] S. Chekanov *et al.*, "Measurement of the Longitudinal Proton Structure Function at HERA," *Phys. Lett. B*, vol. 682, pp. 8–22, 2009.

[58] P. Taels, *Quantum chromodynamics at small Bjorken-x*. PhD thesis, Antwerp U., Antwerp U., 2017.

[59] Y. V. Kovchegov and E. Levin, *Quantum chromodynamics at high energy*, vol. 33. Cambridge University Press, 8 2012.

[60] M. Kuhlen, "QCD at HERA: The hadronic final state in deep inelastic scattering," *Springer Tracts Mod. Phys.*, vol. 150, pp. 1–172, 1999.

[61] L. D. McLerran and R. Venugopalan, "Computing quark and gluon distribution functions for very large nuclei," *Phys. Rev. D*, vol. 49, pp. 2233–2241, 1994.

[62] L. D. McLerran and R. Venugopalan, "Gluon distribution functions for very large nuclei at small transverse momentum," *Phys. Rev. D*, vol. 49, pp. 3352–3355, 1994.

[63] J. Jalilian-Marian, A. Kovner, A. Leonidov, and H. Weigert, "The BFKL equation from the Wilson renormalization group," *Nucl. Phys. B*, vol. 504, pp. 415–431, 1997.

[64] J. Jalilian-Marian, A. Kovner, A. Leonidov, and H. Weigert, "The Wilson renormalization group for low x physics: Towards the high density regime," *Phys. Rev.*, vol. D59, p. 014014, 1998.

[65] A. Kovner, J. Milhano, and H. Weigert, "Relating different approaches to nonlinear QCD evolution at finite gluon density," *Phys. Rev. D*, vol. 62, p. 114005, 2000.

[66] H. Weigert, "Unitarity at small Bjorken x," *Nucl. Phys.*, vol. A703, pp. 823–860, 2002.

[67] E. Iancu, A. Leonidov, and L. D. McLerran, "Nonlinear gluon evolution in the color glass condensate. I," *Nucl. Phys.*, vol. A692, pp. 583–645, 2001.

[68] E. Iancu, A. Leonidov, and L. D. McLerran, "The Renormalization group equation for the color glass condensate," *Phys. Lett.*, vol. B510, pp. 133–144, 2001.

[69] E. Ferreiro, E. Iancu, A. Leonidov, and L. McLerran, "Nonlinear gluon evolution in the color glass condensate. II," *Nucl. Phys.*, vol. A703, pp. 489–538, 2002.

[70] A. H. Mueller, "A Simple derivation of the JIMWLK equation," *Phys. Lett. B*, vol. 523, pp. 243–248, 2001.

[71] E. Iancu and R. Venugopalan, *The Color glass condensate and high-energy scattering in QCD*, pp. 249–3363. 3 2003.

[72] F. Gelis, E. Iancu, J. Jalilian-Marian, and R. Venugopalan, "The Color Glass Condensate," *Ann. Rev. Nucl. Part. Sci.*, vol. 60, pp. 463–489, 2010.

[73] J. L. Albacete and C. Marquet, "Gluon saturation and initial conditions for relativistic heavy ion collisions," *Prog. Part. Nucl. Phys.*, vol. 76, pp. 1–42, 2014.

[74] K. J. Golec-Biernat and M. Wusthoff, "Saturation effects in deep inelastic scattering at low Q**2 and its implications on diffraction," *Phys. Rev.*, vol. D59, p. 014017, 1998.

[75] K. J. Golec-Biernat and M. Wusthoff, "Saturation in diffractive deep inelastic scattering," *Phys. Rev.*, vol. D60, p. 114023, 1999.

[76] A. M. Stasto, K. J. Golec-Biernat, and J. Kwiecinski, "Geometric scaling for the total gamma* p cross-section in the low x region," *Phys. Rev. Lett.*, vol. 86, pp. 596–599, 2001.

[77] A. Freund, K. Rummukainen, H. Weigert, and A. Schafer, "Geometric scaling in inclusive eA reactions and nonlinear perturbative QCD," *Phys. Rev. Lett.*, vol. 90, p. 222002, 2003.

[78] J. Bartels, K. J. Golec-Biernat, and H. Kowalski, "A modification of the saturation model: DGLAP evolution," *Phys. Rev. D*, vol. 66, p. 014001, 2002.

[79] H. Kowalski and D. Teaney, "An Impact parameter dipole saturation model," *Phys. Rev.*, vol. D68, p. 114005, 2003.

[80] A. H. Rezaeian, M. Siddikov, M. Van de Klundert, and R. Venugopalan, "Analysis of combined HERA data in the Impact-Parameter dependent Saturation model," *Phys. Rev. D*, vol. 87, no. 3, p. 034002, 2013.

[81] H. Mantysaari and P. Zurita, "In depth analysis of the combined HERA data in the dipole models with and without saturation," *Phys. Rev.*, vol. D98, p. 036002, 2018.

[82] B. Schenke, P. Tribedy, and R. Venugopalan, "Fluctuating Glasma initial conditions and flow in heavy ion collisions," *Phys. Rev. Lett.*, vol. 108, p. 252301, 2012.

[83] B. Schenke, P. Tribedy, and R. Venugopalan, "Event-by-event gluon multiplicity, energy density, and eccentricities in ultrarelativistic heavy-ion collisions," *Phys. Rev. C*, vol. 86, p. 034908, 2012.

[84] E. Iancu, K. Itakura, and S. Munier, "Saturation and BFKL dynamics in the HERA data at small x," *Phys. Lett.*, vol. B590, pp. 199–208, 2004.

[85] H. Kowalski, L. Motyka, and G. Watt, "Exclusive diffractive processes at HERA within the dipole picture," *Phys. Rev.*, vol. D74, p. 074016, 2006.

[86] G. Watt and H. Kowalski, "Impact parameter dependent colour glass condensate dipole model," *Phys. Rev.*, vol. D78, p. 014016, 2008.

[87] A. G. Shuvaev, K. J. Golec-Biernat, A. D. Martin, and M. G. Ryskin, "Off diagonal distributions fixed by diagonal partons at small x and xi," *Phys. Rev.*, vol. D60, p. 014015, 1999.

[88] Y. Hatta, B.-W. Xiao, and F. Yuan, "Gluon Tomography from Deeply Virtual Compton Scattering at Small-x," *Phys. Rev.*, vol. D95, no. 11, p. 114026, 2017.

[89] I. P. Ivanov, N. N. Nikolaev, and A. A. Savin, "Diffractive vector meson production at HERA: From soft to hard QCD," *Phys. Part. Nucl.*, vol. 37, pp. 1–85, 2006.

[90] J. Bartels, K. J. Golec-Biernat, and K. Peters, "On the dipole picture in the nonforward direction," *Acta Phys. Polon. B*, vol. 34, pp. 3051–3068, 2003.

[91] J. Cepila, J. Nemchik, M. Krelina, and R. Pasechnik, "Theoretical uncertainties in exclusive electroproduction of S-wave heavy quarkonia," *Eur. Phys. J. C*, vol. 79, no. 6, p. 495, 2019.

[92] M. Krelina, J. Nemchik, R. Pasechnik, and J. Cepila, "Spin rotation effects in diffractive electroproduction of heavy quarkonia," *Eur. Phys. J. C*, vol. 79, no. 2, p. 154, 2019.

[93] J. Nemchik, N. N. Nikolaev, and B. G. Zakharov, "Scanning the BFKL pomeron in elastic production of vector mesons at HERA," *Phys. Lett.*, vol. B341, pp. 228–237, 1994.

[94] J. Nemchik, N. N. Nikolaev, E. Predazzi, and B. G. Zakharov, "Color dipole phenomenology of diffractive electroproduction of light vector mesons at HERA," *Z. Phys.*, vol. C75, pp. 71–87, 1997.

[95] J. R. Forshaw, R. Sandapen, and G. Shaw, "Color dipoles and rho, phi electroproduction," *Phys. Rev.*, vol. D69, p. 094013, 2004.

[96] C. Patrignani *et al.*, "Review of Particle Physics," *Chin. Phys.*, vol. C40, no. 10, p. 100001, 2016.

[97] M. L. Good and W. D. Walker, "Diffraction disssociation of beam particles," *Phys. Rev.*, vol. 120, pp. 1857–1860, 1960.

[98] H. I. Miettinen and J. Pumplin, "Diffraction Scattering and the Parton Structure of Hadrons," *Phys. Rev. D*, vol. 18, p. 1696, 1978.

[99] H. Mantysaari and B. Schenke, "Evidence of strong proton shape fluctuations from incoherent diffraction," *Phys. Rev. Lett.*, vol. 117, no. 5, p. 052301, 2016.

[100] J. L. Albacete and A. Soto-Ontoso, "Hot spots and the hollowness of proton–proton interactions at high energies," *Phys. Lett. B*, vol. 770, pp. 149–153, 2017.

[101] A. Kumar and T. Toll, "Investigating the structure of gluon fluctuations in the proton with incoherent diffraction at HERA," *Eur. Phys. J. C*, vol. 82, no. 9, p. 837, 2022.

[102] H. Mäntysaari, B. Schenke, C. Shen, and P. Tribedy, "Imprints of fluctuating proton shapes on flow in proton-lead collisions at the LHC," *Phys. Lett. B*, vol. 772, pp. 681–686, 2017.

[103] J. Berger and A. Stasto, "Numerical solution of the nonlinear evolution equation at small x with impact parameter and beyond the LL approximation," *Phys. Rev.*, vol. D83, p. 034015, 2011.

[104] J. Berger and A. M. Stasto, "Small x nonlinear evolution with impact parameter and the structure function data," *Phys. Rev.*, vol. D84, p. 094022, 2011.

[105] F. D. Aaron *et al.*, "Diffractive Electroproduction of rho and phi Mesons at HERA," *JHEP*, vol. 05, p. 032, 2010.

[106] S. Aid *et al.*, "Elastic photoproduction of rho0 mesons at HERA," *Nucl. Phys. B*, vol. 463, pp. 3–32, 1996.

[107] C. Adloff *et al.*, "Proton dissociative ρ and elastic ϕ electroproduction at HERA," *Z. Phys.*, vol. C75, pp. 607–618, 1997.

[108] F. D. Aaron *et al.*, "Diffractive Electroproduction of rho and phi Mesons at HERA," *JHEP*, vol. 05, p. 032, 2010.

[109] J. Breitweg *et al.*, "Elastic and proton dissociative ρ^0 photoproduction at HERA," *Eur. Phys. J. C*, vol. 2, pp. 247–267, 1998.

[110] S. Chekanov *et al.*, "Exclusive rho0 production in deep inelastic scattering at HERA," *PMC Phys.*, vol. A1, p. 6, 2007.

[111] A. M. Sirunyan *et al.*, "Measurement of exclusive $\rho(770)^0$ photoproduction in ultraperipheral pPb collisions at $\sqrt{s_{\mathrm{NN}}} = 5.02$ TeV," *Eur. Phys. J. C*, vol. 79, no. 8, p. 702, 2019.

[112] C. Alexa *et al.*, "Elastic and Proton-Dissociative Photoproduction of J/psi Mesons at HERA," *Eur. Phys. J.*, vol. C73, no. 6, p. 2466, 2013.

[113] B. B. Abelev *et al.*, "Exclusive J/ψ photoproduction off protons in ultra-peripheral p-Pb collisions at $\sqrt{s_{\mathrm{NN}}} = 5.02$ TeV," *Phys. Rev. Lett.*, vol. 113, no. 23, p. 232504, 2014.

[114] S. Acharya *et al.*, "Energy dependence of exclusive J/ψ photoproduction off protons in ultra-peripheral p?Pb collisions at $\sqrt{s_{\mathrm{NN}}} = 5.02$ TeV," *Eur. Phys. J.*, vol. C79, no. 5, p. 402, 2019.

[115] A. Aktas *et al.*, "Elastic J/psi production at HERA," *Eur. Phys. J.*, vol. C46, pp. 585–603, 2006.

[116] V. Andreev *et al.*, "Measurement of Exclusive $\pi^+\pi^-$ and ρ^0 Meson Photoproduction at HERA," *Eur. Phys. J. C*, vol. 80, no. 12, p. 1189, 2020.

[117] N. Armesto, M. A. Braun, E. G. Ferreiro, and C. Pajares, "Percolation approach to quark - gluon plasma and J / psi suppression," *Phys. Rev. Lett.*, vol. 77, pp. 3736–3738, 1996.

[118] M. Lomnitz and S. Klein, "Exclusive vector meson production at an electron-ion collider," *Phys. Rev. C*, vol. 99, no. 1, p. 015203, 2019.

[119] R. Abdul Khalek *et al.*, "Science Requirements and Detector Concepts for the Electron-Ion Collider: EIC Yellow Report," *Nucl. Phys. A*, vol. 1026, p. 122447, 2022.

[120] P. Agostini *et al.*, "The Large Hadron–Electron Collider at the HL-LHC," *J. Phys. G*, vol. 48, no. 11, p. 110501, 2021.

[121] S. Klein *et al.*, "New opportunities at the photon energy frontier," 9 2020.

[122] C. Marquet and G. Soyez, "The Balitsky-Kovchegov equation in full momentum space," *Nucl. Phys.*, vol. A760, pp. 208–222, 2005.

[123] A. Quarteroni, R. Sacco, and F. Saleri, *Numerical Mathematics*. Springer-Verlag New York, 2000.

[124] L. D. McLerran and R. Venugopalan, "Boost covariant gluon distributions in large nuclei," *Phys. Lett.*, vol. B424, pp. 15–24, 1998.

[125] E. Iancu, K. Itakura, and L. McLerran, "Geometric scaling above the saturation scale," *Nucl. Phys. A*, vol. 708, pp. 327–352, 2002.

[126] A. Mueller and D. Triantafyllopoulos, "The Energy dependence of the saturation momentum," *Nucl. Phys. B*, vol. 640, pp. 331–350, 2002.

[127] J. L. Albacete and Y. V. Kovchegov, "Solving high energy evolution equation including running coupling corrections," *Phys. Rev.*, vol. D75, p. 125021, 2007.

[128] K. J. Golec-Biernat, L. Motyka, and A. Stasto, "Diffusion into infrared and unitarization of the BFKL pomeron," *Phys. Rev. D*, vol. 65, p. 074037, 2002.

[129] I. Balitsky, "Quark contribution to the small-x evolution of color dipole," *Phys. Rev.*, vol. D75, p. 014001, 2007.

[130] E. Iancu, J. D. Madrigal, A. H. Mueller, G. Soyez, and D. N. Triantafyllopoulos, "Resumming double logarithms in the QCD evolution of color dipoles," *Phys. Lett.*, vol. B744, pp. 293–302, 2015.

[131] A. Sabio Vera, "An 'All-poles' approximation to collinear resummations in the Regge limit of perturbative QCD," *Nucl. Phys. B*, vol. 722, pp. 65–80, 2005.

[132] S. Munier and R. B. Peschanski, "Geometric scaling as traveling waves," *Phys. Rev. Lett.*, vol. 91, p. 232001, 2003.

[133] S. Munier and R. B. Peschanski, "Traveling wave fronts and the transition to saturation," *Phys. Rev. D*, vol. 69, p. 034008, 2004.

[134] N. Armesto and M. Braun, "Parton densities and dipole cross-sections at small x in large nuclei," *Eur. Phys. J. C*, vol. 20, pp. 517–522, 2001.

[135] M. Lublinsky, "Scaling phenomena from nonlinear evolution in high-energy DIS," *Eur. Phys. J. C*, vol. 21, pp. 513–519, 2001.

[136] K. Rummukainen and H. Weigert, "Universal features of JIMWLK and BK evolution at small x," *Nucl. Phys. A*, vol. 739, pp. 183–226, 2004.

[137] I. Balitsky and G. A. Chirilli, "Next-to-leading order evolution of color dipoles," *Phys.Rev.*, vol. D77, p. 014019, 2008.

[138] I. O. Cherednikov, T. Mertens, and F. F. Van der Veken, *Wilson lines in quantum field theory*, vol. 24. De Gruyter, 9 2014.

[139] Y. V. Kovchegov and H. Weigert, "Triumvirate of Running Couplings in Small-x Evolution," *Nucl. Phys.*, vol. A784, pp. 188–226, 2007.

[140] I. Balitsky and A. V. Belitsky, "Nonlinear evolution in high density QCD," *Nucl. Phys. B*, vol. 629, pp. 290–322, 2002.

[141] T. Lappi and H. Mäntysaari, "Solving the NLO BK equation in coordinate space," *PoS*, vol. DIS2015, p. 080, 2015.

[142] K. J. Golec-Biernat and A. M. Stasto, "On solutions of the Balitsky-Kovchegov equation with impact parameter," *Nucl. Phys.*, vol. B668, pp. 345–363, 2003.

[143] J. Berger and A. M. Stasto, "Exclusive vector meson production and small-x evolution," *JHEP*, vol. 1301, p. 001, 2013.

[144] C. Marquet, "A Unified description of diffractive deep inelastic scattering with saturation," *Phys. Rev.*, vol. D76, p. 094017, 2007.

[145] N. Armesto, "A Simple model for nuclear structure functions at small x in the dipole picture," *Eur. Phys. J.*, vol. C26, pp. 35–43, 2002.

[146] E. Cazaroto, F. Carvalho, V. Goncalves, and F. Navarra, "Could saturation effects be visible in a future electron-ion collider?," *Phys. Lett. B*, vol. 671, pp. 233–239, 2009.

[147] C. Marquet, M. R. Moldes, and P. Zurita, "Unveiling saturation effects from nuclear structure function measurements at the EIC," *Phys. Lett. B*, vol. 772, pp. 607–614, 2017.

[148] K. J. Eskola, P. Paakkinen, H. Paukkunen, and C. A. Salgado, "EPPS16: Nuclear parton distributions with LHC data," *Eur. Phys. J. C*, vol. 77, no. 3, p. 163, 2017.

[149] M. Arneodo and M. Diehl, "Diffraction for non-believers," in *HERA and the LHC: A Workshop on the Implications of HERA and LHC Physics (Startup Meeting, CERN, 26-27 March 2004; Midterm Meeting, CERN, 11-13 October 2004)*, pp. 425–446, 2005.

[150] A. Deshpande, R. Milner, R. Venugopalan, and W. Vogelsang, "Study of the fundamental structure of matter with an electron-ion collider," *Ann. Rev. Nucl. Part. Sci.*, vol. 55, pp. 165–228, 2005.

[151] C. Royon and C. Baldenegro, "Diffraction and photon exchange processes at the LHC and parton saturation," *Int. J. Mod. Phys. A*, vol. 35, no. 08, p. 2030004, 2020.

[152] H. Hänninen, *Deep inelastic scattering in the dipole picture at next-to-leading order*. PhD thesis, Jyvaskyla U, Jyvaskyla U., 2021.

[153] H. Kowalski, T. Lappi, C. Marquet, and R. Venugopalan, "Nuclear enhancement and suppression of diffractive structure functions at high energies," *Phys. Rev. C*, vol. 78, p. 045201, 2008.

[154] G. Beuf, H. Hänninen, T. Lappi, Y. Mulian, and H. Mäntysaari, "Diffractive deep inelastic scattering at NLO in the dipole picture: The qqg contribution," *Phys. Rev. D*, vol. 106, no. 9, p. 094014, 2022.

[155] M. S. Kugeratski, V. P. Goncalves, and F. S. Navarra, "Saturation in diffractive deep inelastic eA scattering," *Eur. Phys. J. C*, vol. 46, pp. 413–420, 2006.

[156] N. N. Nikolaev, W. Schafer, B. G. Zakharov, and V. R. Zoller, "Unitarity constraints for DIS off nuclei: Predictions for electron-ion colliders," *JETP Lett.*, vol. 84, pp. 537–541, 2007.

[157] F. Aaron *et al.*, "Inclusive Measurement of Diffractive Deep-Inelastic Scattering at HERA," *Eur. Phys. J. C*, vol. 72, p. 2074, 2012.

[158] F. D. Aaron *et al.*, "Deeply Virtual Compton Scattering and its Beam Charge Asymmetry in e+- Collisions at HERA," *Phys. Lett. B*, vol. 681, pp. 391–399, 2009.

[159] A. H. Rezaeian and I. Schmidt, "Impact-parameter dependent Color Glass Condensate dipole model and new combined HERA data," *Phys. Rev. D*, vol. 88, p. 074016, 2013.

[160] M. G. Ryskin, "Diffractive J / psi electroproduction in LLA QCD," *Z. Phys.*, vol. C57, pp. 89–92, 1993.

[161] S. Chekanov *et al.*, "Exclusive electroproduction of phi mesons at HERA," *Nucl. Phys.*, vol. B718, pp. 3–31, 2005.

[162] C. Adloff *et al.*, "Elastic photoproduction of J / psi and Upsilon mesons at HERA," *Phys. Lett.*, vol. B483, pp. 23–35, 2000.

[163] S. Chekanov *et al.*, "Exclusive photoproduction of upsilon mesons at HERA," *Phys. Lett.*, vol. B680, pp. 4–12, 2009.

[164] R. Aaij *et al.*, "Measurement of the exclusive Υ production cross-section in pp collisions at $\sqrt{s} = 7$ TeV and 8 TeV," *JHEP*, vol. 09, p. 084, 2015.

[165] A. M. Sirunyan *et al.*, "Measurement of exclusive Υ photoproduction from protons in pPb collisions at $\sqrt{s_{\mathrm{NN}}} = 5.02$ TeV," *Eur. Phys. J.*, vol. C79, no. 3, p. 277, 2019.

[166] N. Armesto and A. H. Rezaeian, "Exclusive vector meson production at high energies and gluon saturation," *Phys. Rev. D*, vol. 90, no. 5, p. 054003, 2014.

[167] T. Toll and T. Ullrich, "Exclusive diffractive processes in electron-ion collisions," *Phys. Rev. C*, vol. 87, no. 2, p. 024913, 2013.

[168] J. G. Contreras, "Small x gluon shadowing from LHC data on coherent J/ψ photoproduction," *Phys. Rev.*, vol. C96, no. 1, p. 015203, 2017.

[169] B. Abelev *et al.*, "Coherent J/ψ photoproduction in ultra-peripheral Pb-Pb collisions at $\sqrt{s_{NN}} =$ 2.76 TeV," *Phys. Lett. B*, vol. 718, pp. 1273–1283, 2013.

[170] E. Abbas *et al.*, "Charmonium and e^+e^- pair photoproduction at mid-rapidity in ultra-peripheral Pb-Pb collisions at $\sqrt{s_{\rm NN}}$=2.76 TeV," *Eur. Phys. J. C*, vol. 73, no. 11, p. 2617, 2013.

[171] V. Khachatryan *et al.*, "Coherent J/ψ photoproduction in ultra-peripheral PbPb collisions at $\sqrt{s_{NN}}$ = 2.76 TeV with the CMS experiment," *Phys. Lett. B*, vol. 772, pp. 489–511, 2017.

[172] S. Acharya *et al.*, "Coherent J/ψ photoproduction at forward rapidity in ultra-peripheral Pb-Pb collisions at $\sqrt{s_{\rm NN}}$ = 5.02 TeV," *Phys. Lett. B*, vol. 798, p. 134926, 2019.

[173] A. Bursche, "Study of coherent J/ψ production in lead-lead collisions at $\sqrt{s_{\rm NN}}$ = 5 TeV with the LHCb experiment," *Nucl. Phys. A*, vol. 982, pp. 247–250, 2019.

[174] S. Acharya *et al.*, "First measurement of the $|t|$-dependence of coherent J/ψ photonuclear production," *Phys. Lett. B*, vol. 817, p. 136280, 2021.

[175] I. Balitsky and G. A. Chirilli, "Photon impact factor in the next-to-leading order," *Phys. Rev. D*, vol. 83, p. 031502, 2011.

[176] I. Balitsky and G. A. Chirilli, "Photon impact factor and k_T-factorization for DIS in the next-to-leading order," *Phys. Rev. D*, vol. 87, no. 1, p. 014013, 2013.

[177] G. Beuf, "NLO corrections for the dipole factorization of DIS structure functions at low x," *Phys. Rev. D*, vol. 85, p. 034039, 2012.

[178] G. Beuf, "Dipole factorization for DIS at NLO: Loop correction to the $\gamma^*_{T,L} \to q\bar{q}$ light-front wave functions," *Phys. Rev. D*, vol. 94, no. 5, p. 054016, 2016.

[179] G. Beuf, "Dipole factorization for DIS at NLO: Combining the $q\bar{q}$ and $q\bar{q}g$ contributions," *Phys. Rev.*, vol. D96, no. 7, p. 074033, 2017.

[180] H. Hanninen, T. Lappi, and R. Paatelainen, "One-loop corrections to light cone wave functions: the dipole picture DIS cross section," *Annals Phys.*, vol. 393, pp. 358–412, 2018.

[181] B. Ducloue, H. Hanninen, T. Lappi, and Y. Zhu, "Deep inelastic scattering in the dipole picture at next-to-leading order," *Phys. Rev.*, vol. D96, no. 9, p. 094017, 2017.

[182] G. Beuf, T. Lappi, and R. Paatelainen, "Massive Quarks at One Loop in the Dipole Picture of Deep Inelastic Scattering," *Phys. Rev. Lett.*, vol. 129, no. 7, p. 072001, 2022.

[183] H. Mäntysaari and J. Penttala, "Complete calculation of exclusive heavy vector meson production at next-to-leading order in the dipole picture," *JHEP*, vol. 08, p. 247, 2022.

Appendix A

Selected publications

Papers

- D. Bendova, J. Cepila, and J. G. Contreras, “Dissociative production of vector mesons at electron-ion colliders”, Phys. Rev., vol. D99, no. 3, p. 034025, 2019.
  doi:10.1103/PhysRevD.99.034025; arxiv:1811.06479 [hep-ph]

- D. Bendova, J. Cepila, J. G. Contreras, and M. Matas, “Solution to the Balitsky-Kovchegov equation with the collinearly improved kernel including impact-parameter dependence”, Phys. Rev. D, vol. 100, no. 5, p. 054015, 2019.
  doi:10.1103/PhysRevD.100.054015; arXiv:1907.12123 [hep-ph]

- D. Bendova, J. Cepila, J. G. Contreras, V. Goncalves, and M. Matas, “Diffractive deeply inelastic scattering in future electron-ion colliders”, Eur. Phys. J. C, vol. 81, no. 211, 2021.
  doi:10.1140/epjc/s10052-021-09006-x; arXiv:2002.11056 [hep-ph]

- D. Bendova, J. Cepila, J. G. Contreras, and M. Matas, “Photonuclear J/ψ production at the LHC: proton-based versus nuclear dipole scattering amplitudes”, Phys. Lett. B, vol. 817, p. 136306, 2021.
  doi:10.1016/j.physletb.2021.136306; arXiv:2006.12980 [hep-ph]

- D. Bendova, J. Cepila, V. Goncalves, and C. R. Sena, "Deeply virtual Compton scattering at the EIC and LHeC: a comparison among saturation approaches", Eur. Phys. J. C, vol. 82, no. 99, 2022.
  doi:10.1140/epjc/s10052-022-10059-9; arXiv:2002.11056 [hep-ph]

Proceedings

- D. Bendova, J. Cepila, and J. G. Contreras, "Dissociative production of vector mesons within the energy-dependent hot-spot model", PoS (EPS-HEP 2019) 472.

- D. Bendova, J. Cepila, and J. G. Contreras, "Dissociative production of vector mesons as a new tool to study gluon saturation at electron-ion colliders", PoS (LC 2019) 025.

Dissociative production of vector mesons at electron-ion colliders

D. Bendova, J. Cepila, and J. G. Contreras
Faculty of Nuclear Sciences and Physical Engineering, Czech Technical University in Prague, Prague 11519, Czech Republic

(Received 4 December 2018; published 28 February 2019)

We present predictions for the exclusive and dissociative production of vector mesons off protons in an electron-ion collider. The computation is based on the energy-dependent hot spot model that was shown to successfully describe the available photoproduction data. We find that the model also describes correctly all available electroproduction data. In addition, we find that the cross section for dissociative production as a function of the center-of-mass energy of the photon-proton system has a maximum, whose position depends on the virtuality of the photon and the mass of the vector meson. We use these maxima to define a geometrical saturation scale and find that it grows linearly with energy as a function of the scale of the process. This phenomenon can be studied at the proposed electron-ion colliders, JLEIC, eRHIC and LHeC.

DOI: 10.1103/PhysRevD.99.034025

I. INTRODUCTION

Within perturbative quantum chromodynamics (pQCD), the structure of hadrons in terms of its constituent partons evolves with energy or, equivalently, with Bjorken-x. Very precise measurements of the $F_2(x, Q^2)$ structure function of the proton performed at HERA with photons of virtuality Q^2 indicate that the gluon density grows steeply for decreasing x [1]. According to pQCD, this behavior changes at some point where nonlinear effects start to be important and the proton structure enters a regime known as saturation; see, e.g., [2] and references therein.

Exclusive vector meson production in electron-hadron colliders, depicted in Fig. 1(a), has been advocated as a tool to study the saturation phenomenon in the facilities that are under design now, like the EIC or the LHeC [3,4]. In this process, the incoming electron emits a photon which interacts with the proton to produce a vector meson. The photon can be quasireal (γ) or have a large virtuality (γ^*); these cases are known as photo- or electroproduction, respectively. Here, $W_{\gamma p}$ is the center-of-mass energy of the photon-proton system and $-t$ is the square of the momentum transferred in the proton vertex. This process has been extensively investigated at HERA and at the LHC. (For recent reviews see [5,6], respectively.) These measurements have been successfully described by a variety of models including saturation effects; e.g., [7–9]. A recent study addresses in detail the corresponding measurements at future electron-ion colliders [10].

A related process, shown schematically in Fig. 1(b), that has recently attracted renewed attention, is the production of a vector meson accompanied by the dissociation of the scattered proton. In a Good-Walker approach [11,12] this process can be related to fluctuations of the partonic structure of the proton [13,14]. Specifically, it is related to the variance over the different configurations of the partonic structure, and the main contribution to the variance is given by fluctuations in the geometrical configurations in the impact-parameter plane. Using a model with three so-called hot spots, regions of high gluonic density, the authors of [13] showed that the measurement of the cross section for the dissociative photoproduction of J/ψ as a function of $|t|$, at a fixed $W_{\gamma p}$, could be successfully described.

These ideas were extended in [15] by the inclusion of an energy dependence on the number of hot spots, which grows with decreasing x, mimicking the expectations of pQCD. This model successfully describes all available data on the energy dependence of both exclusive and dissociative photoproduction of J/ψ off protons. Furthermore, it predicts that the dissociative cross section grows with energy up to a maximum value and then decreases steeply. These investigations were continued in [16,17] to describe the production off nuclear targets and of different vector mesons, respectively. In [17], it was observed that the position of the maximum of the dissociative cross section depends on the mass of the vector meson in photoproduction processes.

In this article, we apply our model to the case of the dissociative electroproduction of vector mesons. We find that this cross section has a maximum, whose position depends on the virtuality of the photon and the mass of the

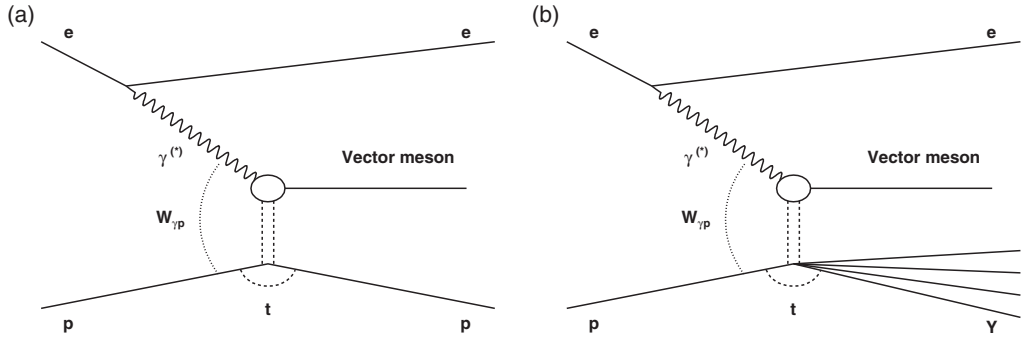

FIG. 1. Diagrams for exclusive (a) and dissociative (b) production of vector mesons in an electron-ion collider. See text for details.

vector meson. We use these maxima to define a geometrical saturation scale and find that it grows linearly with energy as a function of the scale of the process, as reported in Fig 8. The rest of this contribution is organized as follows. A brief description of the formalism is presented in Sec. II. The model predictions are presented and compared to the available data in Sec. III. Section IV introduces the geometrical saturation scale. We close with a brief summary and outlook in Sec. V.

II. DESCRIPTION OF THE FORMALISM

A. The photon-proton scattering amplitude

The diffractive production of a vector meson when a virtual photon interacts with a proton can be well described within the color dipole picture [18,19]. In this case, the scattering amplitude takes the following form (for a detailed derivation see e.g., [7]),

$$\mathcal{A}_{T,L}(x,Q^2,\vec{\Delta}) = i\int \mathrm{d}\vec{r}\int_0^1 \frac{\mathrm{d}z}{4\pi}\int \mathrm{d}\vec{b}\,|\Psi_{\mathrm{V}}^{*}\Psi_{\gamma^*}|_{T,L} \times \exp\left[-i(\vec{b}-(1-z)\vec{r})\vec{\Delta}\right]\frac{\mathrm{d}\sigma_{q\bar{q}}}{\mathrm{d}\vec{b}}, \quad (1)$$

where the subscripts T and L denote the contribution from the transversally, respectively longitudinally, polarized virtual photon. Ψ_{V} is the wave function of the vector meson, Ψ_{γ^*} is the wave function of a virtual photon, which fluctuates into a quark-antiquark dipole, $\vec{r}$ is the transverse size of the color dipole, z is the fraction of the photon longitudinal momentum carried by the quark, $\vec{b}$ is the impact parameter and $\vec{\Delta}^2 \equiv -t$. The Bjorken-x of the exchanged pomeron is, under the assumption of large $W_{\gamma\mathrm{p}}$, given by

$$x = \frac{Q^2+M^2}{W_{\gamma\mathrm{p}}^2+Q^2}, \quad (2)$$

with M being the invariant mass of the given vector meson. Finally, $\mathrm{d}\sigma_{q\bar{q}}/\mathrm{d}\vec{b}$ is the cross section for the interaction of the color dipole and the target.

In this formalism, the exclusive cross section to produce the vector meson V is given by

$$\left.\frac{\mathrm{d}\sigma^{\gamma^* p\to \mathrm{V}p}}{\mathrm{d}|t|}\right|_{T,L} = \frac{(R_g^{T,L})^2}{16\pi}|\langle\mathcal{A}_{T,L}\rangle|^2, \quad (3)$$

while the cross section where the proton dissociates into a system Y is

$$\left.\frac{\mathrm{d}\sigma^{\gamma^* p\to \mathrm{V}Y}}{\mathrm{d}|t|}\right|_{T,L} = \frac{(R_g^{T,L})^2}{16\pi}(\langle|\mathcal{A}_{T,L}|^2\rangle - |\langle\mathcal{A}_{T,L}\rangle|^2). \quad (4)$$

In both cases, the total cross section is given by the sum of the transverse and the longitudinal contributions. The factor $R_g^{T,L}$ is called the skewedness correction [20] and takes into account that there are two values of x involved in the interaction but only one appears in Eq. (1).

There are two ingredients of Eq. (1) that need to be modeled: the wave function to create a vector meson out of the quark-antiquark dipole and the cross section for the interaction of the color dipole and the target. They are discussed in the following.

B. Wave functions of vector meson

The wave functions of vector mesons are modeled assuming that the vector meson is predominantly a $q\bar{q}$ pair with the same polarization structure as the photon. The overlap of the photon-meson wave functions in Eq. (1) is given as

$$|\Psi_{\mathrm{V}}^{*}\Psi_{\gamma^*}|_T = \hat{e}_f e\frac{N_C}{\pi z(1-z)}[m_f^2 K_0(\epsilon r)\phi_T(r,z) - (z^2+(1-z)^2)\epsilon K_1(\epsilon r)\partial_r\phi_T(r,z)], \quad (5)$$

and

$$|\Psi_V^*\Psi_{\gamma^*}|_L = \hat{e}_f e \frac{N_C}{\pi} 2Qz(1-z)K_0(\epsilon r)\left[M\phi_L(r,z) + \delta\frac{m_f^2 - \nabla_r^2}{Mz(1-z)}\phi_L(r,z)\right], \tag{6}$$

where $r \equiv |\vec{r}|$, N_C is the number of colors, the (effective) mass of the given flavor is m_f, and an effective charge is denoted by $\hat{e}_f$. The parameter δ is a switch to include or not the corresponding term; we set it equal to one, which corresponds to the boosted Gaussian model [21–23]. K_i are Bessel functions and

$$\epsilon = z(1-z)Q^2 + m_f^2. \tag{7}$$

The scalar part $\phi_{T,L}$ of the wave function is, in general, model dependent. In the boosted Gaussian model the scalar part is described by the Gaussian distribution

$$\phi_{T,L}(r,z) = N_{T,L}z(1-z)\exp\left(-\frac{m_f^2R^2}{8z(1-z)} - \frac{2z(1-z)r^2}{R^2} + \frac{m_f^2R^2}{2}\right). \tag{8}$$

The parameters of the model are fixed using a normalization condition and the measured electronic decay width (see, e.g., [7]). For the first excited state 2S, the scalar wave function has the form

$$\phi_{T,L}^{2S}(r,z) = \Phi_{T,L}(r,z)\left(1 + \alpha_{2S}\left(2 + \frac{m_f^2R^2}{4z(1-z)} - \frac{4z(1-z)r^2}{R^2} - m_f^2R^2\right)\right). \tag{9}$$

The condition that the 1S and 2S states are orthogonal, fixes the extra parameter α_{2S}.

We have recomputed the values of the parameters for the wave functions of all vector mesons discussed in the following to match them to the measurements gathered in the PDG of 2016 [24]. The parameter values are reported in Table I.

C. Dipole-target cross section

The cross section for the interaction between the color dipole with the proton target is related, via the optical theorem, to the imaginary part of the dipole-proton amplitude $N(x,\vec{r},\vec{b})$:

$$\frac{d\sigma_{q\bar{q}}}{d\vec{b}} = 2N(x,\vec{r},\vec{b}). \tag{10}$$

In order to separate the effects of fluctuations of the proton structure in the transverse plane from the energy dependence of the cross section we proposed in [15] to use the factorized form

$$\frac{d\sigma_{q\bar{q}}}{d\vec{b}} = \sigma_0 N(x,r)T_p(\vec{b}), \tag{11}$$

where $T_p(\vec{b})$ decribes the proton profile in the impact-parameter plane and σ_0 is a normalization parameter, which we fixed to $\sigma_0 = 4\pi B_p$. The interpretation of B_p is discussed below.

The dipole amplitude $N(x,r)$ can be obtained from various parameterizations (for an overview see e.g., [7]) or as the solution of the Balitsky-Kovchegov evolution equation [25,26]. To keep the model as simple as possible, we have chosen the form of the dipole amplitude $N(x,r)$ given by the Golec-Biernat and Wusthoff model [27,28],

$$N(x,r) = \left[1 - \exp\left(-\frac{r^2Q_s^2(x)}{4}\right)\right], \tag{12}$$

where $Q_s(x)$ is the so-called saturation scale, which in this model is given by

TABLE I. Parameters for vector meson (V) wave functions: mass of the vector meson M, effective mass of the given flavor m_f, effective charge $\hat{e}_f$, scalar part parameters N_T, N_L, R^2 and α_{2S}, fixed with the values reported in the 2016 PDG [24].

V	M[GeV]	m_f[GeV]	$\hat{e}_f[-]$	$N_T[-]$	$N_L[-]$	R^2[GeV^{-2}]	$\alpha_{2S}[-]$
ρ^0	0.775 260	0.14	$1/\sqrt{2}$	0.909	0.853	12.95	⋯
ϕ	1.019 461	0.14	1/3	0.918	0.823	11.3	⋯
J/ψ	3.096 90	1.4	2/3	0.582	0.578	2.24	⋯
ψ(2S)	3.686 097	1.4	2/3	0.666	0.658	3.705	−0.6225
$\Upsilon(1S)$	9.460 30	4.2	1/3	0.478	0.478	0.585	⋯
$\Upsilon(2S)$	10.023 26	4.2	1/3	0.614	0.610	0.831	−0.568

$$Q_s^2(x) = Q_0^2\left(\frac{x_0}{x}\right)^{\lambda}. \quad (13)$$

Since the proton is a quantum object, its structure changes from interaction to interaction. To incorporate this effect we use a model of the proton as constituted by hot spots (hs), which represent regions of high gluon density. The positions of these hot spots in the transverse plane fluctuate event-by-event and are described by the proton profile function $T_p(\vec{b})$, which is defined as

$$T_p(\vec{b}) = \frac{1}{N_{\rm hs}}\sum_{i=1}^{N_{\rm hs}} T_{\rm hs}(\vec{b}-\vec{b}_i), \quad (14)$$

where each hot spot is defined as

$$T_{\rm hs}(\vec{b}-\vec{b}_i) = \frac{1}{2\pi B_{\rm hs}}\exp\left(-\frac{(\vec{b}-\vec{b}_i)^2}{2B_{\rm hs}}\right). \quad (15)$$

Each vector $\vec{b}_i$ is obtained from a two-dimensional Gaussian distribution with width B_p and centered at (0,0). Thus, the parameters B_p and $B_{\rm hs}$ can be interpreted as half of the average of the squared radius of the proton and of the hot spot, respectively. In this sense $\sigma_0 = 4\pi B_p$ is a measure of the overall transverse area of the proton.

The key feature of our model is the evolution of the number of hot spots with energy. $N_{\rm hs}$ is a random number drawn from a zero-truncated Poisson distribution, where the Poisson distribution has a mean value,

$$\langle N_{\rm hs}(x)\rangle = p_0 x^{p_1}(1+p_2\sqrt{x}), \quad (16)$$

where p_0, p_1 and p_2 are parameters.

The values of all parameters of our model were fixed in earlier publications [15–17] using J/ψ data from photoproduction at HERA. The values are listed here for completeness: $B_p = 4.7\,\mathrm{GeV}^{-2}$, $B_{\rm hs} = 0.8\,\mathrm{GeV}^{-2}$, $p_0 = 0.011$, $p_1 = -0.58$, $p_2 = 300$, $\lambda = 0.21$, $x_0 = 2\times10^{-4}$ and $Q_0 = 1$ GeV. In order to describe the normalization of the photoproduction of ρ and of ϕ we set $B_p = 8\ \mathrm{GeV}^{-2}$ as done in [17] and consistent with the observations of the H1 Collaboration [29]. For the case of electroproduction discussed below, we set $B_p = 4.7\ \mathrm{GeV}^{-2}$ for all vector mesons.

III. PREDICTIONS AND COMPARISON WITH EXPERIMENTAL DATA

Using the model described above we predict the energy dependence of the exclusive and dissociative production of vector mesons off a proton target for ρ^0, ϕ, J/ψ, $\psi(2S)$, $\Upsilon(1S)$ and $\Upsilon(2S)$ at different virtualities of the exchanged photon. We compare our predictions with data when available. For completeness, we also show the predictions for photoproduction that were presented in [17].

The predictions for the $W_{\gamma p}$ dependence of the exclusive and dissociative cross section of the ρ^0 vector meson are presented in Fig. 2. Predictions are compared with H1 [29–31] and ZEUS data [32,33] for several values of Q^2 and also to the preliminary CMS data [34] for photoproduction in p–Pb collisions at the center-of-mass energy $\sqrt{s} = 5.02$ TeV. The predictions for electroproduction, both exclusive and dissociative, give a very good description of the available data covering virtualities from 2.4 to 35.6 GeV^2. Recently, the H1 Collaboration released preliminary data (not shown in the figure) on the energy dependence of ρ^0 dissociative photoproduction. The predictions of our model are consistent with these preliminary data, although a definitive comparison can only be done after the measurement is published in its final form.

The predictions for the energy dependence of the exclusive and dissociative photo- and electroproduction cross sections of the ϕ vector meson are compared with H1

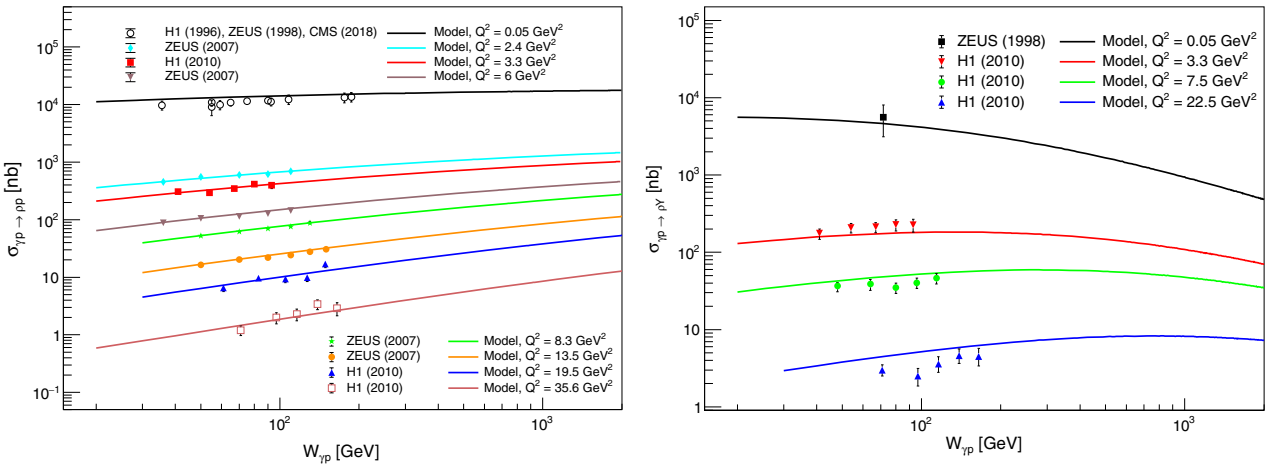

FIG. 2. Comparison of the model predictions (solid lines) with HERA [29–33] and CMS data [34] for the $W_{\gamma p}$ dependence of the exclusive (left) and dissociative (right) photo- and electroproduction cross section of a ρ^0 meson.

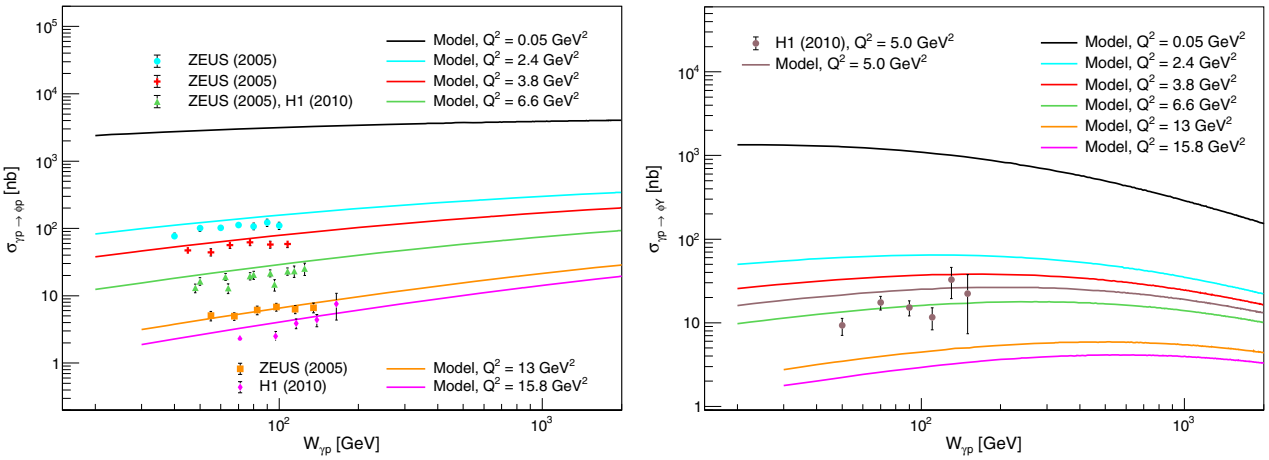

FIG. 3. Comparison of the model predictions (solid lines) with HERA data from H1 [29,31] and ZEUS [35] for the $W_{\gamma p}$ dependence of the exclusive (left) and dissociative (right) photo- and electroproduction cross section of a ϕ meson.

[29,31] and ZEUS data [35] in Fig. 3. The description of the electroproduction data is satisfactory; however, it is not as good as for the case of the ρ^0 meson.

The photoproduction of J/ψ has already been studied in [15,17]. Here we show the same comparison of H1 [36] and ALICE p–Pb data [37] with the model predictions in Fig. 4. Additionally, recent ALICE data [38] are included. These new photoproduction measurements are also correctly described by the predictions. Electroproduction data from H1 [39] are also shown in the figure. The predictions for the exclusive and dissociative cross sections show a good agreement with all these data.

The comparison between the predictions for the exclusive and dissociative photoproduction cross section for the $\Upsilon(1S)$ vector meson and data has been presented in [17]. We present it here again in Fig. 5 to provide a comparison with the electroproduction predictions which are the main topic of this work. The exclusive photoproduction cross section is compared with H1 [40] and ZEUS [41] data from HERA. It is also compared with LHCb data taken in proton-proton collisions at $\sqrt{s} = 7$ TeV and $\sqrt{s} = 8$ TeV at the LHC [42]. The last set of data we compare our predictions with was measured by CMS in p–Pb collisions at $\sqrt{s} = 5.02$ TeV [43]. The data are correctly described by the predictions, although the current uncertainty of the measurement does not allow us to extract strong conclusions regarding the agreement between data and the model. Currently, to our knowledge, there are no electroproduction data for the exclusive or the dissociative process. We expect these measurements to be performed at future electron-ion colliders.

To complete the set of our predictions we present predictions for the excited states $\psi(2S)$ and $\Upsilon(2S)$ in Figs. 6 and 7. Currently, there are no direct data for these

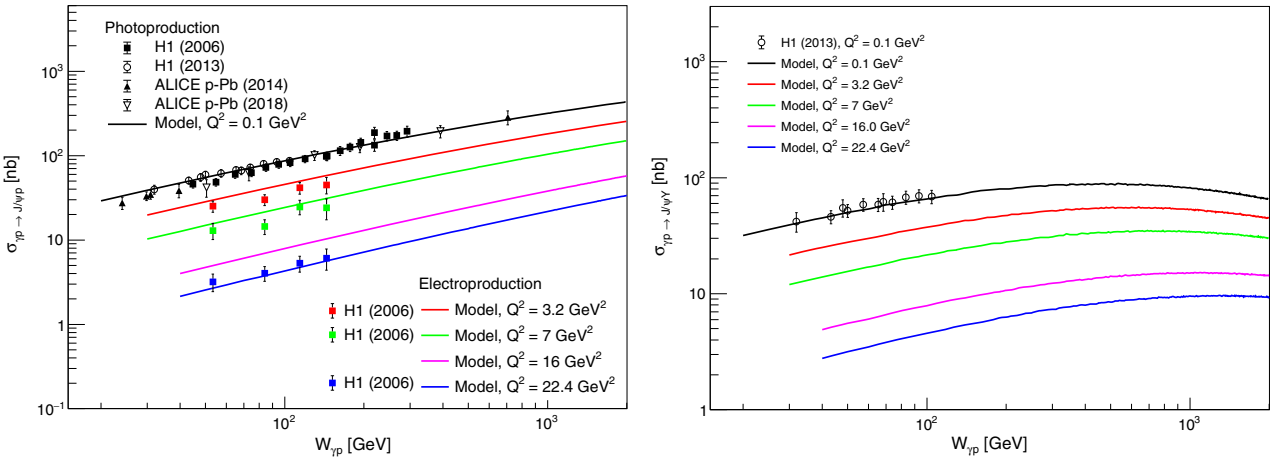

FIG. 4. Comparison of the model predictions (solid lines) with H1 [36,39] and ALICE data [37,38] for the $W_{\gamma p}$ dependence of the exclusive (left) and dissociative (right) photo- and electroproduction cross section of a J/ψ meson.

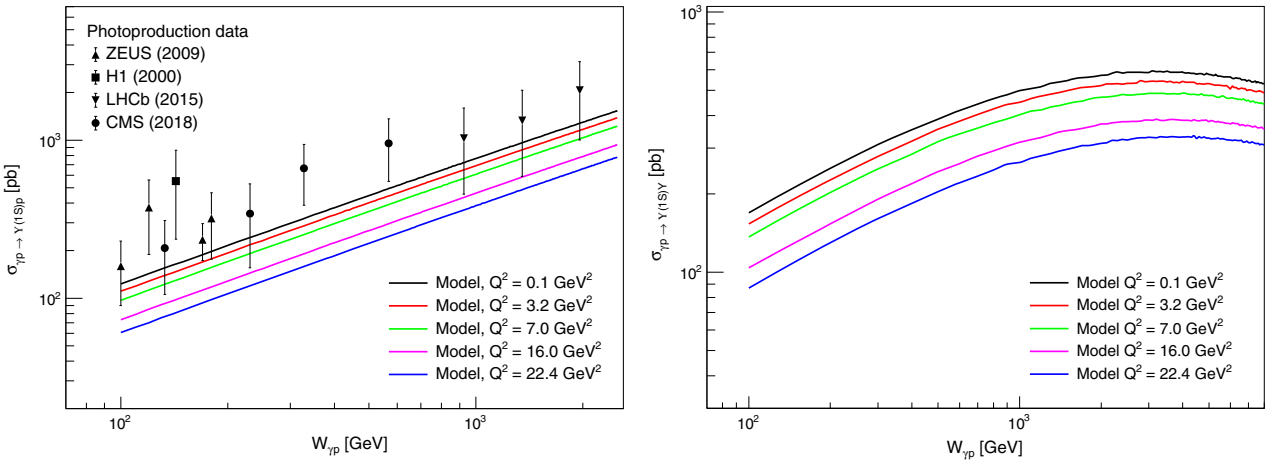

FIG. 5. Comparison of the model predictions (solid lines) with H1 [40], ZEUS [41], LHCb [42] and CMS data [43] for the $W_{\gamma p}$ dependence of the exclusive (left) and dissociative (right) photo- and electroproduction cross section of a $\Upsilon(1S)$ meson.

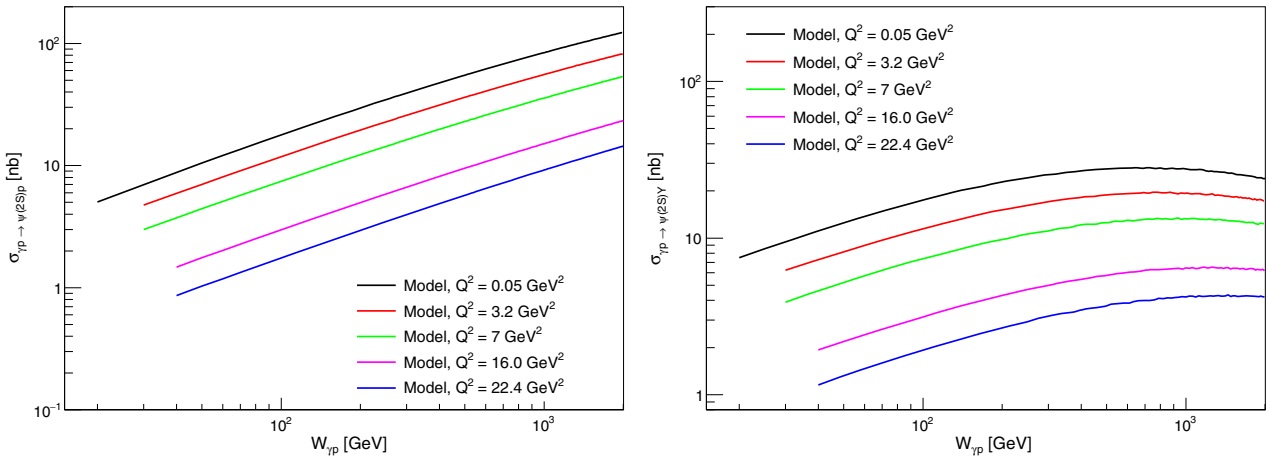

FIG. 6. Model predictions (solid lines) for the $W_{\gamma p}$ dependence of the exclusive (left) and dissociative (right) photo- and electroproduction cross section of a $\psi(2S)$ meson.

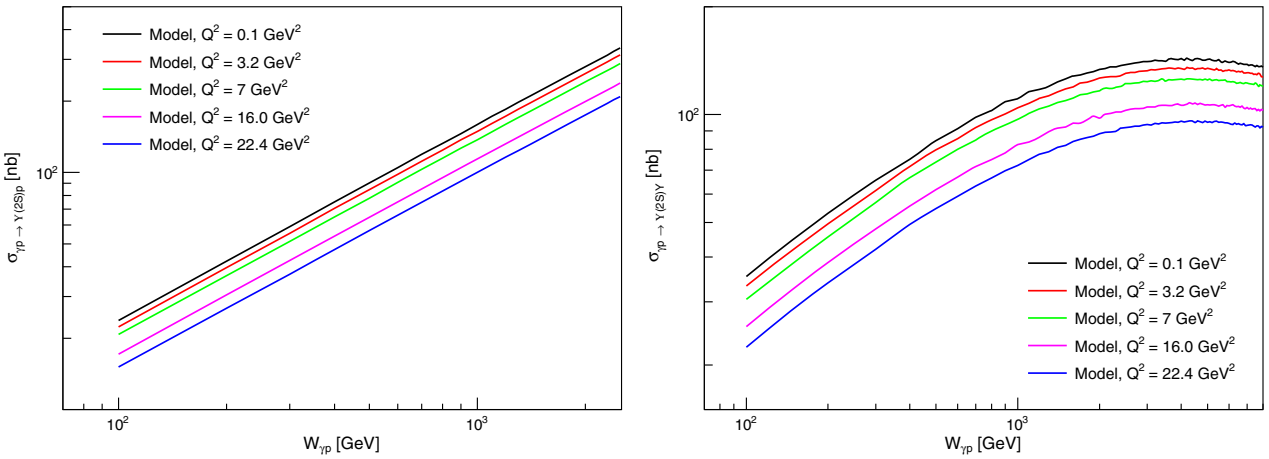

FIG. 7. Model predictions (solid lines) for the $W_{\gamma p}$ dependence of the exclusive (left) and dissociative (right) photo- and electroproduction cross section of a $\Upsilon(2S)$ meson.

particles, but there are photoproduction data from H1 [44] and electroproduction data at $Q^2 = 16$ GeV^2 from ZEUS [45] for the ratio of the exclusive production of $\psi(2S)$ to that of J/ψ. Our predictions describe correctly the measured ratios, although, as in the case of the $\Upsilon(1S)$, the current uncertainty of the measurement does not allow us to extract strong conclusions regarding the agreement between data and the model.

In summary, there is a good agreement between all existing data for the exclusive and the dissociative photo- and electoproduction of vector mesons and the predictions of our model.

IV. GEOMETRIC SATURATION SCALE

A. Introduction of the geometric saturation scale

As already noticed in [15] for the case of J/ψ photoproduction and confirmed in [17] for the photoproduction of ρ^0 and $\Upsilon(1S)$, the behavior of the dissociative cross section as a function of the photon-proton center-of-mass energy is quite striking. At low energies, the cross section rises with $W_{\gamma p}$ to reach a maximum, after which it decreases steeply. The same behavior is observed for the dissociative electroproduction of vector mesons. Interestingly, the position of the maximum depends not only on the mass of the vector meson, but also on the virtuality of the exchanged photon.

The interpretation of this behavior is given by the form of the cross section shown in Eq. (4). The dissociative production measures the variance over the different configurations into which the structure of the proton can fluctuate. In our model, this is given by the different geometrical placements of the hot spots in the impact-parameter plane. As the energy $W_{\gamma p}$ increases, so it does the number of hot spots inside the proton as shown in Eq. (16). As the hot spots have all the same transversal area, the more hot spots there are, the more the proton area is filled. At some point, all the possible configurations start to look alike, because all of them start filling all the available area in the proton and overlap in a process reminiscent of percolation [46]. From this energy onwards the variance over configurations steeply decreases. The maximum of the dissociative cross section defines a well defined energy at a well defined scale. We call this point the *geometric saturation scale* (GSS) and in the following study some of its properties.

B. Energy dependence of the geometric saturation scale

For each of the vector mesons and for each of the virtualities we determine the energy $W_{\rm GSS}$ at which the maximum is found. As the predictions are based on a random process, the value at the maximum may fluctuate a bit, so we chose a region containing the 1% largest values of the cross section to determine the position of the maximum along with an estimation of the associated uncertainty.

Figure 8 shows in the left panel the position of the maximum as a function of $Q^2 + M^2$, which is a measure of the scale of the process. The behavior seems to be linear, so we fitted the extracted maxima to the functional form

$$W_{\rm GSS} = a_0 + a_1(Q^2 + M^2). \tag{17}$$

For the fit we considered only points with $Q^2 + M^2$ larger than 2 GeV^2. The fit is good. The χ^2 per degree-of-freedom is 0.41, the small value reflecting the large assigned uncertainty on the position of the maxima. The parameter

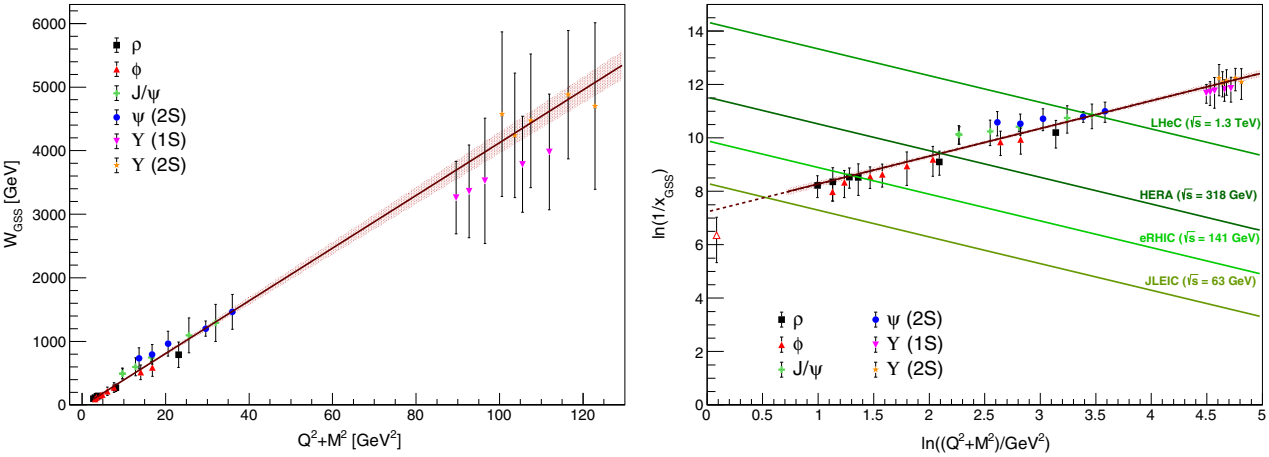

FIG. 8. (Left) Position of the maxima of the dissociative cross sections (markers) and an estimation of the related uncertainty (bars) as a function of $Q^2 + M^2$. The line is a fit to the line defined in Eq. (17) and the band represents the one sigma contour. (Right) the same data as in the left panel, but translating $W_{\rm GSS}$ into $x_{\rm GSS}$ and plotting them in logarithmic variables. The red line is the fit to Eq. (18) The diagonal lines represent the kinematic reach of some of the proposed future electron-ion colliders. See text for details.

values are $a_0 = -21 \pm 11$ GeV and the slope that is obtained is $a_1 = 41.5 \pm 1.8$ GeV^{-1}.

Using Eq. (2) we can translate W_{GSS} into x_{GSS}. The result is shown in the right panel of Fig. 8. The behavior is also linear in the logarithmic variables so we have fit the predictions to

$$\ln(1/x_{\mathrm{GSS}}) = c_0 + c_1 \ln((Q^2 + M^2)/\mathrm{GeV}^2). \quad (18)$$

We found $c_0 = 7.2 \pm 0.2$ and $c_1 = 1.04 \pm 0.06$. The same figure shows the kinematic limit of some of the proposed future electron-ion colliders. This limit is obtained from

$$xys = Q^2, \quad (19)$$

where the inelasticity of the collision is set to $y = 1$ and the center-of-mass energies $\sqrt{s}$ of the accelerators are obtained from the energies of the proton, E_p, and electron, E_e, beams taken from Table I of [10]: $E_e = 10$ GeV, $E_p = 100$ GeV for JLEIC; $E_e = 18$ GeV, $E_p = 275$ GeV for eRHIC; $E_e = 27.5$ GeV, $E_p = 920$ GeV for HERA; and $E_e = 60$ GeV, $E_p = 7$ TeV for LHeC.

It is interesting to notice that even for the collider with the lower energy, one could measure this linear behavior using electroproduction of ρ^0 and of ϕ vector mesons at relatively small virtualities, but in all cases at scales $Q^2 + M^2$ above 1 GeV^2. The detectors at the JLEIC and eRHIC are still under development, but the envisaged capabilities would allow the measurement of ρ^0 and ϕ as discussed in detail in [10]. To investigate the positions of the maxima for J/ψ one needs the LHC and the LHeC for photo- and electroproduction cases, respectively. The positions of the maxima for the Upsilon states seems to be out of reach even for the LHeC.

V. SUMMARY AND OUTLOOK

Using the energy-dependent hot spot model, we have presented predictions for the exclusive and dissociative electroproduction of vector mesons off proton targets. We studied the production of ρ^0, ϕ, J/ψ, $\psi(2S)$, $\Upsilon(1S)$ and $\Upsilon(2S)$ states. We found that the dissociative cross section as a function of $W_{\gamma p}$ presents a maximum and have used this maximum to define a geometrical saturation scale. We found that the energy evolution of this scale is linear in $Q^2 + M^2$ and that this behavior can be studied at the planned JLEIC, eRHIC and LHeC electron-ion colliders.

To be able to perform such measurements, the detectors would have to be instrumented in the forward rapidity regions in order to tag the presence of the products from the dissociative state. Such a technique has been used at HERA in the past; it is also used nowadays at the LHC to reject the dissociative events when measuring the exclusive production channel, so it seems to be feasible if planned in advance.

Mapping the energy evolution of the geometric saturation scale provides an extra handle to investigate quantitatively the high-energy limit of QCD and to study the phenomenon of gluon saturation in the proton.

ACKNOWLEDGMENTS

We thank Victor Gonçalves for useful discussions. This work has been partially supported by the following Grants No. 17-04505S of the Czech Science Foundation (GAČR), COST Action CA15213 THOR, No. LTC17038 of the INTER-EXCELLENCE program at the Ministry of Education, and Youth and Sports of the Czech Republic and the European Regional Development Fund-Project "Brookhaven National Laboratory - participation of the Czech Republic" (No. CZ.02.1.01/0.0/0.0/16 013/0001569).

[1] H. Abramowicz *et al.* (ZEUS and H1 Collaborations), Eur. Phys. J. C **75**, 580 (2015).
[2] F. Gelis, E. Iancu, J. Jalilian-Marian, and R. Venugopalan, Annu. Rev. Nucl. Part. Sci. **60**, 463 (2010).
[3] A. Accardi *et al.*, Eur. Phys. J. A **52**, 268 (2016).
[4] J. Abelleira Fernandez *et al.* (LHeC Study Group), J. Phys. G **39**, 075001 (2012).
[5] P. Newman and M. Wing, Rev. Mod. Phys. **86**, 1037 (2014).
[6] J. G. Contreras and J. D. Tapia Takaki, Int. J. Mod. Phys. A **30**, 1542012 (2015).
[7] H. Kowalski, L. Motyka, and G. Watt, Phys. Rev. D **74**, 074016 (2006).
[8] N. Armesto and A. H. Rezaeian, Phys. Rev. D **90**, 054003 (2014).
[9] V. P. Goncalves, B. D. Moreira, and F. S. Navarra, Phys. Rev. C **90**, 015203 (2014).
[10] M. Lomnitz and S. Klein, Phys. Rev. C **99**, 015203 (2019).
[11] M. L. Good and W. D. Walker, Phys. Rev. **120**, 1857 (1960).
[12] H. I. Miettinen and J. Pumplin, Phys. Rev. D **18**, 1696 (1978).
[13] H. Mäntysaari and B. Schenke, Phys. Rev. Lett. **117**, 052301 (2016).
[14] H. Mäntysaari and B. Schenke, Phys. Rev. D **94**, 034042 (2016).
[15] J. Cepila, J. G. Contreras, and J. D. Tapia Takaki, Phys. Lett. B **766**, 186 (2017).
[16] J. Cepila, J. G. Contreras, and M. Krelina, Phys. Rev. C **97**, 024901 (2018).

[17] J. Cepila, J. G. Contreras, M. Krelina, and J. D. Tapia Takaki, Nucl. Phys. **B934**, 330 (2018).
[18] A. H. Mueller, Nucl. Phys. **B415**, 373 (1994).
[19] A. H. Mueller and B. Patel, Nucl. Phys. **B425**, 471 (1994).
[20] A. G. Shuvaev, K. J. Golec-Biernat, A. D. Martin, and M. G. Ryskin, Phys. Rev. D **60**, 014015 (1999).
[21] J. Nemchik, N. N. Nikolaev, and B. G. Zakharov, Phys. Lett. B **341**, 228 (1994).
[22] J. Nemchik, N. N. Nikolaev, E. Predazzi, and B. G. Zakharov, Z. Phys. C **75**, 71 (1997).
[23] J. R. Forshaw, R. Sandapen, and G. Shaw, Phys. Rev. D **69**, 094013 (2004).
[24] C. Patrignani *et al.* (Particle Data Group), Chin. Phys. C **40**, 100001 (2016).
[25] I. Balitsky, Nucl. Phys. **B463**, 99 (1996).
[26] Y. V. Kovchegov, Phys. Rev. D **60**, 034008 (1999).
[27] K. J. Golec-Biernat and M. Wusthoff, Phys. Rev. D **59**, 014017 (1998).
[28] K. J. Golec-Biernat and M. Wusthoff, Phys. Rev. D **60**, 114023 (1999).
[29] F. D. Aaron *et al.* (H1 Collaboration), J. High Energy Phys. 05 (2010) 032.
[30] S. Aid *et al.* (H1 Collaboration), Nucl. Phys. **B463**, 3 (1996).
[31] C. Adloff *et al.* (H1 Collaboration), Z. Phys. C **75**, 607 (1997).
[32] J. Breitweg *et al.* (ZEUS Collaboration), Eur. Phys. J. C **2**, 247 (1998).
[33] S. Chekanov *et al.* (ZEUS Collaboration), PMC Phys. A **1**, 6 (2007).
[34] A. M. Sirunyan *et al.* (CMS Collaboration), Technical Report No. CMS-PAS-FSQ-16-007, CERN, Geneva, 2018.
[35] S. Chekanov *et al.* (ZEUS Collaboration), Nucl. Phys. **B718**, 3 (2005).
[36] C. Alexa *et al.* (H1 Collaboration), Eur. Phys. J. C **73**, 2466 (2013).
[37] B. B. Abelev *et al.* (ALICE Collaboration), Phys. Rev. Lett. **113**, 232504 (2014).
[38] S. Acharya *et al.* (ALICE Collaboration), arXiv:1809 .03235.
[39] A. Aktas *et al.* (H1 Collaboration), Eur. Phys. J. C **46**, 585 (2006).
[40] C. Adloff *et al.* (H1 Collaboration), Phys. Lett. B **483**, 23 (2000).
[41] S. Chekanov *et al.* (ZEUS Collaboration), Phys. Lett. B **680**, 4 (2009).
[42] R. Aaij *et al.* (LHCb Collaboration), J. High Energy Phys. 09 (2015) 084.
[43] A. M. Sirunyan *et al.* (CMS Collaboration), arXiv: 1809.11080 Eur. Phys. J. (to be published).
[44] C. Adloff *et al.* (H1 Collaboration), Phys. Lett. B **541**, 251 (2002).
[45] H. Abramowicz *et al.* (ZEUS Collaboration), Nucl. Phys. **B909**, 934 (2016).
[46] N. Armesto, M. A. Braun, E. G. Ferreiro, and C. Pajares, Phys. Rev. Lett. **77**, 3736 (1996).

Solution to the Balitsky-Kovchegov equation with the collinearly improved kernel including impact-parameter dependence

D. Bendova, J. Cepila, J. G. Contreras, and M. Matas

Faculty of Nuclear Sciences and Physical Engineering, Czech Technical University in Prague, 115 19 Prah, Czech Republic

(Received 5 August 2019; published 16 September 2019)

The solution to the impact-parameter dependent Balitsky-Kovchegov equation with the collinearly improved kernel is studied in detail. The solution does not present the phenomenon of Coulomb tails at large impact parameters that have affected previous studies. The origin of this behavior is explored numerically. It is found to be linked to the fact that this kernel suppresses large daughter dipoles. Solutions based on a physics motivated form of the initial condition are used to compute predictions for structure functions of the proton and the exclusive photoproduction and electroproduction of vector mesons. A reasonable agreement is found when comparing to HERA and LHC data.

DOI: 10.1103/PhysRevD.100.054015

I. INTRODUCTION

Evolution equations are powerful tools to study the high-energy, equivalently, small-x limit of quantum chromodynamics (QCD) [1–3]. The availability of quality data from HERA [4] and the LHC [5] as well as the need for reliable phenomenology for the proposal of new electron-ion facilities [6,7] have given an extra impulse to the development of these tools.

In this work, the emphasis is placed on the Balitsky-Kovchegov (BK) evolution equation derived independently in the operator-product-expansion formalism by Balitsky [8], and by Kovchegov [9,10] within the color dipole approach [11–13]. It corresponds to the large-number-of-colors limit of the Jalilian-Marian-Iancu-McLerran-Weigert-Leonidov-Kovner (JIMWLK) evolution equations [14–19]. The BK equation describes the evolution with rapidity, Y, of the dipole-target scattering amplitude, $N(\vec{r},\vec{b},Y)$, where $\vec{r}$ is the transverse size of the dipole and $\vec{b}$ the impact parameter of the interaction.

Soon after its introduction, the kernel of the leading order BK equation was modified to include corrections that take into account the running of the coupling constant [20–23]. The resulting equation, referred to as rcBK below, when combined with appropriate initial conditions—embodying nonperturbative properties of the hadronic targets—and disregarding the impact-parameter dependence, produces solutions that have been successfully used to describe a wide variety of phenomena. In particular, the structure function data of the proton as measured at HERA was successfully described [24–27]. A few other applications of these solutions are, for example, gluon production in heavy-ion collisions [28], single particle [29] and J/ψ production in pp and pA collisions [30], dihadron correlations in p-Pb interactions [31] and even the flux of atmospheric neutrinos [32,33].

As already mentioned, these comparisons of rcBK-based predictions to data disregarded the impact-parameter dependence of the dipole amplitude. The reason is that earlier studies of solutions including the impact parameter found that the amplitude developed a powerlike dependence on $b \equiv |\vec{b}|$, the so-called Coulomb tails, which generate an unphysical growth of the cross section [34]. Nonetheless attempts were made to modify the kernel to solve this problem, for example, by adding an *ad hoc* cutoff for large sizes of the daughter dipoles [35]. The solutions found had no more Coulomb tails, but needed an extra, so-called *soft*, contribution to be able to describe HERA data on structure functions [36]. (A similar conclusion also holds for the solutions of the impact-parameter dependent JIMWLK equation [37].) Nonetheless, this approach did a good job when confronted with HERA data on exclusive vector meson production [38].

Recently, the kernel of the leading order equation has been improved by including the resummation of all double collinear logarithms [39] as well as two classes of single logarithmic corrections [40]. (See also early work on this direction in the context of the Balitsky-Fadin-Kuraev-Lipatov (BFKL) equation in [41].) Using this kernel and disregarding the dependence on the impact parameter, it was also possible to obtain a good description of HERA

data on the structure function of the proton. Finally, in the rapid communication [42], we have demonstrated that solutions of the BK equation with the collinearly improved kernel and an appropriate initial condition describe correctly the HERA data on structure functions and the t dependence of the exclusive photoproduction of J/ψ at one energy without the need of any additional *ad hoc* parameter or correction.

In this contribution the studies reported in [42] are extended to discuss in depth the behavior of the collinearly improved kernel and of the solutions of the corresponding BK equation, comparing them to the rcBK case. In addition, more details on the comparison to HERA structure function data are presented, and comparison of our predictions to relevant HERA and LHC data on exclusive vector meson photoproduction and electroproduction is provided. In all cases, the agreement between model and measurements is satisfactory.

The rest of this contribution is organized as follows: In Sec. II the formalism used throughout this work is reviewed. In Sec. III the technical details to solve the collinearly improved impact-parameter dependent BK equation are addressed. In Sec. IV the origin of the suppression at large impact parameters is discussed, the behavior of the solution is contrasted with solutions of the rcBK case, and the shape of the amplitude is shown at different values of rapidity, dipole size and impact parameter. In Secs. V and VI our predictions are confronted with structure function data measured at HERA, and to data for cross sections of exclusive photoproduction and electroproduction of ϕ, J/ψ, $\psi(2S)$, and $\Upsilon(1S)$ vector mesons measured both at HERA and at the LHC, respectively. Section VII contains a brief summary of our findings and presents our conclusions.

II. REVIEW OF THE FORMALISM

A. The Balitsky-Kovchegov equation

The BK evolution equation reads [21,22]

$$\frac{\partial N(\vec{r},\vec{b},Y)}{\partial Y} = \int d\vec{r}_1 K(r,r_1,r_2)(N(\vec{r}_1,\vec{b}_1,Y) + N(\vec{r}_2,\vec{b}_2,Y) - N(\vec{r},\vec{b},Y) - N(\vec{r}_1,\vec{b}_1,Y)N(\vec{r}_2,\vec{b}_2,Y)), \quad (1)$$

where $r \equiv |\vec{r}|$, $r_1 \equiv |\vec{r}_1|$, and $r_2 \equiv |\vec{r}_2| \equiv |\vec{r} - \vec{r}_1|$ are the sizes of the original dipole and of the two daughter dipoles, respectively. Note that these are two-dimensional vectors in the same plane as the impact parameter. The magnitudes of the corresponding impact parameters are $b \equiv |\vec{b}|$, $b_1 \equiv |\vec{b}_1|$, $b_2 \equiv |\vec{b}_2|$. The kernel $K(r,r_1,r_2)$ is discussed below.

In this work, the solution to the BK equation is obtained under the assumption that the scattering amplitude $N(\vec{r},\vec{b},Y)$ depends solely on the sizes of the dipoles and of the impact parameter vectors. In practice, this means to solve the equation

$$\frac{\partial N(r,b,Y)}{\partial Y} = \int d\vec{r}_1 K(r,r_1,r_2)(N(r_1,b_1,Y) + N(r_2,b_2Y) - N(r,b,Y) - N(r_1,b_1,Y)N(r_2,b_2,Y)), \quad (2)$$

subjected to the condition that the angle between $\vec{r}$ and $\vec{b}$ is fixed. We chose to fix this angle at zero, meaning that these vectors are parallel.

B. Kernels of the Balitsky-Kovchegov equation

Several functional forms for the kernel of the BK equation have been proposed. The ones that are mentioned in this work are presented in the following.

The leading order kernel is given by

$$K_{\mathrm{LO}}(r,r_1,r_2) = \frac{\alpha_s^{\mathrm{nr}}}{2\pi}\frac{r^2}{r_1^2 r_2^2}, \quad (3)$$

where the nonrunning coupling, α_s^{nr}, is fixed to a constant value.

The running coupling kernel $K_{\mathrm{rc}}(r,r_1,r_2)$ reads [21]

$$K_{\mathrm{rc}}(r,r_1,r_2) = \frac{N_c\alpha_s(r^2)}{2\pi^2}\left(\frac{r^2}{r_1^2 r_2^2} + \frac{1}{r_1^2}\left(\frac{\alpha_s(r_1^2)}{\alpha_s(r_2^2)} - 1\right) + \frac{1}{r_2^2}\left(\frac{\alpha_s(r_2^2)}{\alpha_s(r_1^2)} - 1\right)\right), \quad (4)$$

where N_c is the number of colors and α_s is the running coupling, which is further discussed in Sec. II C.

The running coupling kernel with a cutoff to tame the Coulomb tails generated by the evolution in the impact parameter is given by [36]

$$K_{\mathrm{rc}}^{\mathrm{bdep}}(r,r_1,r_2) = K_{\mathrm{rc}}(r,r_1,r_2)\Theta\left(\frac{1}{m^2} - r_1^2\right)\Theta\left(\frac{1}{m^2} - r_2^2\right), \quad (5)$$

where Θ is the Heaviside function and m a parameter to limit the size of daughter dipoles.

Finally, the collinearly improved kernel is [40]

$$K_{\mathrm{ci}}(r,r_1,r_2) = \frac{\bar{\alpha}_s}{2\pi}\frac{r^2}{r_1^2 r_2^2}\left[\frac{r^2}{\min(r_1^2,r_2^2)}\right]^{\pm\bar{\alpha}_s A_1} K_{\mathrm{DLA}}(\sqrt{L_{r_1 r}L_{r_2 r}}), \quad (6)$$

where [41]

$$K_{\mathrm{DLA}}(\rho) = \frac{J_1(2\sqrt{\bar{\alpha}_s\rho^2})}{\sqrt{\bar{\alpha}_s\rho}}, \tag{7}$$

J_1 is the Bessel function (the inclusion of the Bessel function into the BK kernel has been previously discussed in [43]), the anomalous dimension is $A_1 = 11/12$, and

$$L_{r_i r} = \ln\left(\frac{r_i^2}{r^2}\right). \tag{8}$$

The sign factor in the exponent $\pm\bar{\alpha}_s A_1$ takes the value of the plus sign when $r^2 < \min(r_1^2, r_2^2)$ and the negative sign otherwise. For the running coupling

$$\bar{\alpha}_s = \alpha_s \frac{N_c}{\pi}, \tag{9}$$

the smallest dipole prescription is used throughout the computation according to

$$\alpha_s = \alpha_s(r_{\min}), \tag{10}$$

where $r_{\min} = \min(r_1, r_2, r)$. This prescription was compared to other prescriptions in [40], where it was found to work adequately in this context. This prescription has also been suggested as the natural option for the BK equation at next-to-leading order (NLO) [44].

C. Treatment of the coupling constant

In this work the running coupling is computed in the variable-number-of-flavors scheme, implemented according to

$$\alpha_{s,n_f}(r^2) = \frac{4\pi}{\beta_{0,n_f}\ln\left(\frac{4C^2}{r^2\Lambda_{n_f}^2}\right)}, \tag{11}$$

where n_f corresponds to the number of flavors that are active, C^2 is an infrared regulator that takes into account the approximations made for the computation of the Fourier transform into the position space and is usually fit to data [25]. The variable β_{0,n_f} is the leading order coefficient of the QCD beta series and is given by relation

$$\beta_{0,n_f} = 11 - \frac{2}{3}n_f. \tag{12}$$

The value of the QCD scale parameter $\Lambda_{n_f}^2$ depends on the number of active flavors. When heavier quarks are active (charm and beauty quarks), its value is obtained from the relation [26]

$$\Lambda_{n_f-1} = (m_f)^{1-\frac{\beta_{0,n_f}}{\beta_{0,n_f-1}}}(\Lambda_{n_f})^{\frac{\beta_{0,n_f}}{\beta_{0,n_f-1}}}. \tag{13}$$

This recursive relation needs to be fixed at one point and for this the usual choice is to take the value of the running coupling at the scale of the mass of the Z^0 boson. In this way, Λ_5 is set with the use of the experimentally measured value of $\alpha_s(M_Z) = 0.1196 \pm 0.0017$, where the Z^0 mass is $M_Z = 91.18\ \mathrm{GeV}/c^2$ [45]. The number of active flavors is set depending on the transverse size of the mother dipole. The condition that governs this relates the mass of the heaviest quark considered to the values of the dipole size r. This condition can be expressed as

$$r^2 < \frac{4C^2}{m_f^2}. \tag{14}$$

Since all dipole sizes are accounted for in the BK evolution equation, there is a need to freeze the coupling at a set value after a certain dipole size is reached [25]. In this work, the coupling is frozen at $\alpha_s^{\mathrm{sat}} = 1$ as in [39].

The value of the parameter C affects the description of data by modifying the speed of the evolution and effectively changes the slope of the structure function. The higher value of this parameter the more the running of the coupling is suppressed and, consequently, the slope in the structure function F_2 is less steep. Figure 1 compares the running of α_s for two values of C: the one used here, $C = 9$, and the one used in [39], $C = 2.586$. The value $C = 9$ was set heuristically and since the solutions reproduce correctly the data, as shown below, it has not been further optimized.

III. IMPACT-PARAMETER SOLUTION TO THE BALITSKY-KOVCHEGOV EQUATION

A. Initial condition

The initial condition, already introduced in [42], depends on the impact parameter; it is suppressed in the regions

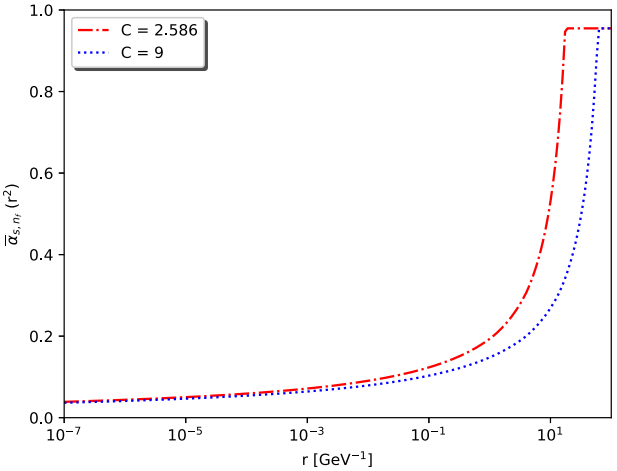

FIG. 1. Comparison between the behavior of $\bar{\alpha}_s$ computed from Eqs. (9) and (11) with $C = 2.586$ (red) and C = 9 (blue).

where r or b reaches large values, in order to respect the geometric nature of the dipole-proton interaction. The shape of its functional form is a combination of the expected behavior in r, which is obtained from the Golec-Biernat Wüsthoff (GBW) model [46], and the impact-parameter dependence, which uses a Gaussian distribution to reflect the expected profile of the proton. Such an approach has been used in similar forms in the past; e.g., in [47–51]. The main new ingredient with respect to the initial condition used in the previous studies [20,35,36,38] is the explicit separation of the contribution from the individual quark and antiquark forming the dipole. The initial condition is given by

$$N(r,b,Y=0)=1-\exp\left(-\frac{1}{2}\frac{Q_s^2}{4}r^2T(b_{q_1},b_{q_2})\right), \quad (15)$$

where b_{q_i} are the impact parameters of the quark and antiquark forming the dipole and

$$T(b_{q_1},b_{q_2})=\left[\exp\left(-\frac{b_{q_1}^2}{2B_G}\right)+\exp\left(-\frac{b_{q_2}^2}{2B_G}\right)\right]. \quad (16)$$

As a first attempt, the angle between $\vec{r}$ and $\vec{b}$ was fixed as shown schematically in Fig. 2. As the results obtained with this initial condition are satisfactory, no further optimization has been considered.

The parameters appearing in this initial condition, Q_s^2 and B_G, have a clear physical interpretation as the saturation scale and as the variance of the Gaussian distribution of the target in impact parameter, respectively. The value of the Q_s^2 parameter is chosen to be 0.496 GeV^2, such that the $F_2(x,Q^2)$ data are correctly described at the rapidity of the initial condition. The relation between x and rapidity is $Y=\ln(x_0/x)$, where $x_0=0.008$. The parameter B_G is set to 3.2258 GeV^{-2} in order to describe the data for exclusive photoproduction of J/ψ off protons at a photon–proton center-of-mass energy $\langle W_{\gamma p}\rangle = 100$ GeV, where as customary $x=(M^2+Q^2)/(W_{\gamma p}^2+Q^2)$ is used; here, M represents the mass of the vector meson.

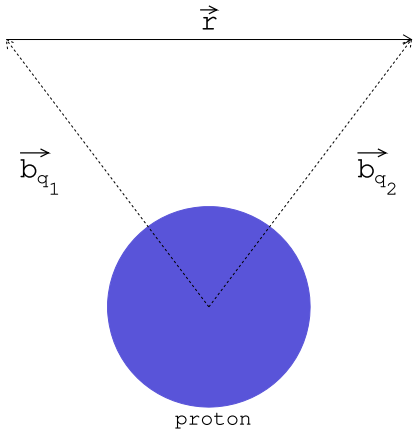

FIG. 2. Schematic picture of the variables that enter the initial condition presented in Eq. (15).

B. Setup for the numerical solution to the equation

The BK evolution equation does not have an analytic solution and therefore has to be solved numerically. The procedure used by us in [27,52] was extended to the case of the impact-parameter dependent BK equation [42] and the solution is evolved in rapidity with a step of $\Delta Y=0.01$.

Fixed grids are used for r and b. They are logarithmic grids of base 10 with 25 evenly spaced points per order of magnitude, spanning the range from 10^{-7} to 10^4 GeV^{-1} for both the r and b variables. The integration over $\vec{r}_1$ is performed in polar coordinates, where r_1 is evaluated in the same grid as r and the polar angle, denoted by θ_{rr_1}, is evaluated in a fixed grid with 21 points separated by a constant step. The numerical integrations are performed applying Simpson's method.

Since the transverse dipole vectors are related as $\vec{r}=\vec{r}_1+\vec{r}_2$, by fixing the values of r and r_1 to the predefined grid, the values of r_2 are in general off the grid. Whenever this happens, linear interpolation in the $\log_{10}$ space is used to get the desired value of $N(r_2,b_2,Y)$. A similar approach is used for obtaining the value of the scattering amplitude whenever the value of b_1 or b_2 is off the grid.

The values of b_1 and b_2 are then computed from the relations $\vec{b}_1=\vec{b}+\vec{r}_2/2$ and $\vec{b}_2=\vec{b}-\vec{r}_1/2$ assuming a fixed angle between $\vec{r}$ and $\vec{b}$. As mentioned above, this angle is set to zero for the results presented below.

The solution to the BK equation has been implemented independently using C++ and the Intel Fortran Compiler. Both implementations have similar performance, with the Fortran version being slightly faster. In a standard personal computer, the program performs the evolution of the dipole amplitude in one unit of rapidity, that is 100 steps for the settings described above, in a bit less than one hour for one set of parameters.

To test the numerical stability of the selection of the grid, the setup was modified and the scattering amplitude was compared at $Y=3$, $r=1/\text{GeV}$ and all values of b. We have changed the step in rapidity from 0.01 to 0.02, the number of steps in r and b per order of magnitude from 25 to 15 and the size of the grid in the polar angle from 21 to 16 and 31 points. Except for the change to 16 points in the grid for polar angles, all other changes produced a difference below the per-mil level. The use of the spare grid in polar angle produced changes almost at one percent level. In summary, with the chosen settings a numerical precision at the percent level, or even below it, is expected.

IV. THE SOLUTION TO THE BK EQUATION

A. Behavior of the collinearly improved kernel

As was shown in [42], the solutions to the BK equation do not exhibit Coulomb tails when using the collinearly improved kernel. This behavior is related to the suppression of this kernel for large values of the size of the daughter dipoles. As an illustration, Fig. 3 shows the ratio of the collinearly improved kernel, see Eq. (4), to the running-coupling kernel, see Eq. (6). (The parameter C for the running coupling in this kernel was chosen to be $C = 9$ just as in the collinearly improved kernel for the sake of a valid comparison.) The ratio is computed at $r = 1$ GeV^{-1} and $\theta_{rr_1} = \pi/2$. Other values produce a similar picture. The figure shows that for large sizes of the daughter dipole the collinearly improved kernel is orders of magnitude smaller than the running-coupling one.

To follow up in more detail the origin of this behavior the kernels are divided into three parts. For the collinearly improved kernel, they are

$$K^1_{\rm ci} = \frac{\bar{\alpha}_s}{2\pi}\frac{r^2}{r_1^2 r_2^2}, \tag{17}$$

$$K^2_{\rm ci} = \left[\frac{r^2}{\min(r_1^2, r_2^2)}\right]^{\pm\bar{\alpha}_s A_1}, \tag{18}$$

$$K^3_{\rm ci} = K_{\rm DLA}(\sqrt{L_{r_1 r} L_{r_2 r}}). \tag{19}$$

The first term, $K^1_{\rm ci}$, is present already at the leading order if one considers a fixed value of the running coupling, $K^2_{\rm ci}$ takes into account the contribution from the single collinear logarithms, and $K^3_{\rm ci}$ resums double collinear logarithms to all orders. The entire collinearly improved kernel is then given by the multiplication of all these factors as

$$K_{\rm ci} = K^1_{\rm ci} K^2_{\rm ci} K^3_{\rm ci}. \tag{20}$$

For the running coupling BK kernel, the separation in three parts is as follows:

$$K^1_{\rm rc} = \frac{N_c \alpha_s(r^2)}{2\pi^2}\frac{r^2}{r_1^2 r_2^2}, \tag{21}$$

$$K^2_{\rm rc} = \frac{N_c \alpha_s(r^2)}{2\pi^2}\frac{1}{r_1^2}\left(\frac{\alpha_s(r_1^2)}{\alpha_s(r_2^2)} - 1\right), \tag{22}$$

$$K^3_{\rm rc} = \frac{N_c \alpha_s(r^2)}{2\pi^2}\frac{1}{r_2^2}\left(\frac{\alpha_s(r_2^2)}{\alpha_s(r_1^2)} - 1\right), \tag{23}$$

whereas the running coupling kernel is then given by the addition of these constituent terms as

$$K_{\rm rc} = K^1_{\rm rc} + K^2_{\rm rc} + K^3_{\rm rc}. \tag{24}$$

The contribution of the three terms is shown in Fig. 4 at $r = 1$ GeV^{-1} and $\theta_{rr_1} = \pi/2$ for each of the two kernels. The fact that the three terms are added in $K_{\rm rc}$, but multiplied in $K_{\rm ci}$ explains numerically the suppression. Even though the first term is essentially the same for both kernels, the additive character of $K_{\rm rc}$ makes it deviate from the collinearly improved kernel at large r_1 values as shown in Fig. 4. There, we can see that even though the kernels are comparable in the low-r_1 region, at large r_1 values, the $K^2_{\rm rc}$ and $K^3_{\rm rc}$ terms become dominant, whereas in the collinearly improved kernel, the $K^1_{\rm ci}$ term suppresses the total value.

The physical reason of this suppression can be traced back to the fact that large daughter dipoles do not follow the time-ordering prescription (that is, they would live longer than the parent dipole) built in when setting up the resummation that leads to the collinearly improved kernel [40,53].

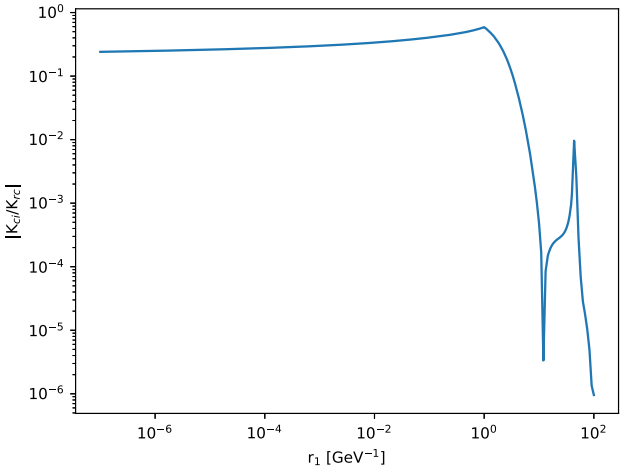

FIG. 3. Absolute value of the ratio $K_{\rm ci}/K_{\rm rc}$ at a fixed dipole size $r = 1$ GeV^{-1} and orientation with respect to the daughter dipole $\theta_{rr_1} = \pi/2$ as a function of the daughter dipole size.

B. Contribution of the kernel terms to the evolution

The suppression for large sizes of the daughter dipole in the kernel is translated as a suppression of the amplitude at large b in the evolution. In this region only large $r_{1,2}$ contribute to the total integral in Eq. (2). This is true because a large impact parameter means that the probing dipole is far away from the target proton and the amplitude is therefore (at the initial condition) exponentially suppressed. Only dipoles with r_1 (r_2) $\sim 2b$ can be oriented so that their impact parameters b_1 (b_2) are small, such that they contribute to the evolution. But, since $K_{\rm ci}$ is suppressed in this region, the integral will be suppressed as well and the scattering amplitude will not grow fast at large b.

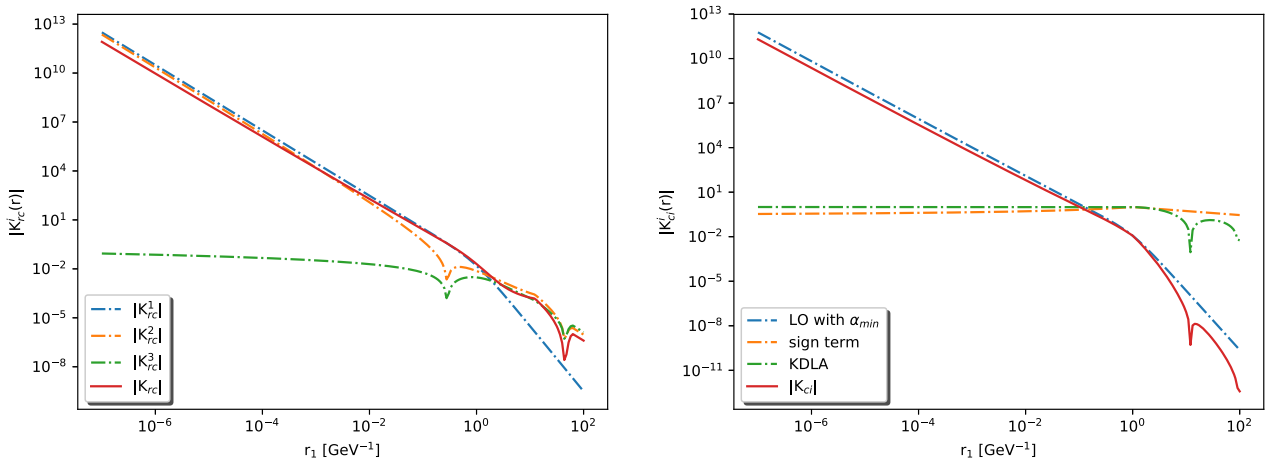

FIG. 4. The three constituent terms of the BK kernel for the running coupling (left) and collinearly improved cases (right) at a fixed dipole size $r = 1$ GeV^{-1} and orientation with respect to the daughter dipole $\theta_{rr_1} = \pi/2$.

This can be numerically studied by computing the contribution to the evolution of the three terms in the collinearly improved kernel. Figure 5 shows the scattering amplitude after evolution to $Y = 3$ using each time a kernel formed with different constituents. It is clearly seen that the impact parameter profile is mostly influenced by the inclusion of the $K^3_{\rm ci}$ term with the Bessel functions. This term originates from resumming double collinear logarithms. Note that also the term $K^2_{\rm ci}$, resumming single collinear logarithms, suppresses the large b region.

C. Behavior of the solution to the BK equation

The evolution of the scattering amplitude as a function of r for different fixed values of b is shown in the upper panels

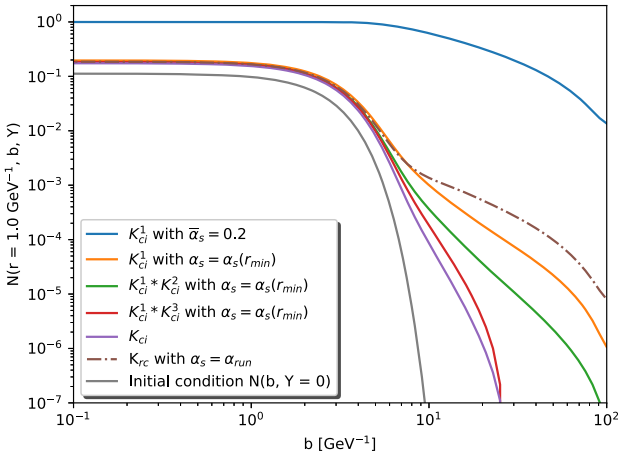

FIG. 5. The scattering amplitude evolved to $Y = 3$ with various kernels illustrates the effect of the different terms in the evolution and demonstrates that the computation based on the $K_{\rm ci}$ kernel does not develop the Coulomb tails seen when the $K_{\rm rc}$ kernel is used.

of Fig. 6, while the lower panels of the same figure show the evolution as a function of b for two fixed values of r. A two-dimensional view of the amplitude at two stages of the evolution is shown in Fig. 7. The amplitude decreases fast for small dipole sizes as expected. The suppression of large dipole sizes imposed in the initial condition is lifted with evolution. Similar behavior was observed in previous studies, e.g., [35]. Nonetheless, in the case of the collinearly improved kernel the growth at the largest dipole sizes is not as fast and a shoulder appears, after which the amplitude is again suppressed. The behavior as a function of impact parameter has been discussed above; the profile impact parameter grows, but the development of Coulomb tails is suppressed. Recently, a similar finding has been reported for the case of NLO BFKL equations at large impact parameters [54].

Finally, Fig. 8 shows $N(r, Y)$, defined as

$$N(r, Y) = \int d^2\vec{b} N(r, b, Y), \tag{25}$$

for different dipole sizes and for two kernels, the running coupling and the collinearly improved. For small dipoles the difference is larger and it grows with rapidity. At larger dipole sizes the difference between both kernels is smaller. Note that for the comparisons to data discussed below, the main numerical contribution comes from the region of relatively large dipoles. For the case of the structure function the main contribution for virtualities between 1 and 10 GeV^2 comes from dipoles of sizes on the range around 0.1/GeV to 10/GeV, see e.g., the lower panel of Fig. 4 in [27].

Another interesting observation is that $N(r, Y)$ is related to the σ_0 parameter introduced in studies based on the rcBK equation without impact-parameter dependence. Basically, σ_0 corresponds to the scale of $N(r, Y)$. Standard values

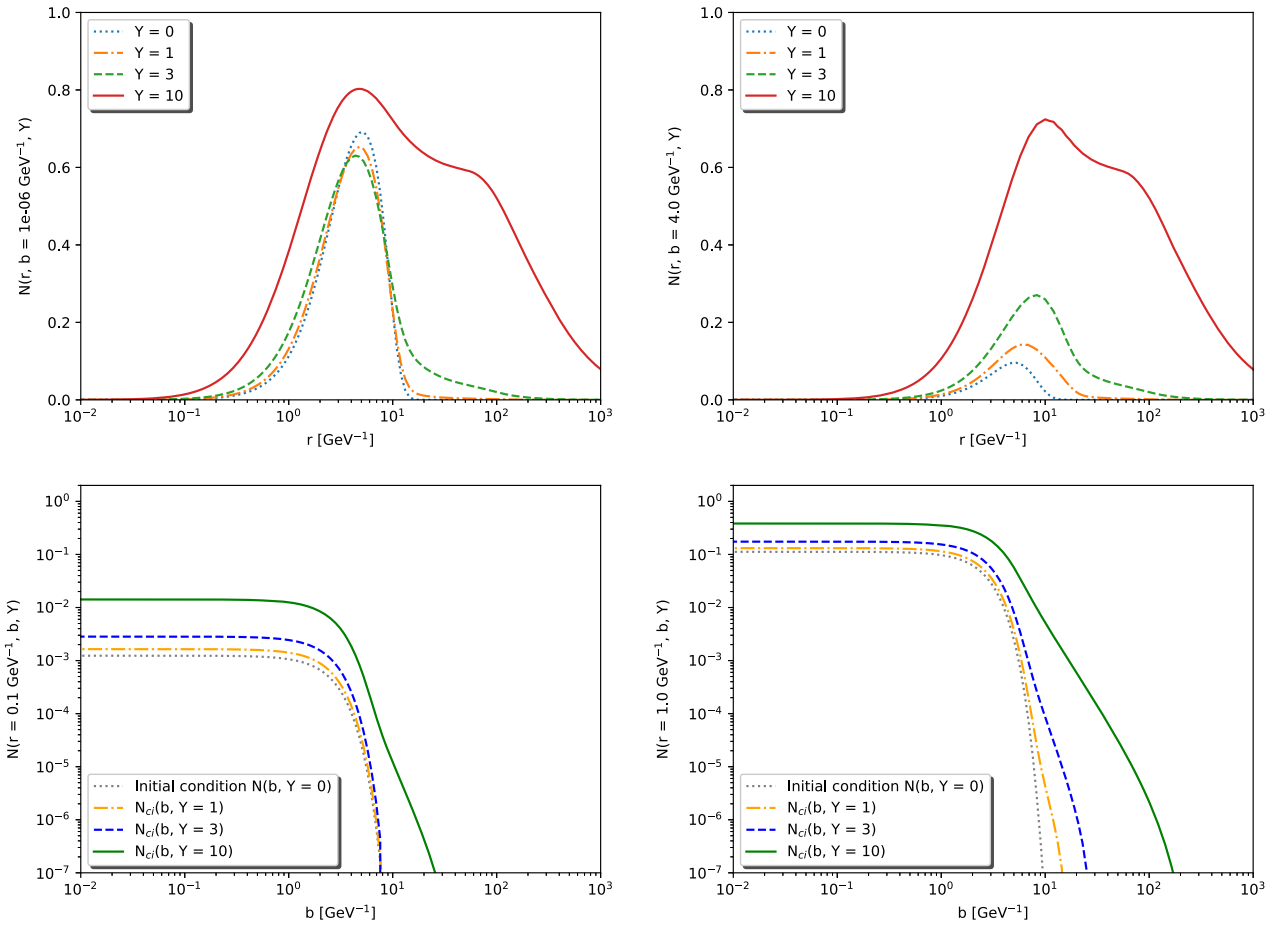

FIG. 6. The scattering amplitude as a solution to the BK equation with the collinearly improved kernel as a function of r for $b = 10^{-6}$ GeV^{-1} (upper left) and $b = 4$ GeV^{-1} (upper right), and as a function of b at $r = 0.1$ GeV^{-1} (lower left) and at $r = 1$ GeV^{-1} (lower right).

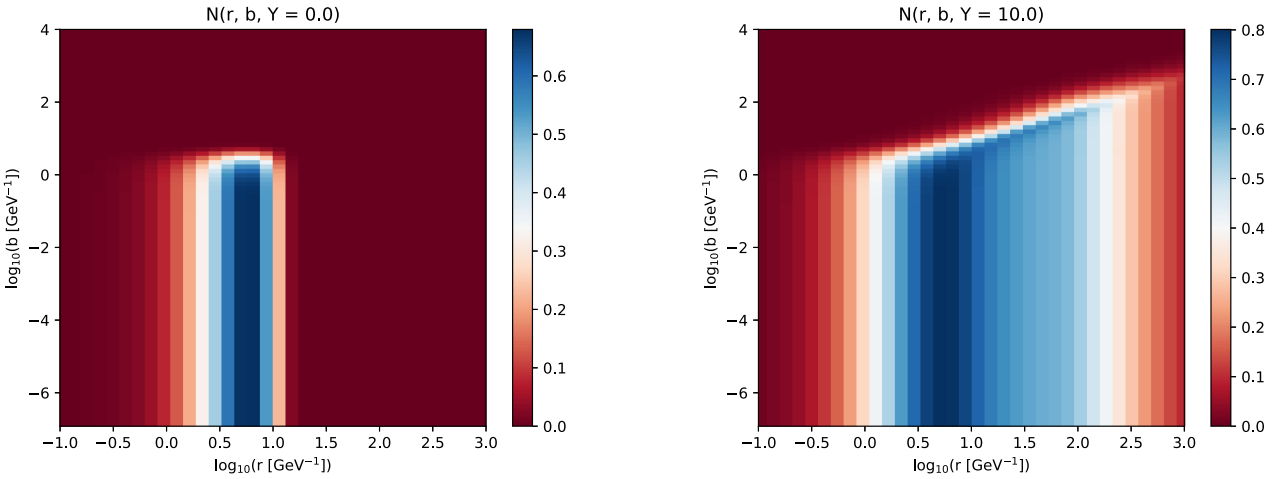

FIG. 7. Evolution of the scattering amplitude from the initial condition at $Y = 0$ (left) to $Y = 10$ (right).

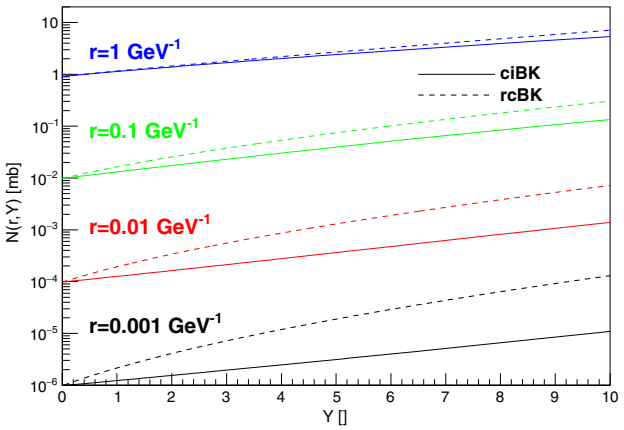

FIG. 8. Growth of the dipole-target amplitude integrated over impact parameter as a function of rapidity for solutions of the BK equations with the running coupling and the collinearly improved kernel.

found for this parameter are a few tens of mb, see e.g., Table I in [26]. Figure 8 justifies the order of magnitude of these values from the perspective of an impact-parameter dependent computation.

V. DEEP INELASTIC SCATTERING

A. Structure function and reduced cross section

Due to the fact that the dipole lives much longer than the typical interaction time, the computation of the total deep-inelastic scattering (DIS) cross section can be written as the convolution of separate terms. One of them is the wave function representing the probability of a virtual photon splitting into a quark-antiquark dipole. Here formulas and notation of [46] are used:

$$|\Psi_T^i(z,\vec{r},Q^2)|^2 = \frac{3\alpha_{\rm em}}{2\pi^2} e_{q_i}^2((z^2+(1-z)^2)\epsilon^2 K_1^2(\epsilon r) + m_{q_i}^2 K_0^2(\epsilon r)), \tag{26}$$

and

$$|\Psi_L^i(z,\vec{r},Q^2)|^2 = \frac{3\alpha_{\rm em}}{2\pi^2} e_{q_i}^2(4Q^2z^2(1-z)^2 K_0^2(\epsilon r)) \tag{27}$$

for the transverse and longitudinal polarization of the incoming photon, respectively, where z is the fraction of the total longitudinal momentum of the photon carried by the quark, K_0 and K_1 are the MacDonald functions, Q^2 is the virtuality of the probing photon, e_{qi} is the fractional charge (in units of elementary charge) of quark i, $\alpha_{\rm em} = 1/137$ and

$$\epsilon^2 = z(1-z)Q^2 + m_{q_i}^2, \tag{28}$$

where m_{q_i} is the mass of the considered quark, which is set to 100 MeV$/c^2$ for light quarks and 1.3 GeV$/c^2$ for charm quark and 4.5 GeV$/c^2$ for bottom quark. Note that the computed structure function does not depend strongly on the value of the mass of the light quarks (as was reported in [40]); this has been checked by also using $m_{u,d,s} = 10$ MeV$/c^2$, which did not influence the description of data. The total wave function then is

$$|\Psi_{T,L}^i(z,\vec{r})|^2 = |\Psi_T^i(z,\vec{r})|^2 + |\Psi_L^i(z,\vec{r})|^2. \tag{29}$$

According to the optical theorem, one can link the dipole-target cross section to the scattering amplitude by

$$\frac{{\rm d}\sigma^{q\bar{q}}(\vec{r},x)}{{\rm d}\vec{b}} = 2N(\vec{r},\vec{b},x). \tag{30}$$

Furthermore, it is usual to shift the value of the x at which the structure function and reduced cross section are computed according to the photoproduction kinematic shift [46],

$$\tilde{x} = x\left(1+\frac{4m_{q_i}^2}{Q^2}\right). \tag{31}$$

Using these ingredients, the relation for the computation of the structure function in the dipole model framework is

$$F_2(x,Q^2) = \frac{Q^2}{4\pi^2\alpha_{\rm em}} \int \sum_i d\vec{r}d\vec{b}dz |\Psi_{T,L}^i(z,\vec{r})|^2 \frac{{\rm d}\sigma^{q\bar{q}}(\vec{r},\tilde{x})}{{\rm d}\vec{b}}, \tag{32}$$

and the reduced cross section is computed as

$$\sigma_{\rm red}(y,x,Q^2) = F_2(x,Q^2) - \frac{y^2}{1+(1-y)^2} F_L(x,Q^2), \tag{33}$$

where $y = Q^2/(sx)$ is the inelasticity of the process, s is the squared of the center-of-mass energy of the collision and $F_L(x,Q^2)$ is given by the relation

$$F_L(x,Q^2) = \frac{Q^2}{4\pi^2\alpha_{\rm em}} \int \sum_i d\vec{r}d\vec{b}dz |\Psi_L^i(z,\vec{r})|^2 \frac{{\rm d}\sigma^{q\bar{q}}(\vec{r},\tilde{x})}{{\rm d}\vec{b}}. \tag{34}$$

B. Comparison to HERA data

The predictive power of this model is evaluated by confronting it with data from HERA on the $F_2(x,Q^2)$ structure function [55] in Fig. 9. A closer look is given in Fig. 10 for two values of the photon virtuality. To quantify

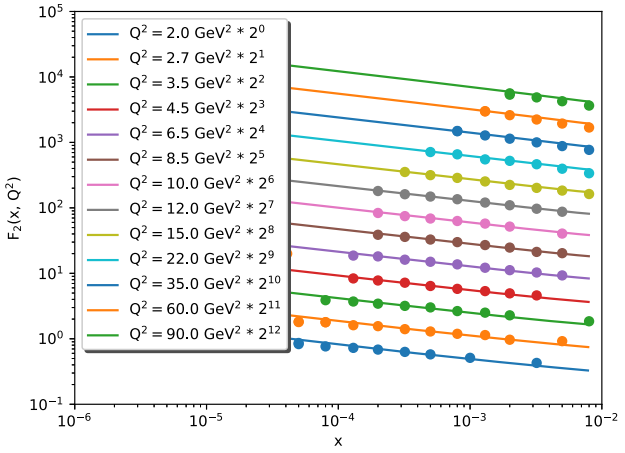

FIG. 9. Comparison of the structure function data from HERA [55] (solid circles) to the prediction of the impact-parameter dependent BK equation with the collinearly improved kernel (lines).

the level of agreement between data and model, Fig. 11 presents the percentage pulls associated with the structure function, which are given by

$$d_{\%} = 100\,\frac{F_2^{\mathrm{BK}}(x,Q^2) - F_2^{\mathrm{HERA}}(x,Q^2)}{F_2^{\mathrm{HERA}}(x,Q^2)} \tag{35}$$

and by $D_{\%}$, which denotes the average of the corresponding values of $d_{\%}$. Finally, for completeness Fig. 12 shows the comparison of the model and data for the charm component of the proton structure function measured at HERA [55].

Overall, the agreement between prediction and data is within a few percent over most of the phase space. For our purposes this level of agreements is satisfactory. First, the equation we are using does not include the full angular dependence. Second, we have not needed to add any *ad hoc* component to describe data and the values of the parameters are reasonable from the point of view of the physics that is being probed. Furthermore, note that the BK equation that we are using is definitely not the last word on the subject. The full equation at NLO has already been computed [44], and a large effort is being done to use it for phenomenology [53,56–59]. There are also recent developments regarding the most adequate variable to evolve the scattering amplitude [60].

VI. PRODUCTION OF VECTOR MESONS

A. Exclusive cross section in the color-dipole approach

Similarly to the DIS process described in the previous section, the diffractive production of a vector meson as a result of the interaction of a virtual photon with the proton can be treated within the color-dipole approach. In this formalism, the exclusive cross section to produce a vector meson V is given by

$$\left.\frac{\mathrm{d}\sigma^{\gamma^* p\to \mathrm{V}p}}{\mathrm{d}|t|}\right|_{T,L} = \frac{(1+\beta^2)(R_g^{T,L})^2}{16\pi}\,|\mathcal{A}_{T,L}|^2, \tag{36}$$

where $\mathcal{A}_{T,L}$ is the scattering amplitude of the process. It is given as a convolution of the overlap of photon-meson wave functions with the dipole cross section given in Eq. (30) (for a detailed derivation see e.g., [61,62]) and takes the following form:

$$\mathcal{A}_{T,L}(x,Q^2,\vec{\Delta}) = i\int \mathrm{d}\vec{r}\int_0^1 \frac{\mathrm{d}z}{4\pi}\int \mathrm{d}\vec{b}\,|\Psi_{\mathrm{V}}^*\Psi_{\gamma^*}|_{T,L} \times \exp\left[-i(\vec{b}-(1-z)\vec{r})\vec{\Delta}\right]\frac{\mathrm{d}\sigma^{q\bar{q}}}{\mathrm{d}\vec{b}}, \tag{37}$$

where the subscripts T, L denote the contribution from the virtual photon with transverse, respectively longitudinal, polarization, Ψ_{γ^*} is the wave function of a virtual photon

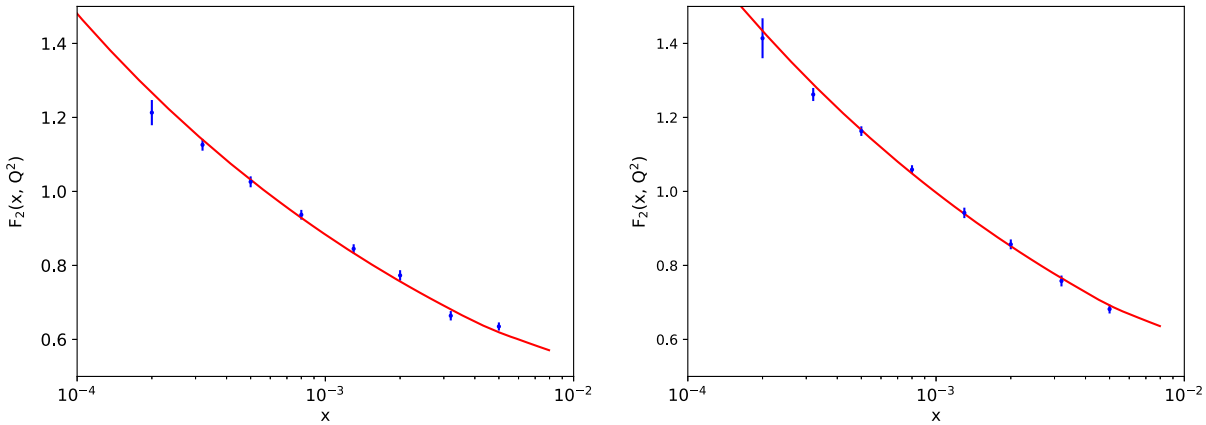

FIG. 10. Close-up comparison of the structure function data from HERA [55] (blue points) to the b-dependent prediction (red line) for $Q^2 = 8.5\ \mathrm{GeV}^2$ (left) and $Q^2 = 12\ \mathrm{GeV}^2$ (right).

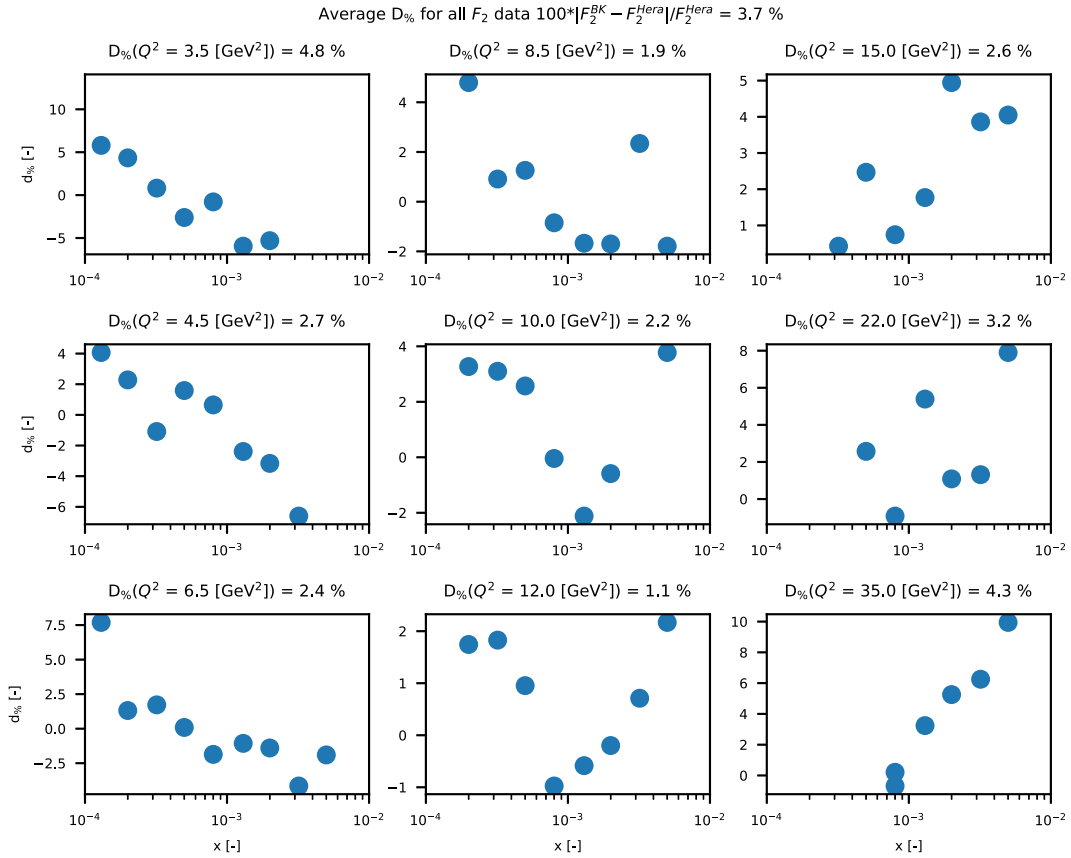

FIG. 11. The percentage pulls for various values of Q^2 and their average value.

which fluctuates into a dipole, Ψ_V represents the wave function of the vector meson, and $\vec{\Delta}^2 \equiv -t$, the square of the four momentum transferred in the proton vertex. Under the assumption of large photon-proton center-of-mass energies $W_{\gamma p}$,

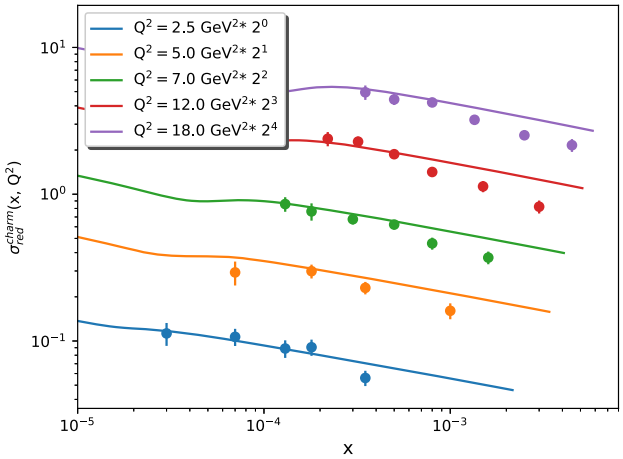

FIG. 12. The comparison of the prediction for the reduced cross section for charm to data from HERA [55].

$$x = \frac{Q^2 + M^2}{W_{\gamma p}^2 + Q^2}, \tag{38}$$

where M is the mass of the given vector meson.

The wave functions of a vector meson are modeled under the assumption that the vector meson is predominantly a $q\bar{q}$ pair with the same polarization and the spin structure as the original photon. The overlap of the photon-meson wave functions in Eq. (37) is given as

$$|\Psi_V^* \Psi_{\gamma^*}|_T = \hat{e}_f e \frac{N_C}{\pi z(1-z)} [m_f^2 K_0(\epsilon r)\phi_T(r,z) - (z^2 + (1-z)^2)\epsilon K_1(\epsilon r)\partial_r \phi_T(r,z)], \tag{39}$$

and

$$|\Psi_V^* \Psi_{\gamma^*}|_L = \hat{e}_f e \frac{N_C}{\pi} 2Qz(1-z)K_0(\epsilon r)\left[M\phi_L(r,z) + \delta \frac{m_f^2 - \nabla_r^2}{Mz(1-z)}\phi_L(r,z)\right], \tag{40}$$

with $\hat{e}_f$ being the effective charge of the given vector meson, ϵ defined by Eq. (28), and the parameter δ is a

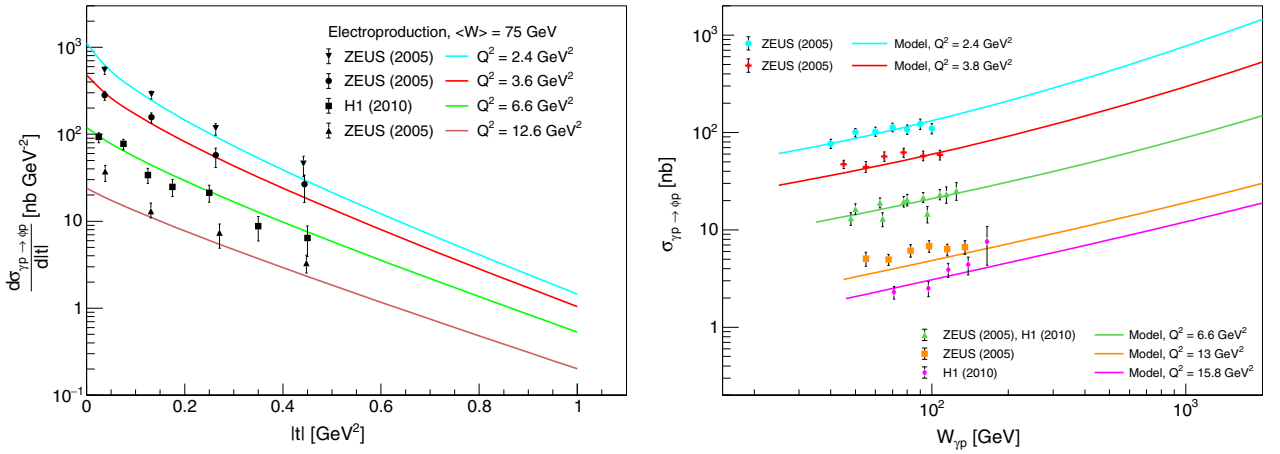

FIG. 13. Comparison of the predictions of the model (solid lines) with HERA data from H1 [68] and ZEUS [69] for the $|t|$ dependence (left) and the $W_{\gamma p}$ dependence (right) of the exclusive electroproduction cross section of the ϕ meson.

switch to include ($\delta = 1$) or exclude ($\delta = 0$) the nonlocal term in the longitudinal contribution. The scalar part $\phi_{T,L}$ of the wave function is, in general, model dependent. For our studies, we use the boosted Gaussian model [63–65] in which the δ parameter is fixed to one. The values of the parameters for the wave functions of all vector mesons are fixed according to Table I in [66].

The total exclusive cross section to produce a vector meson is given by the sum of the transverse and the longitudinal contributions defined by Eq. (36). Moreover two important corrections have to be applied. The derivation of the formula for the exclusive vector meson cross section is performed under the assumption that the scattering amplitude $\mathcal{A}_{T,L}(x, Q^2, \vec{\Delta})$ is purely imaginary. The real part of the amplitude can be accounted for by the extra term $(1 + \beta^2)$ in Eq. (37), where β is the ratio of real to imaginary parts of the scattering amplitude, for details see [61]. The other correction takes into account that there are two values of x involved in the interaction of the dipole with the proton and one should therefore use the off-diagonal gluon distribution for vector meson production. This effect can be accounted for by multiplying the scattering amplitude by a factor $R_g^{T,L}$, called the skewedness correction [67].

B. Comparison to data

Using the model described in this paper, the cross sections for exclusive photoproduction and electroproduction of ϕ, J/ψ, $\psi(2S)$, and $\Upsilon(1S)$ vector mesons are presented at different virtualities of the exchanged photon and they are compared to available experimental data. The presented results are calculated at the scales which allow perturbative treatment of the specific parts of the model.

In Fig. 13 a comparison of our predictions for the $|t|$ distributions and the total cross sections with HERA H1 [68] and ZEUS [69] data for the exclusive electroproduction of the ϕ meson for several values of Q^2 is shown. The predictions give a very good description of the available data, especially at low photon virtualities.

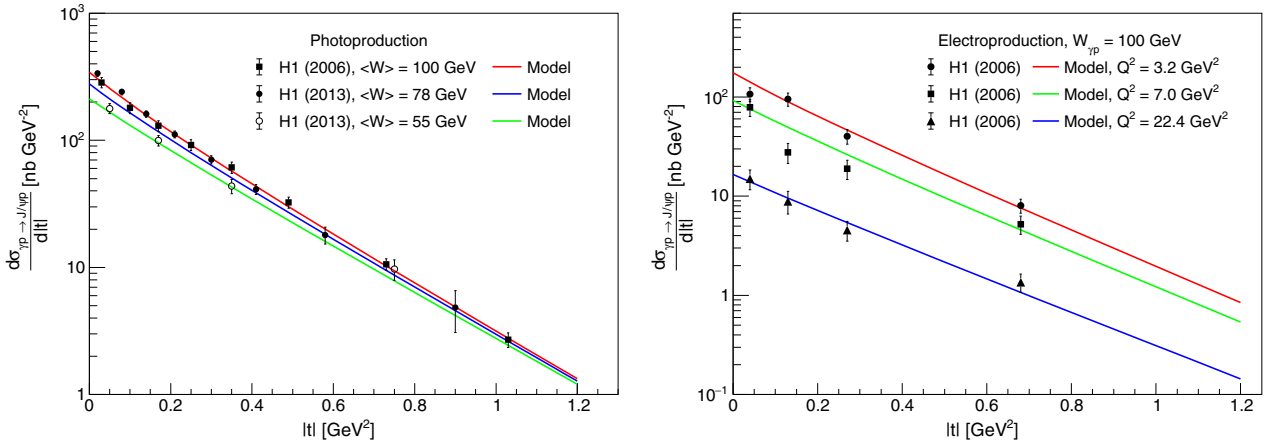

FIG. 14. Comparison of the predictions of the model (solid lines) with HERA data from H1 [70,71] for the $|t|$ dependence of the exclusive photoproduction (left) and electroproduction (right) cross sections of the J/ψ meson.

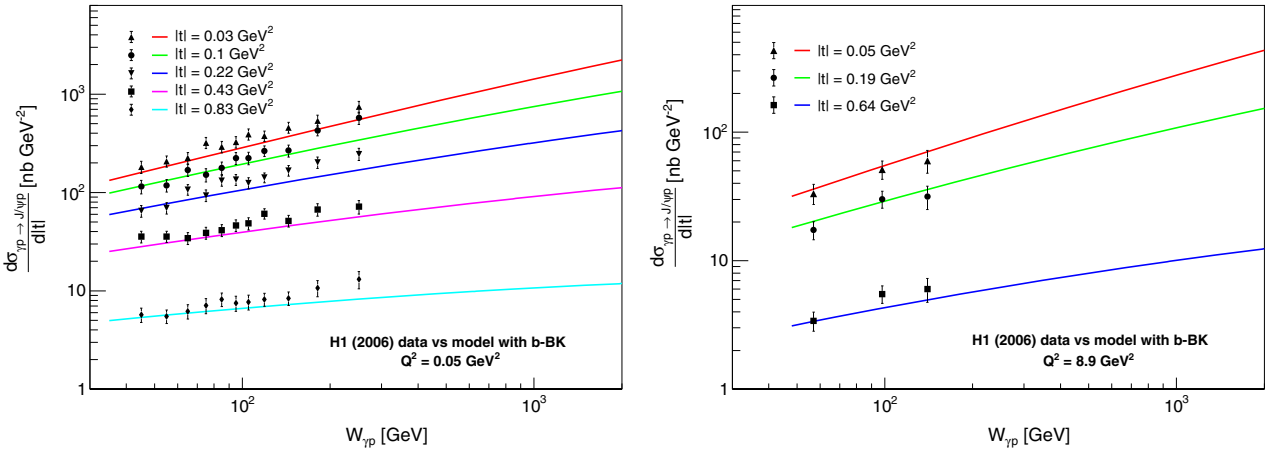

FIG. 15. Comparison of the predictions of the model (solid lines) with HERA data from H1 [70] for the W dependence of the exclusive photoproduction (left) and electroproduction (right) cross sections of the J/ψ meson at fixed $|t|$ values.

The predictions for the exclusive production of the J/ψ meson are compared with the experimental data from H1 [70,71] and ALICE [72,73] experiments in Figs. 14–16, for several different measurements of kinematic observables. In the left panel of Fig. 14, the comparison of the $|t|$ distribution of the photoproduction cross section is presented. The predictions give very good agreement with the data at energies $W_{\gamma p} = 55$ GeV and $W_{\gamma p} = 100$ GeV. The result for $W_{\gamma p} = 78$ GeV is slightly underestimated at low values of $|t|$, however one can notice the very small difference in the measured data with respect to the result for $W_{\gamma p} = 100$ GeV. Since the value of $W_{\gamma p}$ from the experimental data is a mean value estimated from a measured energy range, the result of the model can be considered satisfactory. The same comparison for the electroproduction at three different values of Q^2 can be seen in the right panel of the same figure. Although our predictions do not describe all the data points, we conclude the agreement between the data and the model to be qualitatively good. The same conclusion applies to the comparison of the model predictions with the measured $W_{\gamma p}$ dependence of the exclusive differential photoproduction and electroproduction cross sections at several fixed values of $|t|$ presented in Fig. 15. The agreement of the predictions with the data is very good at low values of $W_{\gamma p}$, however at larger values ($\sim 10^2$ GeV), the predictions are underestimated when compared to experimental photoproduction data. We have also obtained total cross section for the J/ψ production which is presented in the left panel of Fig. 16. The predictions for the electroproduction at three different values of Q^2 give a very good description of the available data. The result for photoproduction gives a

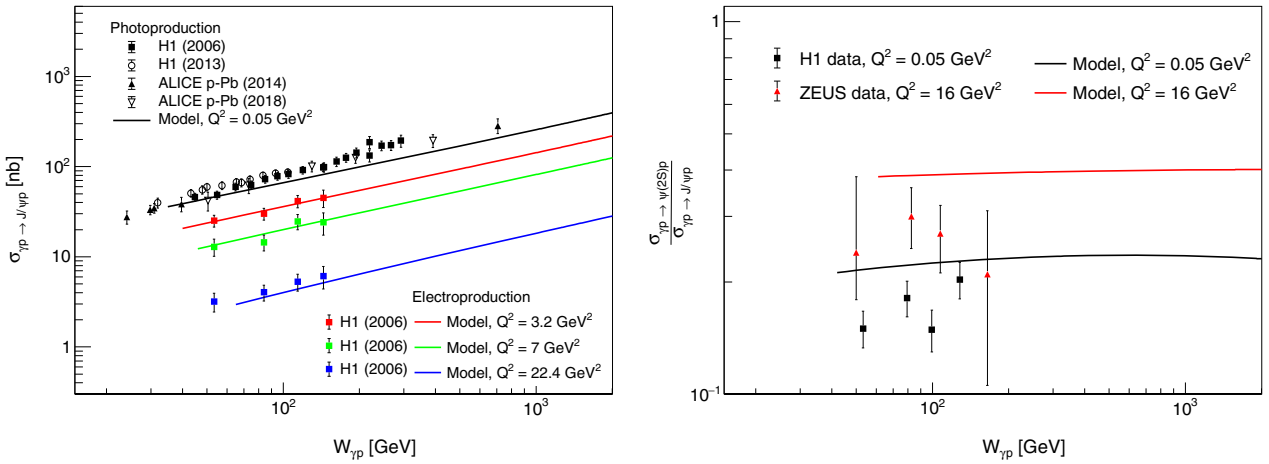

FIG. 16. Comparison of the predictions of the model (solid lines) with HERA data from H1 [70,71] and LHC data from ALICE [72,73] for the $W_{\gamma p}$ dependence of the exclusive photoproduction and electroproduction cross section of the J/ψ meson (left) and with HERA data from H1 [74] and ZEUS [75] for the $W_{\gamma p}$ dependence of the exclusive photoproduction and electroproduction cross section J/ψ/ψ(2S) ratio (right).

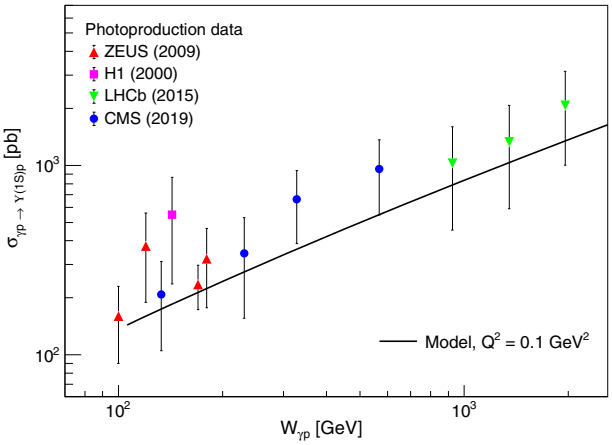

FIG. 17. Comparison of the predictions of the model (solid lines) with the HERA data from H1 [76] and ZEUS [77], and LHC data from LHCb [78] and CMS [79] for the $W_{\gamma p}$ dependence of the exclusive photoproduction cross section of the $\Upsilon(1S)$ meson.

good agreement with the data at low values of $W_{\gamma p}$, however at high energies the result is again underestimated when compared to data.

Also, the exclusive cross section of the $\psi(2S)$ meson was calculated within the model. The experimental data are not available for the total cross sections, but only for a ratio of the $\psi(2S)$ to J/ψ cross sections, the predictions for these ratios for photoproduction and electroproduction at $Q^2 = 16\ \mathrm{GeV}^2$ are calculated and compared to data from H1 [74], and ZEUS [75], respectively, in the right panel of Fig. 16. The description of the data is not very good, yet the large uncertainties of the experimental data do not allow us to make any final conclusions in this case.

To complete the set of the predictions based on the BK equation, the exclusive photoproduction of the $\Upsilon(1S)$ meson is presented in Fig. 17. The prediction is compared with experimental data obtained at HERA by H1 [76] and ZEUS [77] experiments. It is also compared with the two latest measurements—in proton-proton collisions at $\sqrt{s} = 7$ TeV and $\sqrt{s} = 8$ TeV by LHCb [78], and in proton-lead collisions at $\sqrt{s} = 5.02$ TeV by the CMS experiment [79]. The description of the data is good, although the large uncertainties prevent us from making any strong conclusions regarding the agreement of the predictions with the data.

VII. CONCLUSIONS

The solution of the Balitsky-Kovchegov equation with the collinearly improved kernel and including the impact-parameter dependence has been obtained numerically. This solution does not show the so-called Coulomb tails that have appeared in previous attempts to include the impact-parameter dependence. We have shown that the suppression at large values of the impact parameter is due to the suppression of contributions from daughter dipoles of large sizes in the terms of the collinearly improved kernel that deal with the resummation of double and single collinear logarithms.

The solutions based on a physics-inspired initial condition have been confronted with HERA and LHC data of the structure function of the proton measured in deep-inelastic scattering and of exclusive vector meson photoproduction and electroproduction. The predictions described data over a large kinematic range in scale and in energy.

The dipole scattering amplitudes computed in this work are publicly available on the website [80] along with instructions on how to use them.

ACKNOWLEDGMENTS

We would like to thank Dionysios Triantafyllopoulos for fruitful discussions regarding this paper. Our work has been partially supported from Grant No. LTC17038 of the INTER-EXCELLENCE program at the Ministry of Education, Youth and Sports of the Czech Republic, by Grant No. 17-04505S of the Czech Science Foundation, GA ČR and the European Cooperation in Science and Technology (COST) Action CA15213 Theory of hot matter and relativistic heavy-ion collisions (THOR). Computational resources were provided by the Czech Educational and Scientific NETwork (CESNET) LM2015042 grant and the Centrum vzdělávání, výzkumu a inovací v informačních a komunikačních technologiích (CERIT) Scientific Cloud LM2015085, provided under the program Projects of Large Research, Development, and Innovations Infrastructures.

[1] G. Altarelli, Phys. Rep. **81**, 1 (1982).
[2] L. N. Lipatov, Phys. Rep. **286**, 131 (1997).
[3] L. V. Gribov, E. M. Levin, and M. G. Ryskin, Phys. Rep. **100**, 1 (1983).
[4] P. Newman and M. Wing, Rev. Mod. Phys. **86**, 1037 (2014).
[5] K. Akiba *et al.* (LHC Forward Physics Working Group), J. Phys. G **43**, 110201 (2016).
[6] A. Accardi *et al.*, Eur. Phys. J. A **52**, 268 (2016).
[7] J. Abelleira Fernandez *et al.* (LHeC Study Group), J. Phys. G **39**, 075001 (2012).
[8] I. Balitsky, Nucl. Phys. **B463**, 99 (1996).

[9] Y. V. Kovchegov, Phys. Rev. D **60**, 034008 (1999).
[10] Y. V. Kovchegov, Phys. Rev. D **61**, 074018 (2000).
[11] A. H. Mueller, Nucl. Phys. **B335**, 115 (1990).
[12] N. N. Nikolaev and B. Zakharov, Z. Phys. C **49**, 607 (1991).
[13] A. H. Mueller, Nucl. Phys. **B415**, 373 (1994).
[14] J. Jalilian-Marian, A. Kovner, A. Leonidov, and H. Weigert, Phys. Rev. D **59**, 014014 (1998).
[15] J. Jalilian-Marian, A. Kovner, and H. Weigert, Phys. Rev. D **59**, 014015 (1998).
[16] H. Weigert, Nucl. Phys. **A703**, 823 (2002).
[17] E. Iancu, A. Leonidov, and L. D. McLerran, Nucl. Phys. **A692**, 583 (2001).
[18] E. Iancu, A. Leonidov, and L. D. McLerran, Phys. Lett. B **510**, 133 (2001).
[19] E. Ferreiro, E. Iancu, A. Leonidov, and L. McLerran, Nucl. Phys. **A703**, 489 (2002).
[20] N. N. Nikolaev and B. G. Zakharov, Z. Phys. C **64**, 631 (1994).
[21] I. Balitsky, Phys. Rev. D **75**, 014001 (2007).
[22] Y. V. Kovchegov and H. Weigert, Nucl. Phys. **A784**, 188 (2007).
[23] J. L. Albacete and Y. V. Kovchegov, Phys. Rev. D **75**, 125021 (2007).
[24] J. L. Albacete, N. Armesto, J. G. Milhano, C. A. Salgado, and U. A. Wiedemann, Phys. Rev. D **71**, 014003 (2005).
[25] J. L. Albacete, N. Armesto, J. G. Milhano, and C. A. Salgado, Phys. Rev. D **80**, 034031 (2009).
[26] J. L. Albacete, N. Armesto, J. G. Milhano, P. Quiroga-Arias, and C. A. Salgado, Eur. Phys. J. C **71**, 1705 (2011).
[27] J. Cepila and J. G. Contreras, arXiv:1501.06687.
[28] J. L. Albacete and A. Dumitru, arXiv:1011.5161.
[29] T. Lappi and H. Mantysaari, Phys. Rev. D **88**, 114020 (2013).
[30] B. Ducloue, T. Lappi, and H. Mantysaari, Phys. Rev. D **91**, 114005 (2015).
[31] J. L. Albacete, G. Giacalone, C. Marquet, and M. Matas, Phys. Rev. D **99**, 014002 (2019).
[32] J. L. Albacete, J. I. Illana, and A. Soto-Ontoso, Phys. Rev. D **92**, 014027 (2015).
[33] A. Bhattacharya, R. Enberg, Y. S. Jeong, C. S. Kim, M. H. Reno, I. Sarcevic, and A. Stasto, J. High Energy Phys. 11 (2016) 167.
[34] K. J. Golec-Biernat and A. M. Stasto, Nucl. Phys. **B668**, 345 (2003).
[35] J. Berger and A. Stasto, Phys. Rev. D **83**, 034015 (2011).
[36] J. Berger and A. M. Stasto, Phys. Rev. D **84**, 094022 (2011).
[37] H. Mantysaari and B. Schenke, Phys. Rev. D **98**, 034013 (2018).
[38] J. Berger and A. M. Stasto, J. High Energy Phys. 01 (2013) 001.
[39] E. Iancu, J. D. Madrigal, A. H. Mueller, G. Soyez, and D. N. Triantafyllopoulos, Phys. Lett. B **744**, 293 (2015).
[40] E. Iancu, J. D. Madrigal, A. H. Mueller, G. Soyez, and D. N. Triantafyllopoulos, Phys. Lett. B **750**, 643 (2015).
[41] A. Sabio Vera, Nucl. Phys. **B722**, 65 (2005).
[42] J. Cepila, J. G. Contreras, and M. Matas, Phys. Rev. D **99**, 051502 (2019).
[43] L. Motyka and A. M. Stasto, Phys. Rev. D **79**, 085016 (2009).
[44] I. Balitsky and G. A. Chirilli, Phys. Rev. D **77**, 014019 (2008).
[45] K. A. Olive *et al.* (Particle Data Group), Chin. Phys. C **38**, 090001 (2014).
[46] K. J. Golec-Biernat and M. Wusthoff, Phys. Rev. D **59**, 014017 (1998).
[47] H. Kowalski and D. Teaney, Phys. Rev. D **68**, 114005 (2003).
[48] G. Watt and H. Kowalski, Phys. Rev. D **78**, 014016 (2008).
[49] C. Marquet, Phys. Rev. D **76**, 094017 (2007).
[50] H. Mantysaari and B. Schenke, Phys. Rev. Lett. **117**, 052301 (2016).
[51] J. Cepila, J. G. Contreras, and J. D. Tapia Takaki, Phys. Lett. B **766**, 186 (2017).
[52] M. Matas, J. Cepila, and J. Guillermo Contreras Nuno, EPJ Web Conf. **112**, 02008 (2016).
[53] G. Beuf, Phys. Rev. D **89**, 074039 (2014).
[54] C. Contreras, E. Levin, and R. Meneses, arXiv:1906.09603.
[55] F. D. Aaron *et al.* (ZEUS and H1 Collaborations), J. High Energy Phys. 01 (2010) 109.
[56] T. Lappi and H. Mantysaari, Phys. Rev. D **93**, 094004 (2016).
[57] G. Beuf, Phys. Rev. D **96**, 074033 (2017).
[58] B. Ducloue, H. Hanninen, T. Lappi, and Y. Zhu, Phys. Rev. D **96**, 094017 (2017).
[59] H. Hanninen, T. Lappi, and R. Paatelainen, Ann. Phys. (Amsterdam) **393**, 358 (2018).
[60] B. Ducloue, E. Iancu, A. H. Mueller, G. Soyez, and D. N. Triantafyllopoulos, J. High Energy Phys. 04 (2019) 081.
[61] H. Kowalski, L. Motyka, and G. Watt, Phys. Rev. D **74**, 074016 (2006).
[62] I. P. Ivanov, N. N. Nikolaev, and A. A. Savin, Phys. Part. Nucl. **37**, 1 (2006).
[63] J. Nemchik, N. N. Nikolaev, and B. G. Zakharov, Phys. Lett. B **341**, 228 (1994).
[64] J. Nemchik, N. N. Nikolaev, E. Predazzi, and B. G. Zakharov, Z. Phys. C **75**, 71 (1997).
[65] J. R. Forshaw, R. Sandapen, and G. Shaw, Phys. Rev. D **69**, 094013 (2004).
[66] D. Bendova, J. Cepila, and J. G. Contreras, Phys. Rev. D **99**, 034025 (2019).
[67] A. G. Shuvaev, K. J. Golec-Biernat, A. D. Martin, and M. G. Ryskin, Phys. Rev. D **60**, 014015 (1999).
[68] F. D. Aaron *et al.* (H1 Collaboration), J. High Energy Phys. 05 (2010) 032.
[69] S. Chekanov *et al.* (ZEUS Collaboration), Nucl. Phys. **B718**, 3 (2005).
[70] A. Aktas *et al.* (H1 Collaboration), Eur. Phys. J. C **46**, 585 (2006).
[71] C. Alexa *et al.* (H1 Collaboration), Eur. Phys. J. C **73**, 2466 (2013).
[72] B. B. Abelev *et al.* (ALICE Collaboration), Phys. Rev. Lett. **113**, 232504 (2014).
[73] S. Acharya *et al.* (ALICE Collaboration), Eur. Phys. J. C **79**, 402 (2019).
[74] C. Adloff *et al.* (H1 Collaboration), Phys. Lett. B **541**, 251 (2002).

[75] H. Abramowicz *et al.* (ZEUS Collaboration), Nucl. Phys. **B909**, 934 (2016).
[76] C. Adloff *et al.* (H1 Collaboration), Phys. Lett. B **483**, 23 (2000).
[77] S. Chekanov *et al.* (ZEUS Collaboration), Phys. Lett. B **680**, 4 (2009).
[78] R. Aaij *et al.* (LHCb Collaboration), J. High Energy Phys. 09 (2015) 084.
[79] A. M. Sirunyan *et al.* (CMS Collaboration), Eur. Phys. J. C **79**, 277 (2019).
[80] https://hep.fjfi.cvut.cz/

Eur. Phys. J. C (2021) 81:211
https://doi.org/10.1140/epjc/s10052-021-09006-x

THE EUROPEAN PHYSICAL JOURNAL C

Regular Article - Theoretical Physics

Diffractive deeply inelastic scattering in future electron-ion colliders

D. Bendova[1,a], **J. Cepila**[1,b], **J. G. Contreras**[1,c], **V. P. Gonçalves**[2,d], **M. Matas**[1,e]

[1] Faculty of Nuclear Sciences and Physical Engineering, Czech Technical University in Prague, Břehová 7, 11519 Prague, Czech Republic
[2] High and Medium Energy Group, Instituto de Física e Matemática, Universidade Federal de Pelotas (UFPel), Caixa Postal 354, Pelotas, RS 96010-900, Brazil

Received: 1 October 2020 / Accepted: 23 February 2021 / Published online: 3 March 2021

Abstract The impact of nonlinear effects in the diffractive observables that will be measured in future electron-ion collisions is investigated. We present, for the first time, the predictions for the diffractive structure function and reduced cross sections derived using the solution to the Balitsky–Kovchegov equation with the collinearly-improved kernel and including the impact-parameter dependence. We demonstrate that the contribution of the diffractive events is enhanced in nuclear collisions and that the study of the ratio between the nuclear and proton predictions will be useful to discriminate among different models of the dipole-target scattering amplitude and, consequently, will allow us to constrain the description of QCD dynamics in parton densities.

1 Introduction

The understanding of the high-energy (small-x) regime of quantum chromodynamics (QCD) is one of the main challenges of this theory [1–3]. Experimentally, this regime was intensely investigated in ep collisions at HERA (DESY) and has been studied in pp, pA, and AA collisions at RHIC (BNL) and at the LHC (CERN). These experiments indicate that gluons play a dominant role in the structure of hadrons, with the gluon density rapidly increasing at smaller values of x. Theoretically, the growth of the gluon distribution is expected to saturate, with the system forming a Color Glass Condensate (CGC), whose evolution with energy is described by an infinite hierarchy of coupled equations for the correlators of Wilson lines [4–14]. In the mean-field approximation, the first equation of this hierarchy decouples and boils down to a single non-linear integro-differential equation: the Balitsky–Kovchegov (BK) equation [12–16]. Such equation determines, in the large-N_c limit, where N_c is the number of colors, the evolution of the two-point correlation function, which corresponds to the scattering amplitude $\mathcal{N}(x, \boldsymbol{r}, \boldsymbol{b}_t)$ of a dipole off the CGC, where $r = |\boldsymbol{r}|$ is the transverse dipole size and $\boldsymbol{b}_t$ the impact parameter. This quantity encodes the information about the hadronic scattering as well as the nonlinear and quantum effects in the hadron wave function. For recent reviews, see e.g. [1–3].

During recent years, the CGC formalism has been developed at higher accuracy and successfully applied to describe a large set of observables in ep, pp, pA, and AA collisions. Although these results are very promising, there is no clear consensus on whether the onset of the nonlinear regime has been reached. The search for these nonlinear effects is one of the major motivations for the construction of the Electron-Ion Collider (EIC) in the US [17–19], recently approved, as well as for the proposal of future electron-hadron colliders at CERN [20,21]. These colliders are expected to allow for the investigation of the hadronic structure with an unprecedented precision in inclusive and diffractive observables. In particular, electron-nucleus collisions are considered ideal to probe the nonlinear regime [22]. The larger parton densities in the nuclear case, with respect to the proton case, enhance by a factor $\propto A^{1/3}$ the nuclear saturation scale, $Q^2_{s,A}$, which determines the onset of nonlinear effects in QCD dynamics. Such expectations have motivated an intense interest in phenomenology regarding the implications of gluon saturation effects in QCD observables [17–21]. These studies demonstrated that the analysis of diffractive events can be considered a smoking gun of gluon saturation effects in eA collisions [23–42]. In particular, diffractive events are predicted to contribute with half of the total cross section in the asymptotic limit of very high energies, with the other half

[a] e-mail: Dagmar.Bendova@fjfi.cvut.cz
[b] e-mail: jan.cepila@fjfi.cvut.cz
[c] e-mail: jesus.guillermo.contreras.nuno@cern.ch
[d] e-mail: barros@ufpel.edu.br (corresponding author)
[e] e-mail: matas.marek1@gmail.com

being formed by all inelastic processes [43–46]. In addition, the associated observables depend on the square of the scattering amplitude, which makes them strongly sensitive to the underlying QCD dynamics. These results strongly motivate the study of diffraction in eA collisions using as input in the calculations a realistic model for the scattering amplitude.

In this paper, we investigate the impact of nonlinear effects on diffractive observables that can be measured in future electron-hadron colliders. In particular, we predict the diffractive cross section and diffractive structure functions using the color-dipole formalism and different models for the dipole-hadron scattering amplitude considering ep and eA collisions. Our goal is to improve the studies performed in Refs. [23,24,44,46–50] in the following aspects: (i) unlike Refs. [44,47,48,50], we do not assume that the impact-parameter dependence of $\mathcal{N}$ can be factorized as $\mathcal{N}(x, \boldsymbol{r}, \boldsymbol{b}_t) = N(x, \boldsymbol{r})S(\boldsymbol{b}_t)$, where $S(\boldsymbol{b}_t)$ is the target profile function; (ii) the impact-parameter dependence of $\mathcal{N}(x, \boldsymbol{r}, \boldsymbol{b}_t)$ is derived using the BK equation and taking into account the collinear corrections to the kernel of the evolution equation, following the approach proposed in Refs. [51,52] (in Refs. [46,49] the $\boldsymbol{b}$ dependence of $\mathcal{N}$ is an assumption of the phenomenological models considered); (iii) the predictions for eA collisions are derived using the solution of the BK equation for nuclear targets obtained in Ref. [53], which takes into account the collinear corrections and the impact-parameter dependence, instead of the Glauber–Gribov (GG) approach [54–57] used in Refs. [23,24,46]. For completeness of our study, we compare our predictions with those derived using the IP-Sat and b-CGC models [58,59] for the dipole-proton scattering amplitude, generalized for the nuclear case using the GG approach.

The paper is organized as follows. In the next section, we present a brief overview of the color dipole formalism for the description of diffractive deeply inelastic scattering in ep and eA collisions. The impact-parameter dependent BK equation is presented and its solutions for the cases of a proton and a nucleus are discussed. In Sect. 3, we present our predictions for the ratio between the diffractive and the total cross sections as well as for the diffractive structure functions. A comparison to HERA data is presented and the nuclear dependence of the individual components of the diffractive structure functions is discussed in detail. Finally, in Sect. 4 we summarize our main conclusions.

2 Formalism

Diffractive electron-hadron scattering, $eh \to eXh$, is represented in Fig. 1, where the hadron in the final state carries most of the beam momentum and X represents all the other final state particles. The basic idea is that in the $\gamma^* h$ interaction, the hadron remains intact and a hadronic system X

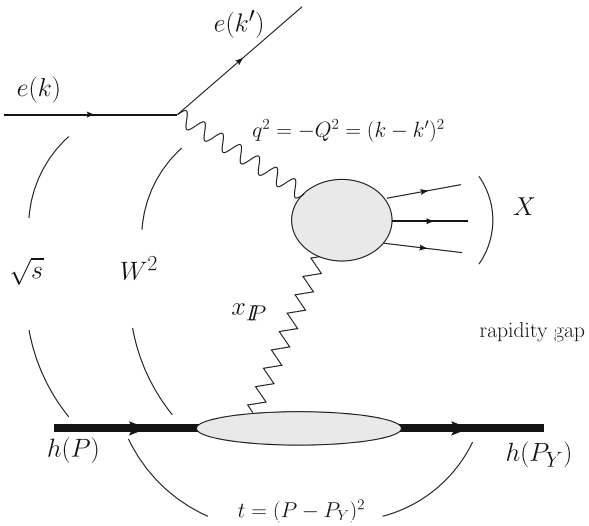

Fig. 1 Diffractive deeply inelastic scattering in electron-hadron collisions, where the hadron can be in particular a proton or a nucleus

with mass M_X is produced with a rapidity gap between them. The fractional longitudinal momentum loss of the hadron is denoted as $x_{I\!P}$ and is related to the photon virtuality Q^2 and M_X^2 as

$$x_{I\!P} = \frac{Q^2 + M_X^2}{Q^2 + W^2}, \tag{1}$$

where W is the photon-hadron center-of-mass energy. In addition, we can define the variable β given by

$$\beta = \frac{Q^2}{Q^2 + M_X^2}, \tag{2}$$

which is related to the Bjorken variable $x = Q^2/(Q^2 + W^2)$ and $x_{I\!P}$ by $x = \beta x_{I\!P}$. The measured diffractive cross section can be expressed as

$$\frac{\mathrm{d}\sigma^{eh\to eXh}}{\mathrm{d}\beta \mathrm{d}Q^2 \mathrm{d}x_{I\!P}} = \frac{4\pi\alpha_{em}^2}{\beta Q^4}\left[1 - y + \frac{y^2}{2}\right]\sigma_r^{D(3)}(x_{I\!P}, \beta, Q^2)\,, \tag{3}$$

where y is the fractional energy loss of the electron in the hadron rest frame and the reduced cross section is related to the diffractive structure functions as

$$\sigma_r^{D(3)}(x_{I\!P}, \beta, Q^2) = F_2^{D(3)}(x_{I\!P}, \beta, Q^2) - \frac{y^2}{1+(1-y)^2} F_L^{D(3)}(x_{I\!P}, \beta, Q^2). \tag{4}$$

Experimentally, diffractive eh scattering is characterized by the presence of a leading hadron at beam rapidities in the final state, and by a rapidity gap in between this hadron and the produced system X. The size of the rapidity gap is $\ln(1/x_{I\!P})$.

Currently, there have been many attempts to describe the diffractive part of the deeply inelastic cross section within

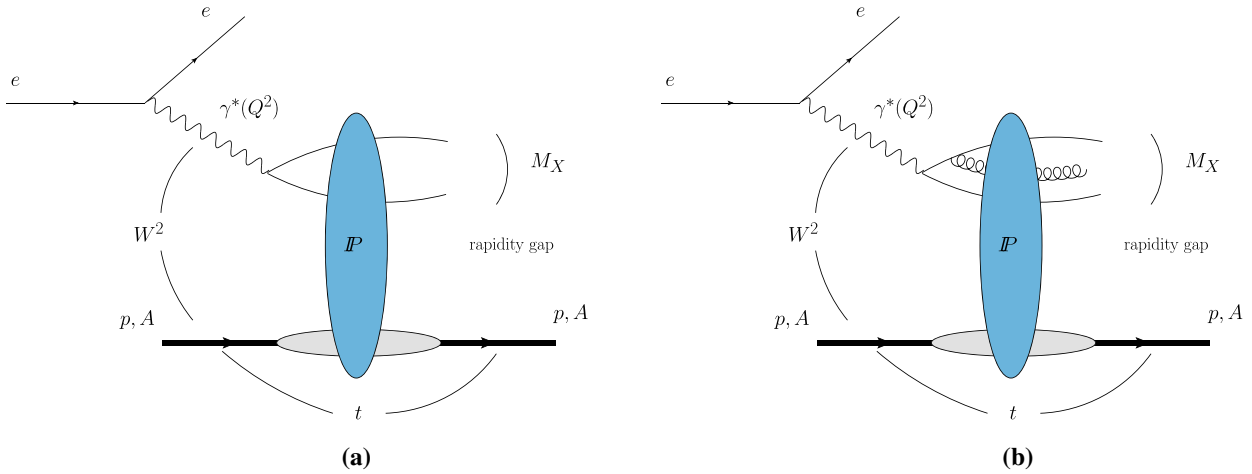

Fig. 2 Diffractive deeply inelastic electron-hadron scattering in the color-dipole formalism, which assumes that the virtual photon fluctuates into a colorless parton Fock state, which interacts elastically with the proton or nucleus. The contributions of $q\bar{q}$ and $q\bar{q}g$ parton Fock states are presented in the left and right panels, respectively

the pQCD, see e.g. Refs. [47,48,60–64]. One of the most successful approaches is the saturation one [47–49] based on the dipole picture of DIS [65–68]. It naturally incorporates the description of both inclusive and diffractive events in a common theoretical framework, as the same dipole-target scattering amplitude enters in the formulation of the inclusive and diffractive cross sections. In this formalism, the total and diffractive cross sections are given by

$$\sigma_{\rm tot}(x,\,Q^2) = \sum_{i=L,\,T} \int {\rm d}z\,{\rm d}^2r |\Psi_i^{\gamma *}(z,\,r)|^2 \int {\rm d}^2\boldsymbol{b}_t \frac{{\rm d}\sigma}{{\rm d}^2\boldsymbol{b}_t}, \tag{5}$$

$$\sigma_{\rm diff}(x,\,Q^2) = \frac{1}{4} \sum_{i=L,\,T} \int {\rm d}z\,{\rm d}^2r |\Psi_i^{\gamma *}(z,\,r)|^2 \times \int {\rm d}^2\boldsymbol{b}_t \left(\frac{{\rm d}\sigma}{{\rm d}^2\boldsymbol{b}_t}\right)^2, \tag{6}$$

where the functions $|\Psi_{T,L}^{\gamma *}(r,\,z)|^2$ represent the probability of the photon with transverse (T) or longitudinal (L) polarization to split into a $q\bar{q}$ pair; these functions can be calculated perturbatively and are expressed by

$$|\Psi_T^{\gamma *}(z,\,r)|^2 = \frac{6\alpha_{em}}{(2\pi)^2} \sum_f e_f^2 \left\{ \left[z^2 + (1-z)^2 \right] \epsilon^2 K_1^2(\epsilon r) + m_f^2 K_0^2(\epsilon r) \right\}, \tag{7}$$

$$|\Psi_L^{\gamma *}(z,\,r)|^2 = \frac{6\alpha_{em}}{(2\pi)^2} \sum_f 4e_f^2 Q^2 z^2 (1-z)^2 K_0^2(\epsilon r), \tag{8}$$

where r is the size of the $q\bar{q}$, z and $(1-z)$ are the momentum fractions of the original photon momentum carried by the quark and anti-quark, respectively, and m_f and e_f are the mass and the charge of a quark with flavor f. Moreover, ${\rm d}\sigma/{\rm d}^2\boldsymbol{b}_t$ denotes the dipole cross section for its scattering off the target at an impact parameter $\boldsymbol{b}_t$; this cross section is related to the dipole-target scattering amplitude $\mathcal{N}(x, \boldsymbol{r}, \boldsymbol{b}_t)$ by

$$\frac{{\rm d}\sigma}{{\rm d}^2\boldsymbol{b}_t} = 2\mathcal{N}(x, \boldsymbol{r}, \boldsymbol{b}_t). \tag{9}$$

In addition, it is possible to extend the color-dipole formalism to estimate the diffractive structure functions. For that, one needs to compute the reduced diffractive cross section $\sigma_r^{D(3)}(x_{I\!P},\,\beta,\,Q^2)$. In Refs. [47,48], the authors have derived expressions for $F_2^{D(3)}$ directly in the transverse momentum space and then transformed them to impact-parameter space where the dipole approach can be applied. Following Refs. [46–49], we assume that the virtual photon fluctuates into a colorless parton Fock state, which interacts elastically with the proton or the nucleus. We include the contributions of $q\bar{q}$ and $q\bar{q}g$ states, with the associated diffractive processes being represented in Fig. 2. Both processes are characterized by the presence of a rapidity gap in the final state due to the color singlet exchange. As a consequence, the diffractive structure function can be expressed by

$$F_2^{D(3)}\left(Q^2, \beta, x_{I\!P}\right) = F_{q\bar{q},L}^D + F_{q\bar{q},T}^D + F_{q\bar{q}g,T}^D, \tag{10}$$

where T and L refer to the polarization of the virtual photon. For the $q\bar{q}g$ contribution, only the transverse polarization is considered, since the longitudinal counterpart has no leading logarithm in Q^2. The computation of the different contributions was done in Refs. [46–49] and here we only quote the final results. The transverse component of the $q\bar{q}$ contribution is given by

$$x_{I\!P} F^D_{q\bar{q},T}(x_{I\!P}, \beta, Q^2) = \frac{N_c Q^4}{16\pi^3\beta} \sum_f e_f^2 \int_{z_0}^{1/2} \mathrm{d}z z(1-z) \times \left\{ \epsilon^2 \left[z^2 + (1-z)^2 \right] \Phi_1 + m_f^2 \Phi_0 \right\}, \tag{11}$$

while the longitudinal contribution is

$$x_{I\!P} F^D_{q\bar{q},L}(x_{I\!P}, \beta, Q^2) = \frac{N_c Q^6}{4\pi^3\beta} \sum_f e_f^2 \int_{z_0}^{1/2} \mathrm{d}z z^3 (1-z)^3 \Phi_0, \tag{12}$$

where $\epsilon^2 = z(1-z)Q^2 + m_f^2$ and the variable z_0 is defined by

$$z_0 = \frac{1}{2}\left(1 - \sqrt{1 - \frac{4m_f^2}{M_X^2}}\right). \tag{13}$$

Moreover, the auxiliary functions $\Phi_{0,1}$ are expressed as follows

$$\Phi_{0,1} = \int \mathrm{d}^2\boldsymbol{b}_t \left[\int_0^\infty \mathrm{d}r r K_{0,1}(\epsilon r) J_{0,1}(kr) \frac{\mathrm{d}\sigma}{\mathrm{d}^2\boldsymbol{b}_t}(\boldsymbol{b}_t, \boldsymbol{r}, x_{I\!P}) \right]^2, \tag{14}$$

with $k^2 = z(1-z)M_X^2 - m_f^2$.
Finally, the transverse $q\bar{q}g$ component is given by

$$x_{I\!P} F^D_{q\bar{q}g,T}(x_{I\!P}, \beta, Q^2) = \frac{\alpha_s \beta}{8\pi^4} \sum_f e_f^2 \int \mathrm{d}^2\boldsymbol{b}_t \int_0^{Q^2} \mathrm{d}\kappa^2 \int_\beta^1 \mathrm{d}z \left\{ \kappa^4 \ln\frac{Q^2}{\kappa^2} \times \left[\left(1 - \frac{\beta}{z}\right)^2 + \left(\frac{\beta}{z}\right)^2 \right] \times \left[\int_0^\infty \mathrm{d}r r \frac{\mathrm{d}\sigma_g}{\mathrm{d}^2\boldsymbol{b}_t} K_2\left(\sqrt{z}\kappa r\right) J_2\left(\sqrt{1-z}\kappa r\right) \right]^2 \right\}, \tag{15}$$

where

$$\frac{\mathrm{d}\sigma_g}{\mathrm{d}^2\boldsymbol{b}_t} = 2\left[1 - \left(1 - \frac{1}{2}\frac{\mathrm{d}\sigma}{\mathrm{d}^2\boldsymbol{b}_t}\right)^2\right]. \tag{16}$$

As pointed out in Ref. [49], at small β and low Q^2, the leading $\ln(1/\beta)$ terms should be resumed and the above expression should be modified. However, as a description with the same quality using Eq. (15) is possible by adjusting the coupling [49] and our focus will be in the predictions for medium values of β, in what follows we will use this expression for our studies.

In the color-dipole formalism, the energy, photon virtuality and atomic number dependencies of diffractive observables are fully determined by the evolution of $\mathcal{N}$ and, consequently, strongly dependent on the description of the QCD dynamics at small-x and large-A. As discussed in the introduction, the Balitsky–Kovchegov (BK) equation is a nonlinear evolution equation in rapidity Y for the dipole-hadron scattering amplitude and is given by [12–16]

$$\frac{\partial\mathcal{N}(\boldsymbol{r}, \boldsymbol{b}_t, Y)}{\partial Y} = \int \mathrm{d}\boldsymbol{r_1}\, K(\boldsymbol{r}, \boldsymbol{r_1}, \boldsymbol{r_2}) [\mathcal{N}(\boldsymbol{r}_1, \boldsymbol{b}_1, Y) + \mathcal{N}(\boldsymbol{r}_2, \boldsymbol{b}_2, Y) - \mathcal{N}(\boldsymbol{r}, \boldsymbol{b}_t, Y) - \mathcal{N}(\boldsymbol{r}_1, \boldsymbol{b}_1, Y)\mathcal{N}(\boldsymbol{r}_2, \boldsymbol{b}_2, Y)]. \tag{17}$$

In the following, $r \equiv |\boldsymbol{r}|$, $r_1 \equiv |\boldsymbol{r}_1|$ and $r_2 \equiv |\boldsymbol{r}_2|$ are the transverse sizes of the original dipole and of the two daughter dipoles, respectively, and the $b_i \equiv \boldsymbol{b}_i$ are the corresponding impact-parameter vectors. During the last years, different functional forms have been proposed for the kernel $K(\boldsymbol{r}, \boldsymbol{r_1}, \boldsymbol{r_2})$ of the BK equation, considering e.g., the corrections that take into account the running of the coupling constant as well as the resummation of collinear logarithms. The studies performed in Refs. [69–71], which disregarded the dependence on the impact parameter, demonstrated that it is possible to obtain a good description of the inclusive HERA data by taking into account these corrections to the kernel. However, in order to describe in detail exclusive processes, it is fundamental to take into account also the impact-parameter dependence of the dipole-target scattering amplitude. In Refs. [51,52], the BK equation was solved for a proton target including the dependence on impact parameter and using the collinearly-improved kernel. The authors have demonstrated that the contribution coming from the large impact parameters is strongly suppressed by the collinear corrections and that the HERA data for the F_2 structure function and for the exclusive vector meson production are reasonably well described. More recently, this approach was extended for nuclear targets in Refs. [53,72]. In what follows, we discuss the main characteristics of these solutions, which are used as input in the calculation of the diffractive observables.

In Fig. 3, we present the solutions of the impact-parameter dependent BK equation with the collinearly-improved kernel for a proton target, denoted as b-dep ciBK hereafter, for a fixed value of b and two values of x. As in Refs. [51,52], the initial condition is given by a combination of the GBW model [47,48] for the dependence on the dipole size r and a Gaussian distribution for the impact-parameter dependence. The parameters have been fixed using HERA data for F_2 and for the $|t|$-distribution of the J/Ψ photoproduction. For comparison, we also present the predictions from the IP-Sat and b-CGC models (see e.g. Refs. [58,73,74]), which are phenomenological models based on the CGC physics and that are also able to describe HERA data. Although the predictions give similar results for small dipoles, they strongly differ at large-r. Such difference is smaller for smaller values of the Bjorken-x, with the onset of saturation being slower in the b-dep ciBK case. This result indicates that observables sensitive to large dipole sizes will be sensitive to the modeling of $\mathcal{N}$.

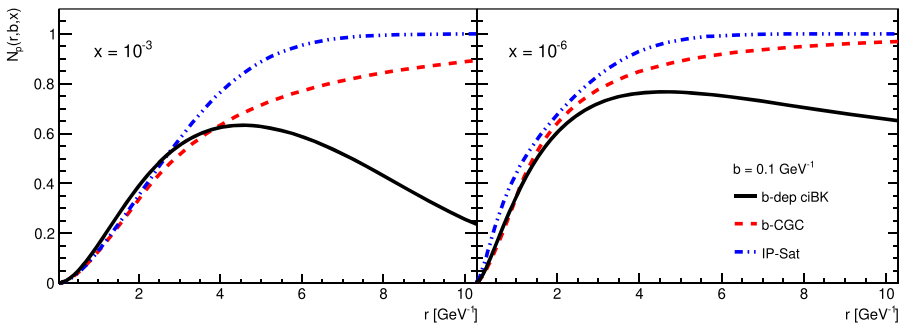

Fig. 3 Dipole-proton scattering amplitude for a fixed impact parameter ($b = 0.1$ GeV^{-1}) and two values of x

In Fig. 4, the BK solution for a nuclear target, denoted b-dep ciBK-A hereafter, is presented for a fixed value of b and two values of x. As in Ref. [53], the initial condition is given by

$$\mathcal{N}_A(\boldsymbol{r}, \boldsymbol{b}_A, Y = 0) = 1 - \exp\left[-\frac{1}{2}\frac{Q_{s0}^2(A)}{4} r^2 T_A(\boldsymbol{b}_{q_1}, \boldsymbol{b}_{q_2})\right], \quad (18)$$

where $\boldsymbol{b}_A$ is the dipole-nucleus impact parameter, $Y = \ln(x_0/x)$ with $x_0 = 0.008$, $\boldsymbol{b}_{q_i}$ are the impact parameters with respect to the dipole constituents, and Q_{s0}^2 is a free parameter determined for each value of A by the comparison between the dipole predictions for F_2^A and those obtained using the collinear formalism and the EPPS16 parametrization [75] for $Y = 0$. The nuclear profile $T_A(\boldsymbol{b}_{q_1}, \boldsymbol{b}_{q_2})$ is given by

$$T_A(\boldsymbol{b}_{q_1}, \boldsymbol{b}_{q_2}) = k\left[T_A(\boldsymbol{b}_{q_1}) + T_A(\boldsymbol{b}_{q_2})\right], \quad (19)$$

where the individual profiles $T_A(\boldsymbol{b}_{q_i})$ are described by a Woods-Saxon distribution and k is the factor which ensures $kT_A(0) = 1$. For comparison, we also present the predictions for $\mathcal{N}_A$ derived using the Glauber–Gribov (GG) formalism [54–57,76], which implies that $\mathcal{N}_A(\boldsymbol{r}, \boldsymbol{b}_A, Y)$ is given by

$$\mathcal{N}_A(\boldsymbol{r}, \boldsymbol{b}_A, Y) = 1 - \exp\left[-\frac{1}{2}\sigma_{dp}(Y, \boldsymbol{r}^2)\, T_A(\boldsymbol{b}_A)\right], \quad (20)$$

where σ_{dp} is the dipole-proton cross section, which is expressed in terms of the dipole-proton scattering amplitude as follows

$$\sigma_{dp}(Y, \boldsymbol{r}^2) = 2\int \mathrm{d}^2\boldsymbol{b}_p\, \mathcal{N}_p(\boldsymbol{r}, \boldsymbol{b}_p, Y), \quad (21)$$

where $\boldsymbol{b}_p$ is the impact parameter for the dipole-proton interaction. In order to estimate the dependence of our predictions on the treatment of the nonlinear effects, we compare the solution of the BK equation for the nuclear case with those derived using the BK solution for the proton as the input in Eq. (20), the said predictions being denoted as b-dep ciBK + GG in what follows. In addition, we also present the predictions obtained using the IP-Sat and b-CGC models as input in the GG formula, which are denoted as IP-Sat + GG and b-CGC + GG, respectively. The results presented in Fig. 4 for $A = 40$ (upper panels) and $A = 208$ (lower panels) indicate that the onset of the nonlinear (saturation) effects ($\mathcal{N} \approx 1$) occurs at smaller values of r for heavier nuclei and for smaller values of x. Such result is indeed not surprising, since the nuclear saturation scale is expected to increase with the atomic number of the nucleus and with the increasing rapidity Y. The BK equation for the nuclear case predicts a faster onset of total saturation for $x = 10^{-3}$ than the predictions derived using the GG formula. On the other hand, for $x = 10^{-6}$, the b-dep ciBK + GG prediction saturates at smaller values of r, with the transition between the linear (small-r) and nonlinear (large-r) regimes being strongly model dependent. Such result motivates the analysis of the impact of these distinct descriptions for the nonlinear effects on the diffractive observables that can be measured in future eA collisions.

3 Results

Initially, let's investigate the impact of the nonlinear effects on the ratio between the diffractive and total cross sections, defined by $R_\sigma = \sigma_{\mathrm{diff}}/\sigma_{\mathrm{tot}}$, which allows us to analyze if the diffractive and inclusive processes have a similar energy-, x-, Q^2- and A-dependencies. The experimental results from HERA indicate a very similar energy-dependence of the diffractive and the total cross section. It is important to emphasize that saturation physics provides a simple explanation for this finding. As shown e.g. in Refs. [44,47,48], the saturation effects suppress the contribution of the large-size dipoles, associated to nonperturbative physics, and implies that the energy dependence is similar for inclusive and diffractive processes. In contrast, to explain this aspect of data using a description based on the collinear factorization is nontrivial. In this case the energy dependence of the inclusive and diffractive cross sections is controlled by the x-dependence of the ordinary and the diffractive parton densities, which is not predicted by the theory. Another important aspect is that in the black-disc limit, where $\frac{\mathrm{d}^2\sigma}{\mathrm{d}^2\boldsymbol{b}} \to 2$, we have that $R_\sigma \to 1/2$. Therefore, this observable can be considered

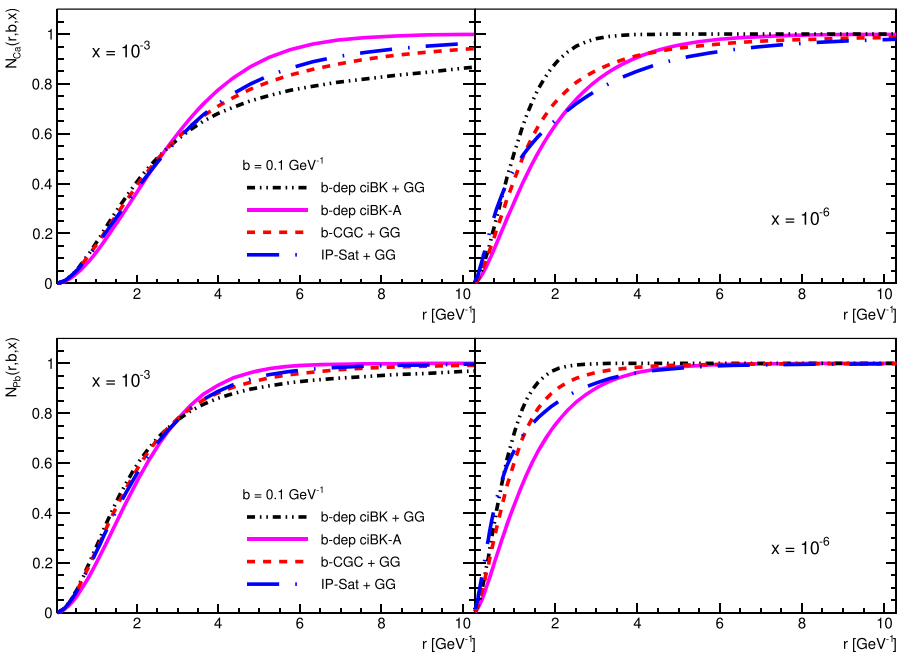

Fig. 4 Dipole-nucleus scattering amplitude for a fixed impact parameter $b = 0.1$ GeV^{-1} and two values of x. Predictions for $A = 40$ (208) are presented in the upper (lower) panels

as a measure of how close to the black-disc limit we are. Previous calculations have demonstrated that R_σ increases with the atomic number A [43–46]. The results presented in Fig. 5 agree with these expectations, with the distinct models predicting that $\approx 20\%$ of the events will be diffractive in ePb collisions. We have verified that this value decreases with the increase of the photon virtuality. Regarding to the x - dependence, we have for $A = 1$ (left panel) that the IP-SAT and b-dep ciBK models predict a flat behaviour while the b-CGC one predicts a mild increasing for smaller values of x, in agreement with the results obtained in Ref. [24]. The b-dep ciBK model predicts the smaller amount of diffractive events. The different behaviours for the x - dependence are associated to the distinct transitions between the linear and nonlinear regimes predicted by these models (see Fig. 3) and the distinct impact parameter dependencies. While in the b-CGC model, the impact parameter dependence is present in the saturation scale, in the other models it is determined by the nucleon profile. As the inclusive and diffractive cross sections are dominated by distinct ranges of impact parameter, with the diffractive one being dominated by larger values of b, one has that the ratio between these cross section is sensitive to these differences. For the nuclear case (middle and right panels), one has that the IP-SAT + GG and b-CGC + GG predictions have a x - dependence similar to that verified for the proton, with the main difference being the higher normalization. In contrast, the b-dep ciBK-A and b-dep ciBK + GG results differ in their predictions for the x-dependence of the ratio, with the b-dep ciBK-A one being almost flat, while the b-dep ciBK + GG model predicts that R_σ increases at smaller values of x. One has verified that this difference arises from the different evolution of the amplitudes in the intermediate - $\boldsymbol{r}$ region, shown in Fig. 4, which is faster in the b-dep ciBK + GG model.

The diffractive cross section $ep \to eXY$ has been measured by the H1 and ZEUS experiments at HERA by tagging the proton in the final state ($Y = p$) or by selecting events with a large rapidity gap between the systems X and Y. In our study, we will focus on the case where the proton or the nucleus remains intact in the final state. Moreover, our analysis will focus on the kinematic range of small Q^2 and $x_{I\!P} \leq 10^{-2}$, which is the range expected to be probed in the future EICs and where the nonlinear effects are predicted to significantly contribute. In Fig. 6, we present our predictions for the β dependence of the diffractive structure function $F_2^{D(3)}$ at fixed Q^2 and $x_{I\!P}$, considering different models for the dipole-proton scattering amplitude. Although the general structure of the β-spectrum for the distinct components is determined by the photon wave function, we have that the normalization of these distinct terms depends on the modeling of the dipole-proton interaction, with the b-dep ciBK prediction being smaller than the other two phenomenological models. Moreover, this model predicts a smaller contribution of the $q\bar{q}g$ component at small-β.

In Fig. 7, we present the predictions for the $x_{I\!P}$-dependence of the reduced diffractive cross section $\sigma_r^{D(3)}(x_{I\!P}, \beta, Q^2)$ at different combinations of the photon virtuality and values of β, considering the b-CGC, IP-Sat, and b-dep ciBK models for the dipole-proton scattering amplitude. The data from H1 are presented for comparison [77]. The $x_{I\!P}$-dependencies of

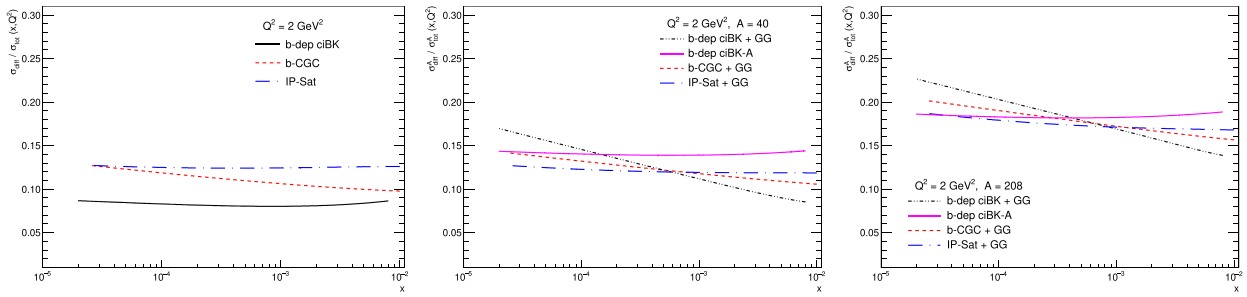

Fig. 5 Predictions for the x dependence of the ratio $R_\sigma = \sigma_{\rm diff}/\sigma_{\rm tot}$ for **a** $A = 1$, **b** $A = 40$ and **c** $A = 208$, considering distinct models for the dipole-target scattering amplitude and a fixed photon virtuality ($Q^2 = 2$ GeV^2)

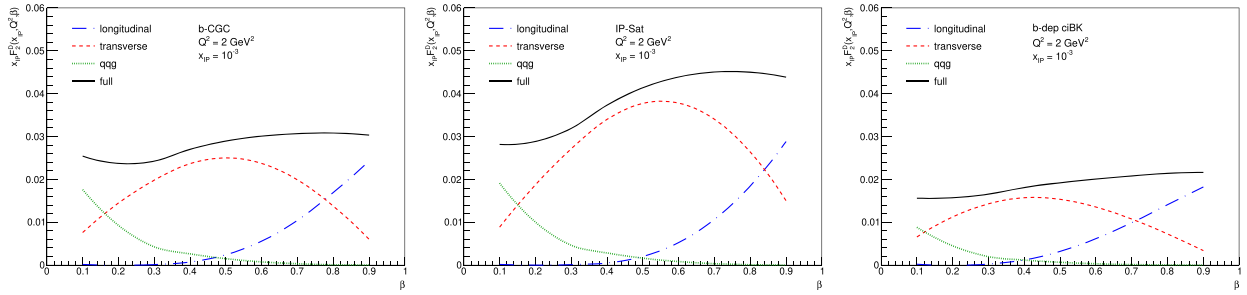

Fig. 6 Predictions for the β dependence of the different components of $F_2^{D(3)}$ considering distinct models for the dipole-proton scattering amplitude

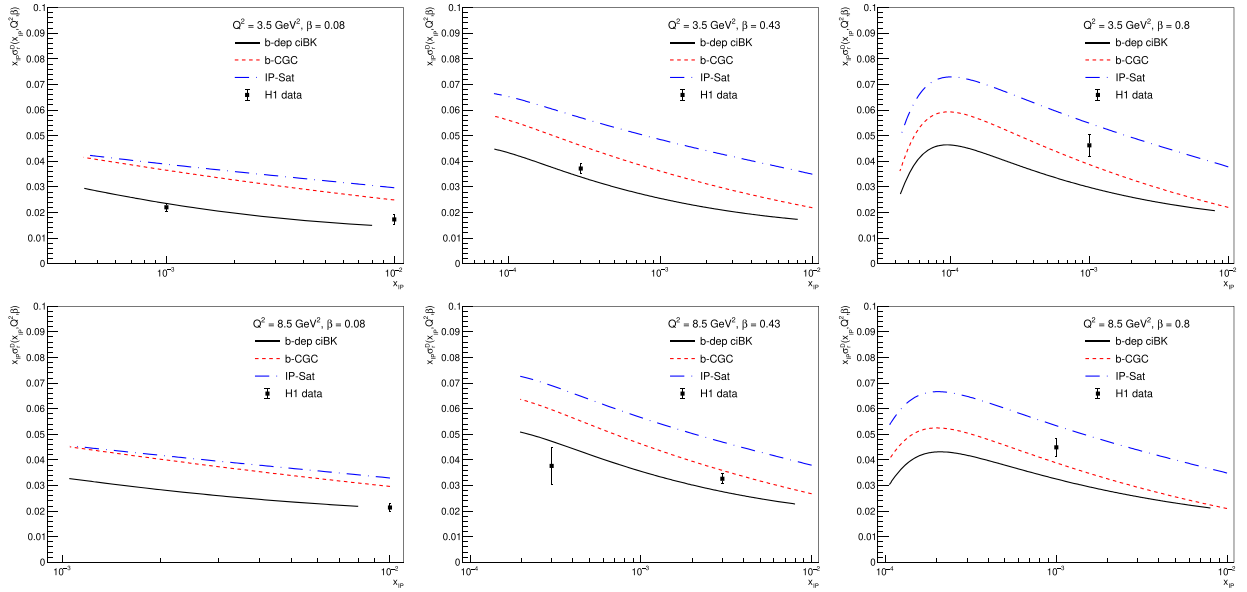

Fig. 7 Predictions for the $x_{I\!P}$-dependence of the reduced diffractive cross section $\sigma_r^{D(3)}(x_{I\!P}, \beta, Q^2)$ at different combinations of the photon virtuality and β, considering the b-CGC, IP-Sat, and b-dep ciBK models for the dipole-proton scattering amplitude. Data from H1 are presented for comparison [77]

the predictions are similar. However, one has that the normalization of the b-dep ciBK prediction is smaller than the b-CGC and IP-Sat one, in agreement with the results derived for the diffractive structure function. We observe that the data for medium and small β is better described by the b-dep ciBK model, but this model underestimates the data at large β values. The opposite situation occurs for the other two models. Unfortunately, due to the scarcity of data, a more definitive conclusion is not possible. However, our results indicate that a future analysis of this observable, to be performed in the EIC and LHeC, will be very useful to constrain the underlying assumptions about the QCD dynamics.

As discussed in previous sections, the impact of nonlinear effects is expected to be enhanced in eA collisions and, as demonstrated in Fig. 5, the contribution from diffractive events is larger in the nuclear case. Such results motivate the study of the diffractive structure functions $F_2^{D(3)}$ and the reduced diffractive cross sections $\sigma_r^{D(3)}(x_{I\!P}, \beta, Q^2)$ for different nuclei. In our analysis, we estimate the behavior of the ratio between these quantities for nuclei and the associated predictions for ep collisions re-scaled by the atomic number A. If the nuclear effects are negligible, such ratios are equal to unity. Therefore, the study of these ratios for different nuclei allows us to investigate the impact of nonlinear corrections in the kinematic range that will be probed in the future electron-ion colliders.

Initially, in Fig. 8, we present our predictions for the β (upper panels), $x_{I\!P}$ (middle panels) and Q^2 (lower panels) dependencies of the ratio $\sigma_r^{D(3),A}(x_{I\!P}, \beta, Q^2)/A \cdot \sigma_r^{D(3),p}(x_{I\!P}, \beta, Q^2)$ for $A = 40$ (left panels) and $A = 208$ (right panels), considering the different models for the dipole-nucleus scattering amplitude. Our results indicate that a future experimental analysis of this observable for two distinct nuclei will be very useful, since the normalization and dependencies on β, $x_{I\!P}$ and Q^2 are strongly dependent on the description of the QCD dynamics. In particular, one can observe that the predictions derived using the impact-parameter dependent BK equation are larger than those obtained using the phenomenological models.

In order to understand the origin of these different behaviours for the reduced cross section, which is the main observable to probe the diffractive processes, in what follows we will investigate how the different components of the diffractive structure function, given by Eq. (10), are impacted by the description of the QCD dynamics. Our analysis is motivated by the fact that, depending on the value of β, $F_2^{D(3)}$ is dominated by a different component (see Fig. 6) and that the future EIC will mainly probe the kinematical range of small inelasticity y, where $\sigma_r^{D(3)} \approx F_2^{D(3)}$. The predictions for the β, $x_{I\!P}$ and Q^2 dependencies of the ratio $F_2^{D(3),A}/AF_2^{D(3),p}$ are presented in Fig. 9 considering the IP-Sat + GG (left panels), b-dep ciBK + GG (middle panels) and b-dep ciBK-A (right panels) models for the dipole-nucleus scattering amplitude. In particular, in Fig. 9 (upper panels) we present our predictions for the β-dependence of the ratio $F_2^{D(3),A}/AF_2^{D(3),p}$ for $A = 208$, $Q^2 = 2\,\text{GeV}^2$ and $x_{I\!P} = 10^{-3}$, which can be potentially studied in the future eA colliders. Moreover, we present the predictions for the different components that contribute to the diffractive structure function. Our results for the IP-Sat + GG model agree with those presented in Ref. [46] using the same approach. However, we show that the predictions are strongly dependent on the modeling of the dipole-target scattering amplitude. In particular, b-dep ciBK models predict a nuclear enhancement of all components that contribute to the diffractive structure function, which is mainly associated with the smaller normalization of the diffractive structure function of the proton in comparison to the IP-Sat model. Such result explain the enhancement observed in the upper panels of Fig. 8 for the b-dep ciBK models. We have that the b-dep ciBK predictions for the β dependence of the sum of the components (denoted full in the figures) are similar, although they predict very distinct behaviours for the longitudinal contribution. However, such difference occurs at small - β, where the contribution of the longitudinal term for $F_2^{D(3)}$ is negligible. It is important to emphasize that we also have estimated the ratio for $A = 40$ and verified that the prediction for the $q\bar{q}g$ is larger than for $A = 208$. Therefore, similarly to Ref. [46], we also predict a strong suppression of the $q\bar{q}g$ component with increasing atomic number A. The predictions for the $x_{I\!P}$-dependence of the ratio $F_2^{D(3),A}/AF_2^{D(3),p}$ are presented in Fig. 9 (middle panels). The results were derived assuming $A = 208$, $Q^2 = 2\,\text{GeV}^2$ and $\beta = 0.8$. or this value of β, the diffractive structure is mostly dominated by the longitudinal and transverse components. One has that the different models predict distinct behaviours for the $x_{I\!P}$-dependence of these components, which implies that the full prediction becomes dependent on the model used to describe the dipole-nucleus interaction. The dependence on the photon virtuality of the ratio $F_2^{D(3),A}/AF_2^{D(3),p}$ is analyzed in Fig. 9 (lower panels) for $A = 208$, $x_{I\!P} = 10^{-3}$ GeV^2 and $\beta = 0.8$. We have that the different models predict that the ratio will be almost constant in the Q^2 range considered, with the main differences being the normalization and the behavior at small - Q^2, which are dependent on the approach.

4 Summary

Future electron-ion collisions will allow us to study the high-gluon density regime of QCD, where the contribution of nonlinear (saturation) effects are expected to determine the behavior of the inclusive, diffractive and exclusive observables. In this paper, we have investigated the impact of these

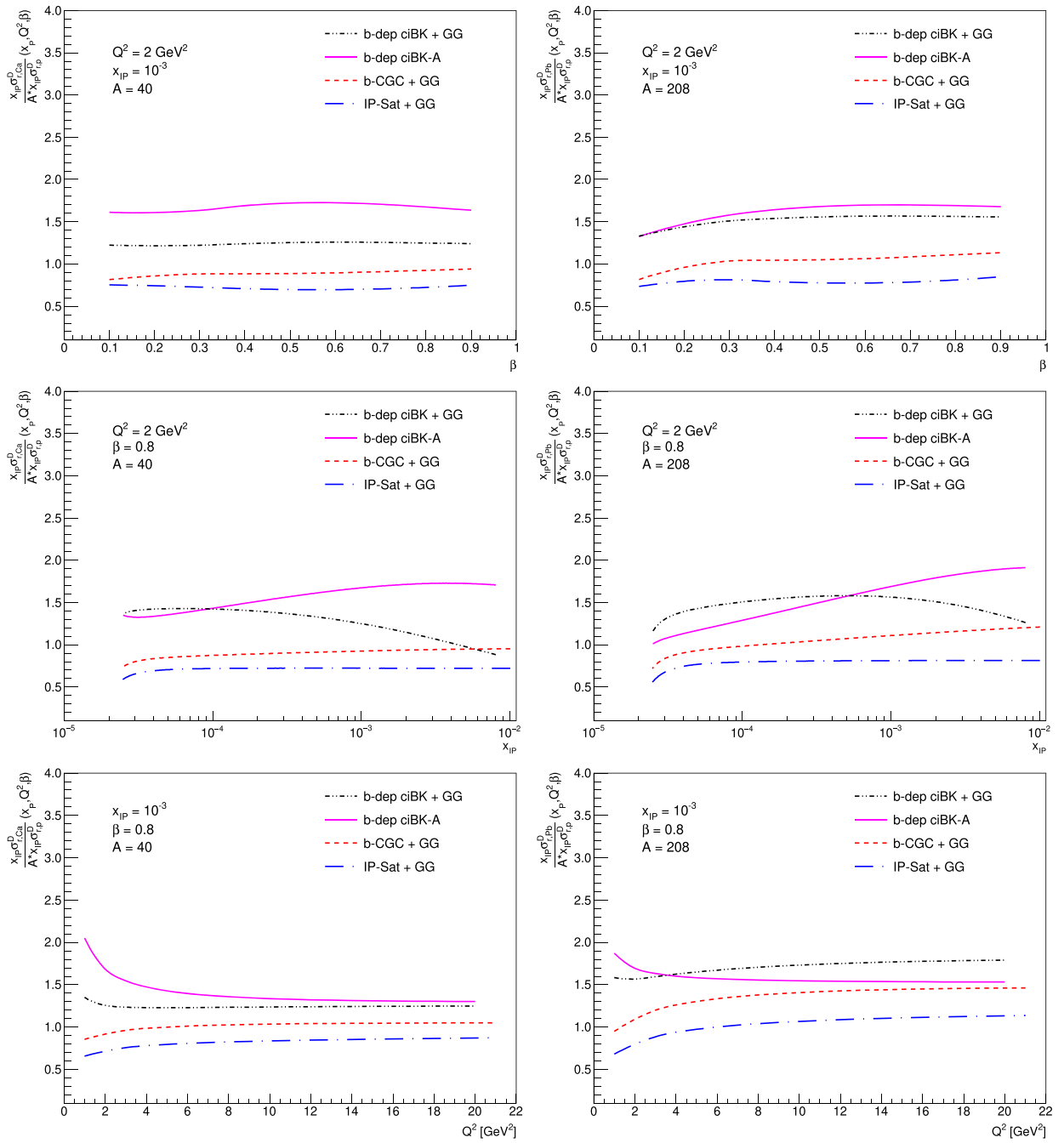

Fig. 8 Predictions for the β (upper panels), $x_{I\!P}$ (middle panels) and Q^2 (lower panels) dependencies of the ratio $\sigma_r^{D(3),A}(x_{I\!P}, \beta, Q^2)/A \cdot \sigma_r^{D(3),p}(x_{I\!P}, \beta, Q^2)$ for $A = 40$ (left panels) and $A = 208$ (right panels) considering the different models for the dipole-nucleus scattering amplitude

effects on diffractive observables. In particular, we have presented, for the first time, the predictions for the diffractive structure functions and reduced diffractive cross sections derived using the solution of the impact-parameter dependent Balitsky–Kovchegov equation for the dipole-target scattering amplitude. We have presented the predictions for ep and eA collisions, considering the kinematic ranges that will be probed by the EIC, LHeC and FCC-eh. It has been demonstrated that the contribution of the diffractive events increases with the atomic number, being of the order of 20% for ePb

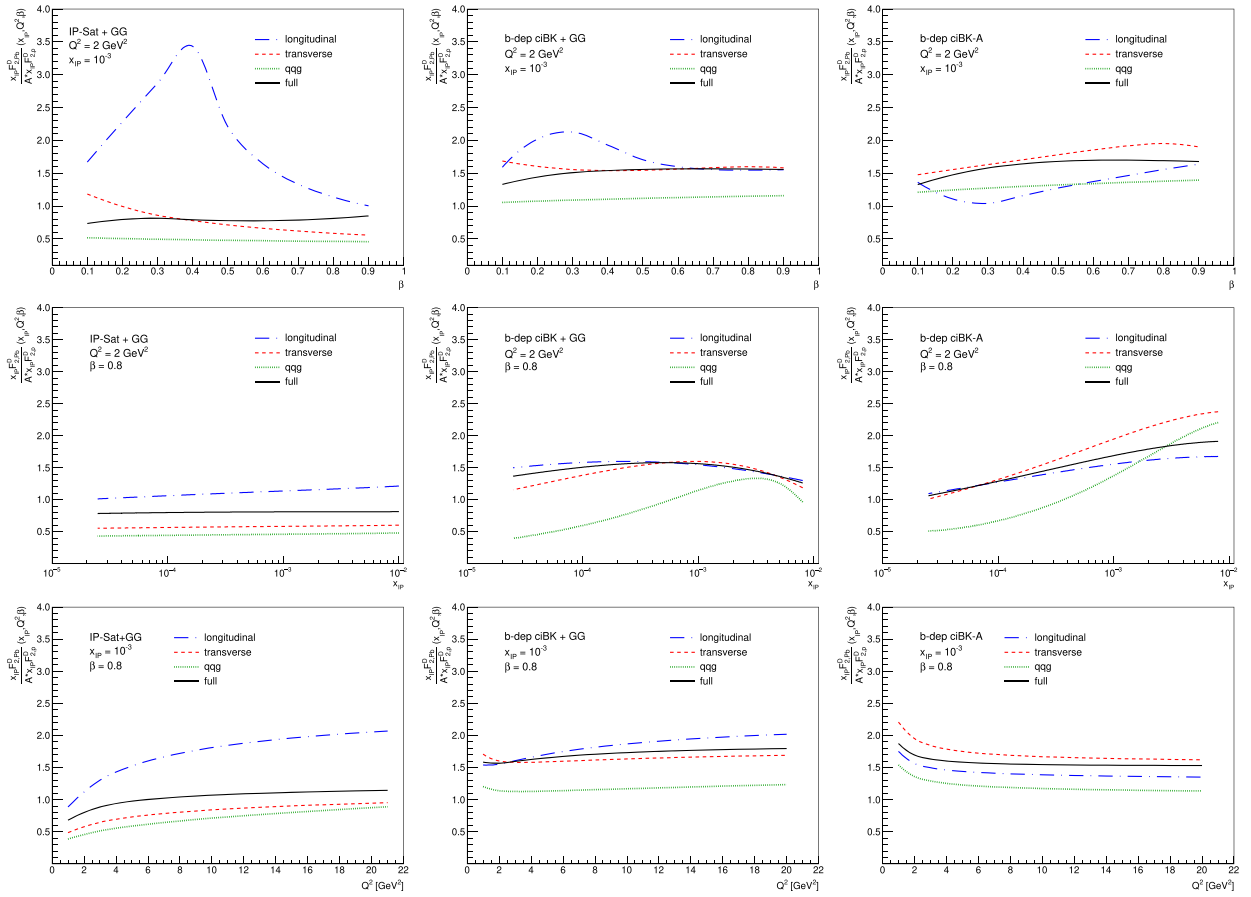

Fig. 9 Predictions for the β, $x_{I\!P}$, and Q^2 dependencies (from top to bottom, respectively) of the ratio $F_2^{D(3),A}/AF_2^{D(3),p}$ for $A = 208$ considering the IP-Sat + GG (left panels), b-dep ciBK + GG (middle panels) and b-dep ciBK-A (right panels) models for the dipole-nucleus scattering amplitude. Predictions for the distinct components are presented separately

collisions, with this prediction being almost independent on the modeling of the dipole-nucleus interaction. Our results for ep collisions indicate that the BK equation satisfactorily describes the data and implies a smaller normalization for the reduced cross section in comparison to the phenomenological models based on the CGC physics. For eA collisions, we have shown that a future experimental analysis of the diffractive observables will be useful to improve our understanding of QCD dynamics at high parton densities.

Acknowledgements VPG would like to thank the members of the Czech Technical University in Prague for the warm hospitality during the beginning of this project. VPG was partially financed by the Brazilian funding agencies CNPq, FAPERGS and INCT-FNA (processes number 464898/2014-5). This work has been partially supported by the grant LTC17038 of the INTER-EXCELLENCE program at the Ministry of Education, Youth and Sports of the Czech Republic, by the grant 18-07846Y of the Czech Science Foundation (GACR) and by the Centre of Advanced Applied Sciences with the number:CZ.02.1.01/0.0/0.0/16-019/0000778. The Centre of Advanced Applied Sciences is co-financed by the European Union.

Data Availability Statement This manuscript has no associated data or the data will not be deposited. [Authors' comment: This is a theoretical research study, and is based upon analysis of the public experimental data, so no additional data are associated with this work.]

Funded by SCOAP[3].

References

1. F. Gelis, E. Iancu, J. Jalilian-Marian, R. Venugopalan, Annu. Rev. Nucl. Part. Sci. **60**, 463 (2010)
2. H. Weigert, Prog. Part. Nucl. Phys. **55**, 461 (2005)
3. J. Jalilian-Marian, Y.V. Kovchegov, Prog. Part. Nucl. Phys. **56**, 104 (2006)
4. J. Jalilian-Marian, A. Kovner, L. McLerran, H. Weigert, Phys. Rev. D **55**, 5414 (1997)
5. J. Jalilian-Marian, A. Kovner, H. Weigert, Phys. Rev. D **59**, 014014 (1999)
6. J. Jalilian-Marian, A. Kovner, H. Weigert, Phys. Rev. D **59**, 014015 (1999)
7. J. Jalilian-Marian, A. Kovner, H. Weigert, Phys. Rev. D **59**, 034007 (1999)
8. A. Kovner, J. Guilherme Milhano, H. Weigert, Phys. Rev. D **62**, 114005 (2000)
9. H. Weigert, Nucl. Phys. A **703**, 823 (2002)
10. E. Iancu, A. Leonidov, L. McLerran, Nucl. Phys. A **692**, 583 (2001)
11. E. Ferreiro, E. Iancu, A. Leonidov, L. McLerran, Nucl. Phys. A **701**, 489 (2002)
12. I.I. Balitsky, Phys. Rev. Lett. **81**, 2024 (1998)
13. I.I. Balitsky, Phys. Lett. B **518**, 235 (2001)
14. I.I. Balitsky, A.V. Belitsky, Nucl. Phys. B **629**, 290 (2002)
15. Y.V. Kovchegov, Phys. Rev. D **60**, 034008 (1999)
16. Y.V. Kovchegov, Phys. Rev. D **61**, 074018 (2000)
17. D. Boer, M. Diehl, R. Milner, R. Venugopalan, W. Vogelsang, D. Kaplan, H. Montgomery, S. Vigdor et al., arXiv:1108.1713 [nucl-th]
18. A. Accardi, J.L. Albacete, M. Anselmino, N. Armesto, E.C. Aschenauer, A. Bacchetta, D. Boer, W. Brooks et al., Eur. Phys. J. A **52**(9), 268 (2016)
19. E.C. Aschenauer et al., Rep. Prog. Phys. **82**(2), 024301 (2019)
20. J.L. Abelleira Fernandez et al. [LHeC Study Group Collaboration], J. Phys. G **39**, 075001 (2012)
21. P. Agostini et al., arXiv:2007.14491 [hep-ex]
22. A. Deshpande, R. Milner, R. Venugopalan, W. Vogelsang, Annu. Rev. Nucl. Part. Sci. **55**, 165 (2005)
23. H. Kowalski, T. Lappi, R. Venugopalan, Phys. Rev. Lett. **100**, 022303 (2008)
24. E.R. Cazaroto, F. Carvalho, V.P. Goncalves, F.S. Navarra, Phys. Lett. B **671**, 233 (2009)
25. V.P. Goncalves, M.S. Kugeratski, M.V.T. Machado, F.S. Navarra, Phys. Rev. C **80**, 025202 (2009)
26. A. Caldwell, H. Kowalski, Phys. Rev. C **81**, 025203 (2010)
27. T. Lappi, H. Mantysaari, Phys. Rev. C **83**, 065202 (2011)
28. T. Toll, T. Ullrich, Phys. Rev. C **87**, 024913 (2013)
29. N. Armesto, A.H. Rezaeian, Phys. Rev. D **90**(5), 054003 (2014)
30. V.P. Gonçalves, D.S. Pires, Phys. Rev. C **91**, 055207 (2015)
31. T. Lappi, H. Mantysaari, R. Venugopalan, Phys. Rev. Lett. **114**(8), 082301 (2015)
32. H. Mantysaari, B. Schenke, Phys. Rev. Lett. **117**(5), 052301 (2016)
33. H. Mantysaari, B. Schenke, Phys. Rev. D **94**(3), 034042 (2016)
34. V.P. Goncalves, F.S. Navarra, D. Spiering, Phys. Lett. B **768**, 299 (2017)
35. J. Cepila, J.G. Contreras, M. Krelina, Phys. Rev. C **97**(2), 024901 (2018)
36. A. Luszczak, W. Schafer, Phys. Rev. C **97**(2), 024903 (2018)
37. H. Mantysaari, R. Venugopalan, Phys. Lett. B **781**, 664–671 (2018)
38. V.P. Goncalves, F.S. Navarra, D. Spiering, Phys. Lett. B **791**, 299–304 (2019)
39. D. Bendova, J. Cepila, J.G. Contreras, Phys. Rev. D **99**(3), 034025 (2019)
40. M. Krelina, V.P. Goncalves, J. Cepila, Nucl. Phys. A **989**, 187–200 (2019)
41. M. Lomnitz, S. Klein, Phys. Rev. C **99**(1), 015203 (2019)
42. H. Mantysaari, B. Schenke, Phys. Rev. C **101**(1), 015203 (2020)
43. N.N. Nikolaev, B.G. Zakharov, V.R. Zoller, Z. Phys, A **351**, 435 (1995)
44. M.S. Kugeratski, V.P. Goncalves, F.S. Navarra, Eur. Phys. J. C **46**, 413 (2006)
45. N.N. Nikolaev, W. Schafer, B.G. Zakharov, V.R. Zoller, JETP Lett. **84**, 537 (2007)
46. H. Kowalski, T. Lappi, C. Marquet, R. Venugopalan, Phys. Rev. C **78**, 045201 (2008)
47. K. Golec-Biernat, M. Wusthoff, Phys. Rev. D **59**, 014017 (1999)
48. K. Golec-Biernat, M. Wusthoff, Phys. Rev. D **D60**, 114023 (1999)
49. C. Marquet, Phys. Rev. D **76**, 094017 (2007)
50. M.A. Betemps, V.P. Goncalves, J.T. de Santana Amaral, Eur. Phys. J. C **66**, 137–146 (2010)
51. J. Cepila, J.G. Contreras, M. Matas, Phys. Rev. D **99**(5), 051502 (2019)
52. D. Bendova, J. Cepila, J.G. Contreras, M. Matas, Phys. Rev. D **100**(5), 054015 (2019)
53. J. Cepila, J.G. Contreras, M. Matas, arXiv:2002.11056 [hep-ph]
54. R.J. Glauber, in *Lecture in Theoretical Physics*, ed. by W.E. Brittin, L.G. Duham, vol 1 (Interscience, New York, 1959)
55. V.N. Gribov, Sov. Phys. JETP **29**, 483 (1969)
56. V.N. Gribov, Sov. Phys. JETP **30**, 709 (1970)
57. A.H. Mueller, Nucl. Phys. B **335**, 115 (1990)
58. H. Kowalski, L. Motyka, G. Watt, Phys. Rev. D **74**, 074016 (2006)
59. H. Kowalski, D. Teaney, Phys. Rev. D **68**, 114005 (2003)
60. J.R. Forshaw, R. Sandapen, G. Shaw, Phys. Lett. B **594**, 283 (2004)
61. A.D. Martin, M.G. Ryskin, G. Watt, Eur. Phys. J. C **44**, 69 (2005)
62. S.J. Brodsky, R. Enberg, P. Hoyer, G. Ingelman, Phys. Rev. D **71**, 074020 (2005)
63. L. Frankfurt, V. Guzey, M. Strikman, Phys. Rep. **512**, 255–393 (2012)
64. N. Armesto, P.R. Newman, W. Slominski, A.M. Stasto, Phys. Rev. D **100**(7), 074022 (2019)
65. N.N. Nikolaev, B.G. Zakharov, Z. Phys. C **49**, 607 (1991)
66. N.N. Nikolaev, B.G. Zakharov, Z. Phys. C **53**, 331 (1992)
67. A.H. Mueller, Nucl. Phys. B **415**, 373 (1994)
68. A.H. Mueller, B. Patel, Nucl. Phys. B **425**, 471 (1994)
69. J.L. Albacete, Nucl. Phys. A **957**, 71–84 (2017)
70. E. Iancu, J.D. Madrigal, A.H. Mueller, G. Soyez, D.N. Triantafyllopoulos, Phys. Lett. B **750**, 643–652 (2015)
71. B. Ducloue, E. Iancu, G. Soyez, D.N. Triantafyllopoulos, Phys. Lett. B **803**, 135305 (2020)
72. D. Bendova, J. Cepila, J.G. Contreras, M. Matas, arXiv:2006.12980 [hep-ph]
73. A.H. Rezaeian, M. Siddikov, M. Van de Klundert, R. Venugopalan, Phys. Rev. D **87**, 034002 (2013)
74. A.H. Rezaeian, I. Schmidt, Phys. Rev. D **88**, 074016 (2013)
75. K.J. Eskola, P. Paakkinen, H. Paukkunen, C.A. Salgado, Eur. Phys. J. C **77**(3), 163 (2017)
76. N. Armesto, Eur. Phys. J. C **26**, 35 (2013)
77. F.D. Aaron et al. (H1), Eur. Phys. J. C **72**, 2074 (2012)

Physics Letters B 817 (2021) 136306

Contents lists available at ScienceDirect

Physics Letters B

www.elsevier.com/locate/physletb

Photonuclear J/ψ production at the LHC: Proton-based versus nuclear dipole scattering amplitudes

D. Bendova *, J. Cepila, J.G. Contreras, M. Matas

Faculty of Nuclear Sciences and Physical Engineering, Czech Technical University in Prague, Czech Republic

ARTICLE INFO

Article history:
Received 24 June 2020
Received in revised form 28 January 2021
Accepted 16 April 2021
Available online 22 April 2021
Editor: W. Haxton

Keywords:
Impact-parameter dependent
Balitsky-Kovchegov equation
Coherent vector meson photoproduction
LHC

ABSTRACT

The coherent photonuclear production of a J/ψ vector meson at the LHC has been computed using two different sets of solutions of the impact-parameter dependent Balitsky-Kovchegov equation. The nuclear dipole scattering amplitudes are obtained either from (i) solutions for this process off proton targets coupled with a Glauber-Gribov prescription, or (ii) from solutions obtained with an initial condition representing the nucleus. These approaches predict different cross sections, which are compared with existing data from ultra-peripheral collisions at the LHC. The latter approach seems to better describe current measurements. Future LHC data should be precise enough to select one of the two approaches as the correct one.

1. Introduction

The exclusive photoproduction of a J/ψ vector meson off a hadron has been recognised for many years as a very sensitive probe of the gluonic structure of hadrons in the perturbative regime of quantum chromodynamics (QCD) [1,2]; thus it has been extensively studied at HERA [3,4]. In recent years, this process has attracted renewed attention. On one hand, due to measurements at the LHC including production off protons and off Pb nuclei and reaching unprecedented energies [5–7]. On the other, because of studies related to the potential of electron-ion colliders [8,9].

As mentioned above, there is plenty of high-quality data from HERA on production off proton targets. Therefore, many computations predicting the behaviour of this process off nuclear targets start from a description of the process off nucleons, where the parameters of the given model are fixed by HERA data, and then apply some form of Glauber formalism to predict the cross sections for photonuclear production. Such an approach has been followed for example in [10–13].

The applicability of using a Glauber approach has been analysed since a long time, e.g. [14,15], but recent advances in the understanding of saturation through the solution of the Balitsky-Kovchegov (BK) equation [16–18] allow for new insights into this question. In particular, the implementation of collinear corrections to the kernel [19,20] (see also [21]) together with a suitable initial condition has been used to find impact-parameter dependent solutions of the BK equation [22], which correctly describe HERA data on vector meson photo- and electroproduction off protons [23]. The use of the collinearly improved kernel allows for phenomenological applications of the BK equation including a dependence on the impact parameter, because it suppresses the so-called Coulomb tails [24]. But as pointed out in [25] this suppression is not valid in all the phase space and the problem of Coulomb tails is still present. Nonetheless, as shown in [22], the suppression in kinematic ranges of interest for current and planned facilities is strong enough to allow for phenomenological studies.

Recently, these advances have been extended to the case of nuclear targets [26] using two approaches: (i) coupling the solution of the BK equation for the case of proton targets to a Glauber-Gribov prescription to obtain the solutions to the nuclear case, and (ii) solving directly the impact-parameter dependent BK equation with an initial condition representing a specific nucleus. In what follows, these two sets of solutions are denoted as b-BK-GG and b-BK-A, respectively.

In this Letter, both approaches are used to predict the cross section for coherent photoproduction of J/ψ vector mesons in Pb–Pb ultra-peripheral collisions (UPC) at the LHC and compare the predictions with data available at different rapidities and at two centre-of-mass energies per nucleon pair, $\sqrt{s_{\rm NN}} = 2.76$ TeV and $\sqrt{s_{\rm NN}} = 5.02$ TeV, corresponding to measurements performed during the LHC Run 1 and Run 2, respectively. It is found that Run 1 measurements at midrapidity strongly disfavour the use of b-BK-GG solutions, and that the expected precision of the measurements with Run 2 data may provide a definitive answer on the question

* Corresponding author.
E-mail address: dagmar.bendova@fjfi.cvut.cz (D. Bendova).

https://doi.org/10.1016/j.physletb.2021.136306

of which approach is the valid one. The rest of this Letter is organised as follows: the next section presents a brief overview of the formalism; Sec. 3 contains the main results, while in Sec. 4 our findings are discussed; the Letter concludes with a brief summary and outlook in Sec. 5.

2. Brief overview of the formalism

In this section a brief overview of the formalism is presented. For the full details see for example [23,26] and references therein.

The cross section for the coherent photoproduction of a J/ψ vector meson, differential on the square of the momentum transfer t at the target vertex, is given by the sum of the contributions from transversely (T) and longitudinally (L) polarised photons:

$$\left.\frac{\mathrm{d}\sigma_{\gamma\mathrm{Pb}}}{\mathrm{d}|t|}\right|_{T,L} = \frac{\left(1+\beta^2\right)\left(R_g^{T,L}\right)^2}{16\pi}|\mathcal{A}_{T,L}|^2. \tag{1}$$

The factor $(1+\beta^2)$ accounts for contributions from the real part of the amplitude, where β is the ratio of real to imaginary parts of the scattering amplitude, while $(R_g^{T,L})^2$ corrects for the so-called skewedness effect [27]. The scattering amplitude of the process is given by

$$\mathcal{A}_{T,L}(x, Q^2, \vec{\Delta}) = i \int \mathrm{d}\vec{r} \int_0^1 \frac{\mathrm{d}z}{4\pi} \int \mathrm{d}\vec{b} |\Psi_V^* \Psi_{\gamma^*}|_{T,L} \times \exp\left[-i\left(\vec{b} - (1-z)\vec{r}\right)\vec{\Delta}\right] \frac{\mathrm{d}\sigma^{q\bar{q}}}{\mathrm{d}\vec{b}}. \tag{2}$$

Here, Ψ_{γ^*} and Ψ_V are the wave functions of a virtual photon fluctuating into a colour dipole and of the dipole producing the vector meson. A detailed description of the wave functions together with the values of the corresponding parameters is outside the scope of this Letter, they can be found in a previous work [28]. The vector $\vec{r}$ represents the dipole size and orientation, and b represents the impact parameter between the dipole and the target. Q^2 denotes the virtuality of the photon and $\vec{\Delta}^2 \equiv -t$. The variable z corresponds to the fraction of the energy of the quark-antiquark dipole carried by the quark, while

$$\frac{\mathrm{d}\sigma^{q\bar{q}}}{\mathrm{d}\vec{b}} = 2N(\vec{r}, \vec{b}; x), \tag{3}$$

where $N(\vec{r}, \vec{b}; x)$ is the dipole scattering amplitude obtained as a solution of the BK equation at a rapidity $Y = \ln(x_0/x)$; here $x_0 \equiv 0.008$ corresponds to the rapidity at the initial condition.

As mentioned before, two sets of dipole scattering amplitudes are used; both were obtained and studied in detail in our previous work [26].[1] In the b-BK-GG approach, the impact-parameter dependent BK equation is solved with an initial condition representing a proton. The solutions at each rapidity are then converted into solutions for a nucleus using the Glauber-Gribov prescription proposed in [29]. In the case of the b-BK-A approach, the initial condition represents the specific nucleus where the impact-parameter part is described with the help of the corresponding Woods-Saxon distribution.

3. Results

The cross section for the coherent photoproduction of a J/ψ vector meson off a Pb target as a function of $|t|$ is shown in Fig. 1 (left) at a centre-of-mass energy of the γPb system $W_{\gamma\mathrm{Pb}} = 121$ GeV, where $W^2_{\gamma\mathrm{Pb}} = M^2_{\mathrm{J}/\psi}/x$ with $M_{\mathrm{J}/\psi}$ the mass of the J/ψ vector meson. Note that not only the absolute magnitude of the cross section is different in the b-BK-A and b-BK-GG approaches, but also that the positions of the diffractive minima are displaced. This particular value of $W_{\gamma\mathrm{Pb}}$ has been chosen, because it corresponds to production in UPC at midrapidity for LHC Run 2 $\sqrt{s_{\mathrm{NN}}}$ energies, as explained below.

Fig. 1 (right) shows the energy dependence of the total γPb cross section, that is integrated over $|t|$. The difference in the absolute value of the cross section when using b-BK-A with respect to b-BK-GG solutions increases with energy from a 30% at $W_{\gamma\mathrm{Pb}} = 35$ GeV to 54% at $W_{\gamma\mathrm{Pb}} = 121$ GeV, reaching already a factor of two at $W_{\gamma\mathrm{Pb}} = 900$ GeV.

The cross section $d\sigma/dy$ for the coherent photoproduction of a J/ψ vector meson in Pb–Pb UPC is shown in Fig. 2 for the LHC energies corresponding to the Run 1 (left) and Run 2 (right). This cross section is given by

$$\frac{d\sigma}{dy} = n_\gamma(y)\sigma_{\gamma\mathrm{Pb}}(y) + n_\gamma(-y)\sigma_{\gamma\mathrm{Pb}}(-y), \tag{4}$$

where the rapidity y of the J/ψ at the LHC is related to $W_{\gamma\mathrm{Pb}}$ by

$$W^2_{\gamma\mathrm{Pb}} = \sqrt{s_{\mathrm{NN}}} M_{\mathrm{J}/\psi} e^{-y}. \tag{5}$$

The flux of photons from the Pb nucleus $n_\gamma(y)$ is computed following the description detailed in [30]. The figure also shows a comparison with existing measurements from the ALICE [31–33] and CMS [34] collaborations as well as with preliminary results from the LHCb collaboration [35].

4. Discussion

Some comments are in order. First, those of technical nature are addressed, followed by those related to the physics insight provided by the results presented in the previous section.

There has been recent interest on the argument of the exponential term in Eq. (2). This factor, introduced in [36], originates from a Fourier Transform term modified to take into account non-forward amplitudes. In [36] the factor is written in a general form, but when used for phenomenology it has been commonly implemented as in Eq. (2). A proposal put forward in [37] and based on symmetry arguments is that the term $(1-z)$ should be $(1-2z)/2$. Using the proposal from [37] produces a 3.5% larger cross section in both the b-BK-A and the b-BK-GG scenarios. This percentage is constant within the studied energy range. Therefore, this issue does not affect significantly the results presented in this Letter.

The corrections to take into account contributions from the real part of the amplitude and the skewedness effect are computed at fixed $|t| = 0.0001$. They depend on energy decreasing slowly with increasing $W_{\gamma\mathrm{Pb}}$. The factor $(1+\beta^2)$ is 1.07 (1.08) around 35 GeV and 1.04 (1.05) at 1 TeV, while $(R_g^{T,L})^2$ is 1.32 (1.34) around 35 GeV and 1.23 (1.27) at 1 TeV for the b-BK-A (b-BK-GG) case.

Recently, it was suggested to change the evolution variable in the BK equation [38]. The group behind this proposal has achieved a good description of HERA data using the rapidity of the dipole or that of the target for the evolution [20,39]. In [40] it was found that the new and the old approaches yield the same phenomenology at NLO for the structure functions measured at HERA, so in this work we will use our previous approach and explore the new proposal elsewhere.

Another issue brought forward in the recent works [38–40] is that the identification of the rapidity Y with Bjorken-x is $Y = \ln(1/x) + \ln(Q^2/Q_0^2)$, where Q^2 is the hard scale of the interaction and Q_0^2 can be identified with the saturation scale in the nucleus,

[1] The amplitudes are available online at https://hep.fjfi.cvut.cz/NuclearbdepBK.php.

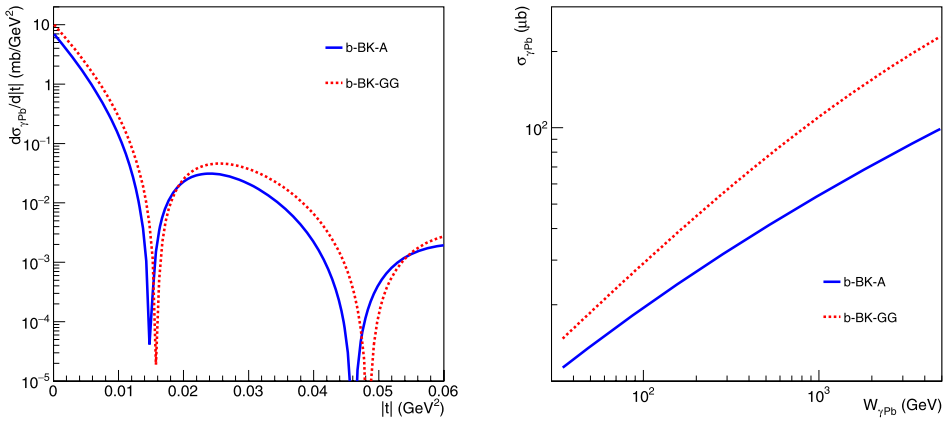

Fig. 1. Left: Cross section for the coherent photoproduction of a J/ψ vector meson off a Pb target as a function of $|t|$ at a centre-of-mass energy of the γPb system $W_{\gamma Pb} = 121$ GeV. Right: Energy dependence for the cross section integrated over $|t|$.

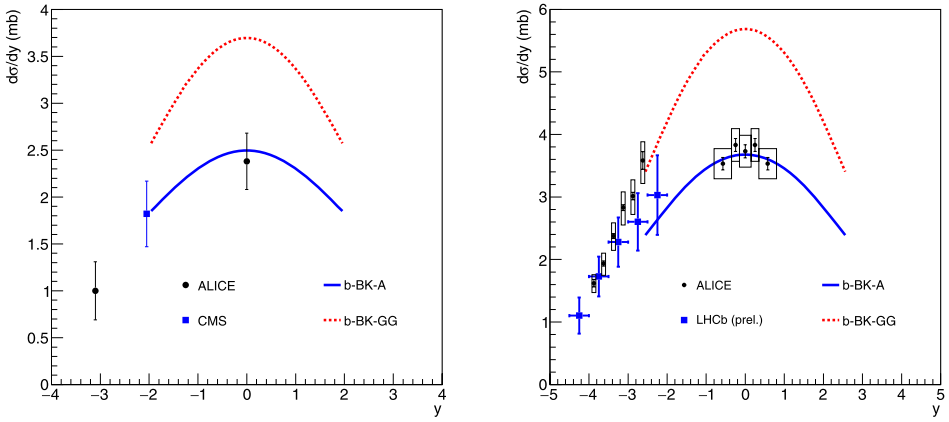

Fig. 2. Cross section for the coherent photoproduction of a J/ψ vector meson in ultra-peripheral Pb–Pb collisions at $\sqrt{s_{NN}} = 2.76$ TeV (left) and $\sqrt{s_{NN}} = 5.02$ TeV (right) corresponding to LHC energies during the Run 1 and Run 2 periods, respectively. The predictions are compared with data from the ALICE [31–33] and CMS [34] collaborations as well as with preliminary results from the LHCb collaboration [35].

which in our model is 0.609 GeV^2 [26]. For the photoproduction of J/ψ, Q^2 can be identified with $M^2_{J/\psi}/4$ (see e.g. [1]). This means that the ratio Q^2/Q_0^2 is in this case constant, which implies in our approach a reinterpretation of $x_0 \to x' Q^2/Q_0^2$ with x' a constant fixed by x_0, $M_{J/\psi}$ and Q_0.

The predictions shown in Fig. 2 cover a restricted range in rapidity. The origin of this limitation is that the initial condition for the evolution of the dipole scattering amplitude in the BK equation corresponds to an initial value of $x_0 = 0.008$. Inserting this into $W^2_{\gamma Pb} = M^2_{J/\psi}/x$ and using Eq. (5) produces a lower limit in y for Eq. (4).

This type of computations involves a series of choices for which, at the moment, there is no definitive theoretical guidance. Nonetheless, once a choice is made to describe an observable, it should be kept fixed in order to have consistent predictions across observables. The approach followed here to compare the predictions from the b-BK-A and b-BK-GG is consistent in the sense that the same wave functions and the same corrections are used.

Using a different prescription for the wave function has as the main effect the change of the normalisation of the cross section, see e.g. [11]. The prescription we chose is, for consistency, the same as in our previous work [23] where we compared our approach to HERA data. Recent developments arguing for the inclusion of D-wave effects find that mainly the excited states are affected and the change in the 1S state is less important [41].

There are also several prescriptions for the argument of the running coupling constant. For consistency with our previous results, we use the smallest-dipole prescription, but note that other prescriptions have also been used to described data, e.g. [39].

The saturation scale in the initial condition of the b-BK-A model is fixed by the central value of the EPPS16 set [42] which embodies most of the knowledge, both at the experimental and the theoretical level, that we currently have about the structure of nuclei. The evolution of this saturation scale is completely determined by the BK equation. The internal parameters not directly related to the targets take the same values in both cases and the subjacent QCD input, namely the BK equation with the collinear corrections, is the same. Furthermore, this implementation of the BK equation and the corresponding solutions including the impact-parameter dependence avoids the introduction of ad hoc parameters or assumptions to describe the distribution of matter in the plane transverse to the γA interaction. The solutions for the proton case used in the b-BK-GG approach described correctly photo and electroproduction data from HERA [23].

The cross sections shown in Fig. 1 (left) demonstrate the presence of diffractive dips. The location of the dips has been put forward as a signature of saturation in γp [43] and γA collision [44]. The facts that the position of the dip changes according to whether a Glauber-Gribov prescription is used or not, and that the change is larger than that observed in [44] between the saturation and the no-saturation cases, casts a warning on the use of this observable.

The flux entering Eq. (4) is fairly constant for lower $W_{\gamma\mathrm{Pb}}$ energies, but it shows a strong cut-off at large energies. As the γA cross section raises with energy as shown in Fig. 1 (right), the two terms in Eq. (4) have a different numerical value at large $|y|$ with the low $W_{\gamma\mathrm{Pb}}$ contribution being dominant. In this region, the predictions for the b-BK-A and b-BK-GG prescriptions are the closest. At midrapidity, both contributions to Eq. (4) are the same and correspond to $W_{\gamma\mathrm{Pb}} = 125$ GeV. Here, the difference in the presented UPC cross sections is the largest as shown in Fig. 2. Comparison with data from the LHC Run 1 indicates a preference for the b-BK-A approach and disagrees with b-BK-GG at a bit more than one-sigma for $|y| = 2$ and more than 3 sigmas for $y = 0$. The currently existing data from the LHC Run 2 does not provide such a clean message because of the large experimental uncertainties as well as the slight apparent discrepancy between ALICE and LHCb results. The data from LHC Run 2 at midrapidity are still being analysed; it is expected that the uncertainties will be smaller than those in the existing measurement. If so, then these new data may help to select one of the two prescriptions as the most adequate approach.

These results, specifically those shown in Fig. 1, are of interest for future electron-ion colliders [8,9] where such a process will be precisely measured for a variety of nuclei, allowing for the study not only of the energy, but also of the A dependence of the cross section for coherent J/ψ photo and electroproduction.

Our results not only highlight that the description of the nuclear shape in the impact-parameter plane is important but give a quantitative prediction of how the evolution of the Glauber-Gribov assumption differs from an evolution completely based on the BK equation. It is important to remark, that before the appearance of the collinearly improved kernel, phenomenologically successful applications of the BK equation described hadrons as large and homogeneous in the transverse direction, while now we have the possibility of providing hadrons with a more detailed structure in the impact-parameter plane and of studying how this structure is reflected in measurements to be performed in current and future facilities.

5. Summary and outlook

The coherent photonuclear production off Pb nuclei in ultra-peripheral collisions at the LHC has been studied using solutions of the impact-parameter dependent BK equation. Two approaches have been compared. Starting from solutions of the proton case coupled to a Glauber-Gribov formalism, or solving directly the impact-parameter dependent BK equation with an initial condition representing the nucleus. Data from the LHC favour the latter approach. Future data at midrapidity should be precise enough to settle the question of the most valid approach in this context. These studies are of interest for the newly approved and planned future electron-ion colliders where this type of process can be studied with more precision and in a variety of ways.

Declaration of competing interest

The authors declare that they have no known competing financial interests or personal relationships that could have appeared to influence the work reported in this paper.

Acknowledgements

This work has been partially supported by grant 18-07880S of the Czech Science Foundation (GACR), grant LTC17038 of the INTER-EXCELLENCE program at The Ministry of Education, Youth and Sports of the Czech Republic, the European Regional Development Fund-Project “Brookhaven National Laboratory - participation of the Czech Republic” with the number CZ.02.1.01/0.0/0.0/16013/0001569, and by the Centre of Advanced Applied Sciences with the number: CZ.02.1.01/0.0/0.0/16-019/0000778. The Centre of Advanced Applied Sciences is co-financed by the European Union.

References

[1] M.G. Ryskin, Diffractive J / psi electroproduction in LLA QCD, Z. Phys. C 57 (1993) 89–92, https://doi.org/10.1007/BF01555742.
[2] S.J. Brodsky, L. Frankfurt, J.F. Gunion, A.H. Mueller, M. Strikman, Diffractive leptoproduction of vector mesons in QCD, Phys. Rev. D 50 (1994) 3134–3144, https://doi.org/10.1103/PhysRevD.50.3134, arXiv:hep-ph/9402283.
[3] I.P. Ivanov, N.N. Nikolaev, A.A. Savin, Diffractive vector meson production at HERA: from soft to hard QCD, Phys. Part. Nucl. 37 (2006) 1–85, https://doi.org/10.1134/S1063779606010011, arXiv:hep-ph/0501034.
[4] P. Newman, M. Wing, The hadronic final state at HERA, Rev. Mod. Phys. 86 (3) (2014) 1037, https://doi.org/10.1103/RevModPhys.86.1037, arXiv:1308.3368.
[5] A.J. Baltz, et al., The physics of ultraperipheral collisions at the LHC, Phys. Rep. 458 (2008) 1–171, https://doi.org/10.1016/j.physrep.2007.12.001, arXiv:0706.3356.
[6] J.G. Contreras, J.D. Tapia Takaki, Ultra-peripheral heavy-ion collisions at the LHC, Int. J. Mod. Phys. A 30 (2015) 1542012, https://doi.org/10.1142/S0217751X15420129.
[7] S.R. Klein, H. Mäntysaari, Imaging the nucleus with high-energy photons, Nature Rev. Phys. 1 (11) (2019) 662–674, https://doi.org/10.1038/s42254-019-0107-6, arXiv:1910.10858.
[8] A. Accardi, et al., Electron ion collider: the next QCD frontier, Eur. Phys. J. A 52 (9) (2016) 268, https://doi.org/10.1140/epja/i2016-16268-9, arXiv:1212.1701.
[9] J. Abelleira Fernandez, et al., A large hadron electron collider at CERN: report on the physics and design concepts for machine and detector, J. Phys. G 39 (2012) 075001, https://doi.org/10.1088/0954-3899/39/7/075001, arXiv:1206.2913.
[10] S.R. Klein, J. Nystrand, Exclusive vector meson production in relativistic heavy ion collisions, Phys. Rev. C 60 (1999) 014903, https://doi.org/10.1103/PhysRevC.60.014903, arXiv:hep-ph/9902259.
[11] T. Lappi, H. Mantysaari, Incoherent diffractive J/Psi-production in high energy nuclear DIS, Phys. Rev. C 83 (2011) 065202, https://doi.org/10.1103/PhysRevC.83.065202, arXiv:1011.1988.
[12] V. Goncalves, B. Moreira, F. Navarra, Investigation of diffractive photoproduction of J/Ψ in hadronic collisions, Phys. Rev. C 90 (1) (2014) 015203, https://doi.org/10.1103/PhysRevC.90.015203, arXiv:1405.6977.
[13] J. Cepila, J.G. Contreras, M. Krelina, Coherent and incoherent J/ψ photonuclear production in an energy-dependent hot-spot model, Phys. Rev. C 97 (2) (2018) 024901, https://doi.org/10.1103/PhysRevC.97.024901, arXiv:1711.01855.
[14] S.J. Brodsky, A.H. Mueller, Using nuclei to probe hadronization in QCD, Phys. Lett. B 206 (1988) 685–690, https://doi.org/10.1016/0370-2693(88)90719-8.
[15] B. Kopeliovich, B. Zakharov, Quantum effects and color transparency in charmonium photoproduction on nuclei, Phys. Rev. D 44 (1991) 3466–3472, https://doi.org/10.1103/PhysRevD.44.3466.
[16] I. Balitsky, Operator expansion for high-energy scattering, Nucl. Phys. B 463 (1996) 99–160, https://doi.org/10.1016/0550-3213(95)00638-9, arXiv:hep-ph/9509348.
[17] Y.V. Kovchegov, Small x F(2) structure function of a nucleus including multiple pomeron exchanges, Phys. Rev. D 60 (1999) 034008, https://doi.org/10.1103/PhysRevD.60.034008, arXiv:hep-ph/9901281.
[18] Y.V. Kovchegov, Unitarization of the BFKL pomeron on a nucleus, Phys. Rev. D 61 (2000) 074018, https://doi.org/10.1103/PhysRevD.61.074018, arXiv:hep-ph/9905214.
[19] E. Iancu, J.D. Madrigal, A.H. Mueller, G. Soyez, D.N. Triantafyllopoulos, Resumming double logarithms in the QCD evolution of color dipoles, Phys. Lett. B 744 (2015) 293–302, https://doi.org/10.1016/j.physletb.2015.03.068, arXiv:1502.05642.
[20] E. Iancu, J.D. Madrigal, A.H. Mueller, G. Soyez, D.N. Triantafyllopoulos, Collinearly-improved BK evolution meets the HERA data, Phys. Lett. B 750 (2015) 643–652, https://doi.org/10.1016/j.physletb.2015.09.071, arXiv:1507.03651.
[21] G. Beuf, Improving the kinematics for low-x QCD evolution equations in coordinate space, Phys. Rev. D 89 (7) (2014) 074039, https://doi.org/10.1103/PhysRevD.89.074039, arXiv:1401.0313.
[22] J. Cepila, J.G. Contreras, M. Matas, Collinearly improved kernel suppresses Coulomb tails in the impact-parameter dependent Balitsky-Kovchegov evolution, Phys. Rev. D 99 (5) (2019) 051502, https://doi.org/10.1103/PhysRevD.99.051502, arXiv:1812.02548.
[23] D. Bendova, J. Cepila, J. Contreras, M. Matas, Solution to the Balitsky-Kovchegov equation with the collinearly improved kernel including impact-parameter dependence, Phys. Rev. D 100 (5) (2019) 054015, https://doi.org/10.1103/PhysRevD.100.054015, arXiv:1907.12123.

[24] K.J. Golec-Biernat, A. Stasto, On solutions of the Balitsky-Kovchegov equation with impact parameter, Nucl. Phys. B 668 (2003) 345–363, https://doi.org/10.1016/j.nuclphysb.2003.07.011, arXiv:hep-ph/0306279.
[25] C. Contreras, E. Levin, R. Meneses, BFKL equation in the next-to-leading order: solution at large impact parameters, Eur. Phys. J. C 79 (10) (2019) 842, https://doi.org/10.1140/epjc/s10052-019-7363-6, arXiv:1906.09603.
[26] J. Cepila, J.G. Contreras, M. Matas, Predictions for nuclear structure functions from the impact-parameter dependent Balitsky-Kovchegov equation, Phys. Rev. C 102 (4) (2020) 044318, https://doi.org/10.1103/PhysRevC.102.044318, arXiv:2002.11056.
[27] A.G. Shuvaev, K.J. Golec-Biernat, A.D. Martin, M.G. Ryskin, Off diagonal distributions fixed by diagonal partons at small x and xi, Phys. Rev. D 60 (1999) 014015, https://doi.org/10.1103/PhysRevD.60.014015, arXiv:hep-ph/9902410.
[28] D. Bendova, J. Cepila, J. Contreras, Dissociative production of vector mesons at electron-ion colliders, Phys. Rev. D 99 (3) (2019) 034025, https://doi.org/10.1103/PhysRevD.99.034025, arXiv:1811.06479.
[29] N. Armesto, A simple model for nuclear structure functions at small x in the dipole picture, Eur. Phys. J. C 26 (2002) 35–43, https://doi.org/10.1007/s10052-002-1021-z, arXiv:hep-ph/0206017.
[30] J.G. Contreras, Gluon shadowing at small x from coherent J/ψ photoproduction data at energies available at the CERN Large Hadron Collider, Phys. Rev. C 96 (1) (2017) 015203, https://doi.org/10.1103/PhysRevC.96.015203, arXiv:1610.03350.
[31] B. Abelev, et al., Coherent J/ψ photoproduction in ultra-peripheral Pb-Pb collisions at $\sqrt{s_{NN}} = 2.76$ TeV, Phys. Lett. B 718 (2013) 1273–1283, https://doi.org/10.1016/j.physletb.2012.11.059, arXiv:1209.3715.
[32] E. Abbas, et al., Charmonium and e^+e^- pair photoproduction at mid-rapidity in ultra-peripheral Pb-Pb collisions at $\sqrt{s_{\rm NN}} = 2.76$ TeV, Eur. Phys. J. C 73 (11) (2013) 2617, https://doi.org/10.1140/epjc/s10052-013-2617-1, arXiv:1305.1467.
[33] S. Acharya, et al., Coherent J/ψ photoproduction at forward rapidity in ultra-peripheral Pb-Pb collisions at $\sqrt{s_{\rm NN}} = 5.02$ TeV, Phys. Lett. B 798 (2019) 134926, https://doi.org/10.1016/j.physletb.2019.134926, arXiv:1904.06272.
[34] V. Khachatryan, et al., Coherent J/ψ photoproduction in ultra-peripheral PbPb collisions at $\sqrt{s_{NN}} = 2.76$ TeV with the CMS experiment, Phys. Lett. B 772 (2017) 489–511, https://doi.org/10.1016/j.physletb.2017.07.001, arXiv:1605.06966.
[35] A. Bursche, Study of coherent J/ψ production in lead-lead collisions at $\sqrt{s_{\rm NN}} =$ 5 TeV with the LHCb experiment, Nucl. Phys. A 982 (2019) 247–250, https://doi.org/10.1016/j.nuclphysa.2018.10.069.
[36] J. Bartels, K.J. Golec-Biernat, K. Peters, On the dipole picture in the nonforward direction, Acta Phys. Pol. B 34 (2003) 3051–3068, arXiv:hep-ph/0301192.
[37] Y. Hatta, B.-W. Xiao, F. Yuan, Gluon tomography from deeply virtual compton scattering at small-x, Phys. Rev. D 95 (11) (2017) 114026, https://doi.org/10.1103/PhysRevD.95.114026, arXiv:1703.02085.
[38] B. Ducloué, E. Iancu, A. Mueller, G. Soyez, D. Triantafyllopoulos, Non-linear evolution in QCD at high-energy beyond leading order, J. High Energy Phys. 04 (2019) 081, https://doi.org/10.1007/JHEP04(2019)081, arXiv:1902.06637.
[39] B. Ducloué, E. Iancu, G. Soyez, D. Triantafyllopoulos, HERA data and collinearly-improved BK dynamics, Phys. Lett. B 803 (2020) 135305, https://doi.org/10.1016/j.physletb.2020.135305, arXiv:1912.09196.
[40] G. Beuf, H. Hänninen, T. Lappi, H. Mäntysaari, Color glass condensate at next-to-leading order meets HERA data, Phys. Rev. D 102 (2020) 074028, https://doi.org/10.1103/PhysRevD.102.074028, arXiv:2007.01645.
[41] M. Krelina, J. Nemchik, R. Pasechnik, J. Cepila, Spin rotation effects in diffractive electroproduction of heavy quarkonia, Eur. Phys. J. C 79 (2) (2019) 154, https://doi.org/10.1140/epjc/s10052-019-6666-y, arXiv:1812.03001.
[42] K.J. Eskola, P. Paakkinen, H. Paukkunen, C.A. Salgado, EPPS16: nuclear parton distributions with LHC data, Eur. Phys. J. C 77 (3) (2017) 163, https://doi.org/10.1140/epjc/s10052-017-4725-9, arXiv:1612.05741.
[43] N. Armesto, A.H. Rezaeian, Exclusive vector meson production at high energies and gluon saturation, Phys. Rev. D 90 (5) (2014) 054003, https://doi.org/10.1103/PhysRevD.90.054003, arXiv:1402.4831.
[44] T. Toll, T. Ullrich, Exclusive diffractive processes in electron-ion collisions, Phys. Rev. C 87 (2) (2013) 024913, https://doi.org/10.1103/PhysRevC.87.024913, arXiv:1211.3048.

Eur. Phys. J. C (2022) 82:99
https://doi.org/10.1140/epjc/s10052-022-10059-9

THE EUROPEAN PHYSICAL JOURNAL C

Regular Article - Theoretical Physics

Deeply virtual Compton scattering at the EIC and LHeC: a comparison among saturation approaches

D. Bendova[1,a], **J. Cepila**[1,b], **V. P. Gonçalves**[2,c], **C. R. Sena**[2]

[1] Faculty of Nuclear Sciences and Physical Engineering, Czech Technical University in Prague, Břehová 7, 11519 Prague, Czech Republic
[2] High and Medium Energy Group, Instituto de Física e Matemática, Universidade Federal de Pelotas (UFPel), Caixa Postal 354, Pelotas, RS 96010-900, Brazil

Received: 13 November 2021 / Accepted: 25 January 2022

Abstract The impact of nonlinear effects in the deeply virtual Compton scattering (DVCS) process that will be measured in future electron-hadron collisions is investigated. We present, for the first time, the predictions derived using the solution to the Balitsky–Kovchegov equation with the collinearly-improved kernel and including the impact-parameter dependence. We estimate the total cross section and t-distribution of the DVCS process in ep and eA collisions and demonstrate that $d\sigma/dt$ is strongly dependent on the assumption for the impact-parameter dependence of the dipole-hadron scattering amplitude. Our results indicate that a future experimental analysis of this process will be useful to discriminate among different models for the saturation physics and, consequently, will allow us to constrain the description of QCD dynamics in parton densities.

1 Introduction

One of the main goals of the future electron-ion colliders at BNL (EIC) [1–3] and CERN (LHeC) [4,5] is to improve our understanding about the quantum 3D imaging of the partons inside the protons and nuclei by measuring the parton position, momentum, and angular momentum with unprecedent precision. Theoretically, all quantum information of how partons are distributed inside hadrons is encoded in the quantum phase space Wigner distributions, which include information on both generalized parton distributions (GPDs) and transverse momentum parton distributions (TMDs), see e.g. Refs. [6–13]. Experimentally, the tomography picture from the hadrons can be revealed in deep inelastic electron-hadron scattering by measurements of exclusive processes, wherein the hadron remains intact after scattering of the lepton probe. One has that the Fourier transform of the associated differential cross sections $d\sigma/dt$, where t is the squared four-momentum transfer between the incoming and scattered hadron, can be used to obtain the transverse spatial distributions of quarks and gluons in both protons and nuclei. In particular, the future experimental analysis of the diffractive dijet production [14–19] and the deeply virtual Compton scattering (DVCS) [20–22] at the EIC and LHeC are expected to directly probe the gluon GPD.

In this paper, we will focus on coherent DVCS processes represented in the Fig. 1, i.e. production of a real photon with the target hadron remaining intact.[1] At large energies, this process is driven by the gluon content of the target, with the cross section being proportional to the square of the scattering amplitude and, consequently, being strongly sensitive to the underlying QCD dynamics. For previous studies, see e.g. Refs. [23–28]. Moreover, the behaviour of $d\sigma/dt$ at small-x is determined by the impact-parameter dependence of the scattering amplitude $\mathcal{N}(x, \boldsymbol{r}, \boldsymbol{b}_t)$ of a dipole off the target, where $\boldsymbol{r}$ is the transverse dipole size and $\boldsymbol{b}_t$ the impact - parameter. The amplitude encodes the information about the hadronic scattering as well as the nonlinear and quantum effects in the hadron wave function [29–31]. In recent years, several groups have proposed different phenomenological approaches to describe $\mathcal{N}(x, \boldsymbol{r}, \boldsymbol{b}_t)$, which are based on the color glass condensate (CGC) formalism [32–37] and successfully describe a large set of observables in ep, pp, pA, and AA collisions. In particular, the IP-Sat [25,38] and b-CGC [39,40] approaches are able to describe the DVCS data obtained in the kinematical range covered

[a] e-mail: dagmar.bendova@fjfi.cvut.cz
[b] e-mail: jan.cepila@fjfi.cvut.cz
[c] e-mail: barros@ufpel.edu.br (corresponding author)

[1] The same final state is also generated by the Bethe–Heitler (BH) process, where the elastic electron-hadron scattering is followed by photon emission off the electron. In our analysis, we will assume that the DVCS contribution can be experimentally separated as was done e.g. at HERA.

Published online: 01 February 2022

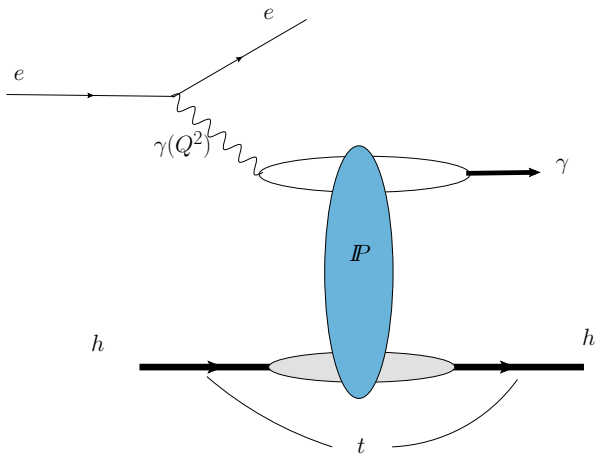

Fig. 1 Deeply virtual Compton scattering in coherent diffractive processes, where the hadron can be a proton or a nucleus

by the HERA experiment. A shortcoming of these models is that the associated $\boldsymbol{b}_t$ dependencies are not based on the solutions of the Balitsky–Kovchegov (BK) equation [41–45], which is the mean-field approximation of the infinite hierarchy of coupled equations for the correlators of Wilson lines predicted by the CGC formalism [32–37,41–43]. Moreover, these models have been proposed for a proton target and its extension for a nuclear target is, in general, performed using the Glauber–Gribov (GG) approach [46–49] (see e.g. Refs. [51–53]). Recently, in Refs. [54–56], the impact-parameter and energy dependencies of $\mathcal{N}(x, \boldsymbol{r}, \boldsymbol{b}_t)$ have been derived by solving the BK equation and taking into account the collinear corrections [57–59] to the kernel of the evolution equation for both proton and nuclear targets. One of the goals of this paper is to estimate the DVCS cross sections using this approach and present, for the first time, a comparison between its predictions and the HERA data. Another goal is to present an extensive comparison between the predictions of the distinct saturation approaches for the energy dependence of the total cross section and for the t-distributions considering the kinematical range covered by the future electron-ion colliders. Our main motivation is to verify if future experimental data for the DVCS process could be used to discriminate between these distinct treatments of the QCD dynamics at high energies.

The paper is organized as follows. In the next section, we present a brief overview of the color dipole formalism for the description of deeply virtual Compton scattering and the distinct models for the dipole-target scattering amplitude used in our analysis. In Sect. 3, we present our predictions for the total cross section and the t-distribution considering ep and eA collisions. Finally, in Sect. 4, we summarize our main conclusions.

2 Formalism

Let us start presenting a brief review of the deeply virtual Compton scattering (DVCS) in electron-hadron collisions, represented in Fig. 1. This process is characterized by a real photon and an intact hadron in the final state, with a rapidity gap separating these systems. In the color dipole approach the scattering amplitude for the exclusive real photon production $\gamma^* h \to \gamma h$ can be factorized in terms of the fluctuation of the virtual photon into a $q\bar{q}$ color dipole, the dipole-hadron scattering by a color singlet exchange ($I\!P$) and the recombination into the exclusive final state γ. As demonstrated e.g. in Refs. [21,22,25], the DVCS amplitude can be written as[2]

$$A^{\gamma^* h\to\gamma h}(x, r, \Delta, Q^2) = \int db_t (2\pi b_t) \int dr (2\pi r) \times \int dz \sum_f (\Psi^*_{\gamma*}\Psi_\gamma)^f J_0(b_t\Delta) J_0([1-2z]r\Delta/2) \frac{d\sigma_{q\bar{q}}}{d^2\boldsymbol{b}_t} \tag{1}$$

where r is the size of the $q\bar{q}$ dipole, $\boldsymbol{b}_t$ is the impact - parameter, $\Delta^2 = -t$, and z and $(1-z)$ are the momentum fractions of the incoming photon carried by the quark and anti-quark, respectively. Moreover, the overlap function $(\Psi^*_{\gamma*}\Psi_\gamma)^f$ is given by

$$(\Psi^*_{\gamma*}\Psi_\gamma)^f = \frac{N_c \alpha_{em}}{2\pi^2} e_f^2 \times \{[z^2 + (1-z)^2]\epsilon_1 K_1(\epsilon_1 r)\epsilon_2 K_1(\epsilon_2 r) + m_f^2 K_0(\epsilon_1 r) K_0(\epsilon_2 r)\}, \tag{2}$$

where m_f and e_f are the mass and the charge of a quark with flavor f. The cross section for the dipole scattering off the target at an impact - parameter $\boldsymbol{b}_t$ is denoted by $\mathrm{d}\sigma_{q\bar{q}}/\mathrm{d}^2\boldsymbol{b}_t$ and it is related to the dipole-target scattering amplitude $\mathcal{N}_h(x, \boldsymbol{r}, \boldsymbol{b}_t)$ by

$$\frac{\mathrm{d}\sigma_{q\bar{q}}}{\mathrm{d}^2\boldsymbol{b}_t} = 2\mathcal{N}_h(\bar{x}, \boldsymbol{r}, \boldsymbol{b}_t), \tag{3}$$

where $\bar{x} = x(1 + 4m_f^2/Q^2)$, with x being the Bjorken variable. As a consequence, one has that the energy, photon virtuality, transverse momentum, and atomic number dependencies of DVCS cross section are determined by the evolution of $\mathcal{N}$ and, consequently, they strongly depend on the description of the QCD dynamics. An important aspect, that must be emphasized, is that although the DVCS cross section is smaller than the vector meson one, it is not affected by the theoretical uncertainties associated to the scarce knowledge

[2] In our analysis we will disregard the correlations between $\boldsymbol{r}$ and $\boldsymbol{b}_t$ in the dipole-target scattering amplitude, which is a good approximation for the calculation of the total cross section and the t-distribution. However, less inclusive observables, as e.g. the electron–photon azimuthal angle correlation, are sensitive to nontrivial spatial correlations in the gluon distribution of the target [22].

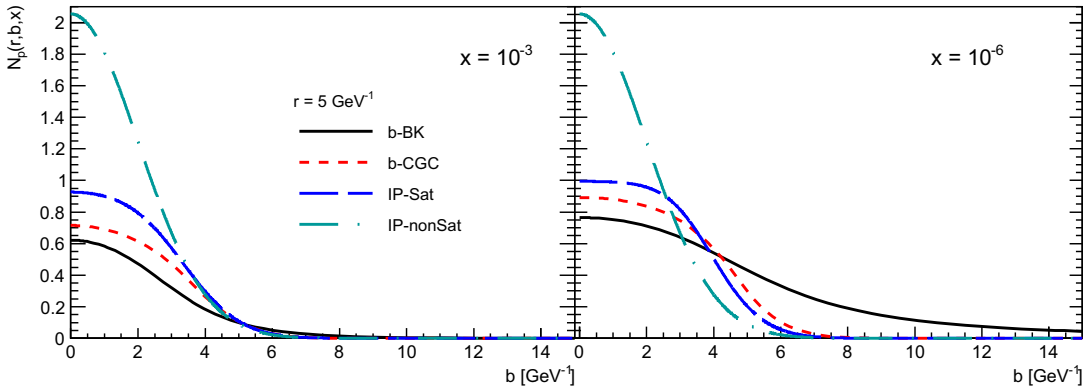

Fig. 2 Predictions of the different nonlinear approaches for the impact – parameter dependence of the dipole-proton scattering amplitude considering two distinct values of x ($= 10^{-3}$ and 10^{-6}) and a fixed dipole size ($r = 5$ GeV^{-1})

of the vector meson wave functions. Which implies that the DVCS process can be considered a direct probe of the QCD dynamics for the dipole-target interaction.

In the CGC formalism [32–37], the scattering amplitude can be obtained by solving the BK equation, which is given by [41–45]

$$\frac{\partial \mathcal{N}(\boldsymbol{r}, \boldsymbol{b}_t, Y)}{\partial Y} = \int \mathrm{d}\boldsymbol{r_1}\, K(\boldsymbol{r}, \boldsymbol{r_1}, \boldsymbol{r_2})[\mathcal{N}(\boldsymbol{r}_1, \boldsymbol{b}_1, Y) + \mathcal{N}(\boldsymbol{r}_2, \boldsymbol{b}_2, Y) - \mathcal{N}(\boldsymbol{r}, \boldsymbol{b}_t, Y) - \mathcal{N}(\boldsymbol{r}_1, \boldsymbol{b}_1, Y)\mathcal{N}(\boldsymbol{r}_2, \boldsymbol{b}_2, Y)], \quad (4)$$

where Y is the rapidity, $r \equiv |\boldsymbol{r}|$, $r_1 \equiv |\boldsymbol{r}_1|$ and $r_2 \equiv |\boldsymbol{r}_2|$ are the transverse sizes of the original dipole and of the two daughter dipoles, respectively, and $b_i \equiv |\boldsymbol{b}_i|$ are the corresponding impact parameters. The evolution runs in rapidity $Y = \ln(x_0/x)$, where x is the Bjorken variable and x_0 gives the initial value of Bjorken variable for the evolution. The form of the kernel, $K(\boldsymbol{r}, \boldsymbol{r_1}, \boldsymbol{r_2})$, depends on the approximations assumed to treat the next-to-leading order corrections associated e.g. to the running of the coupling constant and collinear logarithms that arise in the perturbative expansion. As pointed out in the Introduction, we will focus in this study on the approach proposed in Refs. [54–56], which is based on the solution of the Balitsky–Kovchegov equation for the dipole-hadron scattering amplitude including the dependence on impact-parameter and using the collinearly-improved kernel proposed in Refs. [57–59]. In such approach, the power-like (Coulomb) tail at large impact parameters, found in the solution of the BK equation at leading order in Ref. [60], is suppressed by higher-order corrections that impose time-ordering of the gluon emissions. In Refs. [54,55], the BK equation with the collinearly-improved kernel was solved for a proton target assuming that the initial condition is given by a combination of the GBW model [63,64] for the dependence on the dipole size r and of a Gaussian distribution for the impact-parameter dependence. The parameters have been fixed using HERA data for F_2 and for the $|t|$-distribution of the J/Ψ photoproduction. The resulting solutions will be denoted b-BK in what follows. In Fig. 2, we present the impact-parameter dependence of the b-BK solution for a proton target considering two values of x and a fixed dipole size. Such predictions are compared with the predictions from the IP-Sat and b-CGC models (see e.g. Refs. [25,38,40]), which are phenomenological models based on the CGC physics that assume distinct ad hoc impact-parameter dependencies for the scattering amplitude. In addition, we also present the predictions of the IP-nonSat model, which can be derived from the IP-Sat model by disregarding the impact of the multiple scattering corrections that take into account of the nonlinear QCD effects in this model. Therefore, the comparison between the IP-nonSat predictions and those from the other models allow us to estimate the impact of the saturation effects for a proton target. For $x = 10^{-3}$ (left panel), one has that predictions are similar for large impact - parameters. In contrast, the predictions for small-b are distinct, with the IP-nonSat model violating the unitarity bound expressed by $\mathcal{N}_p \leq 1$. Such violation is also observed for smaller values of x (right panel). Moreover, the distributions predicted by the b-BK, IP-Sat and b-CGC models become wider with the decreasing of x, where the behaviour of $\mathcal{N}_p$ at large-b depends on the dipole model considered. In particular, the b-BK solution predicts a long tail, as already demonstrated in Refs. [54,55]. Such results motivate the study of observables that are sensitive to the impact-parameter dependence and, consequently, to the modelling of $\mathcal{N}$. The t-distributions represent a useful tool here, since t and b are Fourier conjugated variables.

For the nuclear case, the DVCS amplitude can be estimated assuming the Glauber–Gribov (GG) formalism [46–50], as performed e.g. in Refs. [26,28]. In this approach, the dipole-nucleus scattering amplitude $\mathcal{N}_A(\boldsymbol{r}, \boldsymbol{b}_A, Y)$ is given

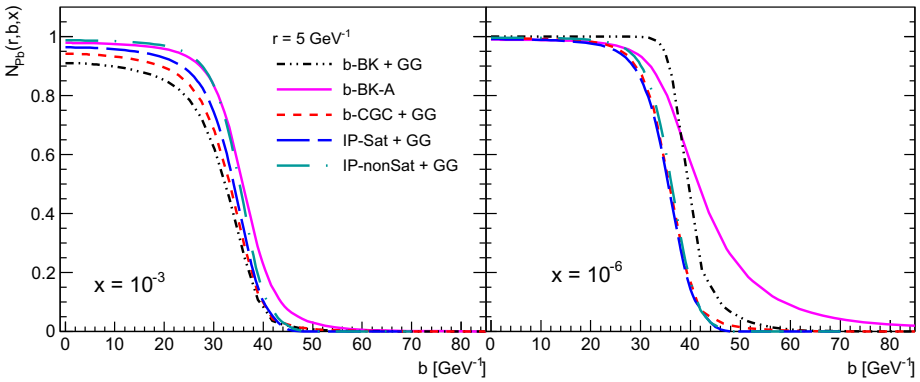

Fig. 3 Predictions of the different nonlinear approaches for the impact-parameter dependence of the dipole-nucleus scattering amplitude considering two distinct values of x ($= 10^{-3}$ and 10^{-6}), a fixed dipole size ($r = 5$ GeV^{-1}), and $A = Pb$

by

$$\mathcal{N}_A(\boldsymbol{r}, \boldsymbol{b}_A, Y) = 1 - \exp\left[-\frac{1}{2}\,\sigma_{dp}(Y, \boldsymbol{r}^2)\,T_A(\boldsymbol{b}_A)\right], \tag{5}$$

where $\boldsymbol{b}_A$ is the dipole-nucleus impact-parameter and the nuclear profile function $T_A(\boldsymbol{b}_A)$ is described by a Woods–Saxon distribution. The dipole-proton cross section, denoted as σ_{dp}, is expressed in terms of the dipole-proton scattering amplitude as follows

$$\sigma_{dp}(Y, \boldsymbol{r}^2) = 2\int \mathrm{d}^2\boldsymbol{b}_p\,\mathcal{N}_p(\boldsymbol{r}, \boldsymbol{b}_p, Y), \tag{6}$$

with $\boldsymbol{b}_p$ being the impact-parameter for the dipole-proton interaction. In this approach, the IP-Sat, IP-nonSat, b-CGC and b-BK models for a proton target can be used as input to estimate $\mathcal{N}_A(\boldsymbol{r}, \boldsymbol{b}_A, Y)$. In what follows, the associated predictions will be denoted as IP-Sat + GG, IP-nonSat + GG, b-CGC + GG and b-BK + GG, respectively. In contrast, $\mathcal{N}_A$ can be directly estimated by solving the BK equation for the nuclear case, following the approach proposed in Refs. [54,55]. In particular, in Ref. [56], the authors extended the approach for a nuclear target assuming that the initial condition is given by

$$\mathcal{N}_A(\boldsymbol{r}, \boldsymbol{b}_A, Y = 0) = 1 - \exp\left[-\frac{1}{2}\frac{Q_{s0}^2(A)}{4}r^2 T_A(\boldsymbol{b}_{q_1}, \boldsymbol{b}_{q_2})\right], \tag{7}$$

where $Y = \ln(x_0/x)$ with $x_0 = 0.008$, $\boldsymbol{b}_{q_i}$ are the impact - parameters with respect to the dipole constituents, and Q_{s0}^2 is a free parameter determined for each value of A by the comparison between the dipole predictions for F_2^A and those obtained using the collinear formalism and the EPPS16 parametrization [61] for $Y = 0$. Moreover, $T_A(\boldsymbol{b}_{q_1}, \boldsymbol{b}_{q_2})$ is the nuclear profile, which is assumed to be given by

$$T_A(\boldsymbol{b}_{q_1}, \boldsymbol{b}_{q_2}) = k\left[T_A(\boldsymbol{b}_{q_1}) + T_A(\boldsymbol{b}_{q_2})\right], \tag{8}$$

where the individual profiles $T_A(\boldsymbol{b}_{q_i})$ are described by a Woods-Saxon distribution and k is the factor which ensures $kT_A(0) = 1$ and implies that Eq. (7) becomes the GBW formula [63,64] for $\boldsymbol{b} = 0$. The associated predictions will be denoted as b-BK-A hereafter. In Fig. 3, we compare the predictions of the different approaches for the impact-parameter dependence of $\mathcal{N}_A$ considering two values of x, a fixed dipole size, and $A = Pb$. One has that all models predict $\mathcal{N}_A \leq 1$, i.e., they all satisfy unitarity. However, the b-dependence is strongly model dependent. In particular, the behaviours predicted by the b-BK + GG and b-BK-A models for small-x and large-b are significantly distinct, with the b-BK-A predicting a longer tail. Such result motivates the analysis of the impact of these distinct descriptions of the nonlinear effects on the t-distributions of the nuclear DVCS process, which could be measured in future eA colliders.

3 Results

In this section we will investigate the impact of the different treatments of the nonlinear effects on the total cross section and t-distributions considering the kinematical range that will be covered by the future electron-ion colliders – EIC and LHeC [1–5]. These two observables are directly related, since the total cross section for the exclusive real photon production is given by

$$\sigma^{\gamma^* h\to\gamma h}(W, Q^2) = \int_{-\infty}^{0} dt\,\frac{d\sigma^{\gamma^* h\to\gamma h}}{dt} = \int_{-\infty}^{0} dt\,\frac{1}{16\pi}\left|A^{\gamma^* h\to\gamma h}(x, r, \Delta, Q^2)\right|^2 \tag{9}$$

where W is the photon-hadron center-of-mass energy, Q^2 is the virtuality of the incoming photon and the amplitude is given by Eq. (1). As in Ref. [25], the differential cross section for a proton target will be multiplied by the factor $R_g^2(1+\beta^2)$ in order to take into account the skewness effect (R_g) and the real part of the scattering amplitude (β). The skewness correction is related to the fact that in the two-gluon exchange limit, the gluons emitted from the quark and antiquark into the dipole can carry different momentum frac-

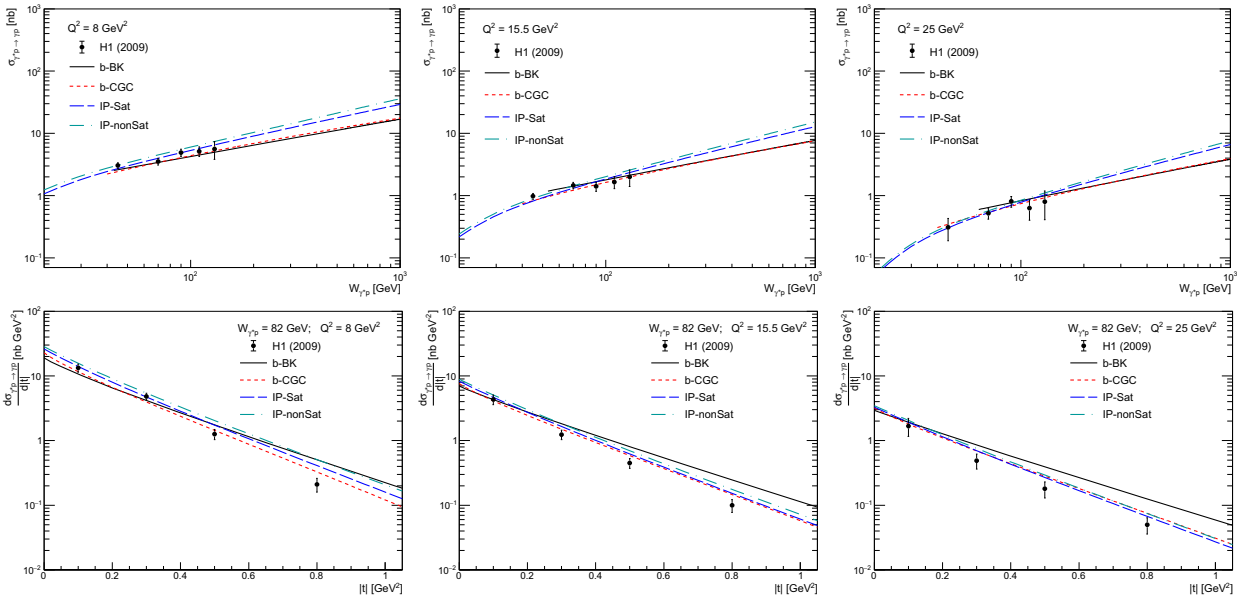

Fig. 4 Predictions for the energy dependence (upper panels) and t-distributions (lower panels) of the DVCS process in ep collisions at HERA derived considering distinct models for the dipole-proton scattering amplitude and different values of the photon virtuality. Data from H1 [66]

tions. Such correction has been derived in the framework of collinear factorization [65], and its application in the dipole approach is still under debate. However, the comparison of the dipole predictions with the HERA data indicate that the skewness and real part corrections are needed to describe the data. In our analysis, we will assume $R_g^2 = 1.1$ and $\beta = 0.3$ for all models considered, which is a good first approximation for the value calculated considering the distinct dipole models. In contrast, for a nuclear target, we will disregard these corrections, since the calculation of R_g and β for the nuclear case is a subject of still ongoing discussions. The IP-Sat and IP-nonSat predictions will be derived using the parameters obtained in Ref. [62]. For the b-CGC model, we consider the parameters adjusted to the latest HERA data in Ref. [40].

Initially, in Fig. 4, we present the predictions for the energy dependence of the total cross section (upper panels) and the cross section $|t|$-distribution (lower panels) assuming different values for the photon virtuality and considering the b-CGC, IP-Sat, IP-nonSat and b-BK models for the dipole-proton scattering amplitude. The data from H1 are presented for a comparison [66]. One has that the HERA data for the energy dependence of the total cross section is well described by all models, with the b-BK and b-CGC predictions being similar. In contrast, the IP-sat and IP-nonSat predictions are steeper in energy, with the IP-nonSat predictions being 20% larger than the IP-Sat one for large energies. Our results indicate that the difference between the predictions increase with energy and with the decreasing of the photon virtuality. Such results are expected, since the impact of the saturation effects is larger for small values of x and/or Q^2. In the lower panels of Fig. 4, we present the results for $d\sigma/dt$, which indicate that the large-t behaviour of the differential distribution is sensitive to dipole model considered. In particular, the b-BK model predicts a milder decrease with t in the kinematical range probed by HERA. This result seems to disfavor the b-BK model with respect to the other CGC-inspired models, with the discrepancy growing with increasing Q^2. This may suggest that effects related to the Q^2 evolution starts to play a role and that the model based on the b-BK solutions doesn't include these effects to a necessary extent. However, since the total cross section seems to be well described and the model provided good description of other processes in previous studies (see e.g. [54,55,67]), we have decided not to disregard this model in the subsequent predictions for future experiments which may come with new results with respect to the previous measurements.

Exclusive events characterized by larger values of $|t|$ than those observed at HERA are expected to be measured in future ep colliders. That will allow us to probe the presence and position of dips predicted to occur in diffractive processes when nonlinear effects are taken into account. In Fig. 5, we present our predictions for the t-distribution of the DVCS process in ep collisions at the EIC (upper panels) and LHeC (lower panels) considering distinct models for $\mathcal{N}_p$. The results indicate that the distribution strongly depends on the model considered. In particular, the IP-nonSat model does not predict the presence of a dip in the $|t|$-distribution. In contrast, the models based on the CGC physics predict dips at large values of $|t|$, with its positions being dependent

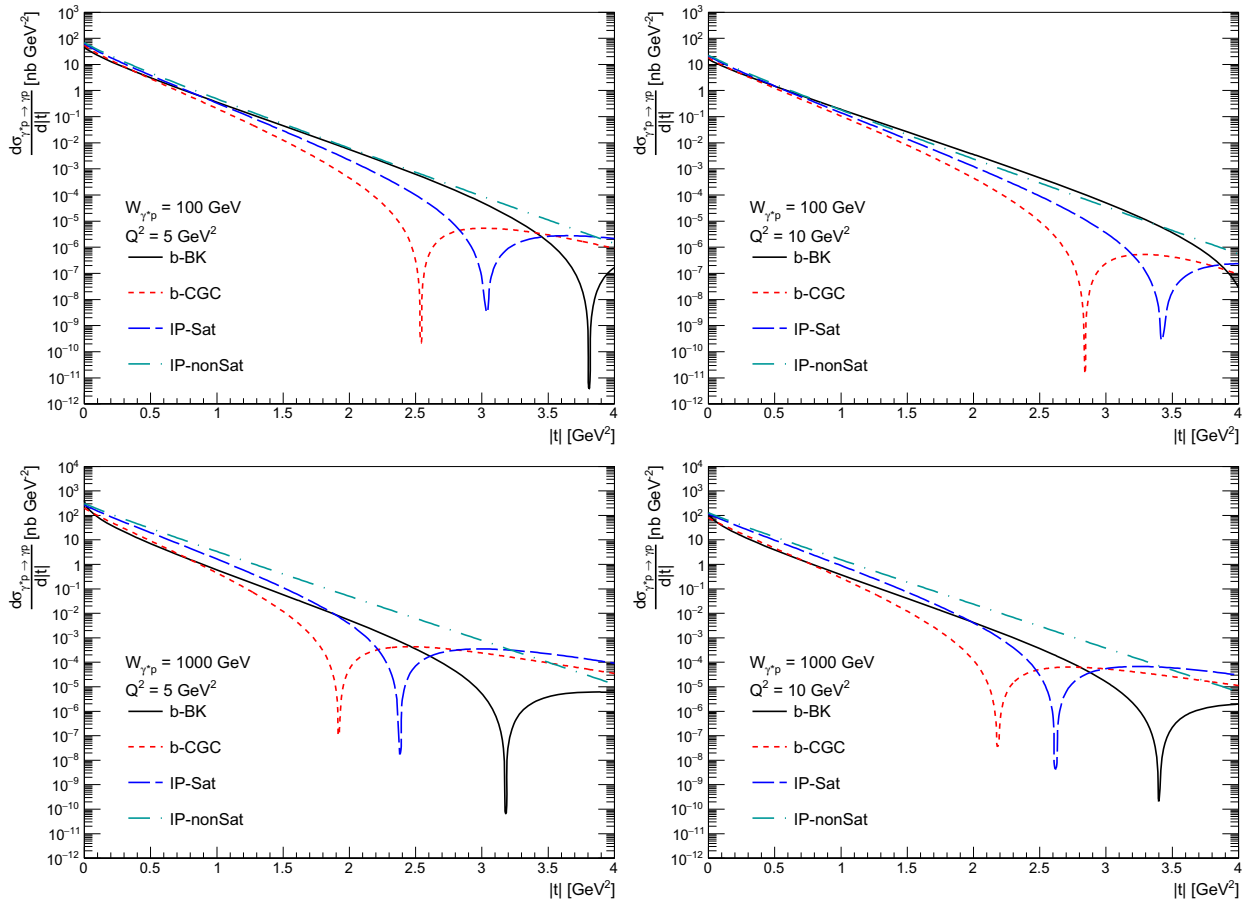

Fig. 5 Predictions for the t-distributions of the DVCS process in ep collisions at the EIC (upper panels) and LHeC (lower panels) derived considering distinct models for the dipole-proton scattering amplitude and different values of the photon virtuality

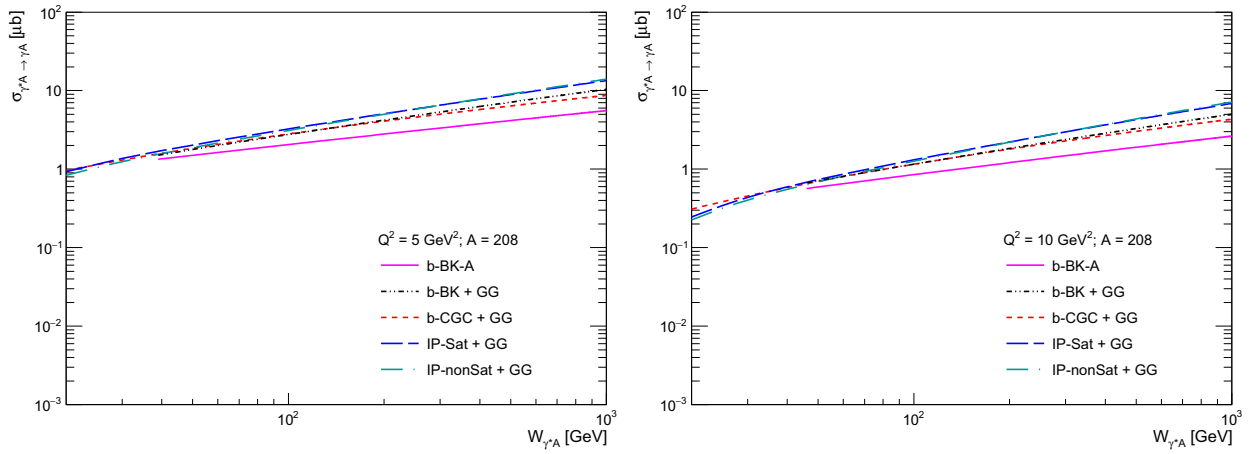

Fig. 6 Predictions for the energy dependence of the nuclear DVCS cross section considering distinct models for the dipole-nucleus scattering amplitude, $A = Pb$, and different values of the photon virtuality

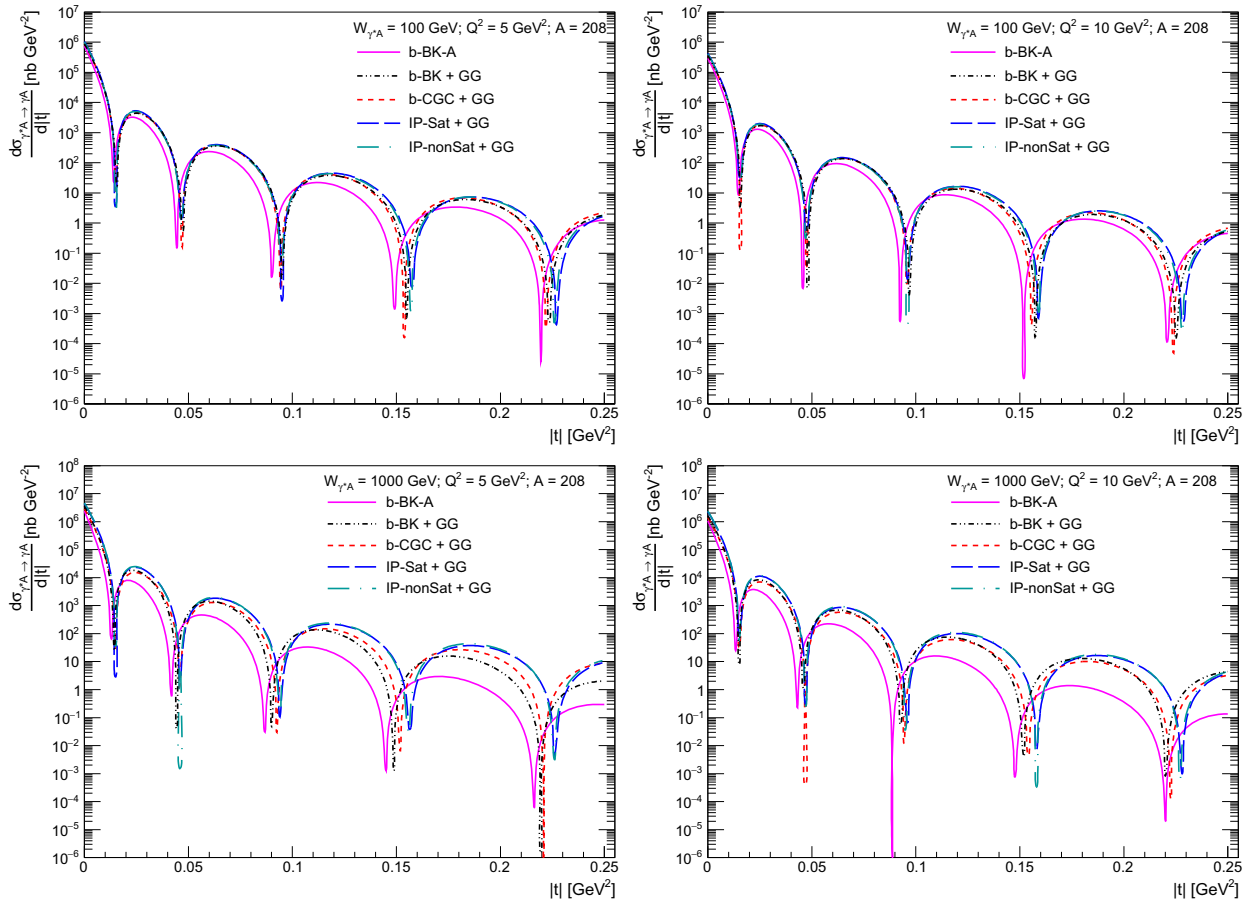

Fig. 7 Predictions for the t-distribution of the nuclear DVCS process at the EIC (upper panels) and LHeC (lower panels) derived considering distinct models for the dipole-nucleus scattering amplitude, $A = Pb$, and different values of the photon virtuality

on the model considered. One has that the first dip occurs for smaller values of $|t|$ when the center-of-mass energy is increased and/or when a smaller value of the photon virtuality is assumed. The large difference in the position of the dips predicted by the distinct models implies that a future measurement could be able to discriminate between these different approaches for the QCD dynamics at high energies.

In what follows, we will consider the DVCS process in eA collisions. Such analysis is motivated by the expectation that nuclei are an efficient amplifier of nonlinear effects [29–31]. The predictions for the energy dependence of the total DVCS cross section for a nuclear target ($A = Pb$) are presented in Fig. 6. One has that they are similar for small W but can differ by a factor $\gtrsim 2$ at the LHeC energy scale. The IP-Sat + GG and IP-nonSat + GG predictions appear to be almost identical for the values of Q^2 considered. We have verified that they start to be different for smaller values of the photon virtuality, where the impact of the nonlinear effects at the proton level becomes more significant. Moreover, the b-CGC + GG and b-BK + GG predictions are similar even with increasing energy, while the b-BK-A one is the lowest of the presented models for the magnitude of the total cross section.

In Fig. 7, we present the predictions for the t-distributions of the nuclear DVCS process at the EIC (upper panels) and LHeC (lower panels) for two values of photon virtuality and $A = Pb$, derived considering distinct models for the dipole-nucleus scattering amplitude. One has that the position of the first two dips are similar for the predictions based on Glauber–Gribov approach and become gradually distinct at larger values of $|t|$. In other words, in order to discriminate the treatment of the QCD dynamics at the proton level, we should probe values of $|t| \gtrsim 0.1$ GeV^2. In contrast, future data for smaller values of $|t|$ can be useful to discriminate between the GG and the b-BK-A approaches for the dipole-nucleus scattering amplitude. Our results indicate that the difference between the predictions increases with the center-of-mass energy, becoming appreciable in the LHeC kinematic range.

A comment is order. One has verified that similar results are obtained for $A = 40$, with the main differences being the smaller normalizations, decrease of the difference between

the predictions and the change in the position of the dips. These results indicate that the study of eA collisions with lighter nuclei can also be useful, in particular due to the different atomic number dependence of the saturation scale predicted by the nonlinear approaches considered in our analysis.

4 Summary

The experimental analysis of the diffractive observables in future electron-hadron collisions at EIC and LHeC is expected to improve our understanding about the QCD dynamics at high parton densities and the multi-dimensional description of the partons within the hadrons. In particular, the study of the deeply virtual Compton scattering is predicted to be a probe of the gluon Wigner distribution. In this paper, we have investigated the impact of the distinct treatments for the nonlinear (saturation) effects on the DVCS process. We have presented, for the first time, the predictions derived using the solution of the impact-parameter dependent Balitsky–Kovchegov equation for the dipole-target scattering amplitude. We have presented these predictions for ep and eA collisions, considering the kinematic ranges that will be probed by the future EIC and LHeC colliders. A comprehensive comparison with the predictions derived using alternative saturation approaches was performed. Our results demonstrate that the cross section and t-distribution are strongly dependent on the assumption for the impact-parameter dependence of the dipole-target scattering amplitude. As a consequence, we predict that the tomography picture of a hadron will be sensitive to the nonlinear effects. Such results indicate that a future experimental analysis of the DVCS process will be useful to improve our understanding of QCD dynamics and hadronic structure.

Acknowledgements VPG would like to thank the members of the Czech Technical University in Prague for the warm hospitality during the beginning of this project. VPG and CRS were partially financed by the Brazilian funding agencies CNPq, FAPERGS and INCT-FNA (processes number 464898/2014-5). This work has been supported by the Centre of Advanced Applied Sciences with the number: CZ.02.1.01/0.0/0.0/16-019/0000778. The Centre of Advanced Applied Sciences is co-financed by the European Union.

Data Availability Statement This manuscript has no associated data or the data will not be deposited. [Authors' comment: This is a theoretical research study, and is based upon analysis of the public experimental data, so no additional data is associated with this work.]

Funded by SCOAP[3].

References

1. D. Boer, M. Diehl, R. Milner, R. Venugopalan, W. Vogelsang, D. Kaplan, H. Montgomery, S. Vigdor et al., arXiv:1108.1713 [nucl-th]
2. A. Accardi, J.L. Albacete, M. Anselmino, N. Armesto, E.C. Aschenauer, A. Bacchetta, D. Boer, W. Brooks et al., Eur. Phys. J. A **52**(9), 268 (2016)
3. E.C. Aschenauer et al., Rep. Prog. Phys. **82**(2), 024301 (2019)
4. J.L. Abelleira Fernandez et al., J. Phys. G **39**, 075001 (2012)
5. P. Agostini et al., arXiv:2007.14491 [hep-ex]
6. X.D. Ji, J. Phys. G **24**, 1181–1205 (1998)
7. K. Goeke, M.V. Polyakov, M. Vanderhaeghen, Prog. Part. Nucl. Phys. **47**, 401–515 (2001)
8. X. Ji, Phys. Rev. Lett. **91**, 062001 (2003)
9. M. Diehl, Phys. Rep. **388**, 41–277 (2003)
10. A.V. Belitsky, X. d Ji, F. Yuan, Phys. Rev. D **69**, 074014 (2004)
11. A.V. Belitsky, A.V. Radyushkin, Phys. Rep. **418**, 1–387 (2005)
12. M. Diehl, Eur. Phys. J. A **52**(6), 149 (2016)
13. Y. Hagiwara, Y. Hatta, T. Ueda, Phys. Rev. D **94**(9), 094036 (2016)
14. Y. Hatta, B.W. Xiao, F. Yuan, Phys. Rev. Lett. **116**(20), 202301 (2016)
15. T. Altinoluk, N. Armesto, G. Beuf, A.H. Rezaeian, Phys. Lett. B **758**, 373–383 (2016)
16. H. Mäntysaari, N. Mueller, B. Schenke, Phys. Rev. D **99**(7), 074004 (2019)
17. F. Salazar, B. Schenke, Phys. Rev. D **100**(3), 034007 (2019)
18. Y. Hatta, N. Mueller, T. Ueda, F. Yuan, Phys. Lett. B **802**, 135211 (2020)
19. D. Boer, C. Setyadi, Phys. Rev. D **104**(7), 074006 (2021)
20. X.D. Ji, Phys. Rev. D **55**, 7114–7125 (1997)
21. Y. Hatta, B.W. Xiao, F. Yuan, Phys. Rev. D **95**(11), 114026 (2017)
22. H. Mäntysaari, K. Roy, F. Salazar, B. Schenke, Phys. Rev. D **103**(9), 094026 (2021)
23. M. McDermott, R. Sandapen, G. Shaw, Eur. Phys. J. C **22**, 655–666 (2002)
24. L. Favart, M.V.T. Machado, Eur. Phys. J. C **29**, 365–371 (2003)
25. H. Kowalski, L. Motyka, G. Watt, Phys. Rev. D **74**, 074016 (2006)
26. M.V.T. Machado, Eur. Phys. J. C **59**, 769–776 (2009)
27. E.C. Aschenauer, S. Fazio, K. Kumericki, D. Mueller, JHEP **09**, 093 (2013)
28. V.P. Gonçalves, D.S. Pires, Phys. Rev. C **91**(5), 055207 (2015)
29. F. Gelis, E. Iancu, J. Jalilian-Marian, R. Venugopalan, Ann. Rev. Nucl. Part. Sci. **60**, 463 (2010)
30. H. Weigert, Prog. Part. Nucl. Phys. **55**, 461 (2005)
31. J. Jalilian-Marian, Y.V. Kovchegov, Prog. Part. Nucl. Phys. **56**, 104 (2006)
32. J. Jalilian-Marian, A. Kovner, L. McLerran, H. Weigert, Phys. Rev. D **55**, 5414 (1997)
33. J. Jalilian-Marian, A. Kovner, and H. Weigert, Phys. Rev. D **59**, 014014 (1999). *ibid.***59**, 014015 (1999). *ibid.***59**, 034007 (1999)
34. A. Kovner, J. Guilherme Milhano, H. Weigert, Phys. Rev. D **62**, 114005 (2000)
35. H. Weigert, Nucl. Phys. A **703**, 823 (2002)
36. E. Iancu, A. Leonidov, L. McLerran, Nucl. Phys. A **692**, 583 (2001)

37. E. Ferreiro, E. Iancu, A. Leonidov, L. McLerran, Nucl. Phys. A **701**, 489 (2002)
38. A.H. Rezaeian, M. Siddikov, M. VandeKlundert, R. Venugopalan, Phys. Rev. D **87**, 034002 (2013)
39. H. Kowalski, D. Teaney, Phys. Rev. D **68**, 114005 (2003)
40. A.H. Rezaeian, I. Schmidt, Phys. Rev. D **88**, 074016 (2013)
41. I.I. Balitsky, Phys. Rev. Lett. **81**, 2024 (1998)
42. I.I. Balitsky, Phys. Lett. B **518**, 235 (2001)
43. I.I. Balitsky, A.V. Belitsky, Nucl. Phys. B **629**, 290 (2002)
44. Y.V. Kovchegov, Phys. Rev. D **60**, 034008 (1999)
45. Y.V. Kovchegov, Phys. Rev. D **61**, 074018 (2000)
46. R.J. Glauber, in *Lecture in Theoretical Physics*, ed. by W.E. Brittin, L.G. Duham, vol. 1 (Interscience, New York, 1959)
47. V.N. Gribov, Sov. Phys. JETP **29**, 483 (1969)
48. V.N. Gribov, Sov. Phys. JETP **30**, 709 (1970)
49. A.H. Mueller, Nucl. Phys. B **335**, 115 (1990)
50. N. Armesto, Eur. Phys. J. C **26**, 35 (2013)
51. H. Kowalski, T. Lappi, R. Venugopalan, Phys. Rev. Lett. **100**, 022303 (2008)
52. E.R. Cazaroto, F. Carvalho, V.P. Goncalves, F.S. Navarra, Phys. Lett. B **671**, 233 (2009)
53. H. Kowalski, T. Lappi, C. Marquet, R. Venugopalan, Phys. Rev. C **78**, 045201 (2008)
54. J. Cepila, J.G. Contreras, M. Matas, Phys. Rev. D **99**(5), 051502 (2019)
55. D. Bendova, J. Cepila, J.G. Contreras, M. Matas, Phys. Rev. D **100**(5), 054015 (2019)
56. J. Cepila, J.G. Contreras, M. Matas, Phys. Rev. C **102**(4), 044318 (2020)
57. J.L. Albacete, Nucl. Phys. A **957**, 71–84 (2017)
58. E. Iancu, J.D. Madrigal, A.H. Mueller, G. Soyez, D.N. Triantafyllopoulos, Phys. Lett. B **750**, 643–652 (2015)
59. B. Ducloue, E. Iancu, G. Soyez, D.N. Triantafyllopoulos, Phys. Lett. B **803**, 135305 (2020)
60. K.J. Golec-Biernat, A.M. Stasto, Nucl. Phys. B **668**, 345–363 (2003)
61. K.J. Eskola, P. Paakkinen, H. Paukkunen, C.A. Salgado, Eur. Phys. J. C **77**(3), 163 (2017)
62. H. Mäntysaari, P. Zurita, Phys. Rev. D **98**, 036002 (2018)
63. K. Golec-Biernat, M. Wusthoff, Phys. Rev. D **59**, 014017 (1999)
64. K. Golec-Biernat, M. Wusthoff, Phys. Rev. D **D60**, 114023 (1999)
65. A.G. Shuvaev, K.J. Golec-Biernat, A.D. Martin, M.G. Ryskin, Phys. Rev. D **60**, 014015 (1999)
66. F.D. Aaron et al. [H1], Phys. Lett. B **681**, 391–399 (2009)
67. D. Bendova, J. Cepila, J.G. Contreras, V.P. Gonçalves, M. Matas, Eur. Phys. J. C **81**(3), 211 (2021)